

Ultrafast Dynamics in Multifunctional Ru(II)-Loaded Polymers for Solar Energy Conversion

Published as part of the *Accounts of Chemical Research* special issue "Ultrafast Excited-State Processes in Inorganic Systems".

Zachary A. Morseth,[†] Li Wang,[†] Egle Puodziukynaite,[§] Gyu Leem,[§] Alexander T. Gilligan,[†] Thomas J. Meyer,[†] Kirk S. Schanze,[§] John R. Reynolds,[‡] and John M. Papanikolas^{*†}

[†]Department of Chemistry, University of North Carolina at Chapel Hill, Chapel Hill, North Carolina 27599, United States

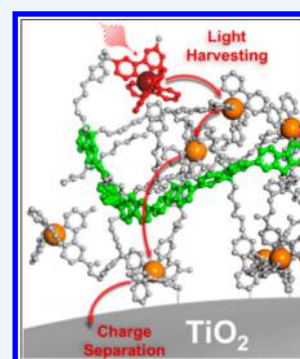
[‡]School of Chemistry and Biochemistry, School of Materials Science and Engineering, Center for Organic Photonics and Electronics, Georgia Institute of Technology, Atlanta, Georgia 30332, United States

[§]Department of Chemistry, Center for Macromolecular Science and Engineering, University of Florida, Gainesville, Florida 32611, United States

CONSPECTUS: The use of sunlight to make chemical fuels (i.e., solar fuels) is an attractive approach in the quest to develop sustainable energy sources. Using nature as a guide, assemblies for artificial photosynthesis will need to perform multiple functions. They will need to be able to harvest light across a broad region of the solar spectrum, transport excited-state energy to charge-separation sites, and then transport and store redox equivalents for use in the catalytic reactions that produce chemical fuels. This multifunctional behavior will require the assimilation of multiple components into a single macromolecular system.

A wide variety of different architectures including porphyrin arrays, peptides, dendrimers, and polymers have been explored, with each design posing unique challenges. Polymer assemblies are attractive due to their relative ease of production and facile synthetic modification. However, their disordered nature gives rise to stochastic dynamics not present in more ordered assemblies. The rational design of assemblies requires a detailed understanding of the energy and electron transfer events that follow light absorption, which can occur on time scales ranging from femtoseconds to hundreds of microseconds, necessitating the use of sophisticated techniques. We have used a combination of time-resolved absorption and emission spectroscopies with observation times that span 9 orders of magnitude to follow the excited-state evolution within polymer-based molecular assemblies. We complement experimental observations with molecular dynamics simulations to develop a microscopic view of these dynamics.

This Account provides an overview of our work on polymers decorated with pendant Ru(II) chromophores, both in solution and on surfaces. We have examined site-to-site energy transport among the Ru(II) complexes, and in systems incorporating π -conjugated polymers, we have observed ultrafast formation of a long-lived charge-separated state. When attached to TiO₂, these assemblies exhibit multifunctional behavior in which photon absorption is followed by energy transport to the surface and electron injection to produce an oxidized metal complex. The oxidizing equivalent is then transferred to the conjugated polymer, giving rise to a long-lived charge-separated state.



INTRODUCTION

Multifunctional molecular and macromolecular assemblies that are able to harvest light, separate charge, and utilize the resulting redox equivalents to drive solar fuels reactions are an integral component in many artificial photosynthetic strategies.^{1,2} Multifunctional behavior is achieved through a combination of fundamental energy and electron transfer events. While both of these processes have been extensively characterized in simple, well-defined systems consisting of only a few (often only two) molecular components, the structural complexity arising from the integration of multiple components leads to dynamical phenomena that are not found in dyads and triads. Thus, functionality in artificial assemblies cannot be understood through studies of individual components or small model systems.

The characterization of dynamical phenomena (e.g., charge and energy migration) in large polymer-based assemblies is a challenging problem. Transport phenomena, for example, depend upon the macromolecular structure, which in turn depends upon the polymer support and the chemical structure of the monomer. The spatial relationship of the monomer's excited-state wave function to other assembly components, rigidity of the polymer, solvent polarity, and the nature of the counterion can influence the structure and affect the exciton dynamics. In large macromolecular systems,^{3–13} the separation between adjacent components is described not by a single distance but rather by a distribution of distances that, in turn,

Received: October 16, 2014

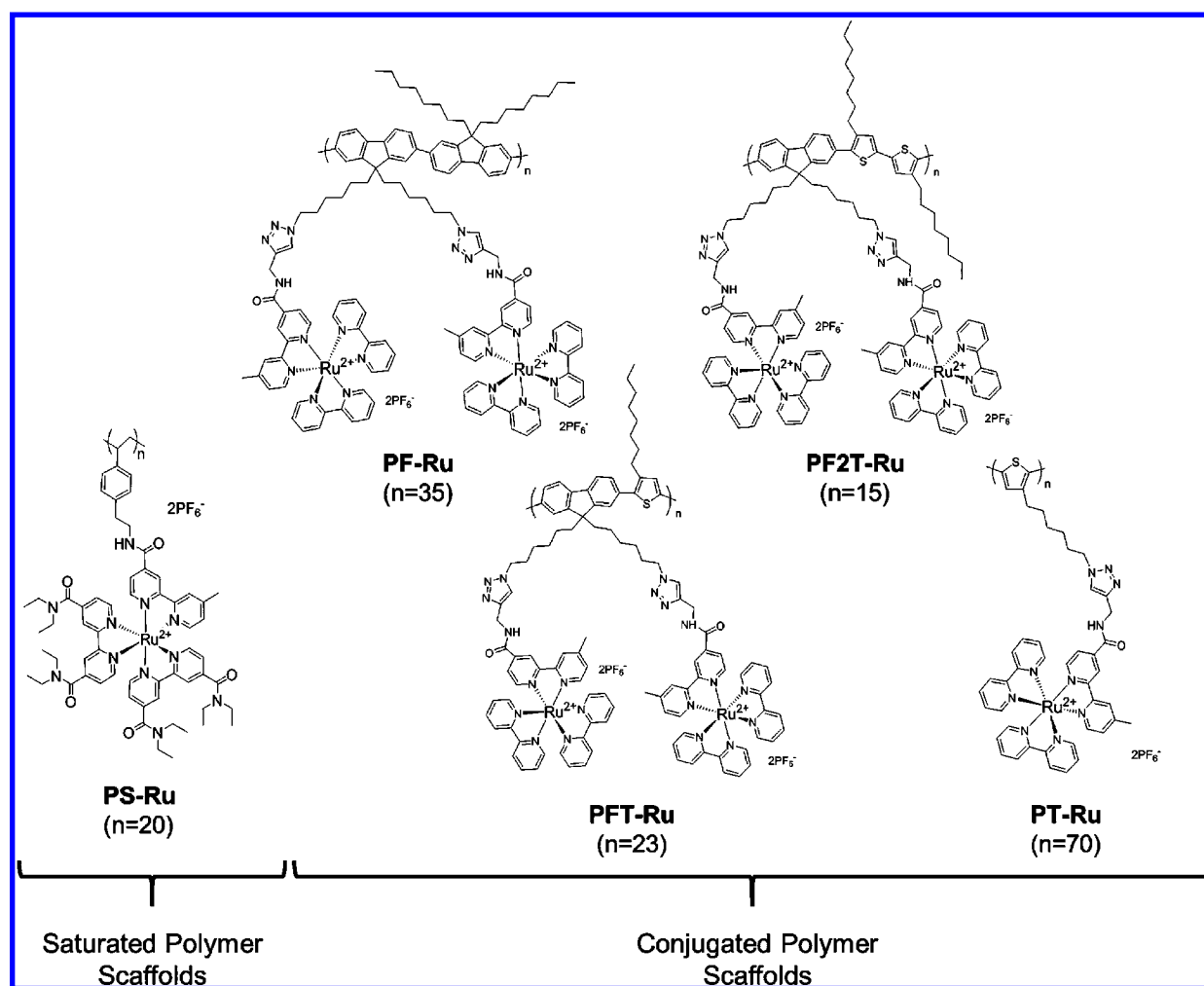


Figure 1. Chemical structures of polymer assemblies consisting of either saturated (PS-Ru) or π -conjugated backbones (PF-Ru, PFT-Ru, PF2T-Ru, and PT-Ru). The variable n refers to the average length of the polymer backbones.

results in a distribution of electron and energy transfer rates. Furthermore, the presence of flexible linkages can give rise to large-scale conformational motions that can occur on time scales similar to the transfer rates,¹⁴ leading to rate constants that may be more influenced by molecular motions than the quantities normally associated with electron and energy transfer, including electronic couplings, reorganization energies, and driving forces.¹⁵ Thus, even the relatively simple process of site-to-site energy transport will exhibit highly nonexponential kinetics, and disentangling contributions from the various dynamical phenomena can oftentimes only be accomplished through the use of sophisticated simulations and modeling to extract intrinsic rates from experimental data.

In this Account, we focus on the ultrafast dynamics of polymeric assemblies consisting of multiple Ru(II) polypyridyl complexes linked together by a polymer backbone (Figure 1). We have used a combination of ultrafast spectroscopic methods and computer simulation (Monte Carlo and molecular dynamics) to characterize the fundamental photophysical processes that take place on time scales ranging from several hundred femtoseconds to hundreds of microseconds. Early work from our laboratory focused on light-harvesting assemblies utilizing poly(styrene) (PS) as the scaffold.^{4,16–19} The electronic states of the polymer lie at higher energy, and as a result, visible excitation occurs at the pendant metal

complexes. The PS serves only a structural function, holding the metal complexes in close proximity to one another to facilitate excited-state transport. More recent work has explored assemblies based on π -conjugated polymers.^{20–22} Here, not only does the polymer serve as a structural support, but because of its strongly allowed $\pi \rightarrow \pi^*$ transitions, it can also function as a secondary light-absorbing component.

Excitation of the polymer results in either energy transfer to the pendants or electron transfer from the polymer to one of the pendant metal complexes, producing a charge-separated state that persists from nanoseconds to microseconds. Multifunctional behavior is readily apparent in PF-Ru assemblies attached to TiO₂. With the use of transient absorption spectroscopy across a broad range of time scales, we observe light harvesting by the pendant complexes, charge separation at the interface, and transfer of the oxidative equivalents to the backbone, resulting in a charge-separated state that persists for several hundreds of microseconds.

■ POLYMER STRUCTURES

The fundamental photophysical processes of energy and electron transfer that take place in these complex assemblies depend on the separation and relative orientation of the individual components. The macromolecular structure is determined by a number of factors, including the torsional

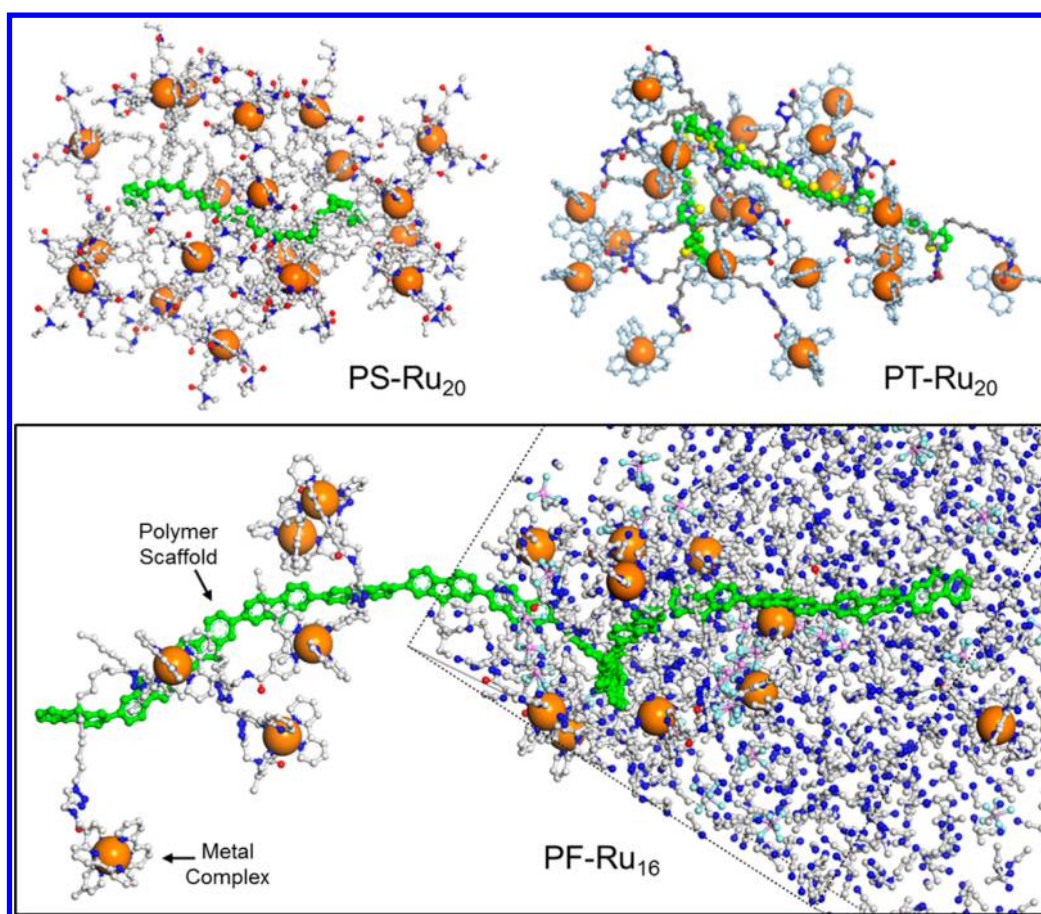


Figure 2. Condensed phase polymer assembly structures obtained from molecular dynamics simulations. Structures were calculated using periodic boundary conditions in the presence of explicit acetonitrile solvent and PF₆⁻ counterions. The polymer scaffold is shown in green color, and the Ru atoms are depicted as orange spheres with enlarged diameters. A portion of the solvent is shown in the PF-Ru₁₆ structure.

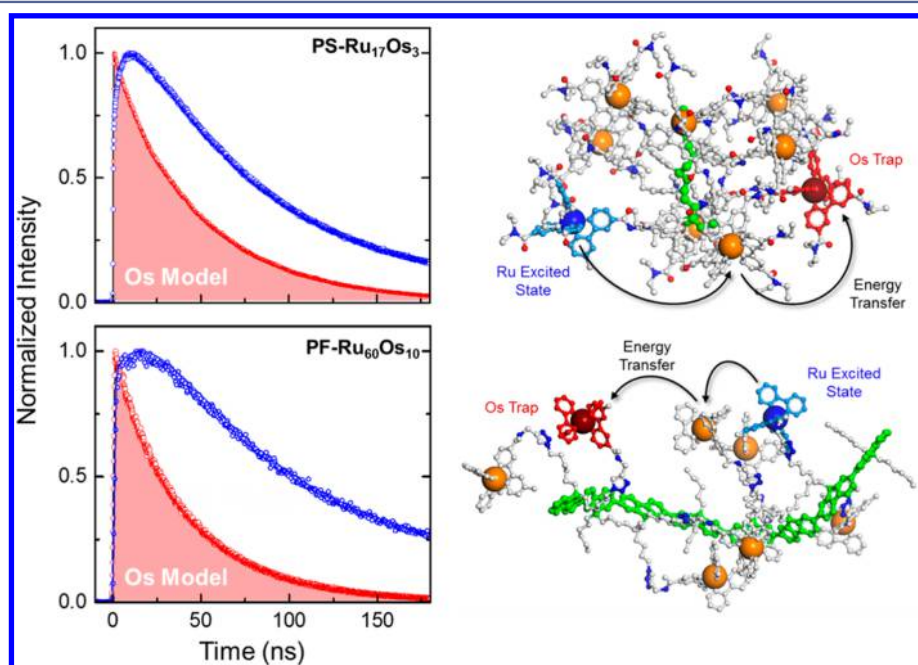


Figure 3. (left) Time resolved emission monitoring Os(II) photoluminescence in PS-Ru₁₇Os₃ and PF-Ru₆₀Os₁₀. (right) Illustration of site-to-site energy transport within a subsection of PS-Ru₁₇Os₃ (upper) and PF-Ru₆₀Os₁₀ (lower). The initial Ru excited state (blue) undergoes energy transfer to adjacent Ru complexes and is ultimately transferred to the Os trap (red).

flexibility of the backbone, the size and spacing of the pendant groups, the length of the side chains, and the solvent, which vary among the five different assemblies shown in Figure 1. In PS-Ru, for example, each repeat unit of the polymer scaffold is functionalized by a metal complex that is connected to the backbone by a short side chain (Figure 2). This dense chromophore loading combined with the flexible nature of the poly(styrene) causes significant twisting of the polymer backbone in order to accommodate the large pendant metal complexes. Monte Carlo and molecular dynamics simulations indicate that the structure is close-packed, with each complex lying within 2–3 Å of its neighbors.⁴ Whereas the macromolecular structure of the PS-Ru system is determined primarily by steric considerations and packing, the poly(fluorene)-Ru (PF-Ru) and poly(thiophene)-Ru (PT-Ru) structures are more heavily influenced by intramolecular and intermolecular forces (Figure 2). The conjugated π -network present in PF and PT reduces the torsional flexibility of the scaffold, resulting in more extended structures, and this combined with the significantly longer side chains leads to larger average separations between adjacent complexes compared with PS-Ru. Solvent can also play a significant role, particularly in the more open PF-Ru and PT-Ru systems. Polar solvents have favorable interactions with the pendant complexes but not the polymer backbone, and as a result the assembly may adopt a structure where the side chains extend out into the solvent or one in which the metal complexes take positions near the polymer to shield it from the more polar environment.

■ SITE-TO-SITE ENERGY TRANSPORT

Site-to-site energy migration is initiated through metal-to-ligand charge transfer (MLCT) excitation of one of the pendant Ru(II) complexes. The singlet MLCT state decays rapidly into a long-lived triplet MLCT, whose lifetime can extend from hundreds of nanoseconds to microseconds.²³ Because of the close proximity of the neighboring complexes, Ru* excitation migrates along the chain in a random-walk like fashion through a series of isoenergetic triplet–triplet (i.e., Dexter) energy transfer events between adjacent complexes. Energy transport is observed by replacing a small fraction of the Ru sites with Os(II) complexes, that is, PS-Ru₁₇Os₃ and PF-Ru₆₀Os₁₀. Because the Os sites have a lower energy excited state, they serve as traps that terminate the site-to-site random walk.^{4,16–18} Thus, photoexcitation of the Ru sites is followed by a delayed rise in the Os* emission, which is a clear signature of the transport of excited-state energy to the Os traps (Figure 3). (Note that the instantaneous rise in the emission intensity at $t = 0$ is not the result of Ru* \rightarrow Os energy transfer, but rather reflects a combination of emission resulting from both direct excitation of the Os sites and weak Ru emission that is also detected at the monitored wavelength, \sim 780 nm).

The energy transport process includes a series of Ru* \rightarrow Ru hops followed by a terminating Ru* \rightarrow Os energy transfer event. The growth in the Os* emission reflects the total time for this process and thus reflects both the hopping time (τ) and the number of hops needed to reach the trap. The latter depends upon the fraction of Os sites; the greater the Os loading, the fewer the number of hops needed and the faster the rise in the photoluminescence intensity. Thus, while the growth indicates the presence of energy transport, the rise time itself is not a direct measure of the intrinsic Ru* \rightarrow Ru hopping time.

Stochastic kinetic simulations provide a means of extracting the microscopic details of energy transport from the experimental data. The first step involves determining the macromolecular structure of the assembly using Monte Carlo simulation methods.⁴ A structure is selected from the ensemble, and each site is assigned to be Ru or Os according to the loading statistics. One of the Ru sites is selected as the initial location of the excited state and energy transfer rate constants (k_{EnT}) are calculated to its nearest neighbors using a Dexter formalism, that is, $k_{\text{EnT}}(R) = k_0 \exp(-\beta R)$, where R is the separation between sites, k_0 is the rate constant at closest contact, and β is an attenuation parameter that determines the falloff of the electronic coupling with distance.¹⁵ Because the chemical linkage connecting adjacent complexes contains a significant number of saturated carbons, the electronic coupling between sites arises primarily from direct orbital overlap between the donor and acceptor complexes. In this limit, β is \sim 1–2 Å⁻¹, making energy transfer extremely short-range.

Energy migration “trajectories” are propagated using a stochastic kinetic algorithm. The simulation averages many trajectories, each obtained by sampling different structures and loading configurations, to produce an output that is “fit” to the experimental data in an *ad hoc* fashion.²⁴ The simulations of energy transport in the PS-Ru₁₇Os₃ assembly reveals a distribution of hopping times ($\tau_{\text{avg}} = 1–3$ ns) with a broad distribution in the number of hops needed to reach the Os trap.

The wide variation in the number of hops needed to reach an Os site is (in part) a reflection of the significant chain-to-chain variation in the Os loading. The fraction of Os sites in PS-Ru₁₇Os₃ is 15%, but this represents an average of the entire ensemble of chains. We estimate that only a quarter of the chains have three Os complexes, while many (\sim 20%) have only one or none, and about 10% have six or more. For chains with a large fraction of Os sites, the number of hops needed to reach the trap may be as small as 2–3, but for chains with only a single Os site it may take tens or even hundreds of hops. The presence of migration trajectories with a large number of Ru* \rightarrow Ru hops is suggested by the persistence of sensitized Os emission 200–400 ns after excitation, well beyond the \sim 50 ns excited-state lifetime of the Os complex (Figure 3).

The energy transfer times observed in the PS-Ru₁₇Os₃ assembly (1–3 ns) are long compared with singlet–singlet (i.e., Förster) energy transfer times observed in many systems.^{25–27} Despite the slower energy transfer time, the transport of the excited state to the Os trap sites is extremely efficient. We estimate that about 95% of the Ru* excited states created on polymer chains with at least one Os complex are eventually transported to a trap site. The high transport efficiency in the PS-Ru assembly stems in part from the dense packing of the metal complexes, which ensures that a Ru* excited state is always in close contact with one of its neighbors. While this dense packing is important, the long lifetime of the Ru* excited state (\sim 1 μ s) also plays a role. Thus, even though the energy transfer time is long (1–3 ns), it is fast compared with the Ru* lifetime, suggesting that the efficiency of a single energy transfer step is greater than 99.7%.

Transient photoluminescence data collected from the PF-Ru₆₀Os₁₀ assembly also exhibits the delayed rise in the Os* emission that is characteristic of site-to-site transport (Figure 3). Compared with PS-Ru₁₇Os₃, the slower rise is suggestive of a longer time scale for energy transport. While we have not yet performed Monte Carlo simulations on this system, analysis of the emission spectra suggests \sim 80% of the Ru* excited states

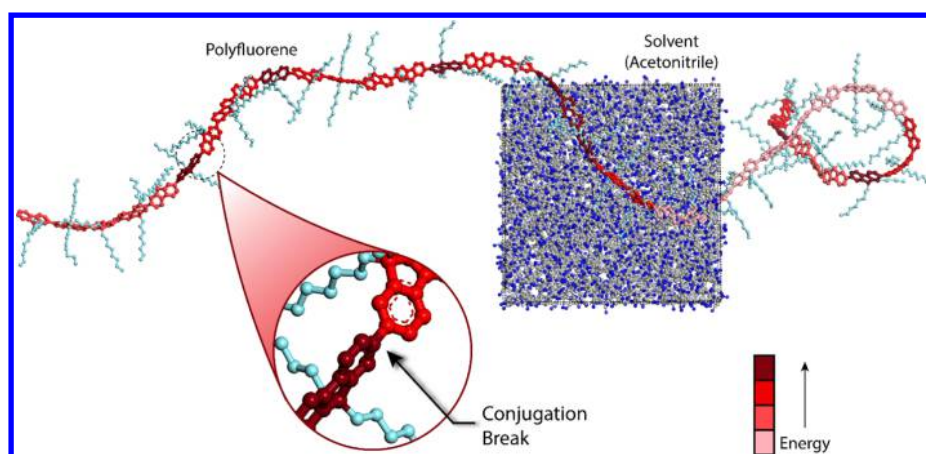


Figure 4. Condensed phase structure of a 40-repeat unit PF in explicit acetonitrile solvent obtained from molecular dynamics simulations. Most of the solvent is omitted for clarity, but a portion is shown for scale. The conformational subunits are colored based on the energy level with darker shades indicating subunits with shorter lengths and hence higher energies. The enlarged section shows a zoomed-in view of adjacent conformational subunits with a conjugation break.

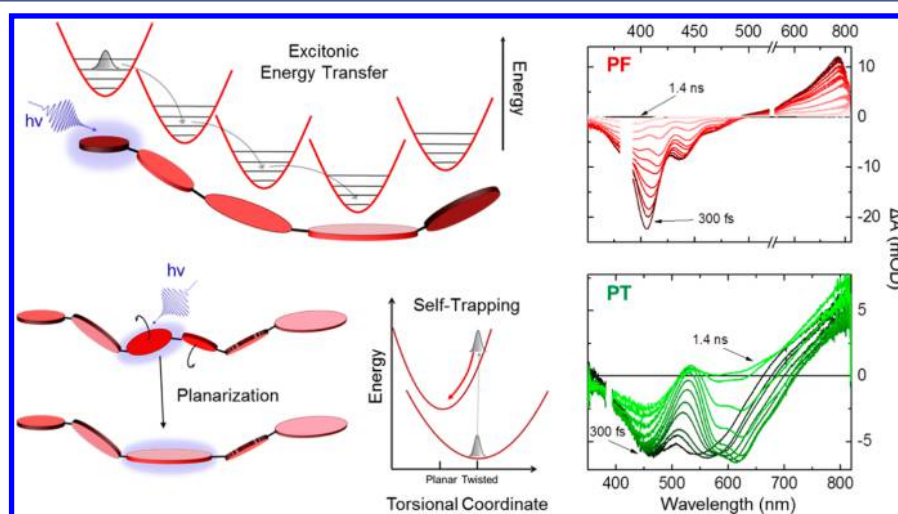


Figure 5. (left) Illustration of excitonic energy transfer (top) and excited-state self-trapping by torsional relaxation (bottom) along a π -conjugated polymer backbone following excitation into a high-energy conformational subunit. (right) Transient absorption difference spectra of unfunctionalized PF (upper) and PT (lower) from 300 fs to 1.4 ns following 388 nm excitation.

produced by photoexcitation are transferred to one of the Os sites. This relatively high efficiency is remarkable, especially given the low packing density of the metal complexes compared with PS-Ru₁₇Os₃ (Figure 3) and the close contact needed for triplet–triplet energy transfer. The high efficiency observed in the PF-Ru₆₀Os₁₀ assembly may be an indication that energy transport is facilitated by the conformational fluctuations that bring two complexes into close proximity where the short-range triplet–triplet energy transfer is possible. If this is the case, then one would anticipate that solvent viscosity could have a dramatic effect on the dynamical behavior when the chromophore density gives rise to large separations between complexes.

Conformational flexibility may not only help overcome the limitations of short triplet–triplet energy transfer distances but also mitigate effects of energetic disorder. The highly charged nature of the polymer and corresponding counterions gives rise to a heterogeneous electrostatic environment that lifts the degeneracy of neighboring sites. The lower energy sites act as shallow traps that impede energy transport. In fluid solution, like the examples discussed above, conformational motion is

constantly changing this environment, and the effects of energetic disorder are masked. When polymer assemblies are dispersed in rigid matrices, this conformational motion is frozen out on the time scale of energy hopping. As a result, energy transfer is biased toward lower energy, and once the lowest energy sites are reached, transport of the excited state slows considerably.²⁸ Transient photoluminescence experiments performed on assemblies embedded in rigid environments show evidence of the loss of conformational flexibility. Whereas emission spectra in fluid solution show little (or no) time-dependent shift in the band position, experiments on PS-Os₂₀ exhibit a clear red shift in the emission band with increasing time after excitation that results from this energetic disorder.¹⁷ The exploitation of conformational flexibility could be a powerful design concept in the development of multifunctional assemblies.

■ COMPETITIVE CHARGE SEPARATION AND ENERGY TRANSFER

In assemblies utilizing π -conjugated polymers, photoexcitation of delocalized $\pi \rightarrow \pi^*$ transitions in the visible gives rise to

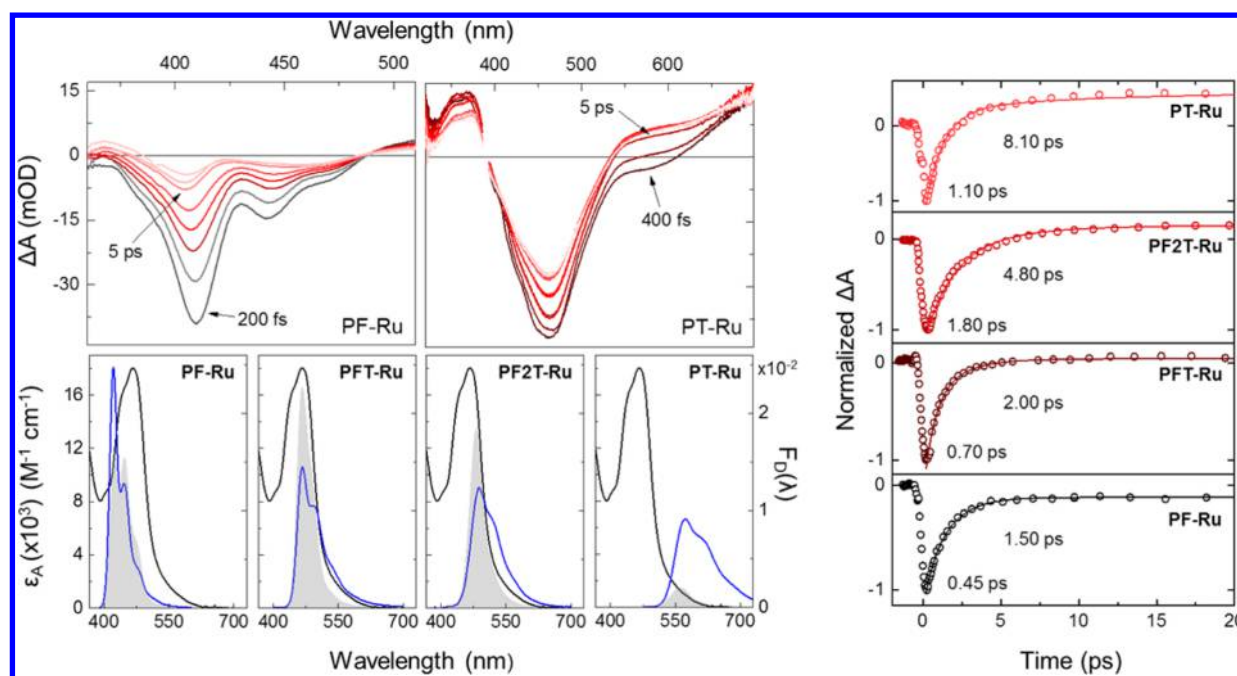


Figure 6. (left, top) Transient absorption difference spectra following primary excitation of the polymer backbone at 388 nm for PF-Ru (upper left) and PT-Ru (upper right). (left, bottom) Ru(II) absorbance ($\epsilon_A(\lambda)$) and normalized (to unit area) polymer emission spectra ($F_D(\lambda)$). The shaded gray area reflects the integrand, $F_D(\lambda)\epsilon_A(\lambda)\lambda^4$, which is scaled for clarity. (right) Kinetic traces of the polymer assemblies showing the initial polymer excited-state quenching during the first 20 ps following excitation.

additional dynamical phenomena. The excited-state dynamics of conjugated polymers have been studied extensively, both in solution and as thin films.^{29–33} Conformational disorder breaks up the conjugation along the backbone as a result of relatively low energy barriers for bond rotations between subunits, resulting in a chain of linked chromophores of varying conjugation lengths,^{34,35} as depicted in the PF structure in Figure 4. The final structure is an energetic compromise between the entropic gain associated with producing a disordered structure and the energetic destabilization that occurs upon breaking the conjugation. The broad absorbance spectrum of the solvated polymer is a manifestation of this disorder, with longer conjugation lengths contributing to the red edge of the spectrum and shorter to the blue.³³

Photoexcitation of PF and PT polymers results in a rich set of dynamical phenomena. On very short time scales (<100 fs), coupling of the excitation to small-scale torsional motions causes rapid relaxation and localization of the exciton onto a small number of monomer units.^{31,36} Transient spectra obtained on longer time scales from PF and PT (i.e., unfunctionalized) chains in solution are dominated by a series of negative-amplitude features in the blue that arise from a combination of ground-state bleach and stimulated emission, as well as a low-energy absorption associated with the singlet excited state of the polymer (Figure 5). The stimulated emission bands decay in amplitude (due to excited-state relaxation) and shift to lower energy with increasing time. The red shift is indicative of torsional relaxation or exciton migration.^{31,33,37,38} In PF, the stimulated emission shifts a few nanometers over several hundreds of picoseconds, due to a combination of large-scale conformational rearrangements and intrachain energy transfer to lower energy sites (Figure 5).^{31,32} In PT, the spectral changes are much more extensive, reflecting slow torsional relaxation that results in large-scale planarization of the backbone, such that by 100 ps, the fully relaxed excitons

are formed. It has been previously shown that additional exciton stabilization is achieved through the presence of strongly coupled low-frequency torsional degrees of freedom,³⁹ which is consistent with the greater spectral evolution (Stokes shift) observed in PT compared with PF. In both PF and PT, the exciton decays through either emission or intersystem crossing to form longer-lived triplet excitons.^{30,31}

The transient spectra obtained from PF-Ru following excitation of the PF backbone are dramatically altered by the presence of the pendant Ru complexes (Figure 6). The stimulated emission feature observed at early times resembles that seen in PF, but in PF-Ru it is quenched within several picoseconds. The transient spectra are also qualitatively different. Whereas in PF the stimulated emission shifts continuously to the red, in PF-Ru this band initially shifts to the red, but after a few picoseconds shifts back to higher energy. This behavior is the result of PF* quenching through a combination of energy and electron transfer mechanisms. Energy transfer to give a singlet Ru excited state (i.e., ${}^1\text{PF}^* + \text{Ru}^{2+} \rightarrow \text{PF} + {}^1\text{Ru}^{2+*}$) occurs with a time constant of 450 fs, accounting for ~85% of the PF* quenching events in PF-Ru, while electron transfer to produce a charge-separated state (i.e., ${}^1\text{PF}^* + \text{Ru}^{2+} \rightarrow \text{PF}^+ + \text{Ru}^{1+}$) takes place on a slower time scale, $\tau = 1.5$ ps. In PF-Ru, the apparent blue shift of the stimulated emission is due to the formation of PF⁺.

Assemblies incorporating PT, as well as scaffolds with mixed thiophene and fluorene content, PFT and PF2T (Figure 1), also show competitive energy and electron transfer. Like PF-Ru, all of these assemblies exhibit negative-going stimulated emission features that are quenched in the presence of the pendant Ru(II) complexes. Analysis of the quenching kinetics reveals that the electron transfer time across this series of polymers is relatively constant, varying between 1 and 2 ps (Figure 6).^{20–22} The energy transfer times, on the other hand, increase with greater thiophene content, and as a result, the

fraction of polymer excited states that decay through the energy transfer pathway also decreases across the series (Table 1).

Table 1. Energy and Electron Transfer Data for π -Conjugated Polymer Assemblies with Pendant Ru(II) Chromophores

assembly	energy transfer/ electron transfer ratio	energy transfer		electron transfer		
		τ (ps)	τ_{RET} (ps)	τ (ps)	$-\Delta G^\circ$ (eV)	λ (eV)
PF-Ru	85:15	0.45	0.45	1.5	0.72	↑
PFT-Ru	75:25	0.7	1.2	2.0	0.45	0.50–0.75
PF2T-Ru	25:75	4.8	4.0	1.8	0.46	
PT-Ru	15:85	8.1	10.0	1.1	0.50	↓

The trend in energy transfer rates across the polymer series can be understood in terms of the absorption and emission properties of assemblies. The rate constant for resonant energy transfer (RET) between a donor (D) and acceptor (A) separated by a distance R is given by

$$\frac{1}{\tau_{\text{RET}}} = \frac{1}{\tau_{\text{D}}} \left(\frac{R_0}{R} \right)^6 \quad (1)$$

where τ_{D} is the excited-state lifetime of the donor and R_0 is the Förster distance, the distance at which energy transfer is 50% efficient. The Förster distance can be estimated from independent spectroscopic measurements of the donor and acceptor according to

$$R_0^6 = A\Phi_{\text{D}}\kappa^2 \int_0^\infty F_{\text{D}}(\lambda)E_{\text{A}}(\lambda)\lambda^4 d\lambda \quad (2)$$

where Φ_{D} is the quantum yield of the donor in the absence of the acceptor and κ is a factor describing the relative orientations

of the donor and acceptor. The constant A is given by $A = 9000(\ln 10)/(128\pi^5 n^4 N_{\text{A}})$, where n is the refractive index and N_{A} is Avogadro's number. The integral in eq 2 describes the product of the emission spectrum of the donor normalized to unity area and the absorption spectrum of the acceptor, as illustrated in Figure 6.

The large energy transfer rate constant observed in the PF-Ru assembly results from the significant spectral overlap between the PF emission and the Ru absorption (Figure 6) and large quantum yield of PF*. The decrease in the energy transfer rate across the series is attributed to a systematic shift in the emission spectrum to lower energy with increasing thiophene content, which results in an overall decrease in the overlap between the donor emission and acceptor absorption, as well as a decrease in the quantum yield of the polymer (Φ_{D}). Energy transfer rates predicted using eq 1 are in good agreement with the experimentally observed values (Table 1).^{20–22}

The lifetime of the charge-separated state produced by electron transfer also depends upon the polymer backbone. While the charge-separated state in PF-Ru undergoes recombination (i.e., back electron transfer) to reform the ground state with $\tau = 6$ ns, in PT-Ru, it decays with $\tau \approx 20 \mu\text{s}$. The dramatic difference between these two assemblies may be a consequence of the high hole mobility of the PT polymer backbone,⁴⁰ which could quickly and efficiently separate the electron and the hole.

MULTIFUNCTIONAL BEHAVIOR

The eventual utilization of molecular assemblies in artificial photosynthetic applications will require that they perform multiple functions, including light harvesting and charge separation, as well as storage and transport of redox equivalents to catalytic sites. Multifunctional behavior is observed in the excited-state photophysics of PF-Ru assemblies anchored to TiO_2 through carboxylate groups placed on ~30% of the Ru

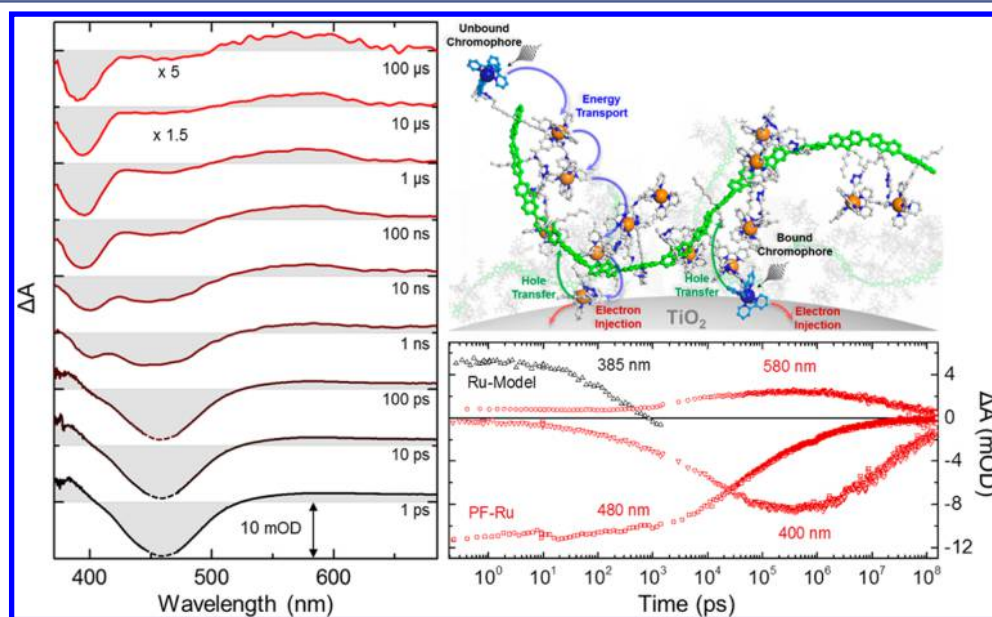


Figure 7. (left) Transient absorption difference spectra of a PF-Ru-loaded TiO_2 film following excitation at 450 nm from 1 ps to 100 μs . The 10 and 100 μs spectra have been scaled for clarity, while regions containing scatter from the 450 nm pump have been marked with a dashed line. (upper right) Illustration of the initial dynamic processes occurring following the excitation of the Ru(II) pendants within the PF-Ru assembly attached to the surface of a TiO_2 nanoparticle. (lower right) Combined kinetics traces from 200 fs to 150 μs for the PF-Ru assembly (red) at 400, 480, and 580 nm and the Ru-model (black) at 385 nm.

complexes.⁴¹ The result is a composite structure, in which the assembly is attached to the surface through a few complexes while the remaining chromophores serve as antennas for light absorption and excited-state transport.

The photophysics of this assembly on TiO₂ were studied across 9 decades of time using transient absorption spectroscopy. Photoexcitation of surface-bound Ru(II) sites results in prompt electron injection into the TiO₂, producing a Ru(III) species. The electron injection process is observed by monitoring the loss of the bipyridine radical anion (bpy^{•-}) absorption at 385 nm (Figure 7). Experiments performed on a model Ru complex that has the same ligand configuration as the pendant complexes in the PF-Ru assembly, but without the polymer backbone, show that the injection process is characterized by both fast ($\tau_1 = 60$ ps) and slow ($\tau_2 = 500$ ps) components.⁴² Following electron injection, the hole on the Ru(III) complex is transferred to the PF backbone, giving rise to the PF⁺ features at 400 and 580 nm that first appear at about 100 ps (Figure 7). The appearance of these features coincides with the loss of the Ru* due to electron injection, implying that hole transfer is fast ($\tau < 100$ ps) compared with the slower injection components. These PF⁺ features continue to grow in amplitude, reaching their peak at ~500 ns (Figure 7). This continued growth is attributed to photoexcitation of unbound complexes, which is followed by site-to-site energy transport of the excited state to the surface, electron injection, and transfer of the hole to the polymer (Figure 7). Charge recombination occurs between electrons within the TiO₂ and holes residing on the PF backbone. Monitoring the loss of the PF⁺ features indicates that the recombination time is greatly extended, with the charge-separated state persisting for up to 150 μ s. The formation of a long-lived charge-separated state is a desirable property for the production of solar fuels as it enables effective transfer of redox equivalents to be used in multielectron catalytic reactions.

SUMMARY AND CONCLUSIONS

The rational design of molecular assemblies for solar energy conversion will require a full understanding of the dynamical processes that occur following the absorption of light. The development of this detailed microscopic picture of the underlying energy and electron transfer events faces several challenges. Because of the structural complexity, the observed kinetics cannot be described by a single rate constant but reflect a superposition of many different processes that may include fundamental energy and electron transfer events, as well as conformational motions. Disentangling these contributions, which can span time scales ranging from femtoseconds to hundreds of microseconds, requires modeling that can link the observed kinetics to the underlying structure. Our work thus far has demonstrated that this is possible in systems exhibiting multiple functions, including light harvesting, charge separation, and storage. The lessons learned are being used in the design of the next generation of assemblies that will integrate catalytic sites for solar fuels production.

AUTHOR INFORMATION

Corresponding Author

*E-mail: john_papanikolas@unc.edu.

Funding

We gratefully acknowledge support from the UNC EFRC: Solar Fuels and Next Generation Photovoltaics, an Energy

Frontier Research Center funded by the U.S. Department of Energy, Office of Science, and Office of Basic Energy Sciences under Award Number DE-SC0001011.

Notes

The authors declare no competing financial interest.

Biographies

Zachary A. Morseth received his B.S. and B.A. from Minnesota State University—Moorhead and is currently a Ph.D. student at UNC—Chapel Hill under the direction of Professor John Papanikolas. His research interests include computational chemistry and the development and application of ultrafast methods in light-harvesting systems.

Li Wang received her undergraduate degree in Chemistry from Shanxi University in China and her Ph.D. in Chemistry from Memorial University in Canada. She then moved to UNC—Chapel Hill to work as a Postdoctoral Associate with Professor John Papanikolas. In 2014, she joined the Research Institute of Environmental Science at Shanxi University in China. Her research interests include the development and application of functional materials for environmental pollution control.

Egle Puodziukynaitė earned her undergraduate degree in Applied Chemistry from Kaunas University of Technology and her Ph.D. in Chemistry from the University of Florida with Professor John Reynolds. In 2013, she moved to University of Massachusetts—Amherst as a Postdoctoral Associate. Her research interests include electroactive and dipole-rich polymer platforms for application in organic optoelectronic devices.

Gyu Leem received his B.S. in chemical engineering from the Hanyang University and Ph.D. in Chemistry from the University of Houston in 2008. In 2009, he moved to LG Chem and worked in the division of petrochemical and polymer before joining the University of Florida with Professor Kirk Schanze as a Postdoctoral Associate in 2012. His research focuses on designing and synthesizing polymer-based metal chromophores for potential use in light-harvesting antennas.

Alexander T. Gilligan is currently completing his B.S. in Chemistry at the UNC—Chapel Hill. As a member of the Papanikolas group, he has performed molecular dynamics simulations on polymer assemblies.

Thomas J. Meyer was an early pioneer in the field of artificial photosynthesis with research published in the 1970s and was the first to design a molecular water oxidation catalyst. He has gained an international reputation in photochemistry, mechanisms, and chemical reactivity and catalysis. He is currently the Arey Professor of Chemistry at UNC—Chapel Hill and Director of the UNC Energy Frontier Research Center. His group is focused on water oxidation, carbon dioxide reduction, and DSPEC water splitting and CO₂ reduction to carbon fuels.

Kirk S. Schanze earned his B.S. in Chemistry from Florida State University and his Ph.D. in Chemistry from the UNC—Chapel Hill. He was appointed a Miller Postdoctoral Fellow at the University of California, Berkeley, and began his independent faculty career at the University of Florida in 1986, where he is currently a University Distinguished Professor and Prominski Professor of Chemistry. His research focuses on organic and organometallic materials chemistry.

John R. Reynolds received his B.S. in Chemistry from San Jose State University, and his M.S. and Ph.D. in Polymer Science and Engineering from the University of Massachusetts. In 1984, he joined the Chemistry faculty at the University of Texas at Arlington, moving to the Chemistry Department at the University of Florida in 1992, and subsequently joining the Schools of Chemistry and Biochemistry, along with Materials Science and Engineering, at the Georgia Institute

of Technology in 2012. His research interests are directed at electrically conducting and electroactive conjugated polymers.

John M. Papanikolas earned his B.A. in Chemistry from Bowdoin College and his Ph.D. in Chemical Physics from the University of Colorado at Boulder. Afterwards, he remained in Boulder as a Postdoctoral Associate, and in 1997, he joined the faculty in the Chemistry Department at UNC—Chapel Hill. His research focuses on the development and application of ultrafast spectroscopic methods to the study of molecular assemblies and nanomaterials.

REFERENCES

- (1) Alstrum-Acevedo, J. H.; Brennaman, M. K.; Meyer, T. J. Chemical Approaches to Artificial Photosynthesis. 2. *Inorg. Chem.* **2005**, *44*, 6802–6827.
- (2) Gust, D.; Moore, T. A.; Moore, A. L. Mimicking Photosynthetic Solar Energy Transduction. *Acc. Chem. Res.* **2001**, *34*, 40–48.
- (3) Sykora, M.; Maxwell, K. A.; DeSimone, J. M.; Meyer, T. J. Mimicking the Antenna-Electron Transfer Properties of Photosynthesis. *Proc. Natl. Acad. Sci. U.S.A.* **2000**, *97*, 7687–7691.
- (4) Fleming, C. N.; Maxwell, K. A.; DeSimone, J. M.; Meyer, T. J.; Papanikolas, J. M. Ultrafast Excited-State Energy Migration Dynamics in an Efficient Light-Harvesting Antenna Polymer Based on Ru(II) and Os(II) Polypyridyl Complexes. *J. Am. Chem. Soc.* **2001**, *123*, 10336–10347.
- (5) Fang, Z.; Ito, A.; Stuartt, A. C.; Luo, H. L.; Chen, Z. F.; Vinodgopal, K.; You, W.; Meyer, T. J.; Taylor, D. K. Soluble Reduced Graphene Oxide Sheets Grafted with Polypyridylruthenium-Derivatized Polystyrene Brushes as Light Harvesting Antenna for Photovoltaic Applications. *ACS Nano* **2013**, *7*, 7992–8002.
- (6) Devadoss, C.; Bharathi, P.; Moore, J. S. Energy Transfer in Dendritic Macromolecules: Molecular Size Effects and the Role of an Energy Gradient. *J. Am. Chem. Soc.* **1996**, *118*, 9635–9644.
- (7) Balzani, V.; Campagna, S.; Denti, G.; Juris, A.; Serroni, S.; Venturi, M. Designing Dendrimers Based on Transition Metal Complexes. *Light-Harvesting Properties and Predetermined Redox Patterns*. *Acc. Chem. Res.* **1998**, *31*, 26–34.
- (8) Nantalaksakul, A.; Reddy, D. R.; Bardeen, C. J.; Thayumanavan, S. Light Harvesting Dendrimers. *Photosynth. Res.* **2006**, *87*, 133–150.
- (9) McCafferty, D. G.; Friesen, D. A.; Danielson, E.; Wall, C. G.; Saderholm, M. J.; Erickson, B. W.; Meyer, T. J. Photochemical Energy Conversion in a Helical Oligoproline Assembly. *Proc. Natl. Acad. Sci. U.S.A.* **1996**, *93*, 8200–8204.
- (10) Knorr, A.; Galoppini, E.; Fox, M. A. Photoinduced Intramolecular Electron Transfer in Dichromophore-appended Alpha-helical Peptides: Spectroscopic Properties and Preferred Conformations. *J. Phys. Org. Chem.* **1997**, *10*, 484–498.
- (11) Serron, S. A.; Aldridge, W. S.; Fleming, C. N.; Danell, R. M.; Baik, M. H.; Sykora, M.; Dattelbaum, D. M.; Meyer, T. J. Evidence for Through-Space Electron Transfer in the Distance Dependence of Normal and Inverted Electron Transfer in Oligoproline Arrays. *J. Am. Chem. Soc.* **2004**, *126*, 14506–14514.
- (12) Wilger, D. J.; Bettis, S. E.; Materese, C. K.; Minakova, M.; Papoian, G. A.; Papanikolas, J. M.; Waters, M. L. Tunable Energy Transfer Rates via Control of Primary, Secondary, and Tertiary Structure of a Coiled Coil Peptide Scaffold. *Inorg. Chem.* **2012**, *51*, 11324–11338.
- (13) Bettis, S. E.; Ryan, D. M.; Gish, M. K.; Alibabaei, L.; Meyer, T. J.; Waters, M. L.; Papanikolas, J. M. Photophysical Characterization of a Helical Peptide Chromophore–Water Oxidation Catalyst Assembly on a Semiconductor Surface Using Ultrafast Spectroscopy. *J. Phys. Chem. C* **2014**, *118*, 6029–6037.
- (14) Davis, W. B.; Ratner, M. A.; Wasielewski, M. R. Conformational Gating of Long Distance Electron Transfer through Wire-like Bridges in Donor-Bridge-Acceptor Molecules. *J. Am. Chem. Soc.* **2001**, *123*, 7877–7886.
- (15) Barbara, P. F.; Meyer, T. J.; Ratner, M. A. Contemporary Issues in Electron Transfer Research. *J. Phys. Chem.* **1996**, *100*, 13148–13168.
- (16) Fleming, C. N.; Dupray, L. M.; Papanikolas, J. M.; Meyer, T. J. Energy Transfer between Ru(II) and Os(II) Polypyridyl Complexes Linked to Polystyrene. *J. Phys. Chem. A* **2002**, *106*, 2328–2334.
- (17) Fleming, C. N.; Jang, P.; Meyer, T. J.; Papanikolas, J. M. Energy Migration Dynamics in a Ru(II)- and Os(II)-Based Antenna Polymer Embedded in a Disordered, Rigid Medium. *J. Phys. Chem. B* **2004**, *108*, 2205–2209.
- (18) Fleming, C. N.; Brennaman, M. K.; Papanikolas, J. M.; Meyer, T. J. Efficient, Long-range Energy Migration in Ru-II Polypyridyl Derivatized Polystyrenes in Rigid Media. Antennae for Artificial Photosynthesis. *Dalton Trans.* **2009**, 3903–3910.
- (19) Shaw, G. B.; Papanikolas, J. M. Triplet-triplet Annihilation of Excited States of Polypyridyl Ru(II) Complexes Bound to Polystyrene. *J. Phys. Chem. B* **2002**, *106*, 6156–6162.
- (20) Wang, L.; Puodziukynaite, E.; Vary, R. P.; Grumstrup, E. M.; Walczak, R. M.; Zolotarskaya, O. Y.; Schanze, K. S.; Reynolds, J. R.; Papanikolas, J. M. Competition between Ultrafast Energy Flow and Electron Transfer in a Ru(II)-Loaded Polyfluorene Light-Harvesting Polymer. *J. Phys. Chem. Lett.* **2012**, *3*, 2453–2457.
- (21) Wang, L.; Puodziukynaite, E.; Grumstrup, E. M.; Brown, A. C.; Keinan, S.; Schanze, K. S.; Reynolds, J. R.; Papanikolas, J. M. Ultrafast Formation of a Long-Lived Charge-Separated State in a Ru-Loaded Poly(3-hexylthiophene) Light-Harvesting Polymer. *J. Phys. Chem. Lett.* **2013**, *4*, 2269–2273.
- (22) Puodziukynaite, E.; Wang, L.; Schanze, K. S.; Papanikolas, J. M.; Reynolds, J. R. Poly(fluorene-co-thiophene)-based Ionic Transition-Metal Complex Polymers for Solar Energy Harvesting and Storage Applications. *Polym. Chem.* **2014**, *5*, 2363–2369.
- (23) McCusker, J. K. Femtosecond Absorption Spectroscopy of Transition Metal Charge-transfer Complexes. *Acc. Chem. Res.* **2003**, *36*, 876–887.
- (24) Gillespie, D. T. Exact Stochastic Simulation of Coupled Chemical-reactions. *J. Phys. Chem.* **1977**, *81*, 2340–2361.
- (25) Chen, Z.; Grumstrup, E. M.; Gilligan, A. T.; Papanikolas, J. M.; Schanze, K. S. Light-Harvesting Polymers: Ultrafast Energy Transfer in Polystyrene-based Arrays of π -Conjugated Chromophores. *J. Phys. Chem. B* **2014**, *118*, 372–378.
- (26) Yeow, E. K. L.; Ghiggino, K. P.; Reek, J. N. H.; Crossley, M. J.; Bosman, A. W.; Schenning, A. P. H. J.; Meijer, E. W. The Dynamics of Electronic Energy Transfer in Novel Multiporphyrin Functionalized Dendrimers: A Time-Resolved Fluorescence Anisotropy. *J. Phys. Chem. B* **2000**, *104*, 2596–2606.
- (27) Kleiman, V. D.; Melinger, J. S.; McMorrow, D. Ultrafast Dynamics of Electronic Excitations in a Light-Harvesting Phenylacetylene Dendrimer. *J. Phys. Chem. B* **2001**, *105*, 5595–5598.
- (28) Akselrod, G. M.; Deotare, P. B.; Thompson, N. J.; Lee, J.; Tisdale, W. A.; Baldo, M. A.; Menon, V. M.; Bulovic, V. Visualization of Exciton Transport in Ordered and Disordered Molecular Solids. *Nat. Commun.* **2014**, *5*, No. 3646.
- (29) Bredas, J. L.; Beljonne, D.; Coropceanu, V.; Cornil, J. Charge-Transfer and Energy-Transfer Processes in π -Conjugated Oligomers and Polymers: A Molecular Picture. *Chem. Rev.* **2004**, *104*, 4971–5003.
- (30) Banerji, N.; Cowan, S.; Vauthey, E.; Heeger, A. J. Ultrafast Relaxation of the Poly(3-hexylthiophene) Emission Spectrum. *J. Phys. Chem. C* **2011**, *115*, 9726–9739.
- (31) Hintschich, S. I.; Dias, F. B.; Monkman, A. P. Dynamics of Conformational Relaxation in Photoexcited Oligofluorenes and Polyfluorene. *Phys. Rev. B* **2006**, *74*, No. 045210.
- (32) Nelson, T.; Fernandez-Alberti, S.; Roitberg, A. E.; Tretiak, S. Nonadiabatic Excited-state Molecular Dynamics: Modeling Photo-physics in Organic Conjugated Materials. *Acc. Chem. Res.* **2014**, *47*, 1155–1164.
- (33) Hwang, I.; Scholes, G. D. Electronic Energy Transfer and Quantum-Coherence in π -Conjugated Polymers. *Chem. Mater.* **2011**, *23*, 610–620.

(34) Bredas, J. L.; Heeger, A. J. Theoretical Investigation of Gas-Phase Torsion Potentials Along Conjugated Polymer Backbones - Polyacetylene, Polydiacetylene, and Polythiophene. *Macromolecules* **1990**, *23*, 1150–1156.

(35) Chen, H. L.; Huang, Y. F.; Lim, T. S.; Su, C. H.; Chen, P. H.; Su, A. C.; Wong, K. T.; Chao, T. C.; Chan, S. L.; Fann, W. Excited-State Backbone Twisting of Polyfluorene as Detected from Photo-thermal After-Effects. *J. Phys. Chem. B* **2009**, *113*, 8527–8531.

(36) Wells, N. P.; Blank, D. A. Correlated Exciton Relaxation in Poly(3-hexylthiophene). *Phys. Rev. Lett.* **2008**, *100*, No. 086403.

(37) Busby, E.; Carroll, E. C.; Chinn, E. M.; Chang, L. L.; Moule, A. J.; Larsen, D. S. Excited-State Self-Trapping and Ground-State Relaxation Dynamics in Poly(3-hexylthiophene) Resolved with Broadband Pump-Dump-Probe Spectroscopy. *J. Phys. Chem. Lett.* **2011**, *2*, 2764–2769.

(38) Westenhoff, S.; Beenken, W. J. D.; Friend, R. H.; Greenham, N. C.; Yartsev, A.; Sundstrom, V. Anomalous Energy Transfer Dynamics Due to Torsional Relaxation in a Conjugated Polymer. *Phys. Rev. Lett.* **2006**, *97*, No. 166804.

(39) Heimel, G.; Daghofer, M.; Gierschner, J.; List, E. J. W.; Grimsdale, A. C.; Mullen, K.; Beljonne, D.; Bredas, J. L.; Zojer, E. Breakdown of the Mirror Image Symmetry in the Optical Absorption/Emission Spectra of Oligo(para-phenylene)s. *J. Chem. Phys.* **2005**, *122*, 54501–54511.

(40) Sirringhaus, H.; Tessler, N.; Friend, R. H. Integrated Optoelectronic Devices Based on Conjugated Polymers. *Science* **1998**, *280*, 1741–1744.

(41) Leem, G.; Morseth, Z. A.; Puodziukynaite, E.; Jiang, J.; Zhen, F.; Gilligan, A. T.; Reynolds, J. R.; Papanikolas, J. M.; Schanze, K. S. Light-Harvesting and Charge-Separation in a π -Conjugated Antenna Polymer Bound to TiO₂. *J. Phys. Chem. C* **2014**, *118*, 28535–28541.

(42) It is interesting to note that this metal complex does not exhibit the sub-picosecond injection component that is commonly observed in dye-sensitized solar cells. Ongoing work in our laboratory suggests that its absence is the result of the ligand functionalization, which acts to lower the energy of the MLCT injecting state and slow injection.

Light Harvesting and Charge Separation in a π -Conjugated Antenna Polymer Bound to TiO_2

Gyu Leem,[†] Zachary A. Morseth,[‡] Egle Puodziukynaite,[†] Junlin Jiang,[†] Zhen Fang,[‡]
Alexander T. Gilligan,[‡] John R. Reynolds,[§] John M. Papanikolas,^{*,‡} and Kirk S. Schanze^{*,†}

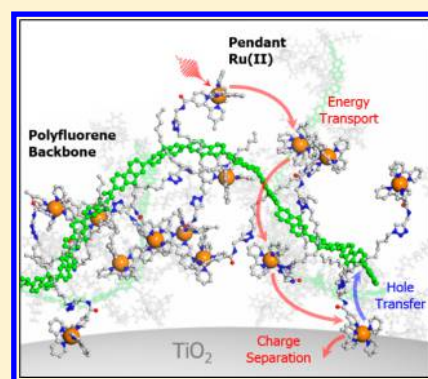
[†]Department of Chemistry, University of Florida, Gainesville, Florida 32611, United States

[‡]Department of Chemistry, University of North Carolina at Chapel Hill, Chapel Hill, North Carolina 27599, United States

[§]School of Chemistry and Biochemistry, School of Materials Science and Engineering, Center for Organic Photonics and Electronics, Georgia Institute of Technology, Atlanta, Georgia 30332, United States

S Supporting Information

ABSTRACT: This paper describes the photophysical and photoelectrochemical characterization of a light harvesting polychromophore array featuring a polyfluorene backbone with covalently attached Ru(II) polypyridyl complexes (PF-Ru-A), adsorbed on the surface of mesostructured TiO_2 (PF-Ru-A// TiO_2). The surface adsorbed polymer is characterized by transmission electron microscopy (TEM), scanning electron microscopy (SEM), and attenuated total reflectance-Fourier transform infrared (ATR-FTIR) spectroscopy, providing evidence for the morphology of the surface adsorbed polymer and the mode of binding. Photoexcitation of the Ru(II) complexes bound to the metal oxide surface (proximal) results in electron injection into the conduction band of TiO_2 , which is then followed by ultrafast hole transfer to the polymer to form oxidized polyfluorene (PF^+). More interestingly, chromophores that are not directly bound to the TiO_2 interface (distal) that are excited participate in site-to-site energy transfer processes that transport the excited state to surface bound chromophores where charge injection occurs, underscoring the antenna-like nature of the polymer assembly. The charge separated state is long-lived and persists for $>100 \mu\text{s}$, a consequence of the increased separation between the hole and injected electron.



INTRODUCTION

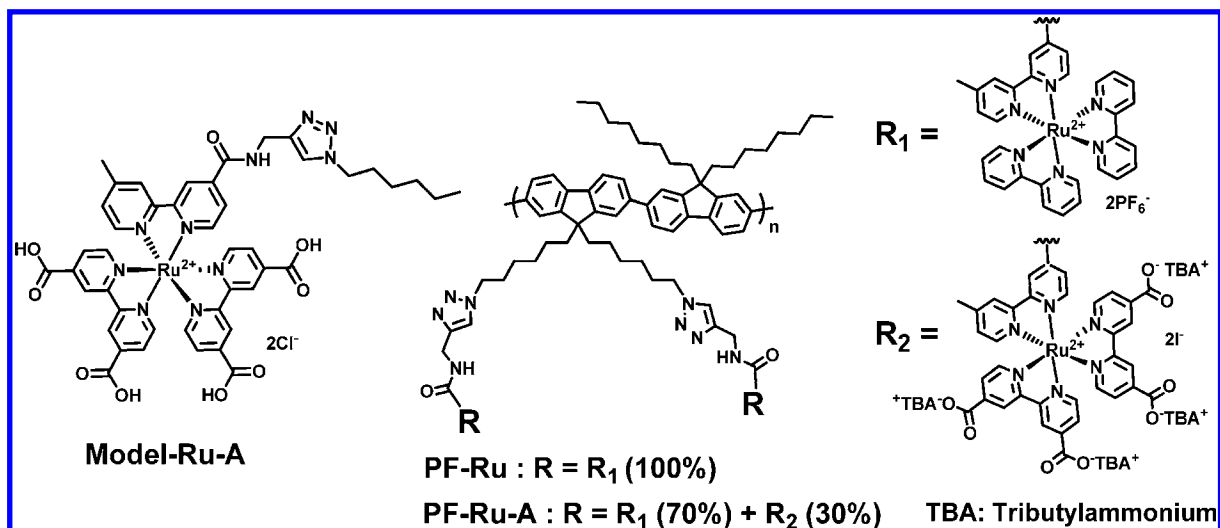
The development of molecular assemblies that mimic the characteristics of photosynthetic systems is central to the realization of solar fuel technologies. Using natural photosynthesis as a guide, artificial photosynthetic assemblies must be able to perform multiple functions spanning light harvesting, charge separation, and charge transfer of the redox equivalents to catalytic sites that drive multielectron reactions such as water oxidation or CO_2 reduction.^{1,2} Coupling of light harvesting to charge separation has been successfully demonstrated in a number of solution phase systems employing a broad range of sensitizers.^{3–5} Although these molecular systems elegantly demonstrate proof-of-concept principles regarding the photophysical mechanisms of directional energy flow, they are typically limited to a single or small group of chromophores and are difficult to synthesize, limiting their scalability to practical solar energy conversion applications. Multichromophore light harvesting assemblies based on polymers,^{6–8} dendrimers,⁹ and peptides¹⁰ are less challenging to synthesize and thus provide a potentially scalable architecture, but only a few examples exist in which multiple functions (e.g., light harvesting, energy transport, charge separation) are incorporated into a single assembly.^{10,11}

We previously reported the synthesis and photophysical study of a polyfluorene (PF)-based Ru(II) polypyridyl assembly (PF-Ru, Chart 1), where selective photoexcitation of the PF backbone gives rise to a kinetic competition between ultrafast energy and electron transfer to the pendant Ru(II) sites, producing a charge-separated state that persists for approximately 6 ns.⁶ In the present investigation, we describe an approach that anchors a structurally similar PF-based assembly through ionic carboxylate-functionalized Ru(II) chromophores to metal oxide (TiO_2) films. When bound to TiO_2 , the polymer exhibits multifunctional characteristics in which light absorption is coupled with energy transport and charge separation. Through pump–probe transient absorption methods the photophysical events are followed on time scales ranging from hundreds of femtoseconds to hundreds of microseconds. Photoexcitation of one of the Ru(II) complexes is followed by energy transport through site-to-site hopping to the interface, where electrons inject (i.e., charge separation) into the TiO_2 . Hole transfer from the oxidized Ru complex to the PF backbone regenerates the chromophore at the interface on the picosecond time scale. The holes that reside on the PF

Received: November 12, 2014

Published: November 17, 2014

Chart 1. Structure of Model-Ru-A, PF-Ru, and PF-Ru-A



backbone are stable for $>100 \mu\text{s}$, implying that the PF serves not only as a structural scaffold but also as a functional element that can transport and potentially store multiple oxidative equivalents, for consumption by relatively slow catalytic cycles.

EXPERIMENTAL SECTION

Materials. The required materials, i.e., 4,4'-dimethyl-2,2'-bipyridyl, selenium dioxide, silver nitrate, potassium dichromate, potassium hydroxide, *N,N'*-dicyclohexylcarbodiimide (DCC), *N*-hydroxysuccinimide (NHS), sodium azide, potassium carbonate, potassium acetate, 1,6-dibromohexane, 1-bromohexane, 1-bromooctane, fluorene, tetrabutylammonium bromide, tributylamine, 1,8-diazabicyclo[5.4.0]undec-7-ene (DBU), sodium ascorbate, 4-(dimethylamino)pyridine (DMAP), *N*-bromosuccinimide, copper(I) bromide (CuBr, 99.999%), hexafluorophosphoric acid solution (~55 wt % in H₂O), hydrochloric acid (37% in water), tetrabutylammonium hydroxide solution (~40 wt % in H₂O), and *N,N,N',N',N''*-pentamethyldiethylenetriamine (PMDETA), were purchased from Sigma-Aldrich. Ammonium hexafluorophosphate (NH₄PF₆), ruthenium(III) chloride hydrate, and *cis*-bis(2,2'-bipyridine)dichlororuthenium(II) dihydrate (Ru(bpy)₂Cl₂·2H₂O) were purchased from Alfa Aesar. Tetrakis(triphenylphosphine)palladium and dichloro[1,1'-bis(diphenylphosphino)ferrocene]palladium(II) dichloromethane adduct (Pd(dppf)Cl₂) were purchased from STREM Chemicals, Inc. All the chemicals were used as received unless otherwise indicated. Silica gel or alumina gel (reactivity grade I) was used for column chromatography. Dry solvents were obtained from a MBRAUN MB-SPS dry solvent system or purified using standard methods.¹² Solvents or liquid reagents for the use in a glovebox were also degassed using at least three freeze–pump–thaw cycles.

Synthesis of the Model-Ru-A and Polymer Assemblies PF-Ru-A. Synthesis details and characterization data for the new materials Model-Ru-A and PF-Ru-A are provided in the Supporting Information.

Fabrication of Dye Sensitized Solar Cells (DSSCs). The DSSCs were fabricated and modified following the literature.^{13,14} Briefly, the TiO₂ paste was doctor-bladed onto a clean FTO glass slide followed by sintering at 500 °C for 30 min with 1 °C of the heating and cooling rate. The TiO₂ layer

thickness was approximately 12–13 μm as measured by SEM. After cooling down to 80 °C, the annealed TiO₂ films were then dipped into the PF-Ru-A solution in a 1:2 (v/v) mixture of acetonitrile:methanol for 48 h. The PF-Ru-A//TiO₂ active cell area was controlled as 0.18 cm² to allow for consistent measurements of IPCE and *J*–*V* characteristics. A Pt counter electrode was prepared by spinning 0.01 M H₂PtCl₆ in isopropyl alcohol on FTO substrates with two holes created using a drill and by sintering 450 °C for 30 min. A Surlyn (25 μm, Solaronix) film as a spacer was sandwiched and fixed together at ~80 °C between PF-Ru-A//TiO₂ photoanode and a Pt counter electrode. Finally, an electrolyte solution containing 0.05 M I₂ and 0.1 M LiI, 0.5 M 4-*tert*-butylpyridine, and 0.6 M 1-methyl-3-*n*-propylimidazolium iodide in an anhydrous nitrite solution was injected into two holes on the Pt counter electrode side.

The current–voltage characteristics of the cells were measured with a Keithley 2400 source meter under AM1.5 (100 mW/cm²) solar simulator. For IPCE measurements, the cells were illuminated by monochromatic light from an Oriel Cornerstone spectrometer, and the current response under short circuit conditions was recorded at 10 nm intervals using a Keithley 2400 source meter.

Characterization Methods. NMR spectra were measured on a Gemini-300 FT-NMR, a VXR 300 FT-NMR, or a Mercury-300 FT-NMR. High-resolution mass spectrometry was performed on a Bruker APEX II 4.7 T Fourier transform ion cyclotron resonance mass spectrometer (Bruker Daltonics, Billerica, MA) or a Finnigan LCQ-quadrupole ion trap (Thermo Finnigan, San Jose, CA). The ATR-FTIR spectra were obtained with a PerkinElmer Spectrum One ATR-FTIR spectrometer. The spectra were collected for 128 scans at a resolution of 4 cm⁻¹. A Hitachi H-7000 TEM was operated at an accelerating voltage of 100 kV to monitor the morphology of PF-Ru-A anchored TiO₂ particles. Analysis of SEM was performed using a Hitachi S-4000 with an accelerating voltage of 10 kV, and additional carbon conductive layers were coated on both bare TiO₂ and PF-Ru-A//TiO₂ films.

Transient Absorption Measurements. Transient absorption measurements were performed using a home-built transient absorption spectrometer. The spectrometer is based on a commercially available ultrafast laser system (Clark MXR

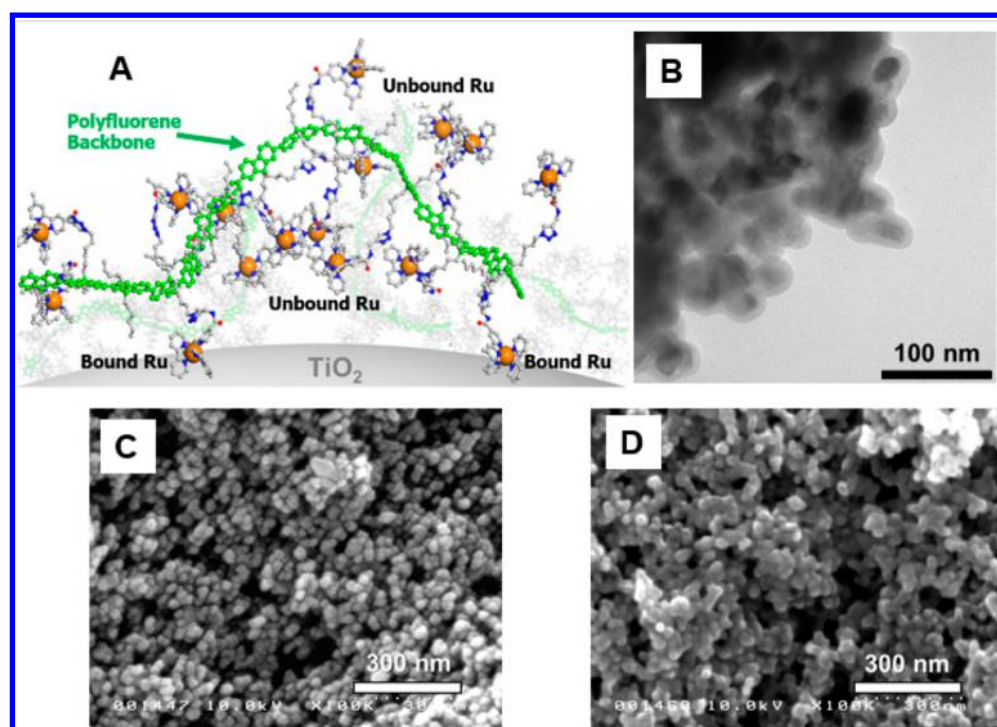


Figure 1. (A) Cartoon of PF-Ru-A anchored onto a TiO_2 surface. (B) TEM image of PF-Ru-A coated onto TiO_2 nanoparticles deposited on a carbon-coated grid. SEM images of as-prepared TiO_2 film (C) before and (D) after the immobilization of PF-Ru-A.

CPA-2210). The system consists of an erbium-doped fiber ring oscillator pumped by a solid-state fiber coupled laser diode operating at 980 nm and a chirped pulse Ti:sapphire regenerative amplifier pumped by a frequency-doubled, Q-switched Nd:YAG laser. Following pulse compression, the amplifier produces pulses centered at 775 nm with 120 fs fwhm duration at 1 kHz with pulse energies of 1.6 mJ/pulse. The 450 nm pump pulse was generated in a 2 mm BBO crystal by sum frequency generation of the 775 nm fundamental and the second harmonic of the 1070 nm signal from an optical parametric amplifier (Light Conversion TOPAS-C). The femtosecond probe pulse is generated by focusing 3 mW of the 775 nm amplifier output into a translating 5 mm thick CaF_2 window. The pump beam is focused onto the sample using a 300 mm lens, and the probe beam is focused and overlapped with a 250 mm spherical aluminum mirror. Spectra were collected on a shot-by-shot (1 kHz) basis over the range of 350–820 nm with a sensitivity of up to 0.1 mOD. The angle between the pump and probe polarization vectors was set to magic angle ($\sim 54.7^\circ$) to avoid polarization effects and ensure that only excited-state population dynamics were being monitored, and the sample was raster scanned to provide for a fresh sample between laser pulses. Following data collection, the frequency chirp in the probe pulse was characterized using the optical Kerr response of liquid CCl_4 in a 2 mm cuvette in a polarization gating geometry. The spectra were chirp-corrected using a data processing program written in LabVIEW.

Sub-nanosecond transient measurements were performed with an Ultrafast Systems EOS spectrometer, in which the probe pulse is generated by continuum generation from a photonic crystal fiber and detected by a fiber-optic coupled multichannel spectrometer with a CMOS sensor. The pump–probe delay is electronically controlled. The kinetic window ranges from 500 ps to 400 μs , and the time resolution of the

instrument is around 500 ps, dictated by the width of the probe pulse and the timing electronics.

For transient absorption sample preparation, thin films of TiO_2 deposited on FTO glass were soaked for 48 h in a solution containing the sensitizer dissolved in a 1:2 (v/v) mixture of acetonitrile:methanol and were placed in a homemade 1 cm quartz cuvette at a 45° angle relative to the front face of the cuvette. All transient absorption experiments were performed with the sensitized films immersed in argon-saturated solutions of 100 mM LiClO_4 dissolved in acetonitrile and were raster scanned to prevent photodegradation of the samples.

Injection yield calculations were determined by comparing the intensity of the 385 nm $\text{bpy}^{\bullet-}$ absorption to the 450 nm ground state bleach. The maximum absorbance at 385 nm occurs when $\Phi_{\text{inj}} = 0\%$, which is observed from the transient absorption spectrum on ZrO_2 , where injection is not possible due to the location of the conduction band edge. The minimum absorbance at 385 nm occurs when $\Phi_{\text{inj}} = 100\%$, in which the transient absorption spectrum represents Ru(III) on TiO_2 . This is approximated as the inverse of the ground state absorption spectrum, normalized to the Ru(II) bleach. By comparing the amplitude of the 385 nm band with respect to these two limits, we can estimate Φ_{inj} as a function of pump–probe delay times.

Transient Absorption Kinetics Fitting Parameters. The fsTA kinetics traces at 385 nm were fit to a biexponential function with an x - and y -offset as implemented in Origin 9.0. The instrument response function (IRF) at 385 nm from the cross-correlation determined the earliest time point in the fitting function. The fitting function was minimized using the Levenberg–Marquardt method until a reduced χ^2 value of $1e^{-9}$ was achieved.

Molecular Dynamics Simulations. The polymer structures for the MD simulations were constructed using the Materials Studio suite (Accelrys Software, Inc., San Diego,

2011). The ground-state geometry of the monomer was optimized using the B3LYP DFT functional and the LANL2DZ basis set, as implemented in Gaussian09 version 09a02.¹⁵ After optimizing the gas-phase monomer structures, the homopolymer was constructed in Materials Studio. The gas-phase geometries of the polymers were then optimized and annealed with atomic charges (NPA) obtained from the Gaussian09 QM calculations. The annealing step consisted of five temperature cycles using the universal force field with the temperature ranging from 300 to 700 K in a time step of 1 fs, with five heating ramps per cycle and 200 dynamics steps per ramp for a total of 1 ns. The simulation cell consisted of an eight-repeat unit polymer, 32 PF₆⁻ (counterion), and 1180 CH₃CN molecules. The cell was then annealed using the same force field as the gas phase polymer with the temperature ranging from 300 to 1200 K in a time step of 1 fs with two heating ramps per cycle and 100 000 dynamics steps per ramp for a total of 800 ps. The annealed simulation cells were then used for molecular dynamics calculations with the canonical ensemble, NVT, at a temperature of 298 K controlled by the Nose thermostat with a *Q*-ratio of 0.01. Dynamics were calculated for a total of 1 ns in each polymer system, and snapshots were collected every 1 ps, giving a trajectory with 1000 snapshots for analysis for each annealed simulation cell.

RESULTS AND DISCUSSION

The chemical structures of the molecular systems studied are shown in Chart 1 which include the model Ru(II) complex (Model-Ru-A) and polymer assemblies PF-Ru and PF-Ru-A. PF-Ru was previously studied⁶ in solution, leading us to design PF-Ru-A to allow anchoring of the assembly to metal oxide surfaces. Within the PF-Ru-A assembly, 30% of the pendant Ru(II) chromophores feature 4,4'-(dicarboxylate)-2,2'-bipyridine ligands allowing for multiple surface binding points randomly positioned along the chain, leaving 70% of the unsubstituted Ru(II) 2,2'-bipyridine chromophores to participate as antennas that transfer excited state energy to surface bound Ru(II) centers.¹⁶ Figure 1A schematically illustrates the structure of PF-Ru-A obtained from solution molecular dynamics (MD) simulations. The MD simulation indicates that the polymer takes on an extended cylindrical conformation, with an effective diameter of approximately 6 nm. In the cartoon PF-Ru-A is shown anchored onto a TiO₂ surface (PF-Ru-A//TiO₂), with surface attachment facilitated by interaction of the polar carboxylate units with the oxide interface.

In the experiments, PF-Ru-A was adsorbed on mesoporous TiO₂ films by deposition from a 1:2 (v/v) mixture of acetonitrile:methanol solution for 48 h, followed by rinsing with MeOH and acetonitrile. The resulting surface was characterized by scanning electron microscopy (SEM), and the polymer modified TiO₂ particles were also imaged by transmission electron microscopy (TEM). Figure 1B shows a TEM image of PF-Ru-A//TiO₂ nanoparticles that were gently removed from a mesoporous film and transferred onto a TEM grid. The TEM image clearly shows an approximately 6 ± 2 nm coating of PF-Ru-A on the TiO₂ nanoparticles; note that this layer thickness is consistent with the diameter of the solution structure obtained from MD simulations, suggesting that the polymer adsorbs as a monolayer on the TiO₂ surface. SEM images of uncoated mesoporous TiO₂ films and PF-Ru-A//TiO₂ films are shown in Figure 1C,D. Analysis of the particle size distribution in the SEM image for the TiO₂ films after the deposition of PF-Ru-A revealed that the particles have an

average size of roughly 26.2 ± 5.5 nm for the uncoated TiO₂ film and 31.9 ± 5.3 nm for PF-Ru-A//TiO₂ films, consistent with the PF-Ru-A layer thickness determined from TEM images. The binding of the PF-Ru-A to the TiO₂ nanoparticles indicated by the images presumably results from the interaction of the ionic carboxylate groups from multiple complexes per chain with the TiO₂ surface.¹⁷

The photoelectrochemical response of the PF-Ru-A//TiO₂ films was tested in a standard dye-sensitized solar cell (DSSC) configuration. Figure 2 shows that the photocurrent action

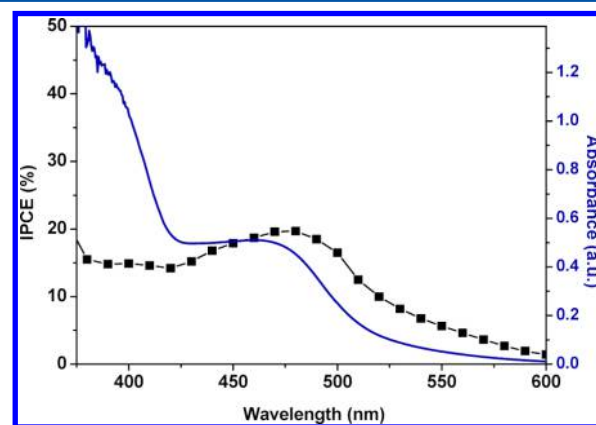


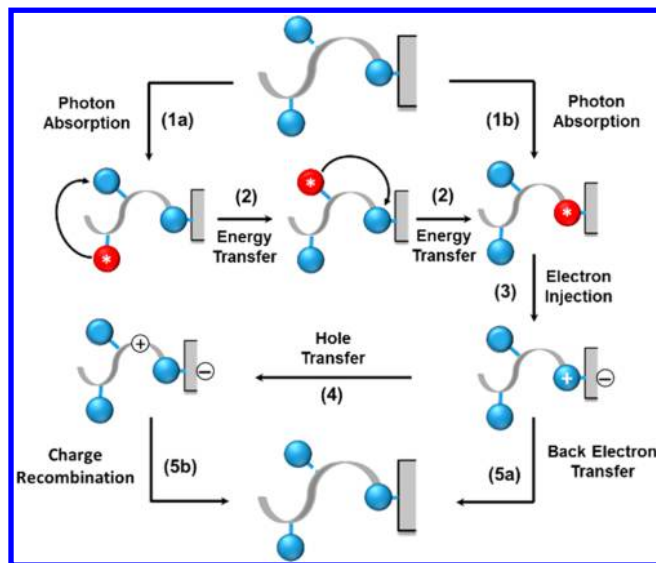
Figure 2. Incident photon to current efficiency (IPCE) spectra of a photoelectrochemical cell based on a PF-Ru-A//TiO₂ photoanode (black solid line with squares). UV-vis absorption spectrum of a PF-Ru-A//TiO₂ photoanode (blue solid curve) for comparison with IPCE plot. Note that the absorption increase for $\lambda < 425$ nm is due to onset of the PF backbone absorption.

spectrum (IPCE) of the PF-Ru-A sensitized solar cell exhibits a peak IPCE value of ~20% at 480 nm. Importantly, the most pronounced band seen in the photocurrent spectrum corresponds to the metal-to-ligand charge transfer (MLCT) absorption of the Ru(II) chromophores. A feature corresponding to absorption of the PF backbone ($\lambda < 425$ nm) is weaker than expected in the photocurrent spectrum, indicating that excitations on the polymer are less efficient in charge injection compared to excitations on the Ru chromophores.¹⁸ In these polymer assemblies, PF excitation decays through competitive PF* to Ru(II) energy and charge transfer pathways.⁶

Energy transfer from PF* to Ru(II)* should give the same photocurrent (on a per absorbed photon basis) as direct photoexcitation of a surface bound Ru(II) unit. On the other hand, deactivation via PF* to Ru(II) charge transfer will likely produce little or no photocurrent due to the kinetic competition between transport of the charge between unbound complexes to the surface for charge injection and the rapid charge recombination time (~6 ns). The reduced photocurrent efficiency observed for PF excitation could indicate that on the TiO₂ surface charge separation/recombination is the dominant decay pathway. The PF-Ru-A//TiO₂ cell exhibited a peak absorbed photon-to-current efficiency (APCE = IPCE/[1 - *T*], where *T* = transmittance) value of ~30% at 480 nm. Under 100 mW, AM 1.5 simulated solar illumination the performance of the PF-Ru-A//TiO₂ DSSC exhibited a photocurrent density–photovoltage (*J*–*V*) curve as shown in Figure S4, with an open-circuit voltage of $V_{oc} = 0.54$ V, short-circuit current density of $J_{sc} = 1.31$ mA/cm², fill factor of FF = 0.59, and overall power conversion efficiency of $\eta = 0.43\%$.

Transient absorption measurements performed on Model-Ru-A//TiO₂ and PF-Ru-A//TiO₂ films reveal a cascading series of energy and electron transfer events that occur following photoexcitation, as illustrated in Scheme 1. Photoexcitation of a

Scheme 1. Schematic Representation of Photophysical Events of PF-Ru-A on the Surface of TiO₂^a



^aBalls represent Ru(L)₃²⁺ chromophores, and the gray ribbon represents the poly(fluorene) backbone.

surface-bound (proximal) Ru(II) chromophore (1b) results in rapid electron injection into TiO₂ (3), followed by the transfer of the hole on the oxidized Ru(III) complex to the PF backbone (4). Excitation of a Ru(II) chromophore that is distal with respect to the interface (1a) can lead to multiple Ru* → Ru energy hopping events (2). Transport of the energy to surface bound chromophores is followed by electron injection (3) and hole transfer to the polymer (4). On longer time scales, back electron transfer between Ru(III) and TiO₂(e⁻) (5a) or charge recombination between PF⁺ and TiO₂(e⁻) (5b) give the original ground state Ru(II) species.

The electron injection process (3) is monitored by fs–ps transient absorption on the Model-Ru-A//TiO₂ film. Spectra acquired shortly after 450 nm excitation of the Model-Ru-A//TiO₂ film (Figure 3A) show the characteristic $\pi \rightarrow \pi^*$ absorption at 385 nm of the reduced polypyridyl radical anion (bpy^{•-}) along with a prominent ground-state bleach at 450 nm and a ligand-to-metal charge transfer (LMCT) and bpy^{•-} band that extends to the red of 500 nm.¹⁹ Loss of the bpy^{•-} absorption at 385 nm without loss of the ground state bleach at 450 nm is the spectral signature of electron injection into the TiO₂. By monitoring the loss of the 385 nm excited state absorption (Figure 3B), the decay is described well by fast ($\tau_1 = 60$ ps) and slow ($\tau_2 = 500$ ps) components. Photoinduced electron injection has been shown to be a multiexponential process, owing to the intrinsic heterogeneity and dynamic relaxation processes following excitation.^{20,21} These slower decay components most likely reflect electron injection from a thermalized ³MLCT excited state, as reported for other Ru(II) dyes.²⁰ The presence of multiple kinetic components has been observed for other related sensitizers and arises from a number of factors, including the dye-binding motifs, electronic coupling, and overlap of the dye donor levels with the TiO₂ acceptor

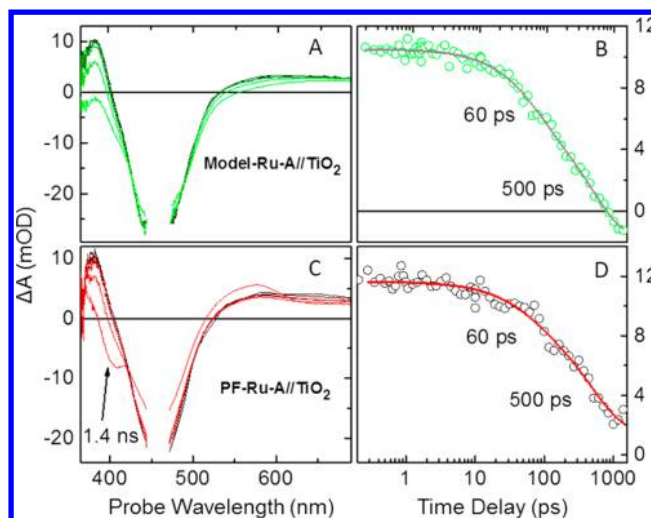


Figure 3. (A) Transient absorption spectra following 450 nm laser excitation for the Model-Ru-A complex on TiO₂ at 0.25, 1, 5, 10, 100, and 1400 ps. (B) Model-Ru-A//TiO₂ kinetics trace at 385 nm. (C) Transient absorption spectra of PF-Ru-A//TiO₂ at 0.25, 1, 5, 10, 100, and 1400 ps. (D) PF-Ru-A//TiO₂ kinetics trace at 385 nm. The films were immersed in argon-saturated acetonitrile with 0.1 M LiClO₄.

states.^{22–24} Furthermore, based on the analysis of the transient spectra,²⁵ there is negligible ultrafast ($\tau < 200$ fs) electron injection in this complex, and by 1.4 ns the overall injection yield is 45%.²⁶

Photoexcitation of the PF-Ru-A//TiO₂ film at 450 nm gives rise to similar spectral features as seen for the Model-Ru-A//TiO₂ film at early times (Figure 3C). The intensity of the 385 nm absorption decays with time components that are similar to the Model-Ru-A complex ($\tau_1 = 60$ ps and $\tau_2 = 500$ ps) (Figure 3D), but the overall injection yield is significantly lower based on inspection of the transient spectra.²⁵ In addition, the transient spectra for the PF-Ru-A//TiO₂ assembly show additional bleach and absorption features at 400 and 580 nm, respectively (Figure 3C), and a concomitant loss of the MLCT ground state bleach at 450 nm. The 400 nm bleach and the 580 nm absorption are both attributed to oxidized PF polymer (PF⁺) on the basis of spectroelectrochemical observations.⁶ The absence of these two features in the transient spectra for PF-Ru-A//ZrO₂ (Figure S5) indicates that formation of PF⁺ is a consequence of charge injection, most likely due to hole transfer from Ru(III), produced by charge injection, to the PF backbone (Scheme 1, step 4). Furthermore, the loss of the bpy^{•-} absorption at 385 nm occurs simultaneously with appearance of the PF⁺ feature at 400 nm, suggesting that hole transfer takes place on a time scale that is short compared to the longer injection components.

The spectral features associated with the formation of PF⁺ at 400 and 580 nm become increasingly pronounced on longer time scales, as seen in Figure 4A,C. Their continued growth during the first 200–300 ns is consistent with triplet–triplet energy transport from unbound Ru(II) complexes through site-to-site hopping to a chromophore bound to the TiO₂ surface, which then undergoes electron injection and hole localization on the PF (Scheme 1, steps 2 and 3). Thus, the time scale associated with the growth of the PF⁺ features at 400 and 580 nm reflects the total time needed for the Ru* created by photoexcitation to reach the interface, which in turn depends upon the Ru* → Ru hopping time as well as the number of

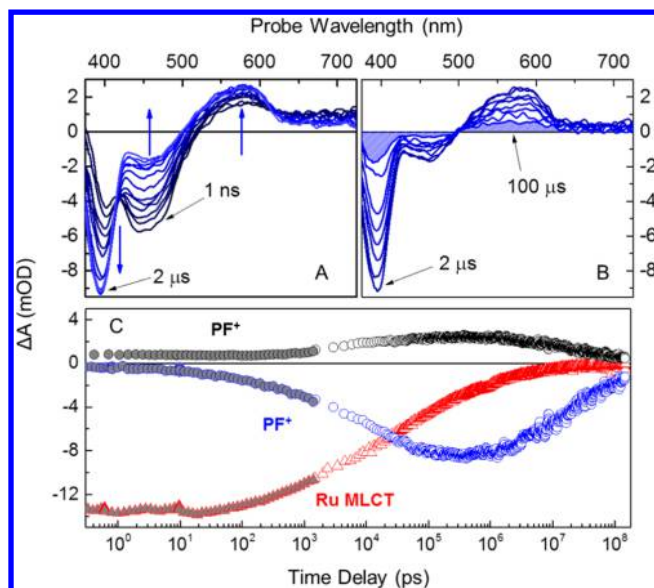


Figure 4. (A) Nanosecond transient absorption spectra of PF-Ru-A//TiO₂ films following excitation at 450 nm from 1 ns to 2 μs. (B) Nanosecond transient absorption spectra of PF-Ru-A//TiO₂ films from 2 to 100 μs. The shaded region is the spectrum at 100 μs. (C) Kinetics traces for PF-Ru-A//TiO₂ films at probe wavelengths 400 nm (blue), 485 nm (red), and 580 nm (black) from 250 fs to 150 μs following 450 nm excitation. The gray-filled points represent the femtosecond and picosecond kinetic traces. The films were immersed in argon-saturated acetonitrile with 0.1 M LiClO₄.

hops. Work on a related polymer assembly^{27–29} suggests that the Ru* → Ru hopping time is <10 ns. Thus, the growth of PF⁺ over 200–300 ns implies that some Ru(II)* excited states may make as many as 20–30 hops prior to charge injection, underscoring the antenna-like nature of the PF-Ru-A polymer assembly. The fraction of unbound Ru(II)* that reach the interface (F_s) can be estimated from the APCE efficiency (η_{APCE}) and the injection efficiency (η_{inj}), i.e., where f_B and f_U are the fractions of complexes that are bound and unbound to the surface, respectively. Using an APCE efficiency of 30% and an injection efficiency of 45%, we estimate (to a lower limit) that approximately 50% of the photoexcitations on unbound complexes are eventually transported to the surface where they can undergo electron injection.

$$F_s = \left(\frac{\eta_{\text{APCE}}}{\eta_{\text{inj}}} - f_B \right) \frac{1}{f_U}$$

By 200–300 ns after photoexcitation, the transient spectrum contains both the prominent features associated with the PF⁺ as well as a significant Ru(II) bleach at 450 nm. Since hole transfer to form the positive polaron repopulates the Ru(II) ground state, the bleach must arise from Ru(III) complexes that have not undergone hole transfer or Ru(II)* excited states that remain. Although it is difficult to distinguish between these two contributions, the rapid hole transfer time would suggest that it is the Ru(II)* that is responsible for the bleach.

Furthermore, the Ru(II) ground state bleach decays before the PF⁺ features (Figure 4B,C), indicating that the transient spectrum observed at the longest times arises almost entirely from the positive polaron, PF⁺. A small population of Ru(III) still exists at 150 μs, most likely a result of the similar oxidation potentials for PF and non-carboxylated Ru(II) chromophores,

leading to an equilibrium between the hole residing on the polymer backbone and the pendant chromophores. The charge-separated state decays through recombination of the injected electron in the TiO₂ with holes on the PF backbone (Scheme 1, 5b). Its lifetime (~150 μs) is significantly longer than that of Model-Ru-A//TiO₂ (Figure S6), consistent with a greater separation between the PF positive polaron and the surface.

CONCLUSION

PF-Ru chromophores functionalized with a small fraction of ionic carboxylate moieties have been prepared by “click” chemistry to attach the mixture of Ru(II) polypyridyl complexes and ester-containing Ru(II) polypyridyl complexes, following the deprotection step to form ionic carboxylate functionalized Ru(II) polypyridyl complexes. With the successful synthesis of PF-Ru-A, the polymer-based chromophores were anchored to TiO₂ films. The solar characteristics demonstrate TiO₂ surface anchoring and light harvesting ability when applied in solar photoelectrochemical cells. These light harvesting mechanisms were studied with femtosecond pump–probe spectroscopy, where direct excitation of the Ru(II) chromophores leads to rapid and efficient electron injection for chromophores directly bound to the TiO₂ surface. This event is followed by ultrafast hole transfer to the polyfluorene chain, thereby facilitating repopulation of the ground state Ru(II) species and avoiding deleterious charge recombination processes. The pendant Ru(II) chromophores undergo energy transfer to surface-bound chromophores on the nanosecond time scale, where electron injection can precede hole transfer to the polymer backbone. Charge recombination for the Ru(II) chromophores occurs on the microsecond time scale, where injected electrons recombine with oxidized chromophores that have not undergone hole transfer, whereas charge recombination involving the oxidized polymer occurs on longer time scales. This study reveals the promise for coupling polymeric assemblies to a semiconductor interface for light harvesting, charge separation, and transient charge storage. Work in progress seeks to include oxidation catalyst centers into the assemblies with the objective of accomplishing water oxidation at the photoanode of a dye-sensitized photoelectrosynthesis cell.

ASSOCIATED CONTENT

Supporting Information

Experimental procedures, ATR-FTIR, TEM, AFM, J – V curve, absorption and emission spectra of PF-Ru-A//TiO₂ films, and transient absorption spectra of PF-Ru-A//ZrO₂ results. This material is available free of charge via the Internet at <http://pubs.acs.org>.

AUTHOR INFORMATION

Corresponding Authors

*E-mail kschanze@chem.ufl.edu (K.S.S.).

*E-mail john_papanikolas@unc.edu (J.M.P.).

Author Contributions

G.L. and Z.A.M. contributed equally.

Notes

The authors declare no competing financial interest.

ACKNOWLEDGMENTS

This material is based on work supported as part of the UNC EFRC: Solar Fuels and Next Generation Photovoltaics, an

Energy Frontier Research Center funded by the U.S. Department of Energy, Office of Science, Office of Basic Energy Sciences, under Award DE-SC0001011. We also thank Karen L. Kelly in the Interdisciplinary Center for Biotechnology Research (ICBR) Electron Microscopy and Bioimaging Laboratory at University of Florida for help with the TEM and SEM.

REFERENCES

- (1) Ashford, D. L.; Song, W.; Concepcion, J. J.; Glasson, C. R. K.; Brennaman, M. K.; Norris, M. R.; Fang, Z.; Templeton, J. L.; Meyer, T. J. Photoinduced Electron Transfer in a Chromophore–Catalyst Assembly Anchored to TiO₂. *J. Am. Chem. Soc.* **2012**, *134*, 19189–19198.
- (2) Song, W.; Glasson, C. R. K.; Luo, H.; Hanson, K.; Brennaman, M. K.; Concepcion, J. J.; Meyer, T. J. Photoinduced Stepwise Oxidative Activation of a Chromophore–Catalyst Assembly on TiO₂. *J. Phys. Chem. Lett.* **2011**, *2*, 1808–1813.
- (3) Tomizaki, K.; Loewe, R. S.; Kirmaier, C.; Schwartz, J. K.; Retsek, J. L.; Bocian, D. F.; Holten, D.; Lindsey, J. S. Synthesis and Photophysical Properties of Light-Harvesting Arrays Composed of a Porphyrin Bearing Multiple Perylene-Monoimide Accessory Pigments. *J. Org. Chem.* **2002**, *67*, 6519–6534.
- (4) Gust, D.; Moore, T. A.; Moore, A. L. Mimicking Photosynthetic Solar Energy Transduction. *Acc. Chem. Res.* **2001**, *34*, 40–48.
- (5) Wasielewski, M. R. Photoinduced Electron Transfer in Supramolecular Systems for Artificial Photosynthesis. *Chem. Rev.* **1992**, *92*, 435–461.
- (6) Wang, L.; Puodziukynaite, E.; Vary, R. P.; Grumstrup, E. M.; Walczak, R. M.; Zolotar'skaya, O. Y.; Schanze, K. S.; Reynolds, J. R.; Papanikolas, J. M. Competition between Ultrafast Energy Flow and Electron Transfer in a Ru(II)-Loaded Polyfluorene Light-Harvesting Polymer. *J. Phys. Chem. Lett.* **2012**, *3*, 2453–2457.
- (7) Wang, L.; Puodziukynaite, E.; Grumstrup, E. M.; Brown, A. C.; Keinan, S.; Schanze, K. S.; Reynolds, J. R.; Papanikolas, J. M. Ultrafast Formation of a Long-Lived Charge-Separated State in a Ru-Loaded Poly(3-hexylthiophene) Light-Harvesting Polymer. *J. Phys. Chem. Lett.* **2013**, *4*, 2269–2273.
- (8) Chen, Z.; Grumstrup, E. M.; Gilligan, A. T.; Papanikolas, J. M.; Schanze, K. S. Light-Harvesting Polymers: Ultrafast Energy Transfer in Polystyrene-Based Arrays of π -Conjugated Chromophores. *J. Phys. Chem. B* **2014**, *118*, 372–378.
- (9) Adronov, A.; Gilat, S. L.; Frechet, J. M. J.; Ohta, K.; Neuwahl, F. V. R.; Fleming, G. R. Light Harvesting and Energy Transfer in Laser-Dye-Labeled Poly(Aryl Ether) Dendrimers. *J. Am. Chem. Soc.* **2000**, *122*, 1175–1185.
- (10) Ma, D.; Bettis, S. E.; Hanson, K.; Minakova, M.; Alibabaei, L.; Fondrie, W.; Ryan, D. M.; Papoian, G. A.; Meyer, T. J.; Waters, M. L.; Papanikolas, J. M. Interfacial Energy Conversion in Ru-II Polypyridyl-Derivatized Oligoproline Assemblies on TiO₂. *J. Am. Chem. Soc.* **2013**, *135*, 5250–5253.
- (11) Sykora, M.; Maxwell, K. A.; DeSimone, J. M.; Meyer, T. J. Mimicking the Antenna-Electron Transfer Properties of Photosynthesis. *Proc. Natl. Acad. Sci. U. S. A.* **2000**, *97*, 7687–7691.
- (12) Armarego, W. L. F.; Chai, C. *Purification of Laboratory Chemicals*, 5th ed.; Butterworth-Heinemann: Oxford, UK, 2003.
- (13) Fang, Z.; Eshbaugh, A. A.; Schanze, K. S. Low-Bandgap Donor–Acceptor Conjugated Polymer Sensitizers for Dye-Sensitized Solar Cells. *J. Am. Chem. Soc.* **2011**, *133*, 3063–3069.
- (14) Lee, Y.-G.; Park, S.; Cho, W.; Son, T.; Sudhagar, P.; Jung, J. H.; Wooh, S.; Char, K.; Kang, Y. S. Effective Passivation of Nanostructured TiO₂ Interfaces with Peg-Based Oligomeric Coadsorbents to Improve the Performance of Dye-Sensitized Solar Cells. *J. Phys. Chem. C* **2012**, *116*, 6770–6777.
- (15) Frisch, M. J.; et al. *Gaussian 09, Revision C.01*; Gaussian, Inc.: Wallingford, CT, 2009.
- (16) The 30% loading of the bis(dicarboxy)bpy Ru(II) on the polyfluorene chain reflects the stoichiometry in the click reaction used to attach the acetylene functionalized Ru(II) chromophores to the azide functionalized polyfluorene.
- (17) Comparison of ATR-IR spectra of PF-Ru-A and PF-Ru-A//TiO₂ (Figure S1) supports the premise that the surface bonding is via the carboxylate groups.
- (18) The absorption of the polyfluorene backbone has a band maximum at 393 nm; see absorption spectrum in Supporting Information, Figure S5.
- (19) Rack, J. J. Electron Transfer Triggered Sulfoxide Isomerization in Ruthenium and Osmium Complexes. *Coord. Chem. Rev.* **2009**, *253*, 78–85.
- (20) Koops, S. E.; O'Regan, B. C.; Barnes, P. R. F.; Durrant, J. R. Parameters Influencing the Efficiency of Electron Injection in Dye-Sensitized Solar Cells. *J. Am. Chem. Soc.* **2009**, *131*, 4808–4818.
- (21) Juozapavicius, M.; Kaucikas, M.; van Thor, J. J.; O'Regan, B. C. Observation of Multiexponential Pico- to Subnanosecond Electron Injection in Optimized Dye-Sensitized Solar Cells with Visible-Pump Mid-Infrared-Probe Transient Absorption Spectroscopy. *J. Phys. Chem. C* **2013**, *117*, 116–123.
- (22) Giokas, P. G.; Miller, S. A.; Hanson, K.; Norris, M. R.; Glasson, C. R. K.; Concepcion, J. J.; Bettis, S. E.; Meyer, T. J.; Moran, A. M. Spectroscopy and Dynamics of Phosphonate-Derivatized Ruthenium Complexes on TiO₂. *J. Phys. Chem. C* **2013**, *117*, 812–824.
- (23) Li, L. S.; Giokas, P. G.; Kanai, Y.; Moran, A. M. Modeling Time-Coincident Ultrafast Electron Transfer and Solvation Processes at Molecule-Semiconductor Interfaces. *J. Chem. Phys.* **2014**, *140*, 234109.
- (24) Asbury, J. B.; Anderson, N. A.; Hao, E. C.; Ai, X.; Lian, T. Q. Parameters Affecting Electron Injection Dynamics from Ruthenium Dyes to Titanium Dioxide Nanocrystalline Thin Film. *J. Phys. Chem. B* **2003**, *107*, 7376–7386.
- (25) Wang, L.; Ashford, D. L.; Thompson, D. W.; Meyer, T. J.; Papanikolas, J. M. Watching Photoactivation in a Ru(II) Chromophore–Catalyst Assembly on TiO₂ by Ultrafast Spectroscopy. *J. Phys. Chem. C* **2013**, *117*, 24250–24258.
- (26) This injection yield is substantially lower than those observed for similar Ru(II) complexes on TiO₂. It is most likely a result of the chemical modification needed to attach the complex to the polymer, which could lead to low-energy MLCT excited states associated with the ancillary ligands that slow electron injection and diminish the overall injection yield.
- (27) Fleming, C. N.; Maxwell, K. A.; DeSimone, J. M.; Meyer, T. J.; Papanikolas, J. M. Ultrafast Excited-State Energy Migration Dynamics in an Efficient Light-Harvesting Antenna Polymer Based on Ru(II) and Os(II) Polypyridyl Complexes. *J. Am. Chem. Soc.* **2001**, *123*, 10336–10347.
- (28) Fleming, C. N.; Jang, P.; Meyer, T. J.; Papanikolas, J. M. Energy Migration Dynamics in a Ru(II)- and Os(II)-Based Antenna Polymer Embedded in a Disordered, Rigid Medium. *J. Phys. Chem. B* **2004**, *108*, 2205–2209.
- (29) Fleming, C. N.; Brennaman, M. K.; Papanikolas, J. M.; Meyer, T. J. Efficient, Long-Range Energy Migration in Ru-II Polypyridyl Derivatized Polystyrenes in Rigid Media. Antennae for Artificial Photosynthesis. *Dalton Trans.* **2009**, 3903–3910.

Poly(fluorene-co-thiophene)-based ionic transition-metal complex polymers for solar energy harvesting and storage applications†

Cite this: *Polym. Chem.*, 2014, 5, 2363Egle Puodziukynaite,^a Li Wang,^b Kirk S. Schanze,^a John M. Papanikolas^b
and John R. Reynolds^{*c}

This paper describes the synthesis, electrochemical and photophysical properties of two poly(fluorene-co-thiophene)-based polymers featuring pendant Ru(II) polypyridyl-based ionic transition metal complexes. These systems combine long-lived excited states of the Ru(II) chromophores and the large optical cross-sections of the conjugated backbones, potentially allowing for polymer-assisted solar radiation-harvesting and storage functions *via* ultrafast energy and charge transfer processes. Modified azide-alkyne “click” cycloaddition chemistry conditions are demonstrated as an effective approach to obtain quantitatively functionalized conjugated polymer-ionic transition metal complex assemblies. Introduction of variable fractions of electron-rich thiophene units into these architectures induces a bathochromic shift in the polyfluorene absorption maxima, while simultaneously stabilizing the oxidized states of the conjugated scaffolds, as determined by electrochemical and *in situ* spectroelectrochemical experiments. The hybrid assemblies exhibit ultrafast energy flow (700 fs to 4.8 ps) and photoinduced charge-separation (1.8–2.0 ps) between the conjugated backbone and the Ru(II) moieties. Notably, the chemical composition of the main-chain repeat unit determines the dominant pathway for decay of the conjugated backbone excited states with the fraction of electron transfer increasing from 25% to 75% upon incorporation of an additional thiophene heterocycle.

Received 10th November 2013
Accepted 27th December 2013

DOI: 10.1039/c3py01582c

www.rsc.org/polymers

Introduction

Ionic transition metal complex (iTMC) assemblies have emerged as attractive light-harvesting, charge transport, and catalytic media for solar electrochemical cells and solar fuel devices.^{1–4} Among such systems, multichromophoric iTMC arrays have attracted a considerable amount of attention due to their large cumulative optical cross-sections and long-lived photostable excited states enabling exciton migration over long distances.^{5–9} Additionally, optical and electrochemical properties of iTMCs can be fine-tuned *via* relatively simple structural modification of their ligands, ultimately affecting both individual rates and direction of exciton hopping in the resultant macromolecular architectures.^{6,9–14}

To date, multi-chromophoric assemblies have been mostly comprised of saturated polymer backbones, such as polystyrene

or polyproline.^{5,8,15} However, while these scaffolds act as facile templates to align the pendant iTMC units thus controlling inter-chromophore exciton migration, intrinsically, such polymers are non-electroactive and do not perform functions related to solar energy harvesting. As a result, we have recently reported a Ru(II)-loaded polyfluorene assembly, where a basis for light harvesting is provided by the electroactive polymer backbone, followed by ultrafast energy and charge transfer processes.¹⁶ In this system, the combination of the large extinction coefficient of the conjugated polymer backbone and the long lifetime of the Ru(II) excited states is demonstrated, allowing for long exciton diffusion lengths. Whereas this polyfluorene-Ru(II)-tris(bipyridyl) hybrid essentially serves as a model system, providing insight into the excitonic processes in this general class of iTMC-conjugated polymer assemblies (Fig. 1), the limitations of this scaffold arise due to the high energy gap of the polymer. Polyfluorene exhibits absorption centered around 390 nm, where the radiation of the solar emission spectrum is limited. Additionally, the energy transfer process is the dominant photophysical phenomenon in this assembly, while electron transfer, leading to high energy redox intermediates, accounts for only ~15% of the total energy absorbed by the polymer backbone.

To utilize the light harvesting potential of hybrid conjugated polymer-iTMC assemblies, inducing a bathochromic shift in

^aDepartment of Chemistry, Center for Macromolecular Science and Engineering, University of Florida, Gainesville, FL 32611-7200, USA

^bDepartment of Chemistry, University of North Carolina at Chapel Hill, Chapel Hill, North Carolina 27599, USA

^cSchool of Chemistry and Biochemistry, School of Materials Science and Engineering, Center for Organic Photonics and Electronics, Georgia Institute of Technology, Atlanta, GA 30332, USA. E-mail: reynolds@chemistry.gatech.edu

† Electronic supplementary information (ESI) available: Detailed experimental and additional synthesis data. See DOI: 10.1039/c3py01582c

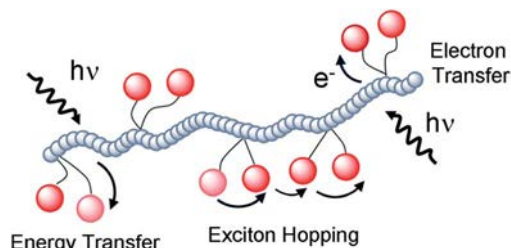


Fig. 1 Controlled exciton and charge transfer processes in a hybrid conjugated polymer–ionic transition metal complex array.

the polymer backbone absorption, as well as increasing the fraction of electron transfer, becomes a necessity. To address this issue, we have recently reported a poly(3-hexylthiophene)–Ru(II) assembly that demonstrates preferential formation of the long-lived charge separated state.¹⁷ However, to fully understand the photophysical properties of conjugated polymer–iTMC hybrids and ultimately explore such architectures as catalytic scaffold building blocks in solar fuel devices, further fine-tuning of energy transfer and charge separation fractions is of importance (Fig. 1). Additionally, precise control of polymer backbone HOMO levels is critical, as this could allow for transition-metal catalyst oxidation by the conjugated main-chain, potentially facilitating the respective water splitting reactions.

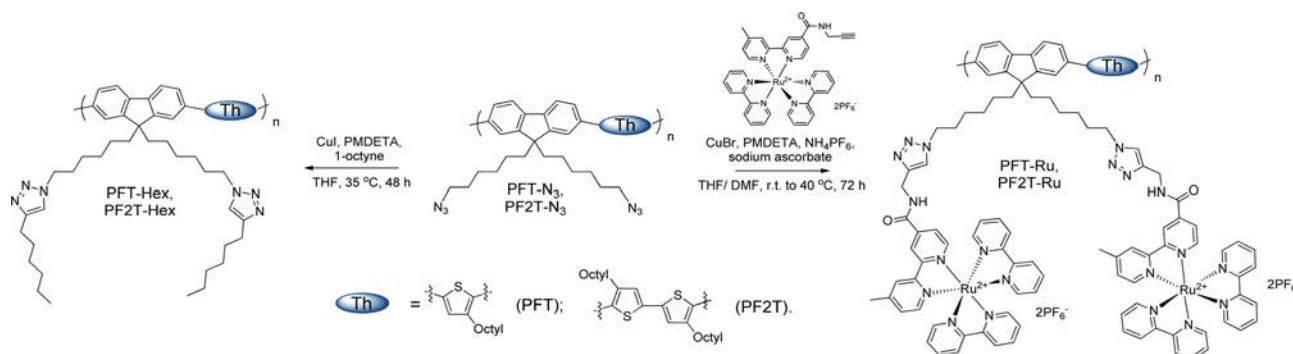
Reported herein are the synthesis and characterization results of a new family of poly(fluorene-*co*-thiophene)–Ru(II) polypyridyl assemblies, where the optical and electronic properties of the polymer backbones are controlled by incorporation of various fractions of electron-rich thiophene units. Modified Cu-assisted “click” chemistry conditions are employed for post-polymerization functionalization of these assemblies, allowing for quantitative “click” conversion under mild conditions. Electrochemical, spectroelectrochemical and photophysical characterization results are given for the polymers synthesized with the focus on establishing the structure–property relationships in these systems. Ultrafast transient absorption experiments suggest a significant increase in the electron transfer fraction (from 25% to 75%) from the polymer backbone to the Ru(II) pendants upon the introduction of an additional thiophene moiety into the repeat unit of the conjugated main-chain.

Efficient formation of charge-separated states in the macromolecular antennae is expected to facilitate electron injection and chromophore-assisted catalytic processes in the respective solar energy-harvesting and storage devices.

Results and discussion

Synthesis

The emphasis of this study was multichromophoric Ru(II) arrays based on perfectly alternating poly(fluorene-*co*-thiophene) (PFT–Ru) and poly(bithiophene-*co*-fluorene) (PF2T–Ru) backbones, as shown in Scheme 1. Polymers PFT–Ru and PF2T–Ru were obtained using a general multi-step route as depicted in Scheme 1, as well as Schemes S1 and S2 (ESI†). The bromide-functionalized polymer precursors were synthesized *via* a Pd-mediated Suzuki cross-coupling approach (Schemes S1 and S2, ESI†) with the yields of their chloroform soluble fractions being 58% and 70%, respectively. The compounds were then treated with sodium azide to obtain PFT–N₃ and PF2T–N₃. These reactive polymers, due to their increased sensitivity to azide-cross-linking,¹⁸ were immediately subjected to the Cu(I)-assisted “click” reaction with an alkynyl-containing amide-functionalized Ru(II) polypyridyl complex to afford PFT–Ru and PF2T–Ru in 88% and 85% yields, correspondingly (Schemes 1, S1 and S2†). This Ru(II) tris(bipyridyl) derivative has been chosen as the coupling partner, as introduction of an electron-withdrawing amide functionality to the 4-position of the 2,2′-bipyridine ligands of the chromophores has been previously demonstrated to contribute to the excited MLCT state dipole alignment in the respective iTMC polystyrene arrays, allowing for orders of magnitude faster Ru* → Ru inter-chromophore exciton hopping rates.⁸ In the “click” reaction, CuBr, PMDETA and sodium ascorbate were used as the Cu(I)-source, base/ligand and reducing agent, respectively. Additionally, an excess of NH₄PF₆ salt was added to the reaction mixture to prevent the Ru(II) complex counter ion exchange, leading to precipitation of the reaction intermediates and the consecutive inhibition of the “click” conversion. In both cases, quantitative functionalization of PFT and PF2T backbones with iTMC units was confirmed using ¹H NMR and IR spectroscopies. Hybrid assemblies PFT–Ru and PF2T–Ru were estimated to contain on average *ca.*



Scheme 1 Synthetic routes to polymers PFT–Ru, PF2T–Ru, PFT–Hex and PF2T–Hex.

46 and 30 pendent Ru(II) units per chain, respectively. Azide-based precursors **PFT-N3** and **PF2T-N3** were also reacted with 1-octyne to obtain hexyl-functionalized model polymers **PFT-Hex** and **PF2T-Hex** (Schemes 1, S1 and S2†).

Photophysical properties

The photophysical properties of **PFT-Ru**, **PF2T-Ru**, and the corresponding model polymers **PFT-Hex** and **PF2T-Hex** were studied by steady state UV-Vis and photoluminescence spectroscopies. Normalized solution absorption and emission spectra of **PFT-Ru**, **PF2T-Ru**, **PFT-Hex** and **PF2T-Hex** are given in Fig. 2, and the optical properties are summarized in Table 1.

As can be seen in Fig. 2A, the model polymers exhibited, in principle, similar UV-Vis absorption behavior with broad absorption bands centered at 399 and 402 nm (Fig. 2 and Table 1). The resemblance of the absorption spectra was hypothesized to arise from the opposing steric and electronic effects. Whereas the presence of an additional electron rich

Table 1 Optical data for compounds **PFT-Ru** and **PF2T-Ru** in acetonitrile and **PFT-Hex** and **PF2T-Hex** in THF

Compound	Abs λ_{\max} , nm (λ_{onset} , nm)	PL λ_{\max} , nm
PFT-Hex	399 (454)	462, 487
PF2T-Hex	402 (462)	485, 512
PFT-Ru	289, 419, 470	456, 644
PF2T-Ru	289, 416, 470	470, 644

thiophene moiety in the polymer repeat unit would be expected to generate a bathochromic shift in the ground state absorption of **PF2T-Hex**, the backbone twisting caused by the sterically bulky thiophene octyl chains adjacent to the fluorene units might result in a decrease in the mean conjugation length and a respective hypsochromic shift. Nonetheless, the slight bathochromic shifts in the peak position (3 nm) and the absorption band onset (6 nm) for **PF2T-Hex** indicated a somewhat lower optical gap, which was consistent with the more electron-rich character of the polymer. More significant variations emerged in the photoluminescence spectra of the two polymers, where an ~ 25 nm red shift, as well as the corresponding increase in the Stokes shift, was observed for **PF2T-Hex**. This finding is most likely indicative of more pronounced conformational relaxation of the polymer backbone upon excitation or/and excitonic energy migration differences between the PFT and PF2T scaffolds.¹⁹ Both polymers exhibited structured emission bands with maxima of 462 nm and 487 nm for **PFT-Hex**, as well as 485 nm and 512 nm for **PF2T-Hex**. The emission quantum yields of the polymers were 0.65 and 0.50 for PFT and PF2T scaffolds, respectively.

Absorption spectra of **PFT-Ru** and **PF2T-Ru** generally resembled a linear combination of the polymer backbone and Ru polypyridyl complex absorption signatures, suggesting little or no electronic interactions in the ground state between the two components. In addition to the π - π^* transitions of the polymer backbones with the maxima at *ca.* 416–419 nm, each absorption spectrum also exhibited shoulders at *ca.* 470 nm characteristic of metal-to-ligand charge transfer (MLCT) of Ru(II) complexes, as well as the bipyridine ligand π - π^* transition centered at around 289 nm. When excited at 388 nm, emission spectra of the hybrid polymers were dominated by the broad featureless Ru(II) complex MLCT triplet emission at 644 nm, and the polymer backbone emission was significantly quenched ($\Phi = 6.0 \times 10^{-4}$ for **PFT-Ru** and $\Phi = 1.3 \times 10^{-3}$ for **PF2T-Ru**). This result was partially attributed to fluorescence resonance energy transfer (FRET) occurring from the polymer backbones to the iTMC units *via* the ¹MLCT excited state and is consistent with literature examples when the donor emission and acceptor absorption spectral signatures overlap.^{16,20,21} Furthermore, in the excitation spectra of the hybrid polymers monitored for the Ru(II) ³MLCT emission at 640 nm (Fig. 2B), the conjugated main-chain absorption spectra could be in part reproduced, in agreement with FRET. Meanwhile, deviations between the polymer backbone absorption and excitation spectra were associated with another excited state relaxation

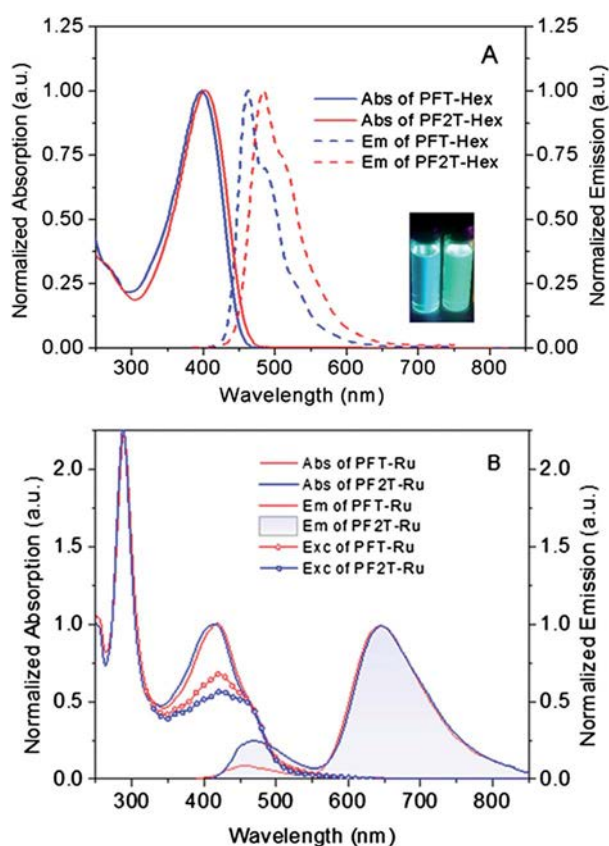


Fig. 2 (A) Normalized absorption and photoluminescence spectra of **PFT-Hex** and **PF2T-Hex** in dilute tetrahydrofuran solutions; along with the corresponding photographs of the polymer solutions under long-wave UV irradiation. (B) Normalized absorption, photoluminescence and excitation spectra of **PFT-Ru** and **PF2T-Ru** in dilute Ar-saturated acetonitrile solutions. All photoluminescence spectra were acquired with λ_{exc} at 388 nm and the excitation spectra were monitored at 640 nm of ³MLCT emission.

pathway, potentially electron transfer, as observed in the case of Ru(II)-functionalized assemblies of polyfluorene and poly(3-hexylthiophene) homopolymers.^{16,17} This variation was more pronounced for **PF2T-Ru** in accordance with a decrease in the integral spectral overlap and the respective energy transfer efficiency.

To gain additional insight into the early time photophysical behavior of the hybrid assemblies, femtosecond transient absorption data were recorded and the kinetic traces of **PFT-Hex**, **PF2T-Hex**, **PFT-Ru**, and **PF2T-Ru** conjugated backbone stimulated emission are shown in Fig. 3. After direct excitation at 388 nm, the stimulated emission of **PFT-Ru** and **PF2T-Ru** backbones decayed biexponentially on an ultrafast time scale (Fig. 3). The emission lifetimes of the hybrids were significantly attenuated when compared to those characteristics of the model polymers exhibiting major transient components of 380 ps for **PFT-Hex** and 405 ps for **PF2T-Hex**. The **PFT-Ru** kinetic trace was dominated by the 700 fs component (75%) with the 2.0 ps (25%) constituent indicating a secondary non-radiative pathway. Meanwhile, the **PF2T-Ru** kinetic trace indicated two components of 1.8 ps (75%) and 4.8 ps (25%). Based on the integral overlap of donor emission and acceptor absorption spectra, the predicted FRET rate constants were estimated to be ~ 1.2 and ~ 4 ps for **PFT-Ru** and **PF2T-Ru**, respectively. As a result, the 700 fs and 4.8 ps components in the kinetic traces of the hybrid polymers were attributed to the energy transfer, whereas the 2.0 and 1.8 ps kinetic components were associated with charge-separation processes.^{16,17} As mentioned previously, the significant decrease of the FRET pathway in the **PF2T-Ru** system was attributed to a small spectral overlap due to the bathochromically shifted emission of the polymer backbone and decreased quantum efficiency, kinetically favoring an electron transfer process. In the case of the model polymers **PFT-Hex** and **PF2T-Hex**, shorter 70 ps and 50 ps time components, as well as the corresponding biexponential character of the transients, were attributed to intrachain exciton migration, structural and/or vibrational relaxation.²²

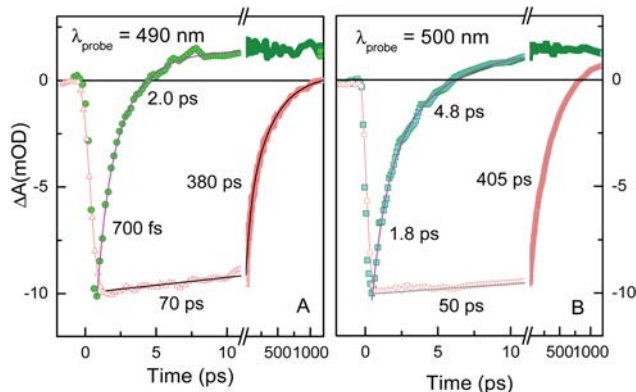


Fig. 3 (A) The decays of the stimulated emission transient signals for **PFT-Hex** (red) and **PFT-Ru** (green) at 490 nm and (B) for **PF2T-Hex** (red) and **PF2T-Ru** (green) at 500 nm along with the respective biexponential fittings.

Electrochemistry

The electrochemical properties of hybrids **PFT-Ru** and **PF2T-Ru** were studied in 0.1 M tetrabutylammonium hexafluorophosphate (TBAPF₆) acetonitrile solutions using a platinum button, platinum flag, and non-aqueous Ag/Ag⁺ electrode (calibrated *versus* the ferrocene/ferrocenium standard redox couple) as working, counter, and reference electrodes, respectively. Electrochemical experiments on **PFT-Hex** and **PF2T-Hex** systems were carried out under similar conditions in dichloromethane and tetrahydrofuran solutions for the oxidation and reduction scans, correspondingly. The cyclic voltammograms (CVs) and differential pulse voltammograms (DPVs) of all the polymers are given in Fig. 4. Redox potentials of the studied systems are summarized in Table 2.

As can be seen in Fig. 4A and C, in CV and DPV experiments, **PFT-Hex** and **PF2T-Hex** systems exhibited quasi-reversible oxidation and reduction transitions with the potentials of 0.45 V and -2.46 V, as well as 0.38 V and -2.37 V for **PFT** and **PF2T** scaffolds, respectively. *Ca.* 70 mV cathodically shifted oxidation potential was characteristic of **PF2T-Hex**, consistent with the more electron-rich character of the polymer backbone.

As expected, hybrid systems **PFT-Ru** and **PF2T-Ru** exhibited cumulative electrochemical behavior of both pendant Ru(II) polypyridyl complexes and polymer backbones. As a result, each cyclic voltammogram contained a single reversible metal-centered Ru^{2+/3+} oxidation wave at *ca.* 0.9 V along with polymer backbone oxidation waves with irreversibility caused by over-oxidation upon high scanning potentials required to study the overall behavior of the assemblies. Forward cathodic scans revealed three ligand-based iTMC reduction waves for **PFT-Ru** and **PF2T-Ru**, essentially similar to those of the parent Ru(II) complex.¹⁶ The lack of band definition and limited reversibility of the reduction transitions upon the reverse cathodic scans for the polymer hybrids were hypothesized to arise due to the high density of the iTMC chromophores, likely resulting in mixed valence states, aggregation owing to partial reduction of the assembly, or different local environments felt by separate iTMC units of the macromolecule. Similar observations were previously made for polystyrene-ruthenium(II) polypyridyl systems with high iTMC functionalization density.²³

Due to partial irreversibility of the redox transitions, DPV experiments were also employed to reliably access the photochemically significant redox potentials of **PFT-Ru** and **PF2T-Ru** using the same conditions as those employed for the CV experiments. This method has been shown to selectively extract faradaic processes and minimize errors due to overpotential generally encountered in CV experiments. Consequently, in both cases, Ru^{2+/3+} and Ru^{2+/1+} transitions were determined to occur at *ca.* 0.9 V and -1.6 V, respectively, with the polymer backbone oxidation onsets appearing at 0.57 V for **PFT** and 0.46 V for **PF2T** (Table 2). It is interesting to note that polymer backbone oxidation waves were observed to occur *ca.* 0.1 V higher potentials in the case of Ru(II)-based systems when compared to the Hex-based analogues. This finding can be partially attributed to the polymer backbone twisting by the bulky iTMC chromophores, causing a decrease in the mean conjugation length of the main chain.

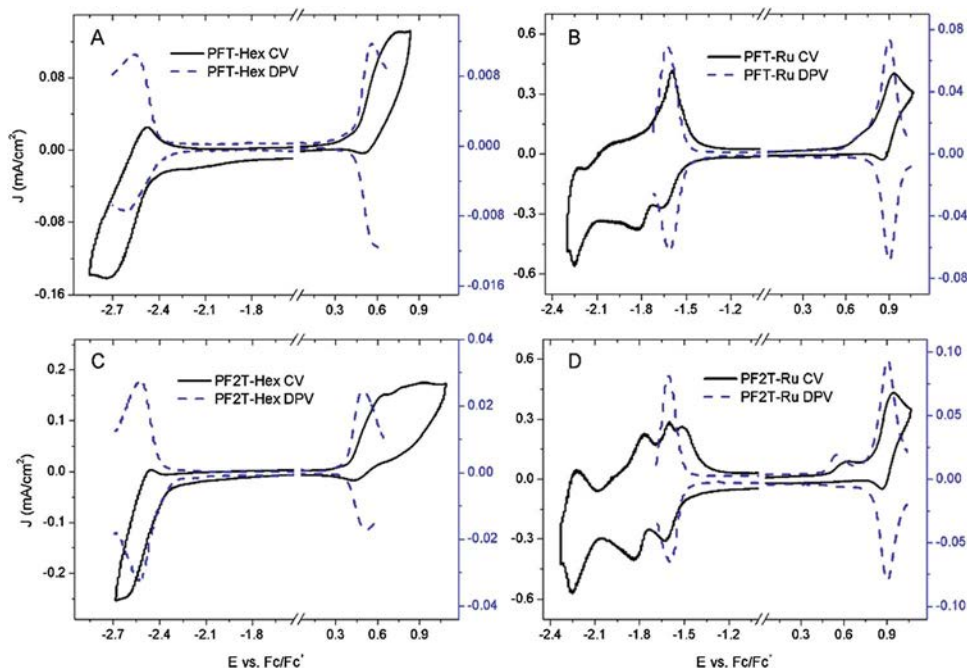


Fig. 4 Cyclic voltammograms and differential pulse voltammograms of PFT-Hex (A) and PF2T-Hex (B) in 0.1 M TBAPF₆ dichloromethane (oxidation scans) or tetrahydrofuran (reduction scans) solutions, as well as those of PFT-Ru (C) and PF2T-Ru (D) in 0.1 M TBAPF₆ acetonitrile solutions. A platinum button, platinum flag and non-aqueous Ag/Ag⁺ electrode (calibrated *versus* the Fc/Fc⁺ standard redox couple) were used as the working, counter and reference electrodes, correspondingly. Cyclic voltammograms were recorded at a 100 mV s⁻¹ scan rate.

Table 2 Electrochemical data for PFT-Hex, PF2T-Hex, PFT-Ru, and PF2T-Ru. Given in parentheses are DPV values

Compound	PFT-Hex	PF2T-Hex	PFT-Ru	PF2T-Ru
E_{ox}^0 , V	0.45 ^a (0.45 ^a)	0.38 ^a (0.37 ^a)	0.59, 0.90 (0.57, ^a 0.90)	0.49, 0.90 (0.46, ^a 0.90)
E_{red}^0 , V	-2.46 ^a (-2.37 ^a)	-2.37 ^a (-2.37 ^a)	-1.67, ^b -1.83, ^b (-2.26 ^b (-1.61))	-1.63, ^b -1.84, ^b (-2.26 ^b (-1.60))

^a Onset values of redox transitions. ^b Peak values of forward cathodic scans. All potentials are given *versus* the Fc/Fc⁺ standard redox couple.

Based on the electrochemical data, an energy level diagram showing the HOMO and LUMO values of PFT-Hex, PF2T-Hex and a monomeric Ru(II) model complex (Ru-M)¹⁶ was constructed (Fig. 5). The onset and $E_{1/2}$ potentials for the polymers and Ru-M, respectively, were used to estimate the HOMO and LUMO values relative to the vacuum level by employing the conversion HOMO (eV) = $E_{\text{ox}} + 5.1$ V and LUMO (eV) = $E_{\text{red}} + 5.1$ V.^{24,25} Additionally, the energy levels of II/III and III/IV redox couples for the Ru(ph-NH-CO-trpy) (bpy)(OH₂)⁴⁺ Ru-C water splitting catalyst²⁶ are given in Fig. 5, provided that NHE is positioned at 4.44 eV *vs.* vacuum (IUPAC recommended value).

As can be seen in Fig. 5, model polymers PFT-Hex and PF2T-Hex possessed higher-lying HOMO and LUMO values by *ca.* 0.4 eV and 0.5 eV, as well as 0.8 eV and 0.7 eV, respectively, when compared to the monomeric complex Ru-M. This finding indicated that both polymer backbones were energetically

capable of undergoing photoinduced charge separation in the hybrid assemblies, with PF2T offering somewhat higher hole stabilization. By analyzing electrochemical and optical data, the driving force of electron transfer from the polymer backbone to the Ru(II) sites was estimated to be $\Delta G^0 = -0.52$ eV and $\Delta G^0 = -0.51$ eV for PFT-Ru and PF2T-Ru, respectively, from a simplified Rehm-Weller equation.^{27,28} These values indicate a minimal thermodynamic activation barrier for the photoinduced electron transfer process in these assemblies, supporting similar assigned electron transfer rate constant values (2.0 and 1.8 ps for PFT-Ru and PF2T-Ru, respectively), observed in the transient absorption spectra (Fig. 3).²⁹ Additionally, it is

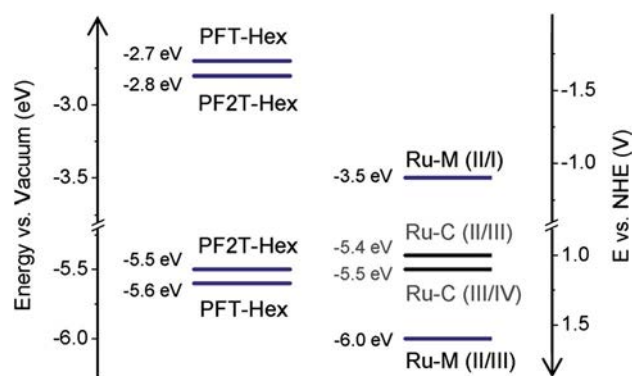


Fig. 5 Energy level diagram showing HOMO and LUMO levels of PFT-Hex, PF2T-Hex and Ru-M *vs.* vacuum and NHE, along with II/III and III/IV redox couple energy levels of the [Ru(ph-NH-CO-trpy)(bpy)(OH₂)⁴⁺] Ru-C water splitting catalyst.

interesting to note that the hybrid assembly backbones are energetically capable of oxidizing the $\text{Ru}(\text{ph-NH-CO-tpy})(\text{bpy})(\text{OH}_2)]^{4+}$ water splitting catalyst to the IV formal redox state, thus showing promise as scaffolds for solar energy storage.

To date, molecular chromophore-assemblies have emerged as defined systems to drive water splitting reactions in dye-sensitized photoelectrosynthesis cells.³⁰ In these scaffolds, surface-bound chromophore excitation results in a charge-separated state, facilitating electron injection into the semiconductor interface and the oxidation of the adjacent water splitting catalyst to drive the respective reaction. As a result, chemical fuels are produced in such devices instead of photocurrent, allowing for solar energy storage. Similarly, when used in conjunction with catalysts, conjugated polymer-iTMC assemblies could function as effective redox shuttles in photochemical reactions with the advantages of large molar absorptivity and high-mobility multi-carrier formation provided by the conjugated backbone.

In situ spectroelectrochemistry

In situ spectroelectrochemical studies³¹ were employed to elucidate the properties of the polymer backbone oxidized and iTMC chromophore reduced states, as these states were anticipated to be the products of photoinduced charge separation. For spectroelectrochemical studies, thin films of the polymers were prepared on ITO-coated glass transparent working electrodes by drop-casting either from acetone (**PFT-Ru** and **PF2T-Ru**) or tetrahydrofuran solutions. Sub-second changes in the polymer film absorption were monitored as they were subjected

to linear sweep voltammetry scans. Spectroelectrochemistry plots for all the polymers are given in Fig. 6.

As can be seen in Fig. 6A and D, upon oxidation of **PFT-Hex** and **PF2T-Hex**, visible region absorption signatures appeared at *ca.* 560 nm and 610 nm, respectively. The 50 nm red shift in the oxidized state absorption peak of **PF2T-Hex** can be attributed to an increase in charge carrier delocalization and, possibly, overall stabilization of the oxidized state. Similar trends were observed upon oxidation of **PFT-Ru** and **PF2T-Ru** (Fig. 6B and E), where the polymer backbone polaron signals arose at *ca.* 585 and 630 nm, respectively. Such observations are consistent with the electrochemistry data (Fig. 4A and C) and the tendency of the **PF2T-Ru** assembly to preferentially undergo electron transfer potentially followed by hole delocalization and stabilization of the charge-separated state. Further oxidation of the hybrid assemblies was accompanied by a bleach of Ru MLCT absorption bands, in agreement with the literature.^{32–34}

Upon reduction (Fig. 6C and F), a signal at *ca.* 550 nm appeared for both assemblies. In accordance with the CV and DPV results and the peak position, this signal was attributed to the formation of a reduced complex $[\text{Ru}^{\text{II}}(\text{L})_2(\text{L}^-)]^+$ ($\text{Ru}(\text{I})$), as 4,4'-disubstituted $\text{Ru}(\text{II})$ polypyridines generally exhibit red shifted absorption bands resembling those of the 2+ state MLCT upon first reduction.^{12,16,34} In the hybrid macromolecular antennae, along with the positive polarons on the conjugated polymer backbones, $\text{Ru}(\text{I})$ is an anticipated product of photoinduced charge separation, as well as a high-energy redox intermediate, facilitating electron injection into the conduction band of the semiconductor in solar photoelectrochemical cells.

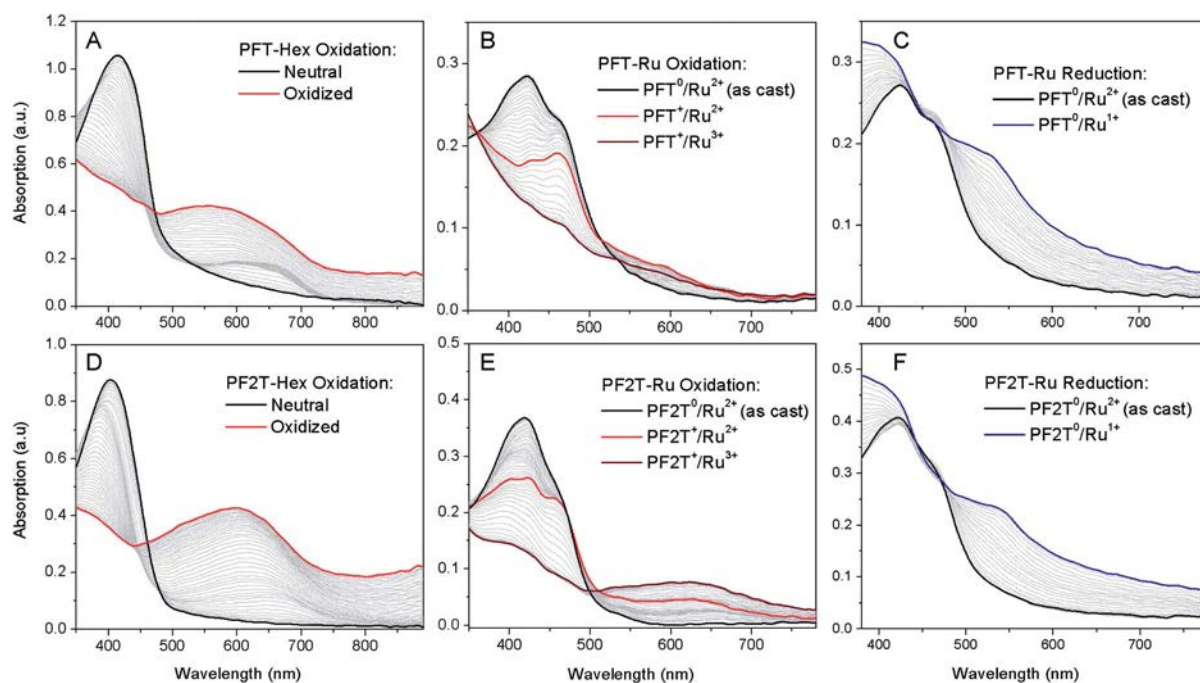


Fig. 6 Spectroelectrochemistry data for **PFT-Hex** (A) and **PF2T-Hex** (B) films immersed in 0.1 M TBAPF_6 acetonitrile solution, as well as **PFT-Ru** (B and C) and **PF2T-Ru** (E and F) films immersed in 0.1 M TBAPF_6 tetrahydrofuran solution. ITO/glass, platinum flag and silver wire pseudoreference electrode were used as the working, counter and reference electrodes, respectively.

Conclusions

A new family of ionic transition complex conjugated polymers based on fluorene and thiophene repeat units have been synthesized *via* the Pd-mediated Suzuki cross-coupling and the 1,3-dipolar “click” cycloaddition chemistry approach. The resulting scaffolds exhibit a bathochromic shift in absorption maxima and, thus, an increase in the solar radiation spectrum coverage when compared to their previously reported polyfluorene analogues. Additionally, variable fractions of electron rich thiophene units stabilize the oxidized states and allow for an efficient control of energy and charge transfer pathways in the assemblies. A combination of long-lived Ru(II) tris(bipyridine) excited states, large optical cross-sections of the conjugated backbones, as well as defined photophysical interactions between the two building blocks, provides a basis for the application of these hybrid polymers in solar energy harvesting and storage architectures.

Acknowledgements

This material is based wholly upon work supported by the UNC EFRC: Solar Fuels, an Energy Frontier Research Center funded by the U.S. Department of Energy, Office of Science, Office of Basic Energy Sciences under Award number DE-SC0001011.

Notes and references

- B. Oregan and M. Gratzel, *Nature*, 1991, **353**, 737–740.
- D. Moonshiram, J. W. Jurss, J. J. Concepcion, T. Zakharova, I. Alperovich, T. J. Meyer and Y. Pushkar, *J. Am. Chem. Soc.*, 2012, **134**, 4625–4636.
- J. J. Concepcion, J. W. Jurss, P. G. Hoertz and T. J. Meyer, *Angew. Chem., Int. Ed.*, 2009, **48**, 9473–9476.
- J. J. Concepcion, J. W. Jurss, J. L. Templeton and T. J. Meyer, *J. Am. Chem. Soc.*, 2008, **130**, 16462–16463.
- L. M. Dupray, M. Devenney, D. R. Striplin and T. J. Meyer, *J. Am. Chem. Soc.*, 1997, **119**, 10243–10244.
- M. Sykora, K. A. Maxwell, J. M. DeSimone and T. J. Meyer, *Proc. Natl. Acad. Sci. U. S. A.*, 2000, **97**, 7687–7691.
- B. Happ, A. Winter, M. D. Hager and U. S. Schubert, *Chem. Soc. Rev.*, 2012, **41**, 2222–2255.
- C. N. Fleming, L. M. Dupray, J. M. Papanikolas and T. J. Meyer, *J. Phys. Chem. A*, 2002, **106**, 2328–2334.
- S. M. Baxter, W. E. Jones, E. Danielson, L. Worl, G. Strouse, J. Younathan and T. J. Meyer, *Coord. Chem. Rev.*, 1991, **111**, 47–71.
- S. Campagna, F. Puntoriero, F. Nastasi, G. Bergamini and V. Balzani, *Top. Curr. Chem.*, 2007, **280**, 117–214.
- W. F. Wacholtz, R. A. Auerbach and R. H. Schmehl, *Inorg. Chem.*, 1986, **25**, 227–234.
- C. M. Elliott and E. J. Hershenhart, *J. Am. Chem. Soc.*, 1982, **104**, 7519–7526.
- A. Juris, V. Balzani, F. Barigelletti, S. Campagna, P. Belser and A. Von Zelewsky, *Coord. Chem. Rev.*, 1988, **84**, 85–277.
- K. Kalyanasundaram, *Coord. Chem. Rev.*, 1982, **46**, 159–244.
- D. G. McCafferty, D. A. Friesen, E. Danielson, C. G. Wall, M. J. Saderholm, B. W. Erickson and T. J. Meyer, *Proc. Natl. Acad. Sci. U. S. A.*, 1996, **93**, 8200–8204.
- L. Wang, E. Puodziukynaite, R. P. Vary, E. M. Grumstrup, R. M. Walczak, O. Y. Zolotarskaya, K. S. Schanze, J. R. Reynolds and J. M. Papanikolas, *J. Phys. Chem. Lett.*, 2012, **3**, 2453–2457.
- L. Wang, E. Puodziukynaite, E. M. Grumstrup, A. C. Brown, S. Keinan, K. S. Schanze, J. R. Reynolds and J. M. Papanikolas, *J. Phys. Chem. Lett.*, 2013, **4**, 2269–2273.
- H. J. Kim, A. R. Han, C.-H. Cho, H. Kang, H.-H. Cho, M. Y. Lee, J. M. J. Frechet, J. H. Oh and B. J. Kim, *Chem. Mater.*, 2012, **24**, 215–221.
- H. L. Vaughan, F. M. B. Dias and A. P. Monkman, *J. Chem. Phys.*, 2005, **122**, 014902.
- J. A. Faiz, R. M. Williams, M. Silva, L. De Cola and Z. Pikramenou, *J. Am. Chem. Soc.*, 2006, **128**, 4520–4521.
- G. J. Wilson, W. H. F. Sasse and A. W. H. Mau, *Chem. Phys. Lett.*, 1996, **250**, 583–588.
- E. Busby, E. C. Carroll, E. M. Chinn, L. Chang, A. J. Moule and D. S. Larsen, *J. Phys. Chem. Lett.*, 2011, **2**, 2764–2769.
- Y. L. Sun, Z. Chen, E. Puodziukynaite, D. M. Jenkins, J. R. Reynolds and K. S. Schanze, *Macromolecules*, 2012, **45**, 2632–2642.
- C. M. Cardona, W. Li, A. E. Kaifer, D. Stockdale and G. C. Bazan, *Adv. Mater.*, 2011, **23**, 2367–2371.
- B. C. Thompson, Conjugated Polymer Electrochromic and Light-Emitting Devices, Ph.D. thesis, University of Florida, 2005.
- D. L. Ashford, D. J. Stewart, C. R. Glasson, R. A. Binstead, D. P. Harrison, M. R. Norris, J. J. Concepcion, Z. Fang, J. L. Templeton and T. J. Meyer, *Inorg. Chem.*, 2012, **51**, 6428–6430.
- D. Rehm and A. Weller, *Isr. J. Chem.*, 1970, **8**, 259–271.
- H. Oevering, M. N. Paddon-Row, M. Heppener, A. M. Oliver, E. Cotsaris, J. W. Verhoeven and N. S. Hush, *J. Am. Chem. Soc.*, 1987, **109**, 3258–3269.
- R. A. Marcus, *Rev. Mod. Phys.*, 1993, **65**, 599–610.
- D. L. Ashford, W. Song, J. J. Concepcion, C. R. K. Glasson, M. K. Brennaman, M. R. Norris, Z. Fang, J. L. Templeton and T. J. Meyer, *J. Am. Chem. Soc.*, 2012, **134**, 19189–19198.
- D. Y. Liu, A. D. Chilton, P. Shi, M. R. Craig, S. D. Miles, A. L. Dyer, V. W. Ballarotto and J. R. Reynolds, *Adv. Funct. Mater.*, 2011, **21**, 4535–4542.
- P. M. S. Monk, R. J. Mortimer and D. R. Rosseinsky, *Electrochromism and Electrochromic Devices*, Cambridge University Press, Cambridge, 2007.
- R. J. Mortimer, A. L. Dyer and J. R. Reynolds, *Displays*, 2006, **27**, 2–18.
- E. Puodziukynaite, J. L. Oberst, A. L. Dyer and J. R. Reynolds, *J. Am. Chem. Soc.*, 2012, **134**, 968–978.

Ultrafast Formation of a Long-Lived Charge-Separated State in a Ru-Loaded Poly(3-hexylthiophene) Light-Harvesting Polymer

Li Wang,^{†,‡} Egle Puodziukynaite,^{†,‡} Erik M. Grumstrup,[†] Aaron C. Brown,[†] Shahar Keinan,[†] Kirk S. Schanze,[‡] John R. Reynolds,^{*,§} and John M. Papanikolas^{*,†}

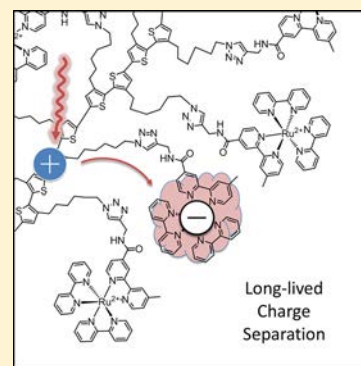
[†]Department of Chemistry, University of North Carolina at Chapel Hill, Chapel Hill, North Carolina 27599, United States

[‡]Department of Chemistry, University of Florida, Gainesville, Florida 32611-7200, United States

[§]School of Chemistry and Biochemistry, School of Materials Science and Engineering, Center for Organic Photonics and Electronics, Georgia Institute of Technology, Atlanta, Georgia 30332, United States

S Supporting Information

ABSTRACT: A light-harvesting macromolecular assembly (PT-Ru) consisting of a poly(3-hexylthiophene) (P3HT) scaffold and pendant Ru(II) polypyridyl complexes that exhibits rapid and efficient formation of a long-lived charge-separated state is described here. Photoinduced electron transfer from the polymer backbone to Ru(II) was investigated by femtosecond transient absorption spectroscopy. Photoexcitation at 388 nm results in the excitation of both the polymer backbone and Ru(II) complexes, with relative excitation probabilities of 60 and 40%, respectively. The dominant pathway (~85%) for decay of the polymer excited state is direct electron transfer from the polymer scaffold to Ru(II), forming a positive polaron and a reduced complex $[\text{Ru}^{\text{II}}(\text{L})_2(\text{L}^-)]^+$, denoted Ru(I). The charge-separated state $\text{PT}^{+\bullet}\text{-Ru(I)}$ is long-lived, persisting for 20–60 μs , and is attributed to the high mobility of holes on the polymer backbone, which facilitates spatial separation of the electron and hole, delaying recombination. The remaining 15% of the polymer excited states undergo an alternate deactivation mechanism, possibly energy transfer to Ru(II), forming Ru(II)^* . Ru(II)^* formed by either direct excitation or energy transfer undergoes back energy transfer to the scaffold, forming the low-lying polymer triplet state on the nanosecond time scale.



SECTION: Spectroscopy, Photochemistry, and Excited States

Hybrid materials that combine the chemical functionality of Ru(II) polypyridyl coordination complexes with the light-harvesting ability of organic materials are particularly attractive for next-generation solar energy conversion applications. Ruthenium(II) complexes have visible absorption bands that produce long-lived, photostable excited states and electronic properties that can be tuned through synthetic manipulation, yielding complexes capable of performing charge separation and catalytic functions.^{1–3} While extremely versatile, they are limited by relatively weak absorptivities ($\epsilon \approx 10^4 \text{ M}^{-1} \text{ cm}^{-1}$) compared to organic systems, thus necessitating longer path lengths for efficient light collection. Furthermore, catalytic water splitting requires their attachment to electrodes or the presence of redox mediators to deliver the multiple redox equivalents needed for this multielectron reaction. On the other hand, organic materials such as conjugated polymers have large extinction coefficients and exhibit rapid energy transport, making them ideal for light-harvesting functions.^{4,5} In addition, a single chain can store multiple charge carriers (electrons or holes) and thus serve as a reservoir of redox equivalents that can be used in multielectron catalytic reactions, such as water splitting. However, their short singlet-state lifetimes compete with charge separation, and they lack the chemical versatility of metals to perform catalytic functions.

We have developed a series of modular macromolecular assemblies that combine the functionality of conjugated polymers with Ru(II) coordination complexes. One example from this series is a light-harvesting assembly utilizing a polyfluorene scaffold (PF-Ru),⁶ where rapid energy transfer of the PF^* excited state to the pendant complexes ($\tau_{\text{EnT}} = 500 \text{ fs}$) yields a long-lived ³MLCT excited state. This Letter describes an assembly incorporating poly(3-hexylthiophene) (P3HT) as the polymer scaffold that consists of ~85 thiophene repeat units, each functionalized with a metal complex (PT-Ru, Figure 1A; $\text{PT} \equiv \text{poly}[3\text{-}(6\text{-bromohexyl})\text{thiophene}]$). In contrast to PF-Ru, where energy transfer dominates, the primary relaxation pathway in PT-Ru is electron transfer, which results in the rapid formation of a $\text{PT}^{+\bullet}\text{-Ru(I)}$ charge-separated (CS) state ($\text{Ru(I)} \equiv [\text{Ru}^{\text{II}}(\text{L})_2(\text{L}^-)]^+$) within 1–2 ps. Once formed, the CS state persists for tens of microseconds, most likely due to a high hole mobility on the polymer that allows the charges to become spatially separated from each other, delaying recombination.⁷ The formation of long-lived CS states is critical to the function of solar energy devices because it allows more time for slower

Received: May 27, 2013

Accepted: June 26, 2013

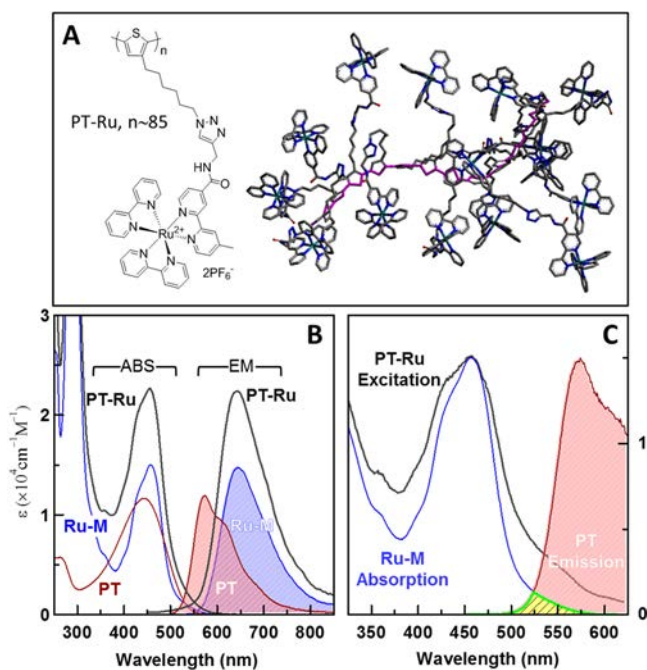


Figure 1. (A) Chemical structure of the PT-Ru assembly (left) and 3D structure obtained from molecular dynamics simulation of a PT-Ru assembly with 15 repeat units. Simulations included 300 explicit acetonitrile solvent molecules and 30 PF₆⁻ counterions, which are not shown for clarity. Atoms highlighted in magenta show the polythiophene backbone. (B) Absorption and emission spectra of the PT-Ru assembly, model polymer (PT), and model Ru complex (Ru-M). The PT-Ru and Ru-M spectra were obtained in acetonitrile; PT was obtained in THF. Extinction coefficients for polymers are per repeat unit. Emission spectra are scaled to the intensity of their absorption spectra. (C) Comparison of the excitation spectrum (black) of PT-Ru monitored at 640 nm and the absorption spectrum of Ru-M. The yellow region depicts the spectral overlap between the absorption spectrum of Ru-M and emission spectrum of PT.

processes, such as catalytic reactions, to take place before deactivation via back electron transfer can occur.

The PT-Ru assembly was synthesized via a multistep route, as shown in Scheme S1 (Supporting Information). The regioregular PT scaffold was obtained using the Grignard metathesis (GRIM) polymerization approach^{8,9} and treated with sodium azide to yield poly[3-(6-azidohexyl)thiophene]. Finally, the azide-functionalized polymer and an alkynyl-containing Ru(II) polypyridyl complex were combined under Cu(I)-assisted “click” chemistry conditions^{6,10–12} to afford the PT-Ru assembly, which was obtained with essentially quantitative azide–alkyne cycloaddition conversion.

The absorption spectrum of PT-Ru (Figure 1B) shows a strong low-energy band centered at 450 nm that has contributions from both the Ru(II) complexes and the polythiophene backbone. The PT (Scheme S1, Supporting Information) absorption, which corresponds to the lowest-energy $\pi \rightarrow \pi^*$ transition, is broad and featureless with a molar absorptivity of $1.2 \times 10^4 \text{ cm}^{-1} \text{ M}^{-1}$ per repeat unit at its maximum, 445 nm. The MLCT transition of the model Ru(II) complex (Ru-M, Scheme S2 (Supporting Information)) is centered at 455 nm with $\epsilon = 1.5 \times 10^4 \text{ cm}^{-1} \text{ M}^{-1}$. Excited-state formation is partitioned between the Ru(II) complexes and the polymer backbone, and at 388 nm, 60% of the incident light is absorbed by the polymer and the remaining 40% is absorbed by the Ru(II) complexes.

When excited at 388 nm, the emission spectrum of PT-Ru is dominated by an intense ³MLCT emission band at 640 nm. A slight distortion on the high-energy side of the band relative to the Ru(II) monomer complex is attributed to the polythiophene polymer. The PT emission in tetrahydrofuran (THF) has clear vibronic structure with a 0–0 transition at 575 nm, an excited-state lifetime of 580 ps, and a quantum yield of 0.27.¹³ The relatively weak contribution of the polythiophene to the overall emission in PT-Ru, despite significant photon absorption by the polymer backbone, is indicative of an efficient quenching of the polythiophene excited state by the Ru(II) complex.

In principle, polythiophene excited-state quenching can occur through either an energy- or electron-transfer process or a combination of the two. In the limit that energy transfer plays no role, the ³MLCT emission observed in the PT-Ru assembly would arise entirely from direct excitation of the Ru(II) complexes, and the emission excitation spectrum would match the absorption spectrum of the Ru(II) model. This is not the case. The excitation spectrum of PT-Ru monitored at 640 nm is significantly broader than the ground-state absorption spectrum of the Ru-M complex. This suggests that energy transfer does contribute to the polythiophene quenching, although other observations described below indicate that it is a relatively minor contributor.

The excited-state dynamics following 388 nm photoexcitation of PT-Ru (in acetonitrile) and PT (in THF) are monitored using broad-band pump–probe spectroscopy on time scales ranging from femtoseconds to microseconds. In both cases, experiments were performed in solution at low concentration in order to minimize contributions from chain–chain interactions.

Transient absorption spectra for the PT system are shown in Figure 2A. At $\Delta t = 0$, the spectrum is characterized by a ground-state bleach at 450 nm and stimulated emission band centered at 550 nm. The bleach feature exhibits a slight shift toward the blue as it decays in amplitude with $\tau \approx 585$ ps. The stimulated emission evolves to lower energy, shifting 25 nm in the first 50 ps and another 5 nm over the next 200–300 ps, ultimately resulting in a structured spectrum with peaks at 575 and 615 nm. This time-dependent red shift is attributed to excited-state self-trapping by torsional relaxation rather than the excitonic energy transfer to lower-energy segments.¹⁴

The transient spectra of the PT-Ru assembly differ significantly from those of PT (Figure 2B). The absorption band at ~ 370 nm is the result of direct excitation of the pendant Ru(II) complexes. The bleach feature that extends from 400 to 500 nm is significantly broader than the Ru* bleach, especially at early times, suggesting that it results from a combination of the loss of polythiophene and Ru(II) ground-state absorption, as well as stimulated emission from the polythiophene excited state. The stimulated emission (500–600 nm) is quenched during the first 1–2 ps and replaced by an absorption band at 550 nm. Even at 50 ps, long after the polythiophene excited state has decayed away, the transient spectrum does not resemble that of Ru*, indicating the presence of a quenching mechanism other than energy transfer.

Spectroelectrochemical data provide insight into the photo-product and the band assignments. Figure 2D shows difference spectra obtained by subtracting the ground-state absorption spectrum of the assembly, $A(\lambda)$, from the spectra obtained following quantitative oxidation (A_{Ox}) or reduction (A_{Red}), that is

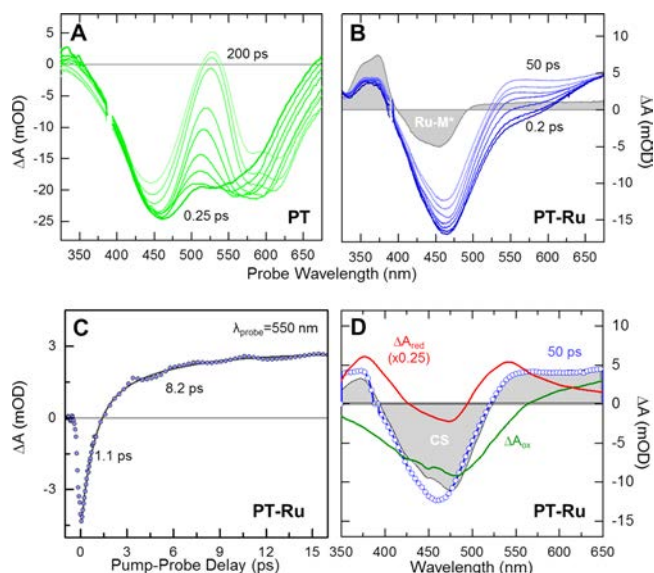


Figure 2. (A) Transient absorption spectra of PT in THF at 0.25, 0.5, 1, 2, 5, 10, 50, 100, and 200 ps. (B) Transient absorption spectra of PT-Ru in acetonitrile at 0.20, 0.25, 0.35, 0.50, 0.75, 2, and 50 ps, as well as Ru-M (gray, shaded). All transient spectra were obtained at an excitation wavelength (λ_{exc}) of 388 nm (50 nJ/pulse). (C) Kinetic trace from PT-Ru monitored at 550 nm (circles); the solid line is a fit to a biexponential model with fast (1.1 ps, 85%) and slow (8.2 ps, 15%) components. (D) Comparison of the PT-Ru transient absorption spectrum at 50 ps (blue circle) with the transient absorption spectrum of the $\text{PT}^{+\bullet}\text{-Ru(I)}$ CS state, ΔA_{CS} , predicted by spectroelectrochemistry (gray shaded). The red and green lines are contributions from the reduced (ΔA_{Red}) and oxidized (ΔA_{Ox}) species, respectively.

$$\Delta A_{\text{Ox}} = A_{\text{Ox}}(\lambda) - A(\lambda) \quad (1)$$

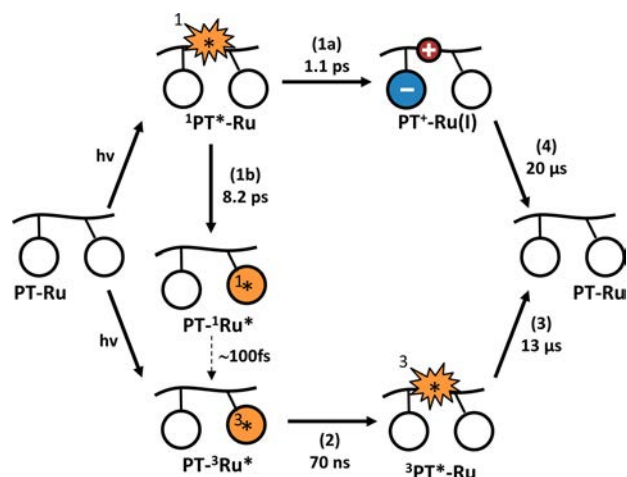
$$\Delta A_{\text{Red}} = A_{\text{Red}}(\lambda) - A(\lambda) \quad (2)$$

These spectra represent contributions of oxidized ($\text{PT}^{+\bullet}\text{-Ru}$) and reduced (PT-Ru(I)) species to the transient absorption spectrum. The ΔA_{Red} spectrum shows two bands centered at 375 and 540 nm that are assigned to Ru(I). The ΔA_{Ox} spectrum reveals one broad bleach centered at 475 nm that corresponds to the loss of absorption intensity upon oxidation of the polythiophene ($\text{PT}^{+\bullet}\text{-Ru}$), and a weak absorption to the red of 550 nm that is assigned to the positive polaron absorption.⁷

These spectra suggest that photoexcitation of the polythiophene results in the formation of a CS state by direct electron transfer from the polymer backbone to the pendant Ru(II). The transient spectrum arising from the CS state (ΔA_{CS}) can be estimated from a superposition of ΔA_{Ox} and ΔA_{Red} , that is, $\Delta A_{\text{CS}} = \Delta A_{\text{Ox}} + 0.25 \times \Delta A_{\text{Red}}$.⁷ The factor of 0.25 is present because in the electrochemical oxidation/reduction of the assembly, ~ 4 times as many reduced complexes can be accommodated as positive polarons on a single polymer chain. The similarity between the transient spectrum and ΔA_{CS} (Figure 2D) indicates that charge separation is the primary quenching mechanism of the polythiophene excited state (1a in Scheme 1).

The time scale for charge separation is obtained by monitoring the growth of the 550 nm signal as a function of pump-probe delay (Figure 2C). The growth is well-described by a biexponential function with a large fast (1.1 ps, 85% \pm 5%)

Scheme 1. Illustration of the Dynamic Processes Resulting from Photoexcitation of the PT-Ru Assembly in Acetonitrile



and a smaller slow (8.2 ps, 15% \pm 5%) component. The presence of two kinetic components indicates that the two dynamical processes arise from different “states” in the assembly. Molecular dynamics simulations of a 15 repeat unit model polymer in explicit solvent (Figure 1A) show a broad distribution of nearest distances between the polymer backbone and Ru(II) complexes that span 0.5–2.2 nm. While $\sim 40\%$ of Ru chromophores are less than 1 nm from the backbone, there is a significant fraction with a greater separation. This distribution could be the origin of the biexponential kinetics, with faster quenching to the complexes situated near the backbone and slower quenching occurring when the complex is farther away.

The fast component is assigned to the electron-transfer process (1a, Scheme 1). The electron transfer from polythiophene to Ru(II) displays no temperature dependence (Figure 3) in its rate constant, suggesting that it is probably

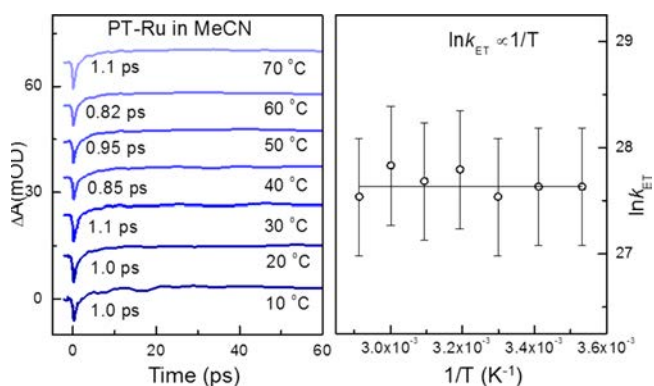


Figure 3. (A) Kinetic traces of PT-Ru at 550 nm in acetonitrile under different temperatures, with excitation at 388 nm at 50 nJ/pulse. (B) The plot of $\ln k_{\text{ET}}$ versus $1/T$. Error bars represent a 2% standard deviation obtained from the fitting of the electron-transfer rate, k_{ET} .

facilitated by a small activation barrier. The thermodynamic driving force (ΔG°) is estimated to be -0.49 eV from the redox potentials (Supporting Information), which, given the small barrier, implies a reorganization energy of ~ 0.5 eV.¹⁵

The physical origin of the slower (8.2 ps) component is less certain. One possibility is that it reflects a competitive polythiophene excited state to Ru(II) energy-transfer pathway

(1b, Scheme 1). We recently reported on a Ru(II)-loaded polyfluorene system, where energy- and electron-transfer quenching both occur. In that case, rapid energy transfer (85%) is facilitated by a large spectral overlap between the polymer emission and Ru(II) absorption (i.e., $\int \epsilon(\bar{\nu})F(\bar{\nu}) d(\bar{\nu})$) that gives rise to energy transfer on the femtosecond time scale.^{6,16} The spectral overlap between the PT emission and Ru(II) absorption is about a factor of 2.7 smaller in this system (2.8×10^{-14} versus $7.4 \times 10^{-14} \text{ cm}^{-4}$ for PF-Ru). We estimate from the spectral overlap in PT-Ru, as well as the lifetime and quantum yield measurements, that the energy-transfer rate k_{EnT} is $\sim (10 \text{ ps})^{-1}$, which is comparable to the 8.2 ps component.

Dynamic spectral evolution on the nanosecond to microsecond time scale (Figure 4) was monitored using an

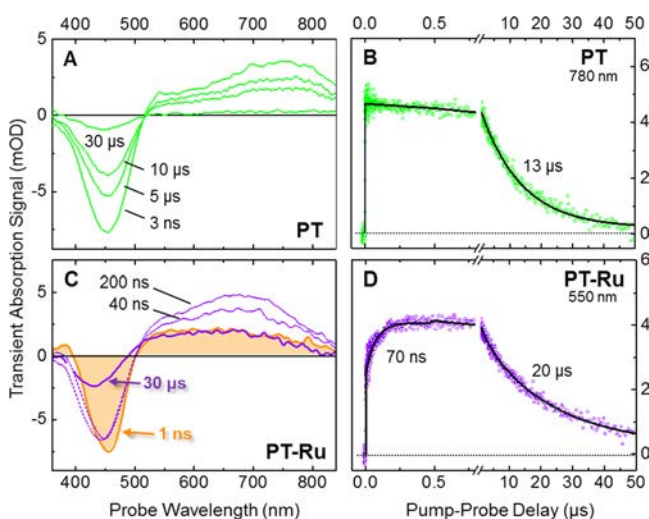


Figure 4. (A) Transient absorption spectra of PT in THF with excitation at 388 nm. (B) Kinetic traces at 780 nm of PT in THF. (C) Transient absorption spectra of PT-Ru in acetonitrile with excitation at 388 nm. (D) Kinetic trace at 550 nm of PT-Ru in acetonitrile.

electronically delayed continuum probe pulse generated by a diode-laser-pumped photonic crystal fiber with ~ 500 ps time resolution. On the nanosecond time scale, an absorption band centered ~ 700 nm emerges in the PT-Ru transient spectra (Figure 4C). The band grows with a rise time of 70 ns, reaching a maximum intensity at about 200 ns, after which it decays on the microsecond time scale (Figure 4D). This band is remarkably similar in both position and lifetime to the near-infrared excited-state absorption observed in PT (Figure 4A), which decays with $\tau = 13 \mu\text{s}$ (Figure 4B), and has been attributed by others to a triplet excited state of the polymer.^{17,18} Its growth in PT-Ru implies a delayed formation of ${}^3\text{PT}^*\text{-Ru}$, most likely through a PT-Ru^* to ${}^3\text{PT}^*\text{-Ru}$ energy transfer (2, Scheme 1), which is then followed by excited-state decay (3, Scheme 1) on the microsecond time scale. Assignment to triplet back transfer is also supported by the observation of the low quantum efficiency per complex ($\Phi = 0.13 \times \Phi_{\text{Ru-M}}$) and the short (<100 ns) lifetime of the ${}^3\text{MLCT}$ state compared to that of the Ru(II) model complex ($\Phi_{\text{Ru-M}} = 0.095, 1.25 \mu\text{s}$). We note that this process is not competitive with the ultrafast charge injection that typically occurs from Ru excited states into TiO_2 and thus should not interfere with light harvesting in the traditional sense.

By $30 \mu\text{s}$, the 700 nm absorption band in PT-Ru has disappeared, and the absorption band that remains matches the

intensity and shape of the 1 ns spectrum, other than the smaller amplitude of bleach (Figure 4C). At this point, the ${}^3\text{PT}^*\text{-Ru}$ formed either by direct excitation or back energy transfer has decayed back to the ground state, suggesting that the remaining absorption is due almost entirely to the CS state, $\text{PT}^{+\bullet}\text{-Ru(I)}$. The CS state persists for tens of microseconds, eventually undergoing back electron transfer (4, Scheme 1) with $\tau \approx 20 \mu\text{s}$, which is comparable to the mean polaron lifetime in polythiophene thin films ($17 \mu\text{s}$).¹⁹ As compared with the polyfluorene assembly, the lifetime of the CS state of $\text{PT}^{+\bullet}\text{-Ru(I)}$ is several hundred-fold longer than the 6 ns observed in $\text{PF}^{+\bullet}\text{-Ru(I)}$.⁶ This long-lived state is perhaps a consequence of the high hole mobility in polythiophene, which would enable the hole to become spatially separated from the Ru(I) and delay recombination.⁷

The PT-Ru assembly couples the functional elements of both conjugated polymers and metal complexes. Photoexcitation of the PT scaffold is followed by rapid electron transfer to produce a $\text{PT}^{+\bullet}\text{-Ru(I)}$ CS state (85% yield, based on amplitudes of kinetic components) that exhibits a $\sim 20 \mu\text{s}$ lifetime. The formation of a long-lived CS state is critical for solar energy conversion applications.

■ ASSOCIATED CONTENT

Supporting Information

Experimental procedures, characterization data, electrochemistry, and spectroelectrochemistry results. This material is available free of charge via the Internet at <http://pubs.acs.org>.

■ AUTHOR INFORMATION

Corresponding Author

*E-mail: john_papanikolas@unc.edu (J.M.P.); reynolds@chemistry.gatech.edu (J.R.R.).

Author Contributions

[‡]L.W. and E.P. contributed equally.

Notes

The authors declare no competing financial interest.

■ ACKNOWLEDGMENTS

This work was supported by the UNC EFRC: Center for Solar Fuels, an Energy Frontier Research Center funded by the U.S. Department of Energy, Office of Science, Office of Basic Energy Sciences under Award Number DE-SC0001011. L.W. also thanks Professor David W. Thompson at Memorial University for the academic consultations and suggestions.

■ REFERENCES

- (1) Concepcion, J. J.; Jurss, J. W.; Templeton, J. L.; Meyer, T. J. One Site is Enough. Catalytic Water Oxidation by $[\text{Ru}(\text{tpy})(\text{bpm})(\text{OH}_2)]^{2+}$ and $[\text{Ru}(\text{tpy})(\text{bpz})(\text{OH}_2)]^{2+}$. *J. Am. Chem. Soc.* **2008**, *130*, 16462–16463.
- (2) Kaveevivitchai, N.; Chitta, R.; Zong, R.; El Ojaimi, M.; Thummel, R. P. A Molecular Light-Driven Water Oxidation Catalyst. *J. Am. Chem. Soc.* **2012**, *134*, 10721–10724.
- (3) Duan, L.; Bozoglian, F.; Mandal, S.; Stewart, B.; Privalov, T.; Llobet, A.; Sun, L. A Molecular Ruthenium Catalyst with Water-Oxidation Activity Comparable to that of Photosystem II. *Nature* **2012**, *4*, 418–423.
- (4) Collini, E.; Scholes, G. D. Coherent Intrachain Energy Migration in a Conjugated Polymer at Room Temperature. *Science* **2009**, *323*, 369–373.
- (5) Schindler, F.; Jacob, J.; Grimsdale, A. C.; Scherf, U.; Müllen, K.; Lupton, J. M.; Feldmann, J. Counting Chromophores in Conjugated Polymers. *Angew Chem. Int. Ed.* **2005**, *44*, 1520–1525.

(6) Wang, L.; Puodziukynaite, E.; Vary, R. P.; Grumstrup, E. M.; Walczak, R. M.; Zolotarskaya, O. Y.; Schanze, K. S.; Reynolds, J. R.; Papanikolas, J. M. Competition Between Ultrafast Energy Flow and Electron Transfer in a Ru(II)-Loaded Polyfluorene Light-Harvesting Polymer. *J. Phys. Chem. Lett.* **2012**, 2453–2457.

(7) Takeda, N.; Miller, J. R. Poly(3-decylthiophene) Radical Anions and Cations in Solution: Single and Multiple Polarons and Their Delocalization Lengths in Conjugated Polymers. *J. Phys. Chem. B* **2012**, 116, 14715–14723.

(8) Loewe, R. S.; Khersonsky, S. M.; McCullough, R. D. A Simple Method to Prepare Head-to-Tail Coupled, Regioregular Poly(3-alkylthiophenes) Using Grignard Metathesis. *Adv. Mater.* **1999**, 11, 250–253.

(9) Kiriya, A.; Senkovskyy, V.; Sommer, M. Kumada Catalyst-Transfer Polycondensation: Mechanism, Opportunities, and Challenges. *Macromol. Rapid Commun.* **2011**, 32, 1503–1517.

(10) Rostovtsev, V. V.; Green, L. G.; Fokin, V. V.; Sharpless, K. B. A Stepwise Huisgen Cycloaddition Process: Copper(I)-Catalyzed Regioselective “Ligation” of Azides and Terminal Alkynes. *Angew. Chem., Int. Ed.* **2002**, 41, 2596–2599.

(11) Binder, W. H.; Sachsenhofer, R. ‘Click’ Chemistry in Polymer and Materials Science. *Macromol. Rapid Commun.* **2007**, 28, 15–54.

(12) Meldal, M. Polymer “Clicking” by CuAAC Reactions. *Macromol. Rapid Commun.* **2008**, 29, 1016–1051.

(13) Measured with comparison to a Ru(II) polypyridyl complex in MeCN and corrected for the difference of the solvent refractive indexes.

(14) Busby, E.; Carroll, E. C.; Chinn, E. M.; Chang, L. L.; Moule, A. J.; Larsen, D. S. Excited-State Self-Trapping and Ground-State Relaxation Dynamics in Poly(3-hexylthiophene) Resolved with Broadband Pump–Dump–Probe Spectroscopy. *J. Phys. Chem. Lett.* **2011**, 2, 2764–2769.

(15) Marcus, R. A.; Sutin, N. Electron Transfers in Chemistry and Biology. *Biochim. Biophys. Acta* **1985**, 811, 265–322.

(16) Faiz, J. A.; Williams, R. M.; Silva, M. J. J. P.; De Cola, L.; Pikramenou, Z. A Unidirectional Energy Transfer Cascade Process in a Ruthenium Junction Self-Assembled by α - and β -Cyclodextrins. *J. Am. Chem. Soc.* **2006**, 128, 4520–4521.

(17) Kraabel, B.; Moses, D.; Heeger, A. J. Direct Observation of the Intersystem Crossing in Poly(3-octylthiophene). *J. Chem. Phys.* **1995**, 103, 5102–5108.

(18) Wohlgenannt, M.; Jiang, X. M.; Vardeny, Z. V. Confined and Delocalized Polarons in π -Conjugated Oligomers and Polymers: A Study of the Effective Conjugation Length. *Phys. Rev. B* **2004**, 69, 241204.

(19) Kinoshita, K.; Koayashi, T.; Nagase, T. N.; Photoinduced, H. Absorption in P3HT/PCBM Bulk Heterostructures. *Mater. Sci. Forum* **2010**, 658, 503–506.

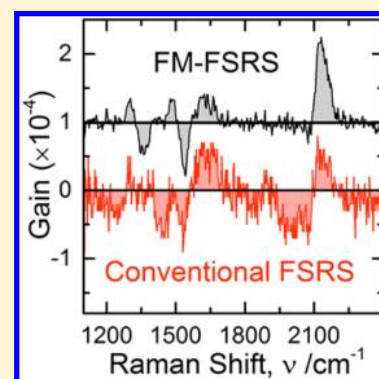
Frequency Modulated Femtosecond Stimulated Raman Spectroscopy of Ultrafast Energy Transfer in a Donor–Acceptor Copolymer

Erik M. Grumstrup,[†] Zhuo Chen,[‡] Ryan P. Vary,[†] Andrew M. Moran,[†] Kirk S. Schanze,[‡] and John M. Papanikolas^{*,†}

[†]Department of Chemistry, University of North Carolina at Chapel Hill, Chapel Hill, North Carolina 27514, United States

[‡]Department of Chemistry and Center for Macromolecular Science and Engineering, University of Florida, Gainesville, Florida 32611, United States

ABSTRACT: A Raman-pump frequency modulation scheme and an automated signal-processing algorithm are developed for improved collection of time-resolved femtosecond stimulated Raman spectra. Together, these two advancements remove the broad background signals endemic to FSRS measurements and retrieve signals with high sensitivity. We apply this frequency-modulated femtosecond stimulated Raman spectroscopy (FM-FSRS) to the characterization of ultrafast energy transport in a copolymer comprised of polystyrene linked oligo(phenylene–ethynylene) donor and thiophene–benzothiadiazole acceptor chromophores. After photoexcitation of the donor, ultrafast energy transfer is monitored by the decay of donor vibrational modes and simultaneous growth of acceptor modes. The FM-FSRS method shows clear advantages in signal-to-noise levels, mitigation of artifact features, and ease of data processing over the conventional FSRS technique.



INTRODUCTION

Time-resolved femtosecond stimulated Raman spectroscopy (FSRS) has become an important tool for studying a broad range of excited state photophysics in solvated chromophores including charge transfer processes, isomerization kinetics, and excited state proton transfer.^{1–10} In transient absorption measurements, insight into evolving photophysics is often obscured by overlapping electronic resonances. In contrast, FSRS probes vibrational resonances, which are also sensitive to excited state character but exhibit much narrower lineshapes in condensed phase samples.¹¹ As a consequence, FSRS offers distinct advantages over transient absorption spectroscopy, where excited state dynamics are often obscured by the broad linewidths characteristic of electronic resonances.

Despite these advantages, FSRS remains a technique that is practiced by relatively few researchers. Adoption is difficult for a number of reasons. Chief among these is that FSRS is formally a fifth order process (photoinduced change to the stimulated Raman spectrum), making its signal size 1–2 orders of magnitude smaller than the intensity changes typically found in transient absorption. Compounding the difficulty is that, in contrast to many nonlinear spectroscopies, the signal is not emitted in a background-free direction. Rather, the FSRS signal is emitted in the same direction as the probe beam, requiring its isolation from other more intense signals. While many of these additional signals can be removed by pump modulation, as in transient absorption, analysis of FSRS spectra still requires subtraction of a large background that is often an order of magnitude larger than the FSRS signal itself.

Background subtraction is not straightforward. It requires an elaborate, painstaking data processing procedure before the desired signals are isolated, and in cases where a dense collection of overlapping resonances are present, delineation of exactly where the baseline lies is often ambiguous. Compounding this problem is that small wavelength dependent variations in the detection sensitivity, whether due to the imaging optics in the spectrometer or the array detector itself, can introduce artifacts that are difficult to distinguish from actual FSRS peaks. Together these difficulties constitute a significant barrier to routine application of the technique.

In this paper we describe an experimental method and an automated data-processing algorithm that mitigate these problems. We expand upon conventional FSRS instrumentation by incorporating a spatial light modulator to control the center frequency of the Raman-pump beam, ω_{RP} . We collect two FSRS spectra obtained at different Raman-pump center frequencies, f_1 and f_2 , where $\Delta\omega_{RP} = f_2 - f_1$ is $\sim 30 \text{ cm}^{-1}$. By subtracting these two spectra, we generate a FSRS difference spectrum that removes much of the background. The FSRS spectrum is reconstructed from the difference spectrum using a simple, automated numerical algorithm that requires only two parameters as input. While similar strategies that modulate the Raman pump frequency have been employed in ground and excited state Raman spectroscopies, the lack of a straightfor-

Received: May 6, 2013

Revised: June 9, 2013

Published: June 12, 2013

ward reconstruction algorithm that leaves peak shapes intact has prevented widespread adoption.^{12–14}

Collection of the FSRS difference spectra and subsequent reconstruction has many advantages over conventionally processed single-Raman-pump frequency spectra. In addition to an improved signal-to-noise ratio and dramatically reduced background contributions, the frequency modulated FSRS (FM-FSRS) technique eliminates detector artifacts from the recovered spectra. Further, while use of a spatial light modulator makes FM-FSRS highly flexible and paves the way for more elaborate pulse shaping strategies, a simple mechanical slit and a computer controlled actuator can easily be substituted, making this technique readily accessible.

EXPERIMENTAL METHODS

Materials. Synthesis of the OPE-TBT polymer is described elsewhere.¹⁵ For the spectroscopic experiments the polymer was dissolved in THF to achieve an OD of 2 ($\sim 180 \mu\text{mol}$ in polymer repeat unit concentration) and placed in a 2 mm cuvette. All experiments were performed at room temperature.

FM-FSRS Spectrometer. Time-resolved FSRS spectra are collected on a home-built spectrometer diagrammed in Figure 1. A Ti:sapphire regenerative amplifier (Clark-MXR CPA2210)

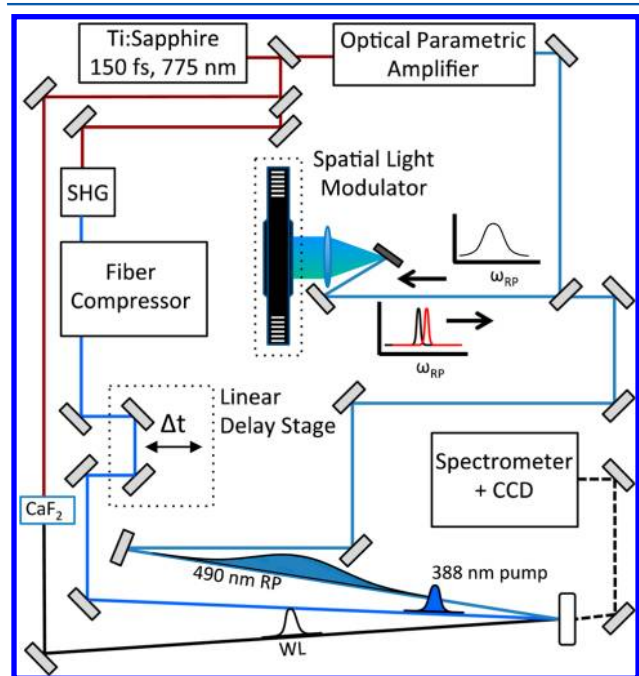


Figure 1. Schematic of the FSRS spectrometer. Three pulses are overlapped in the sample: the 388 nm pump pulse, the Raman pump (RP) pulse tunable by the spatial light modulator, and the white light (WL) continuum. The FSRS signal is emitted in the same direction as the WL continuum and detected on a high-speed diode array.

generates 150 fs fwhm pulses centered at 775 nm. Approximately 100 mW of this beam is frequency doubled in a 2 mm BBO crystal and coupled into a home-built, hollow fiber waveguide filled with Ar at 20 psig for spectral broadening. Prism compression results in 35 fs fwhm pump pulses, which are focused to a $125 \mu\text{m}$ spot by a 300 mm lens at the sample ($250 \mu\text{J}/\text{cm}^2$).

The stimulated Raman response is generated by a pair of pulses, consisting of a narrow bandwidth Raman-pump (RP) pulse and a broadband white light (WL) continuum that arrive

at the sample simultaneously. The 490 nm Raman-pump pulse is generated in a 2 mm BBO crystal via sum frequency of the 775 nm fundamental and the 1332 nm signal from an optical parametric amplifier (Light Conversion TOPAS-C). It is then coupled into a 4-f, zero dispersion optical compressor with a CRI 128 pixel dual mask spatial light modulator (SLM) placed at the Fourier plane. The SLM is used to attenuate all but a narrow band ($\sim 1 \text{ nm}$) of the spectrum, effectively acting as a computer-controlled slit. The WL continuum is generated by focusing a small portion (3 mW) of the 775 nm amplifier output into a translating CaF_2 window. The WL continuum is collected and collimated by a spherical mirror. The Raman pump and continuum are focused into the sample with a 300 mm lens and a 250 mm spherical aluminum mirror, respectively. The WL is dispersed by a 0.15 m spectrograph with a 1200 g/mm grating and detected on a diode array capable of reading out at the 1 kHz repetition rate of the laser.

The pump and Raman-pump beams are passed through a dual blade mechanical chopper synched to the laser pulse repetition rate. The Raman-pump beam is chopped at half the frequency of the pump beam so that four interleaved spectra are collected at up to shot-to-shot rates. A typical FM-FSRS spectrum involves the measurement of 1000 sets of interleaved spectra at $\omega_{\text{RP}} = f_1$. The computer controlled SLM shifts the center frequency of the Raman pump pulse by $20\text{--}30 \text{ cm}^{-1}$ to $\omega_{\text{RP}} = f_2$, and an additional 1000 sets of interleaved spectra are acquired. The instrument can resolve changes in the Raman gain as small as $\sim 1 \times 10^{-4}$ when conventional data processing techniques are employed. However, because pixel-to-pixel variations are subtracted out with the FM-FSRS method, better signal-to-noise levels are achievable and improve the minimum resolvable peak amplitude to $\sim 2 \times 10^{-5}$.

RESULTS AND DISCUSSION

Time resolved FSRS probes the change in the stimulated Raman spectrum following photoexcitation, allowing it to follow photoinduced dynamics through the evolution of vibrational modes. In this three-pulse technique, the sample first interacts with an electronically resonant pump pulse (ω_{Pu}) creating ground and excited state populations. After a well-defined delay, Δt , the sample interacts with two temporally overlapped pulses, a broadband white light continuum (WL) and a spectrally narrow Raman-pump (RP) pulse centered at ω_{RP} . Stimulated Raman transitions are detected as changes in the WL intensity at wavelengths corresponding to $\omega_{\text{RP}} \pm \omega_{\text{vib}}$. FSRS can be used to follow the evolution of the vibrational spectrum using only visible lasers and without the need for expensive IR detectors.

Despite this advantage, FSRS remains a technique that has not enjoyed widespread use, in part because of the difficulty in disentangling the Raman features from the broad background that is also present. The remainder of the paper describes the FM-FSRS technique, which provides a straightforward means of isolating the FSRS response, and its application to energy transport in a donor–acceptor assembly consisting of oligo-(phenylene–ethynylene) (OPE) and thiophene–benzothiadiazol (TBT) chromophores (Figure 2A). Section A describes the characterization of energy transport in this assembly using transient absorption spectroscopy for comparison with the FSRS technique. Section B discusses the difficulties associated with recovering FSRS spectra using conventional techniques. In Section C, the benefits of employing frequency modulation FSRS are discussed and FSRS spectra collected in the

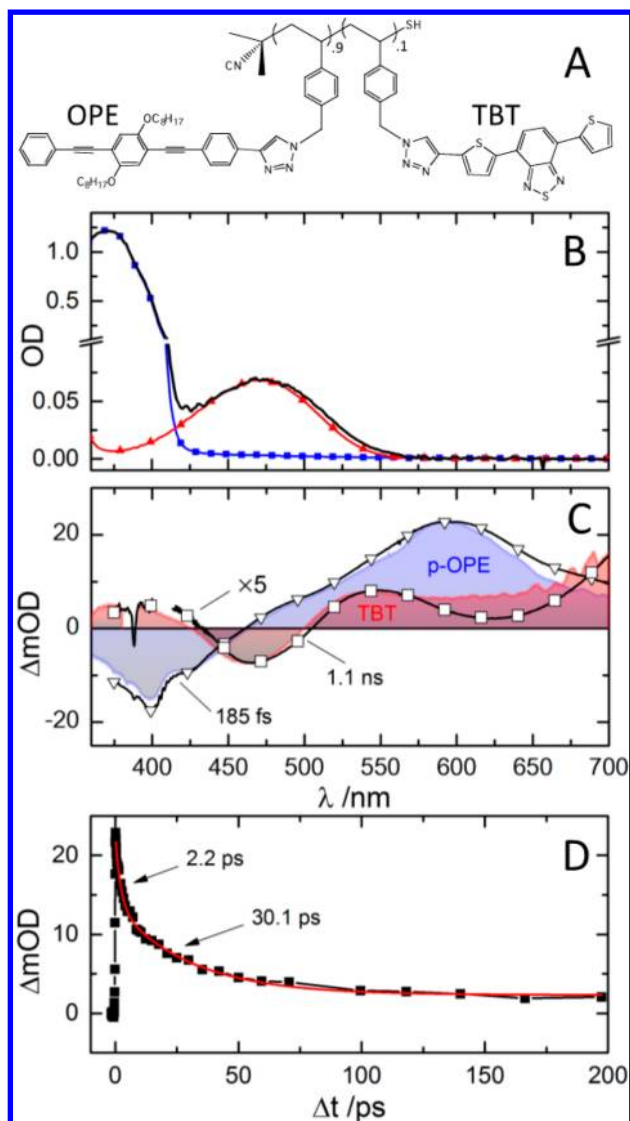


Figure 2. (A) Structure of the 90% oligo(phenylene-ethynylene) (OPE) and 10% thiophene-benzothiadiazol (TBT) copolymer. (B) UV-vis spectra of the donor-acceptor copolymer (black) and of the model systems, p-OPE (blue squares) and TBT (red triangles). The p-OPE and TBT spectra are normalized to the copolymer spectrum at 370 and 470 nm, respectively. (C) Transient absorption spectra of the copolymer at pump-probe delay times of 185 fs (hollow triangles) and 1.1 ns (hollow squares). The normalized transient spectra for the p-OPE (blue filled) and TBT (red filled) model systems at $\Delta t = 100$ ps are shown for comparison. (D) Single wavelength kinetics at $\lambda = 600$ nm showing quenching of OPE* (black squares). A biexponential fit with fast (2.2 ps) and slow (30.1 ps) time components is shown in red.

conventional manner are compared to those collected using FM-FSRS methods. Section D describes application of FM-FSRS to the OPE-TBT donor-acceptor copolymer. This system exhibits a complex and dense FSRS spectrum with low signal amplitudes and thus provides an excellent test of the method. Section E gives a step-by-step description of the reconstruction algorithm, compares it to other procedures, and discusses the limitations of the FM-FSRS method.

A. Transient Absorption Monitoring of Ultrafast Energy Transfer in OPE-TBT. The OPE-TBT assembly is a random copolymer comprised of OPE and TBT monomer

units linked to a polystyrene scaffold. Each chain consists of ~ 60 repeat units with an average TBT loading of about 10%. This is the same polymer as P-10 in ref 15. The UV-vis spectrum of the copolymer in THF (black solid) is shown in Figure 2B along with spectra of the TBT model acceptor (red triangles) and the OPE donor homopolymer (blue squares). Comparison of the spectrum of the copolymer to its constituent model systems suggests that though the polystyrene backbone maintains the chromophores in proximity, the electronic states of the donor and acceptor remain unperturbed. Comparison of the absorbance of donor and acceptor model systems indicates that photoexcitation of the copolymer at 388 nm creates 98.9% OPE* species.

Figure 2C shows transient absorption (TA) spectra of the copolymer following 388 nm photoexcitation by the pump beam ($250 \mu\text{J}/\text{cm}^2$). At early pump-probe delay times ($\Delta t = 185$ fs) the TA spectrum of the copolymer (hollow triangles) is predominately OPE* in nature, as can be seen by comparison with the donor homopolymer TA spectrum (blue shaded). At late times ($\Delta t = 1.1$ ns), the copolymer spectrum (hollow squares) is largely TBT* in nature (red shaded), suggesting that pendent donor chromophores are quenched by energy transfer to the lower energy acceptor sites with relatively high efficiency. The decay of the donor absorption at 600 nm (Figure 2D) is biphasic with time constants of 2.2 ± 0.3 ps (0.44) and 30.1 ± 3.0 ps (0.66). The faster component reflects quenching of OPE* species that are formed within proximity to a TBT acceptor, while the slower time component arises from OPE* that must first undergo OPE* \rightarrow OPE energy migration prior to the OPE* \rightarrow TBT quenching step.

B. Difficulty in Isolating FSRS Signal. FSRS spectra are obtained following photoexcitation of the OPE chromophores at 388 nm by the femtosecond pump pulse. The RP beam is tuned to 490 nm to take advantage of resonance enhancement of the OPE excited state and TBT ground state absorptions. Resonance enhancement dramatically increases the stimulated Raman signal intensity, which applies equally regardless of whether the RP beam is resonant with the ground or excited state absorption. The FSRS spectra were collected on the Stokes side of the RP beam by monitoring the white light continuum between 492 and 562 nm, which corresponds to $\nu = 100\text{--}2600 \text{ cm}^{-1}$.

The difficulties with retrieving small FSRS signals are illustrated by the series of spectra shown in Figure 3. The basic observable is the ratio of the WL intensity in the presence of the pump pulse to that observed in its absence, i.e., $S(\nu) = I(\nu)/I_0(\nu)$. In the absence of the RP pulse, the experimental configuration is identical to that of transient absorption, and $S(\nu) - 1$ is equivalent to the transient absorption signal $\Delta I(\nu)/I(\nu)$. Panel A shows $S(\nu)$ for the OPE-TBT copolymer obtained 12 ps after photoexcitation. The two spectra were collected with (black) and without (red) the RP beam and are denoted S_{ON} and S_{OFF} , respectively. The overall negative signal that is observed is a result of the excited state absorption in this spectral region. With the RP beam present, FSRS transitions should appear as narrow features on this broad background, but at this scale, they are not visible. Rather, the structure that is observed, in both spectra, is a consequence of variation in sensitivity across the array detector or perhaps spectral inhomogeneities in the WL spectrum. It is only in calculation of the Raman gain (Figure 3B), where the RP "ON" spectrum has been divided by the RP "OFF" spectrum, i.e.,

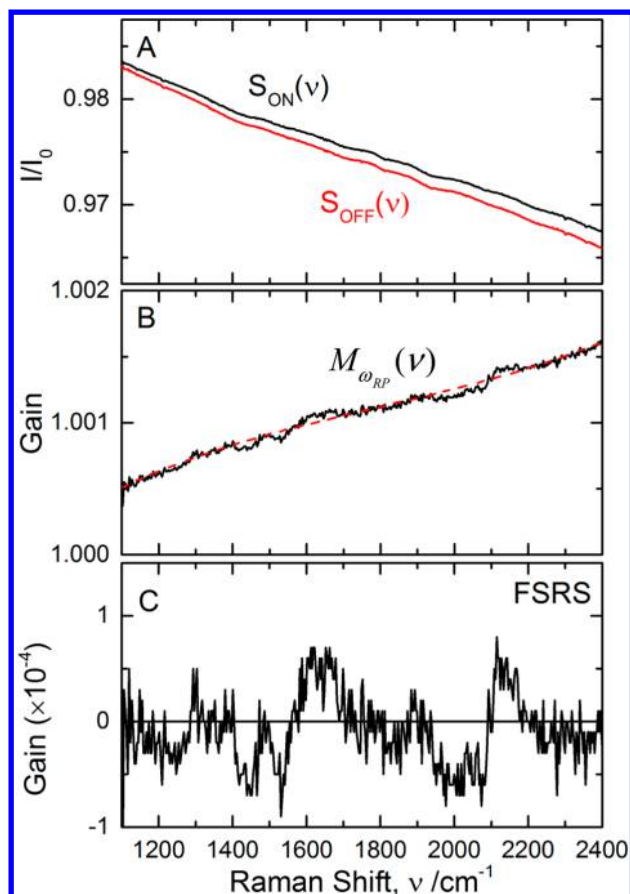


Figure 3. Summary of conventional FSRS data processing. (A) Transient absorption spectra of the copolymer collected with (black) and without (red) the presence of the RP pulse at 12 ps delay following excitation. The photoinduced stimulated Raman peaks are indistinguishable from the background. (B) Division of S_{ON} by S_{OFF} off gives $M_{\omega_{\text{RP}}}(\nu)$ shown in black. Here the modulations from photoinduced stimulated Raman processes are visible; however, they are still small compared to the low frequency background. Subtraction of a fourth order polynomial fit (red dashed) results in the FSRS spectrum shown in panel C.

$$M_{\omega_{\text{RP}}}(\nu) = \frac{S_{\text{ON}}(\nu)}{S_{\text{OFF}}(\nu)} \quad (1)$$

that structure from FSRS contributions is observed.

This nominally removes the transient absorption contribution, and yet even here, a significant background component (in the form of deviation of the baseline from 1.0) remains. This background primarily arises from a fifth order, electronically resonant process whereby the absorption spectrum is perturbed by sequential interactions with both pump and RP pulses prior to interaction with the WL beam.^{16,17} In this particular case, $M_{\omega_{\text{RP}}}(\nu)$ is greater than unity because the 490 nm RP beam directly excites the TBT sites, resulting in stimulated emission.

Accurate removal of the pump–pump–probe background is necessary for interpretation of the time-resolved FSRS spectra. While several techniques have been developed to isolate the FSRS signal, the most widely employed scheme subtracts either a polynomial or a spline fit of the background.^{4,18} This method operates on two assumptions. First, the spectrum is assumed to contain portions that are clearly identifiable as containing no

FSRS peaks (and can thus be included in the fit) and portions that should be excluded so as not to weight the desired peaks in the fit. Second, the background signal is assumed to be smoothly varying and thus accurately modeled by a simple function, such as a polynomial. This procedure, though generally successful, suffers from a number of drawbacks. Primary among these is the requirement for definition of regions of the collected signal to fit as “background” while excluding from the fit those portions of the spectrum that are desired. This can be straightforward in cases where excited state gain is high and peaks are well-resolved; however, broad peaks, small signal sizes, and congested spectra complicate the process, and the possibility of introducing human bias during the fitting procedure makes the current practice unsatisfactory. Distinguishing portions of the spectrum that contain FSRS signals and assigning relative signs of peaks can also be unintuitive. Erroneous assignments of this nature can readily skew results and introduce experimental bias. For example, it is not clear in Figure 3B whether the modulations between 1300 and 1700 cm^{-1} should be interpreted as purely positive-going peaks with the background drawn as a tangent between valleys or whether there are negative-going peaks that also contribute. Because of the ambiguity in determining where the baseline lies, we have fit the entire spectrum to a fourth-order polynomial shown in Figure 3B (red dashed), with no regard for whether FSRS signals contribute or not. Subtraction of the fit yields the FSRS spectrum shown in Figure 3C.

C. Frequency Modulated FSRS (FM-FSRS). The shortcomings of current FSRS analysis methods are overcome by collecting two separate FSRS spectra with shifted RP frequencies, $\omega_{\text{RP}} = f_1$ and $\omega_{\text{RP}} = f_2$, where $\Delta f = f_1 - f_2 \approx 30 \text{ cm}^{-1}$ (Figure 4A). Frequency modulated FSRS (FM-FSRS) takes advantage of the fact that broad background components and pixel-to-pixel variations in the detector are unaffected by the small shift in the RP frequency, but the Raman features shift by an amount Δf . By subtracting the spectrum with RP frequency f_2 from that at f_1 , we calculate a FSRS difference spectrum.

$$D_{f_1, f_2}(\nu) = M_{f_1}(\nu) - M_{f_2}(\nu) \quad (2)$$

The difference spectrum shown in Figure 4B has a background contribution that is reduced by an order of magnitude relative to the single frequency spectra of Figure 4A and can be used to reconstruct the FSRS spectrum with minimal distortion (Figure 4C) using a straightforward integration algorithm described in detail in section E.

The spectrum obtained via FM-FSRS exhibits diminished high-frequency noise relative to the spectrum retrieved by the conventional technique (reproduced in Figure 4C for comparison).¹⁹ This noise arises from pixel-to-pixel differences in the detector, and because it cannot be removed by increased signal averaging, it limits the sensitivity of the conventional FSRS technique. Calculation of the difference spectrum in the FM-FSRS technique results in cancellation of pixel-to-pixel variations, resulting in a lower noise level. With a conventional FSRS spectrum calculation, the lower noise limit with our instrument is $\sim 5 \times 10^{-5}$; however, further reduction to a level of $\sim 1 \times 10^{-5}$ is achievable with FM-FSRS. The more consequential difference between the two spectra is the discrepancy in peak location. The spectrum obtained with the FM-FSRS method shows a peak at 1350 cm^{-1} , whereas the conventional FSRS spectrum lacks this peak and has an

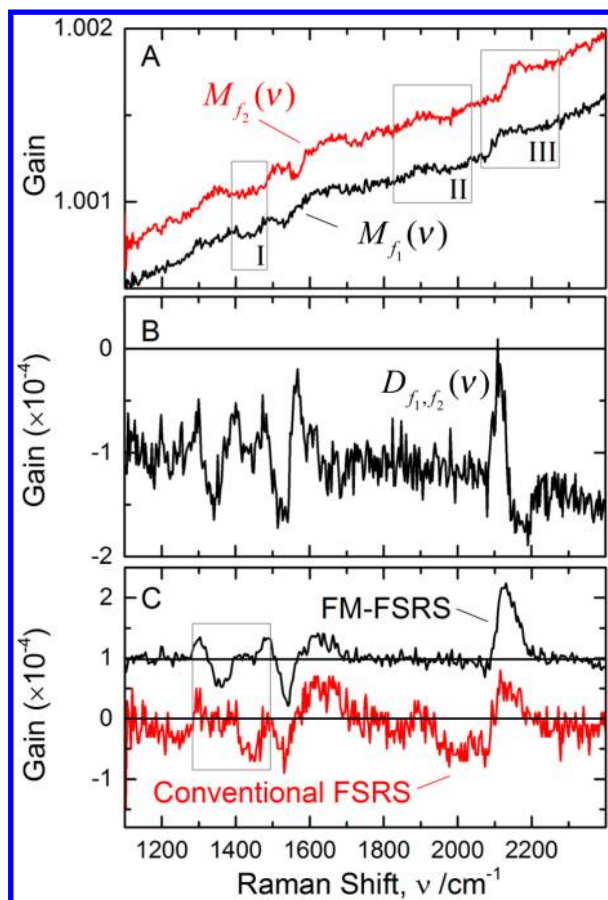


Figure 4. (A) Single frequency FSRS spectra of the copolymer at $\Delta t = 12$ ps collected with RP frequency, $\omega_{\text{RP}} = f_1$ (red) and $\omega_{\text{RP}} = f_2$ (black). The gray boxes highlight portions of the spectrum that arise from ω_{RP} independent spectral fluctuations (I and II) and ω_{RP} dependent FSRS peaks (III). Without modulation of the RP frequency, such features can be indistinguishable. (B) FSRS difference spectrum, $D_{f_1, f_2}(\nu)$, arrived at by subtracting $M_{f_2}(\nu)$ from $M_{f_1}(\nu)$. (C) Comparison of FSRS spectra retrieved by the conventional technique of subtracting a polynomial fit (red) and via the FM-FSRS method (black, offset to 1×10^{-4}). The qualitative discrepancies between the two methods in the boxed spectral region between 1300 and 1500 cm^{-1} arise from detection artifacts highlighted in panel A that are ω_{RP} independent (see text). These artifacts are eliminated in the FM-FSRS spectrum.

additional negative-going peak at 1450 cm^{-1} . These features are highlighted by the box in Figure 4C. Close examination shows that both peaks are present in the raw data and decay on qualitatively similar time scales as other features in the spectrum. While these characteristics are consistent with a molecular resonance, the peak at 1450 cm^{-1} is independent of RP excitation frequency, revealing that it is in fact an artifact of the imaging optics or detector. As discussed in section D below, the peak in the FM-FSRS spectrum at 1350 cm^{-1} is correct, corresponding to a photoinduced loss of gain from the ground state stimulated Raman spectrum.

This example illustrates the insidious nature of imaging artifacts that can arise in FSRS spectra. In the case above, the spurious peak is comparable in size to the actual Raman features. Such imaging artifacts are produced by imperfections (e.g., dust) on the optics after the WL beam is dispersed by the grating in the spectrograph or by sensitivity variation across the detector array. Further, because these artifacts scale with the

difference in intensity between RP OFF and RP ON spectra, they decay with the same time constant as the pump–pump–probe background, making them exceptionally difficult to distinguish from molecular resonances. Here the advantages of acquiring difference spectra are highlighted; while the artifact remains in the spectrum obtained by the conventional procedure and is indistinguishable from the actual Raman modes, the spurious feature is completely subtracted out in the FM-FSRS method, since it is not RP frequency dependent. In Figure 4A, we have highlighted regions of the single frequency spectra, $M_{\omega_{\text{RP}}}(\nu)$, where artifacts (I and II) and a molecular resonance (III) are present. In FM-FSRS, the molecular resonance shifts with the RP frequency, creating a derivative-like line shape in the difference spectrum, whereas the artifacts remain stationary and are consequently removed upon calculation of the difference spectrum.

D. FM-FSRS Monitoring of Ultrafast Energy Transfer in OPE-TBT. We have performed FM-FSRS measurements on the OPE-TBT copolymer, as well as the p-OPE and TBT model systems for comparison (Figure 5). The wavelength of the RP beam was set at 490 nm ($320 \mu\text{J}/\text{cm}^2$) to minimize spectral congestion and take advantage of resonance enhancement. With this choice for the RP wavelength we are able to clearly identify the OPE and TBT contributions to the copolymer FSRS spectrum.

TBT Monomer. Because the RP pulse is electronically resonant with the ground state absorption, the TBT FM-FSRS spectrum (Figure 5A) is dominated by two negative-going features at 1355 and 1538 cm^{-1} (labeled I and II, respectively) that correspond to pump-induced loss of ground state Raman gain. The negative-going features correlate with transitions observed in the ground state stimulated Raman spectrum (labeled I' and II'). Spectra simulated using DFT methods at the B3LYP/6-31G* level (Figure 5B) indicate that these ground state modes involve concerted motion by several rings in the TBT moiety. Since the 490 nm RP beam is not resonant with the TBT excited state absorption, the positive features arising from these same modes on the excited state (denoted III and IV) are much less intense.

The FM-FSRS spectra of the TBT model system do not show any delay-dependent dynamical evolution. An absence of dynamical shifting in the FSRS spectra indicates that relaxation of the initially formed excited state occurs too quickly to be resolved by the finite time resolution of the experiment or that the accompanying shift of vibrational modes due to relaxation of the electron density is too small to be spectrally resolved. This later scenario arises because of (lifetime or dispersive) peak broadening that obscures the shift or because of intrinsic spectral resolution limitations of the instrument.

OPE Homopolymer (p-OPE). In the case of the OPE homopolymer, the FM-FSRS spectra (Figure 5C) possess both positive- and negative-going features that stem from the pump-induced excited state population, which reflects the fact that the RP overlaps with both excited state absorption and stimulated emission bands of OPE.²¹ It does not overlap with the ground state absorption spectrum, and as a result, the ground state stimulated Raman spectrum (Figure 5D) exhibits generally small signal intensity, and the ground state modes appear only as weak negative-going features superimposed on the more intense excited state bands in the FM-FSRS spectrum.

The spectrum is characterized by several overlapping modes between 1100 and 1500 cm^{-1} which we have not specifically

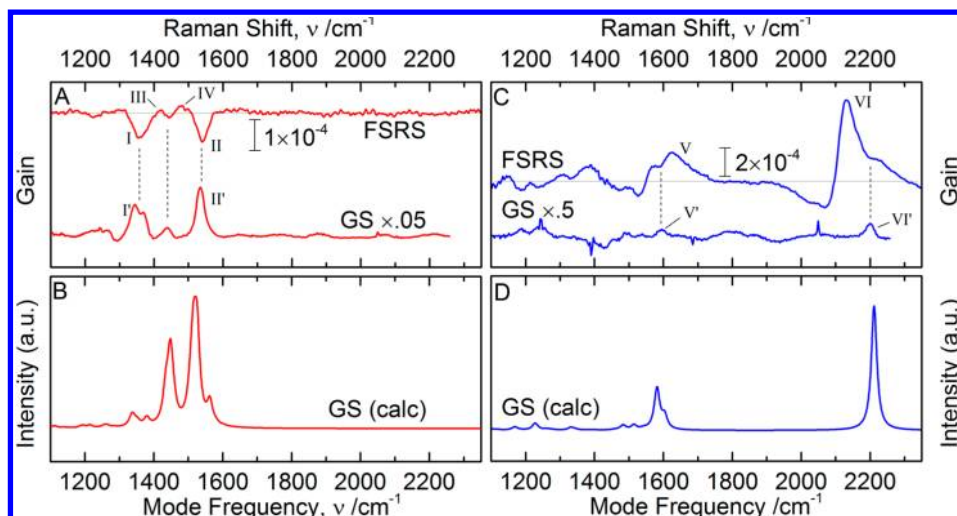


Figure 5. (A) FM-FSRS spectra of the model system TBT at Δt of 10 ps. Also shown is the ground state stimulated Raman spectrum of TBT. The dashed lines correlate features in ground and FSRS spectra. (B) Calculated TBT ground state Raman spectrum with 30 cm^{-1} Gaussian lineshapes. (C) FSRS spectrum at $\Delta t = 10\text{ ps}$ and ground state stimulated Raman spectra of p-OPE. Dashed gray lines are drawn correlating features associated with the OPE ground and photoinduced stimulated Raman spectra. (D) Calculated OPE ground state Raman spectrum. The frequency scales for the calculated spectra in panels B and D were multiplied by 0.9614 to account for overestimation of the bond strength at the B3LYP/6-31G* level.²⁰

assigned; however, simulated spectra obtained using DFT methods (Figure 5D) indicate these modes generally involve concerted breathing motion by the three aryl rings in OPE. The OPE FM-FSRS spectrum also exhibits strong features peaked at 1625 and 2130 cm^{-1} (labeled V and VI, respectively). On the basis of calculations and comparison with the ground state stimulated Raman spectrum (Figure 5C), we have assigned peak V to the symmetric deformation mode primarily localized on the central aryl ring on OPE. This feature is shifted to higher energy and significantly broadened compared to the corresponding ground state mode, labeled V'. Peak VI, centered at 2130 cm^{-1} , corresponds to the symmetric alkyne stretch in OPE. Like peak V, peak VI is significantly broadened relative to the ground state mode, VI', but is shifted to lower energy, presumably because of a weakening of the alkyne bond upon photoexcitation.

While the cause of the significant broadening of peaks V and VI is not clear, its source could arise from a combination of three factors. Additional excited state modes that are convolved together by the resolution of our instrument is a likely contributor, especially in the case of peak VI where there is a significant shoulder on the blue edge of the peak. The second source of broadening may arise because excited states along the homopolymer OPE model system undergo site to site hopping on time scales ($\sim 2\text{ ps}$) that are comparable to the vibrational dephasing time, broadening the natural line width of individual modes.¹⁵ Finally, since each individual chromophore within the sample experiences a slightly different environment because of interactions with the bath, inhomogeneous broadening may also contribute if the electronic wave functions are perturbed sufficiently to affect the vibrational frequency in these varied sites. Advances in excitation and detection schemes for FSRS measurements will be useful for delineating these contributions.²²

Copolymer. The delay dependent FM-FSRS spectra of the OPE-TBT copolymer are shown in Figure 6A. Comparison of early time spectra of the copolymer to the spectrum of the model p-OPE homopolymer (labeled at bottom) suggest that photoexcitation at 388 nm primarily produces OPE excited

states. As the delay time increases, there is a decay of the features associated with the donor OPE moiety and the simultaneous growth of the features associated with the acceptor moiety. By 400 ps , the FSRS spectrum that began as almost purely donor in nature has been transformed to one that is almost purely acceptor. (The TBT model FM-FSRS spectrum is shown and labeled at the top of Figure 6A for comparison.) The intensity of the alkyne stretch on the OPE at 2130 cm^{-1} (blue squares) and the TBT acceptor ring breathing mode at 1538 cm^{-1} (red triangles) are shown in Figure 6B. The transients are well modeled by a biexponential function with an offset. A global fit of the kinetics found time constants of 2.1 ± 0.4 and $27 \pm 4\text{ ps}$ in approximately equal proportion, consistent with the results from transient absorption measurements.

E. FM-FSRS Data Analysis Algorithm. We illustrate the FM-FSRS spectral signal processing algorithm in Figure 7 using the $\Delta t = 12\text{ ps}$ spectrum from Figure 6A as an example. Two measurements, shown in Figure 7A, are collected whose RP frequencies, f_1 and f_2 , differ by 28 cm^{-1} . Each of these measurements is equivalent to a conventional FSRS spectrum.

Because the RP beam is often tuned to be electronically resonant with the excited state absorption spectrum, the desired stimulated Raman peaks are convolved with a signal that arises from (primarily) the pump–pump–probe signal, in which the sample is excited by sequential interactions with both pump and RP beams. In the limit that the electronic resonance ($\sim 700\text{ cm}^{-1}$) is much broader than the bandwidth of the RP beam (25 cm^{-1}), the background arising from electronic resonances should only be weakly dependent on small shifts of the excitation frequency.²³ In contrast, vibrational resonances have natural linewidths ($\sim 10\text{ cm}^{-1}$) that are comparable to the spectral bandwidth of the RP beam and are sensitively dependent on the beam's frequency. Consequently, by shifting the RP frequency a small amount, Δf (on the order of the bandwidth), and collecting another gain measurement, we perturb the stimulated Raman spectrum by Δf while leaving the background largely unchanged, enabling almost complete elimination of the background through calculation of a FSRS difference spectrum.

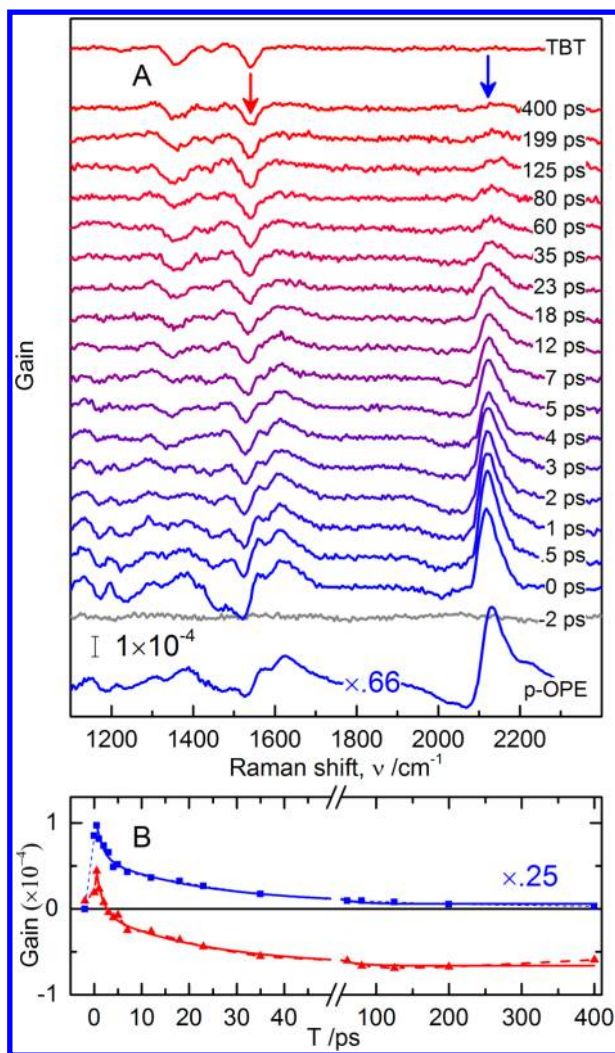


Figure 6. (A) FSRS spectra showing photoinduced changes of the TBT-OPE stimulated Raman spectrum for pump–probe delays of -1 to 400 ps. The excited state alkyne stretch at 2130 cm^{-1} decays as OPE* is quenched by TBT. Growth of the three ground state aromatic “bleaches” at 1355 , 1444 , and 1538 cm^{-1} indicates the formation of TBT*. (B) Single frequency kinetics showing decay of OPE donor alkyne stretch at 2130 cm^{-1} (blue squares) and simultaneous growth of TBT acceptor aromatic stretch at 1538 cm^{-1} (red triangles) modes as indicated by the arrows in panel A. The global biexponential fits of the donor and acceptor mode kinetics are shown in blue (thick) and red (thick), respectively.

The FSRS difference spectrum shown in Figure 7B (black) is obtained by subtracting the two measurements in Figure 7A. While the low frequency background (due to noise, small differences in intensity of the two RP beams, or subtle differences in the absorption spectrum) is not completely eliminated, it is greatly reduced, revealing the stimulated Raman features much more clearly than in either of the measurements shown in Figure 7A. Another benefit of collecting the difference spectrum is that subtraction removes nearly all differences in pixel-to-pixel sensitivity of the detector, a source of noise that is often greater than the magnitude of the measured FSRS signals. While other methods have been developed to mitigate this source of noise by averaging over different areas of the detector,²⁴ calculating the difference spectrum subtracts out these contributions completely rather than averaging over two detector regions with slightly different sensitivities. We also

note that sensitivity varies not only between adjacent pixels leading to high frequency noise but also across small regions of the imaged spectrum, causing spurious peaks. As discussed previously, such regions of reduced sensitivity can arise from imperfections of the imaging optics (from dust or coating flaws) that are placed after the grating in a spectrometer or due to the detector array itself.²⁵ We have observed this effect in our own instrument. While such spurious peaks are present in the conventional FSRS implementation involving a single RP frequency, we note that the difference spectrum is completely free of these artifacts.

The FSRS difference spectrum is reminiscent of the derivative spectra obtained from a variety of experimental methods, including EPR. Though it is an accurate spectroscopic signature of the molecular system, interpretation is more intuitive if the conventional spectrum is reconstructed. The numerical operation for reconstruction (i.e., integration) from the derivative spectrum is just the cumulative sum of elements. The FSRS difference spectrum, however, is not a true derivative, and thus, the reconstruction algorithm must be modified to avoid peak broadening, shifting, and an artificial amplification of signal (and noise) amplitude.

When the two RP beams at $\omega_{rp} = f_1$ and $\omega_{rp} = f_2$ are separated by a discrete amount (δ detector pixels), the reconstructed signal at pixel n (R_n) is given by

$$R_n(\nu) = R_{n-\delta}(\nu) + D_n(\nu) \quad (3)$$

where D_n is the difference signal at pixel n and where $R_{n-\delta}$ is the reconstructed signal at pixel $n - \delta$. While the reconstruction should in principle be exact, application of eq 3 to actual difference spectra reveals two complications.

First, because reconstruction proceeds by a cumulative sum, even the small offset seen in the difference spectrum (black) in Figure 7B causes a large background (effectively the net area under the difference spectrum) to accumulate as reconstruction proceeds from the red to blue edge of the spectrum. To eliminate this component, we fit the entire difference spectrum with a fourth order polynomial (Figure 7B, red dashed) prior to reconstruction which, when subtracted from the difference spectrum, removes any residual low frequency background contribution to the spectrum and centers it at zero (Figure 7C). This automated procedure is entirely robust, as the desired signal peaks in the FSRS difference spectrum deviate equally in positive and negative directions relative to the nonzero baseline. This is in contrast with fitting single Raman frequency FSRS spectra (as is done conventionally) where the spectrum is asymmetric with respect to the zero signal and the polynomial fit is pulled upward (downward) by positive (negative) going peaks.

The second complication of reconstruction from the difference spectrum arises from the recursive nature of eq 3. This artifact manifests as an accumulation of high frequency oscillation that recurs with a period of δ , superimposed with the reconstructed spectrum (Figure 7D). While this source of oscillation is minimal for high signal-to-noise FSRS signals, we have found its removal to be necessary when high frequency (pixel-to-pixel) noise is within a factor of 10 of the desired signals. To obtain FM-FSRS spectra free of this periodic modulation, we Fourier transform the reconstructed FM-FSRS spectrum (into inverse pixel space, ν_{pix}) and then attenuate components at $1/\delta$ and its harmonics with a simple notch filter as shown in Figure 7E. The functional form of the notch filter is

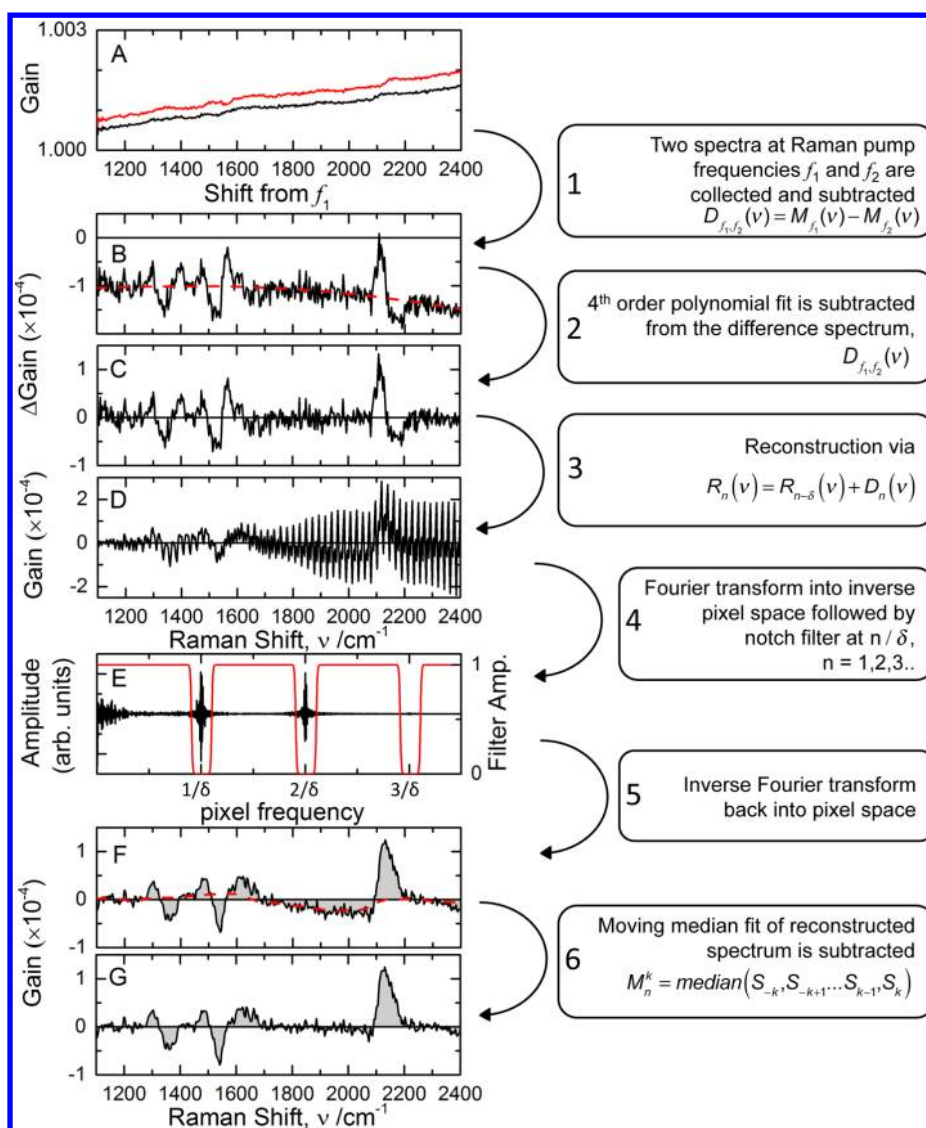


Figure 7. (A) Raw spectra collected for each of the two RP frequencies. (B) Difference spectrum calculated from spectra shown in panel A (black). The red dashed curve is a fourth order polynomial fit of difference spectrum. (C) Residual after polynomial fit is subtracted from difference spectrum in panel B. (D) Reconstructed spectrum with periodic noise artifact arising from the recursive nature of reconstruction. (E) Fourier transform spectrum (black) and notch filter (red) used to remove the high frequency artifact and its higher harmonics. (F) Inverse Fourier transform produces the reconstructed spectrum (black). Also shown is the moving median fit (red dashed) that represents baseline drift. (G) Final FSRS spectrum obtained by subtraction of the red curve from the black curve.

a product of hyperbolic tangent functionals centered at harmonics of $1/\delta$,

$$F(\nu_{\text{pix}}) = \prod_{n=1,2,3,\dots} \left[1 - \frac{1}{2} \left\{ \tanh \left(\frac{\nu_{\text{pix}} - \left(\frac{n}{\delta} - w \right)}{\alpha} \right) + \tanh \left(\frac{\left(\frac{n}{\delta} + w \right) - \nu_{\text{pix}}}{\alpha} \right) \right\} \right] \quad (4)$$

Here, the parameters w and α determine the width and sharpness of the notch, respectively. Following application of the noise filter, we perform the inverse Fourier transform and recover the FSRS spectrum, now free of the recursive artifact (Figure 7F, black solid).

While the spectrum in Figure 7F largely reproduces the expected peaks in the spectrum, we have found that some spectra accumulate a slight baseline drift because mid-frequency, low-amplitude variations in the spectrum are not adequately fit by the low order polynomial fit. These variations are often quite small ($< 5 \times 10^{-5}$); however, when low fluence and small Raman cross sections produce small signal sizes, it may be necessary to correct for this drift. We have chosen to use a moving median filter, which has been successfully employed to isolate narrow peaks from their low frequency background.²⁶ The moving median is a parametric fit of the trend in a data series, which operates by finding the median value of a window of length $2k + 1$ elements centered at pixel n , as shown in eq 5.

$$M_n^k = \text{median}(S_{-k}, S_{-k+1}, \dots, S_{k-1}, S_k) \quad (5)$$

This filter is particularly well suited to eliminating a low amplitude baseline, as the maxima and minima that correspond to FSRS peaks occupy the extremes of the sorted window of pixel values, S . After subtraction of the moving median fit of the data (shown in Figure 7F, red dashed), the algorithm arrives at the final FSRS spectrum, as shown in Figure 7G.

In effect, the moving median filter acts as a mid-band filter. It serves to remove background that is higher frequency than that which is removed by the polynomial fit while leaving the sharp FSRS peaks unperturbed. Figure 8 illustrates this effect by simulating a spectrum consisting of five narrowband Gaussian peaks (to represent the desired FSRS peaks) convolved with a broad Gaussian background, a low amplitude sinusoidal modulation, and high frequency random noise. Panel A

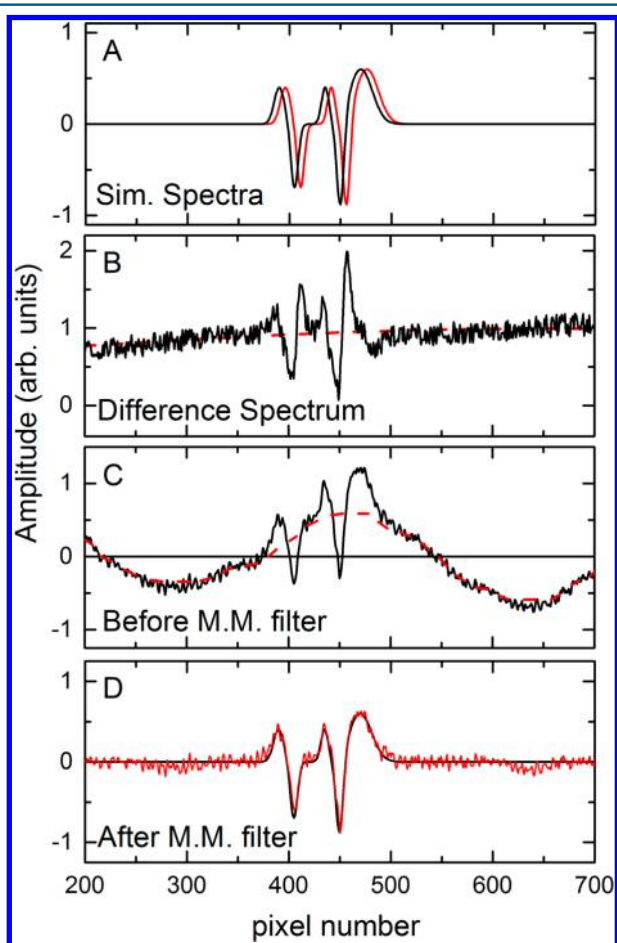


Figure 8. (A) Simulated FSRS spectrum (black) constructed from a sum of five variable width Gaussian peaks. The red spectrum, which is shifted six pixels higher, is subtracted from the black spectrum to produce an ideal difference spectrum. (B) To the ideal difference spectrum, a broad Gaussian background, a low amplitude sin function, and random noise are added to simulate a typical experimental spectrum (black). Subtraction of a fourth order polynomial fit (red dashed) from the spectrum eliminates the low amplitude background in the region of the simulated peaks, leaving the difference spectrum centered at 0. (C) Reconstruction of the difference spectrum after subtraction of the polynomial fit yields the black spectrum. The low amplitude sine functional modulates the baseline in the reconstructed spectrum. After application of the moving median filter (red, dashed), the reconstructed spectrum reproduces the expected line shape shown in panel D with little baseline deviation. The ideal spectrum is reproduced in panel D for comparison.

shows the initial input spectra used to produce the simulated difference spectrum. The two spectra are identical; however, the red trace is shifted six pixels to simulate the effect of shifting the RP frequency. Panel B shows the simulated difference spectrum with added background and noise (black) as well as its corresponding fourth order polynomial fit (red dashed). Since the polynomial is a global fit, the overall trend to the baseline is subtracted, but the low amplitude mid-frequency modulations remain in the difference spectrum. The reconstructed spectrum, prior to application of the moving median filter, is shown in panel C. The desired peaks are clearly distinguishable in this spectrum; however, the baseline has significant positive- and negative-going deviations that arise from the mid-frequency background component that was not adequately modeled with the low order polynomial. Application of the moving median filter (red, dashed) readily removes this component, yielding a final spectrum shown in panel D (red) that favorably compares with the initial input spectrum, which is reproduced for comparison (black).

Figure 8 shows that FM-FSRS can remove low frequency background contributions and reliably reproduce complex, dense spectra with minimal artifacts. This is especially important because while RP modulation schemes are superior in cancellation of noise and imaging artifacts, background removal is still a necessity and subsequent reconstruction of the spectrum must be carefully performed to avoid artifacts.

Background removal from FSRS spectra is especially difficult because well-established techniques such as low-pass Fourier filters or wavelet decompositions often introduce ringing artifacts to the lineshapes.¹⁴ These filtering methods operate on the assumption that the Raman peaks of interest are primarily composed of higher frequency components, whereas the background is purely low frequency. However, the desired FSRS peaks do in fact have low frequency components, and by removal of enough low frequency amplitude from the Fourier transform to eliminate the background, ringing artifacts are introduced that qualitatively alter the Raman spectrum.²⁷ It is important to note that while the FM-FSRS method does use a Fourier filter, it is used to eliminate high frequency noise, a procedure that has much less risk of distorting peak shapes.

While several steps are required to process the final FSRS spectrum, they are all completely automated and require no input from the experimenter beyond a choice of two parameters: the polynomial order for fitting the FSRS difference spectrum and length of the window for the moving median filter. In this work, we have found that fourth order polynomials and median windows that are a factor of ~ 5 larger than the FSRS peak widths were good choices. Rational choice of these two parameters will lead to robust and accurate reconstruction of most spectra; however, there are limitations to the algorithm.

The most notable is an attenuation of peaks with broad linewidths. This is illustrated in Figure 9 where a spectrum consisting of a series of Gaussian peaks of varying widths is examined. Figure 9A shows the simulated difference spectrum. The reconstructed spectra obtained before and after the application of the moving medium filter are depicted in Figure 9B and Figure 9C, respectively. The number shown near the midpoint of each peak in Figure 9C is the fwhm (in pixels) of the input peak shape. As the peak width approaches the window size of the moving median filter (we used a median window size of 101 pixels), distortion from the algorithm becomes considerable, leading to both attenuation and

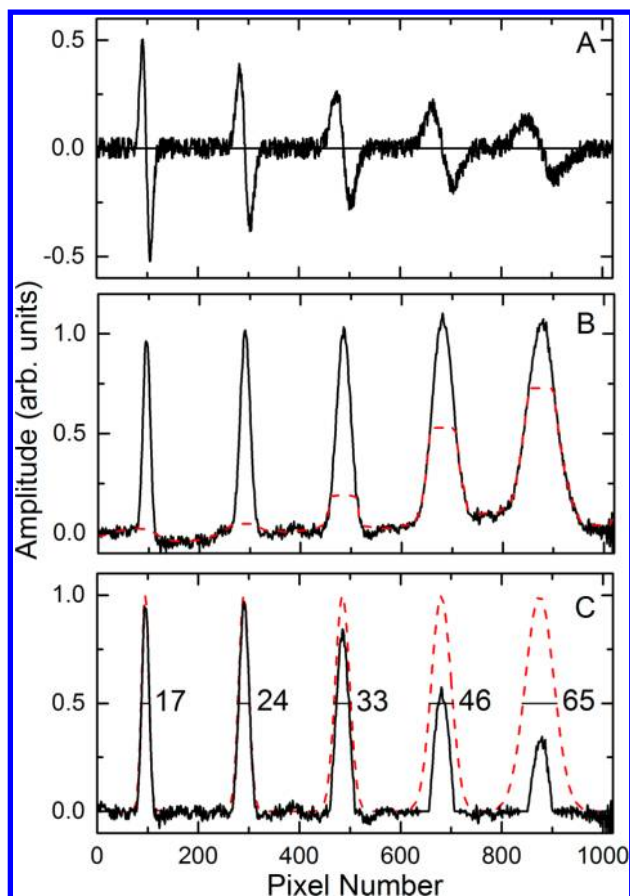


Figure 9. (A) Simulated FSRS difference spectrum comprising five increasing width peaks and random noise. (B) Reconstructed spectra prior to application of the moving median filter (black). The moving median with a window size $(2k + 1)$ of 101 pixels is shown in red, dashed. (C) Final FSRS spectra recovered by the FM-FSRS method, after application of the moving median filter. As the peak widths (fwhm are indicated to the right of each peak) approach the size of the moving median window, attenuation and narrowing of the reconstructed peaks (black) occur. The red dashed trace shows the input peak shapes.

narrowing of the reconstructed peaks. This behavior illustrates that the FM-FSRS reconstruction algorithm loosely operates on the separation of frequencies between FSRS peaks and background. As desired signals begin to span the same frequency range as the background, differentiation between the two becomes increasingly difficult. Nevertheless, for most systems, the conditions necessary for accurate retrieval of the FSRS spectrum should be fulfilled, making FSRS data processing less susceptible to producing spurious peaks, less prone to bias from the experimenter, and exceedingly simple and fast.

CONCLUSION

We have developed an improved method for collection and processing of FSRS spectra called frequency-modulated FSRS, and we have demonstrated its utility on ultrafast energy transfer in a donor–acceptor copolymer. Employing a spatial light modulator to spectrally modulate the RP frequency allows facile collection of high-sensitivity, artifact free spectra and sets the stage for enhancements to FSRS via femtosecond pulse shaping methods. In addition, the data processing algorithm developed here filters background signals from electronic absorption

pathways and fully reconstructs the FSRS spectrum without experimenter input, paving the way for widespread application of the technique to chemical systems with complex, dense spectra.

AUTHOR INFORMATION

Corresponding Author

*E-mail: john_papanikolas@unc.edu.

Notes

The authors declare no competing financial interest.

ACKNOWLEDGMENTS

This material is based upon work solely supported as part of the UNC EFRC: Center for Solar Fuels, an Energy Frontier Research Center funded by the U.S. Department of Energy, Office of Science, Office of Basic Energy Sciences under Award DE-SC0001011.

REFERENCES

- (1) Yoshizawa, M.; Kurosawa, M. Femtosecond Time-Resolved Raman Spectroscopy Using Stimulated Raman Scattering. *Phys. Rev. A* **1999**, *61* (013808), 1–6.
- (2) Kukura, P.; McCamant, D. W.; Yoon, S.; Wandschneider, D. B.; Mathies, R. A. Structural Observation of the Primary Isomerization in Vision with Femtosecond-Stimulated Raman. *Science* **2005**, *310*, 1006–1009.
- (3) Laimgruber, S.; Schachenmayr, H.; Schmidt, B.; Zinth, W.; Gilch, P. A Femtosecond Stimulated Raman Spectrograph for the Near Ultraviolet. *Appl. Phys. B: Lasers Opt.* **2006**, *85*, 557–564.
- (4) Kukura, P.; McCamant, D. W.; Mathies, R. A. Femtosecond Stimulated Raman Spectroscopy. *Annu. Rev. Phys. Chem.* **2007**, *58*, 461–488.
- (5) McCamant, D. W. Re-Evaluation of Rhodopsin's Relaxation Kinetics Determined from Femtosecond Stimulated Raman Line-shapes. *J. Phys. Chem. B* **2011**, *115*, 9299–9305.
- (6) Frontiera, R. R.; Henry, A.-I.; Gruenke, N. L.; Van Duyne, R. P. Surface-Enhanced Femtosecond Stimulated Raman Spectroscopy. *J. Phys. Chem. Lett.* **2011**, *2*, 1199–1203.
- (7) Brown, K. E.; Veldkamp, B. S.; Co, D. T.; Wasielewski, M. R. Vibrational Dynamics of a Perylene–Perylenediimide Donor–Acceptor Dyad Probed with Femtosecond Stimulated Raman Spectroscopy. *J. Phys. Chem. Lett.* **2012**, *3*, 2362–2366.
- (8) Rhinehart, J. M.; Challa, J. R.; McCamant, D. W. Multimode Charge-Transfer Dynamics of 4-(Dimethylamino)benzointrile Probed with Ultraviolet Femtosecond Stimulated Raman Spectroscopy. *J. Phys. Chem. B* **2012**, *116*, 10522–10534.
- (9) Liu, W.; Han, F.; Smith, C.; Fang, C. Ultrafast Conformational Dynamics of Pyranine during Excited State Proton Transfer in Aqueous Solution Revealed by Femtosecond Stimulated Raman Spectroscopy. *J. Phys. Chem. B* **2012**, *116*, 10535–10550.
- (10) Kuramochi, H.; Takeuchi, S.; Tahara, T. Ultrafast Structural Evolution of Photoactive Yellow Protein Chromophore Revealed by Ultraviolet Resonance Femtosecond Stimulated Raman Spectroscopy. *J. Phys. Chem. Lett.* **2012**, *3*, 2025–2029.
- (11) Hamaguchi, H.; Gustafson, T. L. Ultrafast Time-Resolved Spontaneous and Coherent Raman Spectroscopy: The Structure and Dynamics of Photogenerated Transient Species. *Annu. Rev. Phys. Chem.* **1994**, *45*, 593–622.
- (12) Shreve, A. P.; Cherepy, N. J.; Mathies, R. A. Effective Rejection of Fluorescence Interference in Raman Spectroscopy Using a Shifted Excitation Difference Technique. *Appl. Spectrosc.* **1992**, *46*, 707–711.
- (13) Weigel, A.; Ernsting, N. P. Excited Stilbene: Intramolecular Vibrational Redistribution and Solvation Studied by Femtosecond Stimulated Raman Spectroscopy. *J. Phys. Chem. B* **2010**, *114*, 7879–7893.
- (14) Kloz, M.; Grondelle, R. V.; Kennis, J. T. M. Wavelength-Modulated Femtosecond Stimulated Raman Spectroscopy—Approach

towards Automatic Data Processing. *Phys. Chem. Chem. Phys.* **2011**, *13*, 18123–18133.

(15) Chen, Z.; Grumstrup, E. M.; Gilligan, A. T.; Papanikolas, J. M.; Schanze, K. S. Light Harvesting Polymers: Ultrafast Energy Transfer in Polystyrene Based Arrays of π -Conjugated Chromophores. *J. Phys. Chem. Lett.*, submitted.

(16) Frontiera, R. R.; Shim, S.; Mathies, R. A. Origin of Negative and Dispersive Features in Anti-Stokes and Resonance Femtosecond Stimulated Raman Spectroscopy. *J. Chem. Phys.* **2008**, *129* (064507), 1–6.

(17) Sun, Z.; Lu, J.; Zhang, D. H.; Lee, S.-Y. Quantum Theory of (Femtosecond) Time-Resolved Stimulated Raman Scattering. *J. Chem. Phys.* **2008**, *128* (144114), 1–13.

(18) McCamant, D. W.; Kukura, P.; Yoon, S.; Mathies, R. A. Femtosecond Broadband Stimulated Raman Spectroscopy: Apparatus and Methods. *Rev. Sci. Instrum.* **2004**, *75*, 4971–4980.

(19) To make the comparison more meaningful, we have not subtracted out the contribution from photoinduced loss of ground state mode gain as is conventionally performed.

(20) Cramer, C. J. *Essentials of Computational Chemistry*; John Wiley and Sons Ltd.: New York, 2002.

(21) Nakamura, R.; Hamada, N.; Abe, K.; Yoshizawa, M. Ultrafast Hydrogen-Bonding Dynamics in the Electronic Excited State of Photoactive Yellow Protein Revealed by Femtosecond Stimulated Raman Spectroscopy. *J. Phys. Chem. B* **2012**, *116*, 14768–14775.

(22) Mukamel, S.; Biggs, J. D. Communication: Comment on the Effective Temporal and Spectral Resolution of Impulsive Stimulated Raman Signals. *J. Chem. Phys.* **2011**, *134* (161101), 1–4.

(23) Mukamel, S. *Principles of Nonlinear Optical Spectroscopy*; Oxford University Press: Oxford, U.K., 1995.

(24) Challa, J. R.; Du, Y.; McCamant, D. W. Femtosecond Stimulated Raman Spectroscopy Using a Scanning Multichannel Technique. *Appl. Spectrosc.* **2012**, *66*, 227–232.

(25) Yetzbacher, M. K.; Courtney, T. L.; Peters, W. K.; Kitney, K. A.; Smith, E. R.; Jonas, D. M. Spectral Restoration for Femtosecond Spectral Interferometry with Attosecond Accuracy. *J. Opt. Soc. Am. B* **2010**, *27*, 1104–1117.

(26) Moore, A. W.; Jorgenson, J. W. Median Filtering for Removal of Low-Frequency Background Drift. *Anal. Chem.* **1993**, *65*, 188–191.

(27) Diniz, P. S. R.; da Silva, E. A. B.; Netto, S. L. *Digital Signal Processing*; Cambridge University Press: Cambridge, U.K., 2010.

Competition between Ultrafast Energy Flow and Electron Transfer in a Ru(II)-Loaded Polyfluorene Light-Harvesting Polymer

Li Wang,^{†,#} Egle Puodziukynaite,^{‡,#} Ryan P. Vary,[†] Erik M. Grumstrup,[†] Ryan M. Walczak,[‡] Olga Y. Zolotar'skaya,[‡] Kirk S. Schanze,[‡] John R. Reynolds,^{*,‡,§} and John M. Papanikolas^{*,†}

[†]Department of Chemistry, University of North Carolina at Chapel Hill, Chapel Hill, North Carolina 27599, United States

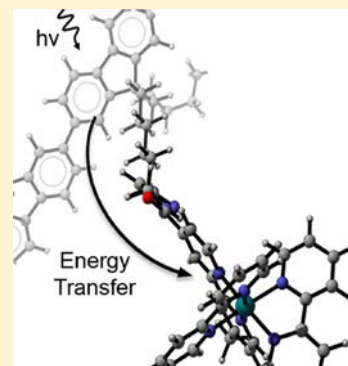
[‡]Department of Chemistry, Center for Macromolecular Science and Engineering, University of Florida, Gainesville, Florida 32611-7200, United States

[§]School of Chemistry and Biochemistry, School of Materials Science and Engineering, Center for Organic Photonics and Electronics, Georgia Institute of Technology, Atlanta, Georgia 30332, United States

S Supporting Information

ABSTRACT: This Letter describes the synthesis and photophysical characterization of a Ru(II) assembly consisting of metal polypyridyl complexes linked together by a polyfluorene scaffold. Unlike many scaffolds incorporating saturated linkages, the conjugated polymer in this system acts as a functional light-harvesting component. Conformational disorder breaks the conjugation in the polymer backbone, resulting in a chain composed of many chromophore units, whose relative energies depend on the segment lengths. Photoexcitation of the polyfluorene by a femtosecond laser pulse results in the excitation of polyfluorene, which then undergoes direct energy transfer to the pendant Ru(II) complexes, producing Ru(II)* excited states within 500 fs after photoexcitation. Femtosecond transient absorption data show the presence of electron transfer from PF* to Ru(II) to form charge-separated (CS) products within 1–2 ps. The decay of the oxidized and reduced products, PF⁺• and Ru(I), through back electron transfer are followed using picosecond transient absorption methods.

SECTION: Energy Conversion and Storage; Energy and Charge Transport



Ruthenium (II) polypyridyl complexes have been targeted extensively for use in next-generation solar energy conversion applications. This interest stems in large part from their visible absorption bands that produce long-lived, photo-stable excited states. Furthermore, their electronic properties can be tuned through synthetic manipulation, and a wide array of ligand structures have been designed, yielding complexes capable of performing charge separation and catalytic functions.^{1–3} This synthetic flexibility has also facilitated their incorporation into molecular light-harvesting assemblies utilizing a variety of scaffold architectures. While these complexes are extremely versatile, they are limited by relatively weak absorptivities ($\epsilon \approx 10^4 \text{ M}^{-1} \text{ cm}^{-1}$) compared to organic systems, thus requiring longer path lengths for efficient light collection.

Conjugated polymers (CPs), on the other hand, have large extinction coefficients on a per-chain basis. Conformational disorder and chemical defects break the conjugation of the backbone, leading to the formation of linked, yet “isolated”, chromophores^{4–6} that exhibit fast intra- and interchain excited-state transport.⁶ It is this combination of large absorptivity and fast energy transport that give CPs an extraordinary “light-harvesting” ability. While energy transfer along the chain is rapid, the short singlet state lifetime limits the exciton diffusion

length, posing a major challenge for those developing organic-based devices.

In this Letter, we report on a Ru(II) polypyridyl assembly (PF–Ru) consisting of a number average of approximately 70 metal complexes linked together by a polyfluorene backbone. Unlike the well-documented derivatized polystyrene systems,^{7–10} in which the polymer only acts as a scaffold, the PF chain acts as an efficient, multichromophoric antenna that absorbs light and transfers the photonic energy to the pendant Ru(II) complexes, resulting in a long-lived excitation that can potentially be used to drive charge separation and/or catalytic functions.

Synthesis of the PF–Ru assembly (Figure 1) was realized by reacting an azide-functionalized polyfluorene with an alkyne-containing Ru(II) polypyridyl complex under Cu(I)-assisted “click” chemistry^{11–13} conditions. Quantitative azide–alkyne cycloaddition was verified by ¹H NMR and FTIR spectroscopies. The azide-containing polyfluorene precursor was obtained via the Pd-mediated Suzuki cross-coupling^{14–16} approach and consecutive treatment with sodium azide.

Received: July 18, 2012

Accepted: August 15, 2012

Published: August 15, 2012

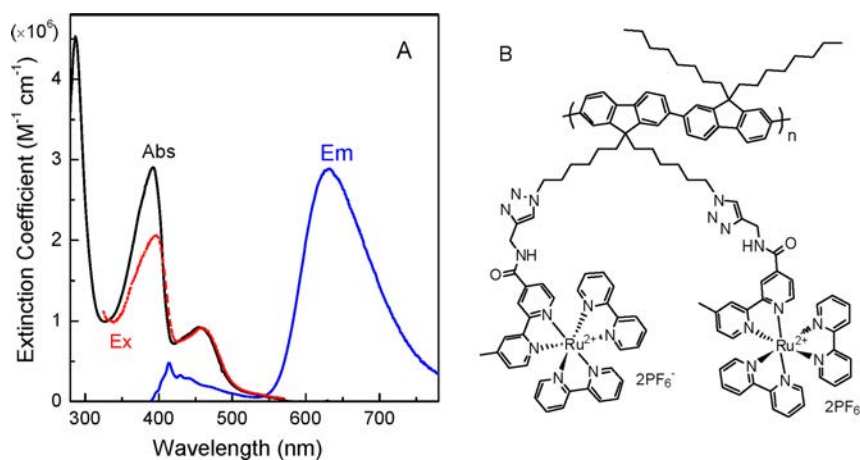


Figure 1. (A) Steady-state absorption (black), emission (blue), and emission excitation (red) spectra of PF–Ru in benzonitrile at room temperature. The emission spectrum was obtained following excitation at 390 nm; the weak band at 420 nm and the stronger band at 630 nm are emission from the PF scaffold and $^3\text{MLCT}$ state, respectively. The excitation spectrum was measured with $\lambda_{\text{mon}} = 630$ nm at 298 K. (B) Structure of Ru(II)-functionalized polyfluorene.

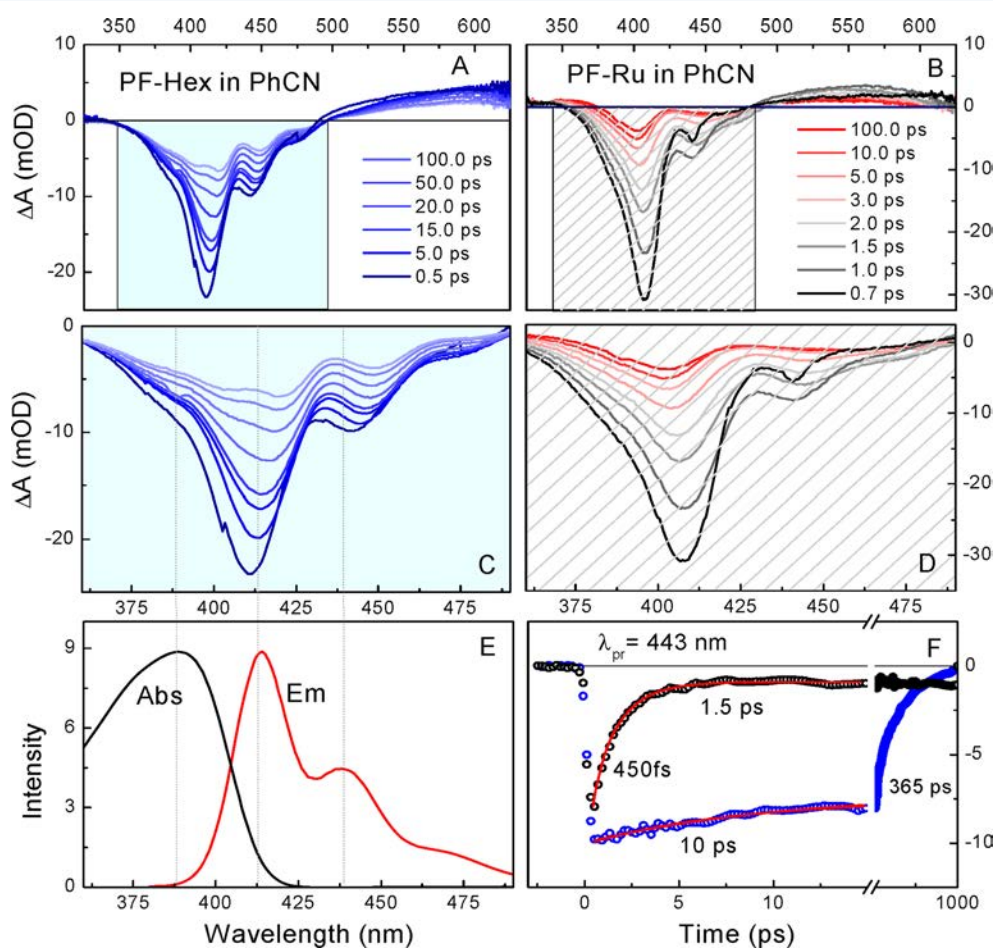
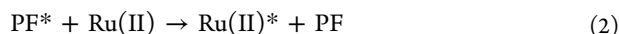


Figure 2. (A) Femtosecond transient absorption spectra of PF–Hex in benzonitrile at different delays (blue). Excitation was at 388 nm, and the pump pulse energy was 25 nJ/pulse. The instrument response was 250 fs. (B) Femtosecond transient absorption spectrum of PF–Ru in benzonitrile at different delays. Excitation was at 388 nm, and the pump pulse energy was 50 nJ/pulse. (C) Expanded view of the ground-state bleach and stimulated emission region for PF–Hex. Stimulated emission shows a clear red shift with increasing delay. (D) Expanded view of the ground-state bleach and stimulated emission of PF–Ru, showing the evolution from a structured spectrum characteristic of PF* (gray/black) at early times to the CS state (red) at later times. (E) Ground-state absorption (black) and emission (red) of PF in benzonitrile. (F) The decays of the transient signals at 443 nm for both PF–Hex and PF–Ru. Both have biexponential decay forms. PF–Ru ($\tau_1 = 450 \pm 20$ fs and $\tau_2 = 1.50 \pm 0.10$ ps) and PF ($\tau_1 = 10 \pm 0.30$ ps and $\tau_2 = 365 \pm 1.70$ ps).

Detailed synthesis and characterization data are provided in the Supporting Information (SI).

The absorption spectrum of PF–Ru (Figure 1A) closely corresponds to a superimposition of the individual spectra for the PF and Ru(II) polypyridyl complex, that is, the $\pi \rightarrow \pi^*$ transition of PF (395 nm), the MLCT transition of the Ru(II) complex (456 nm), and the $\pi \rightarrow \pi^*$ transition localized on the bipyridyl (bpy) ligand (288 nm). From the spectroscopic data, it is clear that the transitions from each component show little or no spectral shift, suggesting an absence of significant electronic coupling between PF and the Ru(II) polypyridyl complex in the ground state. It is notable that PF has a remarkably high molar absorptivity ($2.9 \times 10^6 \text{ cm}^{-1} \text{ M}^{-1}$), which corresponds to an extinction coefficient of $\sim 10^5$ per repeat unit, or about 3–4 times greater than that of the attached Ru(II) complexes.

Excitation of the Polymer Backbone. Photoexcitation of an alkyl-only “click”-substituted polyfluorene (PF–Hex (**10**); see the SI) at 388 nm results in a bright blue singlet-state PF* emission (quantum yield, $\Phi = 0.91$) with λ_{max} at 420 nm. The emission band has a clear vibronic progression with $\hbar\omega = 1400 \text{ cm}^{-1}$ and a lifetime of 380 ps. The emission spectrum of the PF–Ru system, however, is distinctly different when compared with that of PF–Hex (Figure 1A). It shows a very weak emission band at 420 nm and an intense 630 nm ³MLCT Ru(II) emission. The fluorescence excitation spectrum obtained while monitoring the ³MLCT emission (Figure 1, red line) nearly reproduces the ground-state absorption spectrum, suggestive of significant excitation energy transfer, that is



The fraction of PF* undergoing energy transfer (η_{EnT}) can be estimated from quantum yield measurements

$$\eta_{\text{EnT}} = \left(\frac{\Phi_{\text{PF–Ru}}}{\Phi_{\text{Ru}}} - f_{\text{Ru}} \right) \frac{1}{f_{\text{PF}}} \quad (3)$$

where $f_{\text{Ru}} \approx 0.1$ and $f_{\text{PF}} \approx 0.9$ are the fractions of Ru* and PF* created by 388 nm excitation, respectively. The quantum yield observed for 630 nm emission following 388 nm excitation is 0.095 for PF–Ru ($\Phi_{\text{PF–Ru}}$) and 0.11 for the Ru(II) model complex (as shown in the SI) (Φ_{Ru}), obtained under identical experimental conditions. On the basis of this, we estimate that $\eta_{\text{EnT}} = 85 \pm 8\%$. However, the excitation spectrum is not superimposable on the ground-state absorption spectrum at $\lambda < 400 \text{ nm}$, indicating that the fluorescence efficiency ($\Phi_{\text{PF–Ru}}$) is dependent on the excitation frequency. This observation provides direct spectroscopic evidence for the onset of another nonradiative decay pathway.

The early time dynamics of PF–Ru and PF–Hex after direct excitation of the PF backbone at 388 nm were probed using femtosecond transient absorption spectroscopy. The full spectra and representative kinetic trace for both PF–Hex and PF–Ru dissolved in benzonitrile (PhCN) are shown in Figure 2. At $t = 0$, the transient spectrum of PF–Hex (Figure 2A) has a prompt bleach due to the loss of the ground state of PF–Hex at 380–400 nm, as well as three vibronic stimulated emission bands at 420, 445, and 475 nm and a broad excited-state absorption band extending from 500 to 700 nm. The decay of the 443 nm feature (Figure 2F) indicates a PF* excited-state

lifetime of $\sim 370 \text{ ps}$. The red shift of the stimulated emission bands with increasing pump–probe delay (Figure 2C) most likely reflects either excited-state migration along the PF backbone as it seeks out lower-energy segments or the temporal evolution involving the dynamic planarization of the polymer backbone following photoexcitation.

The transient spectra from the PF–Ru system at early times are similar to that of PF (Figure 2B), consistent with the initial formation of the PF* state. However, in contrast to PF–Hex, the loss of the structured stimulated emission in PF–Ru is much faster than that of PF–Hex, occurring with both fast (450 fs) and slow (1.5 ps) kinetic components (Figure 2F). As the structured PF* spectrum disappears, it is replaced by bleach features centered at 406 and 450 nm and a broad absorption centered at 550 nm. While the 450 nm bleach is consistent with Ru(II)* formed by energy transfer (eq 2a), the sharp 406 nm band is not, indicating the presence of another photoproduct channel.

Evolution on time scales ranging from nanoseconds to microseconds, with 500 ps time resolution, was monitored by using a continuum probe pulse generated by a diode-laser-pumped photonic crystal fiber. Band assignments were made on the basis of several key observations in the spectra (Figure 3A) and kinetics (Figure 3B) obtained on the nanosecond time

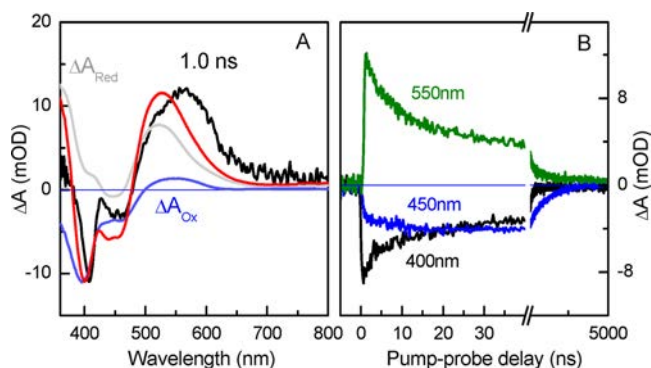


Figure 3. (A) Transient absorption spectrum of PF–Ru in benzonitrile obtained at 1.0 ns after photoexcitation at 388 nm. The gray line, labeled ΔA_{Red} , is the difference between the absorption spectra for the reduced and the neutral PF–Ru. The blue line, labeled ΔA_{Ox} , is the difference between the absorption spectra of oxidized Ru(III) and PF* and neutral PF–Ru. The red line is the sum of the oxidized and reduced difference spectra for PF–Ru. (B) Kinetic traces at 400, 450, and 550 nm of PF–Ru with 388 nm excitation.

scale. In particular, the MLCT bleach at 450 nm and the 550 nm band decay on different time scales (Figure 3B), suggesting that the visible absorption is not simply the Ru(II)* excited-state absorption that is typically observed to the red of 500 nm. Instead, the 550 nm absorption decays on the same time scale as the 406 nm bleach, indicating that the species giving rise to the two different features are kinetically correlated.

Spectroelectrochemical data provide insight into the band assignments. Difference spectra obtained by subtracting the absorption spectrum of the assembly, $A(\lambda)$, from the spectra obtained following quantitative oxidation or reduction, that is

$$\Delta A_{\text{Ox}} = A_{\text{Ox}}(\lambda) - A(\lambda) \quad (4)$$

$$\Delta A_{\text{Red}} = A_{\text{Red}}(\lambda) - A(\lambda) \quad (5)$$

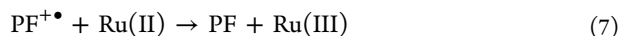
are also shown in Figure 3A. These spectra represent contributions of oxidized (PF*, Ru(III)) and reduced (Ru(I))

species to the transient absorption spectrum. The ΔA_{Red} spectrum shows a band centered at 520 nm that is assigned to Ru(I). The ΔA_{Ox} spectrum reveals two bleach features at 390 and 450 nm that correspond to loss of absorption intensity upon oxidation of the polymer backbone and metal complex, respectively, as well as a weak absorption of the oxidized polymer ($\text{PF}^{+\bullet}$) at 540 nm. These spectra suggest that photoexcitation of the PF backbone also results in the formation of a charge-separated (CS) state by direct electron transfer from PF^* to Ru(II), that is



The sum of ΔA_{Ox} and ΔA_{Red} , depicted as the red line in Figure 3, provides an estimate of the contribution of the CS state to the transient spectrum. This analysis suggests that the 550 nm visible absorption in the transient spectrum arises primarily from Ru(I), with perhaps a weak contribution from $\text{PF}^{+\bullet}$, and the 406 nm bleach reflects the loss of the ground-state polymer absorption upon oxidation. The kinetic correlation between the 406 nm bleach and 550 nm absorption indicates that the formation of the CS state during the first few picoseconds is followed by back electron transfer on the nanosecond time scale.

The bleach feature at 450 nm is most likely due to Ru(II)* formed via energy transfer. Having said that, the electrochemical measurements indicate similar oxidation potentials for PF and Ru(II), suggesting that subsequent hole transfer from the polymer to the metal complex is possible, that is



and thus the 450 nm bleach may also contain contributions from Ru(III).

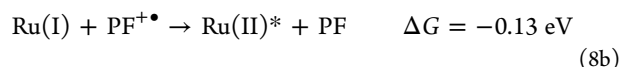
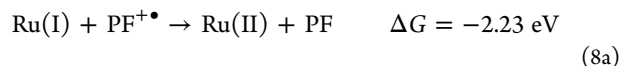
Quenching of the PF^* occurs through parallel energy- and electron-transfer mechanisms (eqs 2 and 6), both taking place on ultrafast time scales. Close inspection of the transient spectra, particularly the evolution of the 410 nm bleach feature, enables the disentanglement of these two processes. The position of the 410 nm feature is relatively constant during the first picosecond but then blue shifts over the next 2–3 ps to its final position at 406 nm as the CS features are established. On the basis of this, we assign the faster 450 fs component to energy transfer (eq 2) and the slower 1.5 ps component to charge separation (eq 6). The other vibronic features in the PF–Ru spectra at 443 and 478 nm do not show the time-dependent red shift associated with expansion of the excited state and/or exciton migration that was observed in PF (Figure 2D), indicating that the PF^* quenching occurs before these processes can occur.

Regardless of the exact assignment, it is clear that both energy transfer and electron transfer are taking place on ultrafast time scales. Rapid energy transfer is presumably the result of a large overlap between the PF emission and the Ru(II) absorption, most likely producing a $^1\text{MLCT}$ excited state through a dipole–dipole coupling mechanism.^{17–19} Ultrafast electron transfer is likely facilitated by a small barrier and/or a large electronic coupling. The similarity between the driving force ($\Delta G^\circ \approx -0.72$ eV) and estimates of the reorganization energy ($\lambda = 0.5$ – 1.0 eV) based on dielectric continuum models and comparisons with other systems point toward the possibility of a nearly activation-less electron-transfer process.²⁰ The magnitudes of the two rate constants indicate an energy-transfer efficiency, $\eta_{\text{EnT}} = k_{\text{EnT}}/(k_{\text{EnT}} + k_{\text{CS}})$, of $77 \pm 6\%$. The similarity between this value and that

determined from the emission spectra ($85 \pm 8\%$) suggests that the partitioning between the energy-transfer and electron-transfer pathways is governed by kinetic competition.

Decay of the CS state occurs by back electron transfer on the nanosecond time scale, resulting in a decay of both the 550 and 406 nm bands. The decay traces are multiexponential, with both fast and slow kinetic components (Figure 3B). The fast component at 5.5–6.5 ns is assigned to the back electron transfer of the initially formed CS products (eq 6). The slower component likely reflects either Ru(II)* decay or slower back electron transfer events that are delayed due to either electron or hole migration to other sites. The 550 nm signal decays to baseline within 0.85 μs (Figure 3B), signifying a complete loss of the CS products and residual excited states.

Back electron transfer could result in the formation of either ground- or excited-state Ru(II), that is



Given the presence of Ru(II)* formed by direct excitation and also energy transfer, it is difficult to distinguish between these two processes. The large driving force for formation of ground-state Ru(II) most likely places that process in the inverted regime, which would suggest excited-state formation. However, formation of Ru(II)* would involve the transfer of an electron from the Ru metal, which would correspond to a longer electron-transfer distance than formation of Ru(II), where the electron would transfer from the bpy ligand.

The PF–Ru system combines functional elements of both the conjugated polymer and the metal complex. The polymer provides efficient light harvesting and energy transport that enables energy to be collected and funneled to specific locations. This energy can then be efficiently off-loaded to, and exploited by, pendant metal complexes designed for charge separation or photocatalytic functions. In addition, the PF–Ru system also demonstrates a photoinduced long-range electron transfer.

■ ASSOCIATED CONTENT

📄 Supporting Information

Experimental procedures, characterization data, electrochemistry, and spectroelectrochemistry results. This material is available free of charge via the Internet at <http://pubs.acs.org>.

■ AUTHOR INFORMATION

Corresponding Author

*E-mail: john_papanikolas@unc.edu (J.M.P); reynolds@chemistry.gatech.edu (J.R.R.).

Author Contributions

#These authors contributed equally.

Notes

The authors declare no competing financial interest.

■ ACKNOWLEDGMENTS

This material is based on work supported as part of the UNC EFRC: Solar Fuels and Next Generation Photovoltaics, an Energy Frontier Research Center funded by the U.S. Department of Energy, Office of Science, Office of Basic Energy Sciences under Award Number DE-SC0001011. We also acknowledge support for the purchase of instrumentation

from UNC SERC (the “Solar Energy Research Center Instrumentation Facility” funded by the US Department of Energy – Office of Energy Efficiency & Renewable Energy under Award Number DE-EE0003188). L.W. also thanks Professor David W. Thompson at Memorial University for the academic consultations and suggestions.

REFERENCES

- (1) Alstrum-Acevedo, J. H.; Brennaman, M. K.; Meyer, T. J. Chemical Approaches to Artificial Photosynthesis. 2. *Inorg. Chem.* **2005**, *44*, 6802–6827.
- (2) Concepcion, J. J.; Jurss, J. W.; Templeton, J. L.; Meyer, T. J. One Site is Enough. Catalytic Water Oxidation by $[\text{Ru}(\text{tpy})(\text{bpm})(\text{OH}_2)]^{2+}$ and $[\text{Ru}(\text{tpy})(\text{bpz})(\text{OH}_2)]^{2+}$. *J. Am. Chem. Soc.* **2008**, *130*, 16462–16463.
- (3) Jurss, J. W.; Concepcion, J. J.; Butler, J. M.; Omberg, K. M.; Baraldo, L. M.; Thompson, D. G.; Lebeau, E. L.; Hornstein, B.; Schoonover, J. R.; Jude, H.; et al. Electronic Structure of the Water Oxidation Catalyst *cis,cis*- $[(\text{bpy})_2(\text{H}_2\text{O})\text{Ru}^{\text{III}}\text{ORu}^{\text{III}}(\text{OH}_2)(\text{bpy})_2]^{4+}$, The Blue Dimer. *Inorg. Chem.* **2012**, *51*, 1345–1358.
- (4) Schindler, F.; Lupton, J. M.; Feldmann, J.; Scherf, U. A Universal Picture of Chromophores in π -Conjugated Polymers Derived from Single-Molecule Spectroscopy. *Proc. Natl. Acad. Sci. U.S.A.* **2004**, *101*, 14695–14700.
- (5) Schindler, F.; Jacob, J.; Grimsdale, A. C.; Scherf, U.; Mallen, K.; Lupton, J. M.; Feldmann, J. Counting Chromophores in Conjugated Polymers. *Angew. Chem., Int. Ed.* **2005**, *44*, 1520–1525.
- (6) Collini, E.; Scholes, G. D. Coherent Intrachain Energy Migration in a Conjugated Polymer at Room Temperature. *Science* **2009**, *323*, 369–373.
- (7) Dupray, L. M.; Devenney, M.; Striplin, D. R.; Meyer, T. J. An Antenna Polymer for Visible Energy Transfer. *J. Am. Chem. Soc.* **1997**, *119*, 10243–10244.
- (8) Fleming, C. N.; Dupray, L. M.; Papanikolas, J. M.; Meyer, T. J. Energy Transfer between Ru(II) and Os(II) Polypyridyl Complexes Linked to Polystyrene. *J. Phys. Chem. A* **2002**, *106*, 2328–2334.
- (9) Fleming, C. N.; Jang, P.; Meyer, T. J.; Papanikolas, J. M. Energy Migration Dynamics in a Ru(II)- and Os(II)-Based Antenna Polymer Embedded in a Disordered, Rigid Medium. *J. Phys. Chem. B* **2004**, *108*, 2205–2209.
- (10) Sykora, M.; Maxwell, K. A.; DeSimone, J. M.; Meyer, T. J. Mimicking the Antenna-Electron Transfer Properties of Photosynthesis. *Proc. Natl. Acad. Sci. U.S.A.* **2000**, *97*, 7687–7691.
- (11) Binder, W. H.; Sachsenhofer, R. ‘Click’ Chemistry in Polymer and Materials Science. *Macromol. Rapid Commun.* **2007**, *28*, 15–54.
- (12) Becer, C. R.; Hoogenboom, R.; Schubert, U. S. Click Chemistry beyond Metal-Catalyzed Cycloaddition. *Angew. Chem., Int. Ed.* **2009**, *48*, 4900–4908.
- (13) Le Droumaguet, B.; Velonia, K. Click Chemistry: A Powerful Tool to Create Polymer-Based Macromolecular Chimeras. *Macromol. Rapid Commun.* **2008**, *29*, 1073–1089.
- (14) Sakamoto, J.; Rehahn, M.; Wegner, G.; Schlüter, A. D. Suzuki Polycondensation: Polyarylenes  la Carte. *Macromol. Rapid Commun.* **2009**, *30*, 653–687.
- (15) Suzuki, K.; Kobayashi, A.; Kaneko, S.; Takehira, K.; Yoshihara, T.; Ishida, H.; Shiina, Y.; Oishic, S.; Tobita, S. Reevaluation of Absolute Luminescence Quantum Yields of Standard Solutions Using a Spectrometer with an Integrating Sphere and a Back-Thinned CCD Detector. *Phys. Chem. Chem. Phys.* **2009**, *11*, 9850–9860.
- (16) Schlüter, A. D. The Tenth Anniversary of Suzuki Polycondensation (SPC). *J. Polym. Sci., Part A: Polym. Chem.* **2001**, *39*, 1533–1556.
- (17) Faiz, J. A.; Williams, R. M.; Silva, M. J. J. P.; De Cola, L.; Pikramenou, Z. A Unidirectional Energy Transfer Cascade Process in a Ruthenium Junction Self-Assembled by α - and β -Cyclodextrins. *J. Am. Chem. Soc.* **2006**, *128*, 4520–4521.
- (18) Tyson, D. S.; Castellano, F. N. Intramolecular Singlet and Triplet Energy Transfer in a Ruthenium(II) Diimine Complex Containing Multiple Pyrenyl Chromophores. *J. Phys. Chem. A* **1999**, *103*, 10955–10960.
- (19) Wilson, G. J.; Sasse, W. H. F.; Mau, A. W.-H. Singlet and Triplet Energy Transfer Processes in Ruthenium(II) Bipyridine Complexes Containing Covalently Bound Arenes. *Chem. Phys. Lett.* **1996**, *250*, 583–588.
- (20) Marcus, R. A. Electron Transfer Reactions in Chemistry. Theory and Experiment. *Rev. Mod. Phys.* **1993**, *65*, 599–610.

Tunable Energy Transfer Rates via Control of Primary, Secondary, and Tertiary Structure of a Coiled Coil Peptide Scaffold

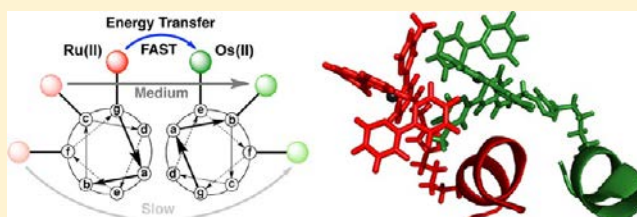
Dale J. Wilger,[†] Stephanie E. Bettis,[†] Christopher K. Materese,[†] Maria Minakova,[†] Garegin A. Papoian,^{*,‡} John M. Papanikolas,^{*,†} and Marcey L. Waters^{*,†}

[†]Department of Chemistry, CB 3290, University of North Carolina, Chapel Hill, North Carolina 27599, United States

[‡]Department of Chemistry and Biochemistry, University of Maryland, College Park, Maryland 20742, United States

S Supporting Information

ABSTRACT: Herein we report energy transfer studies in a series of Ru(II) and Os(II) linked coiled-coil peptides in which the supramolecular scaffold controls the functional properties of the assembly. A general and convergent method for the site-specific incorporation of bipyridyl Ru(II) and Os(II) complexes using solid-phase peptide synthesis and the copper-catalyzed azide–alkyne cycloaddition is reported. Supramolecular assembly positions the chromophores for energy transfer. Using time-resolved emission spectroscopy we measured position-dependent energy transfer that can be varied through changes in the sequence of the peptide scaffold. High level molecular dynamics simulations were used in conjunction with the spectroscopic techniques to gain molecular-level insight into the observed trends in energy transfer. The most efficient pair of Ru(II) and Os(II) linked peptides as predicted by molecular modeling also exhibited the fastest rate of energy transfer (with $k_{\text{EnT}} = 2.3 \times 10^7 \text{ s}^{-1}$ (42 ns)). Additionally, the emission quenching for the Ru(II) and Os(II) peptides can be fit to binding models that agree with the dissociation constants determined for the peptides via chemical denaturation.



I. INTRODUCTION

The design of molecular materials capable of performing complex functions is pivotal to “bottom-up” approaches in molecular electronics,¹ sensing,^{1a,2} and solar energy conversion.^{3,4} The most common strategy for building artificial assemblies uses covalent bond formation to connect molecular components with rigid linkers that dictate both distance and orientation. While this approach provides exquisite control over spatial parameters,⁵ the optimization of functional performance often requires the development of new synthetic routes making the implementation very difficult, especially as the number of molecular components increases. Alternatively, chromophores have been placed on easily synthesized scaffolds such as polymers,⁶ dendrimers,^{1a,3c,7} and organogels.⁸ However this approach can yield assemblies that are not monodisperse in molecular weight or chemical composition and incorporate many different morphological constituents. While large systems are readily made and some control over the primary structure is possible, the flexible scaffolds result in solution structures that vary from one assembly to the next.

Another approach to achieve functional architectures draws inspiration from natural systems, which combine simple molecular building-blocks to form highly complex functional systems. Nature exploits relatively weak noncovalent interactions to achieve functional architectures with a hierarchical control, in which sequence defines structure and self-assembly, which defines function. Proteins, lipids, and oligonucleotides form the structural framework that organize functional elements in spatial proximity and with well-defined orienta-

tions.⁹ To this end, functionalized biological molecules such as oligonucleotides,¹⁰ amyloid-like peptide fibrils,¹¹ and even derivatized virus coated proteins have been designed and investigated as functional materials.¹² These types of designed systems^{11,13–15} that mimic the organizational strategies of biomolecules provide a number of advantages, including design flexibility, ease of synthesis, and spatial control of functionality through *supramolecular architectures* that allow for fine-tuning of materials properties.

Herein we report the design of an artificial polypeptide system based on a heterodimeric coiled-coil architecture in which the primary sequence defines both the secondary and the tertiary structure, resulting in self-assembly, which provides fine control of the positioning of octahedral tris(bipyridyl) transition metal complexes $[M^{\text{II}}(\text{bpy})_3]^{2+}$ ($M = \text{Ru}$ or Os , $\text{bpy} = 2,2'$ -bipyridyl). Coiled-coils are a common protein motif and provide structural architecture for many important protein scaffolds including α -keratin¹⁶ and tropomyosin.¹⁷ Moreover, the sequence-structure rules are well-defined, allowing for the design of highly tunable supramolecular architectures by control of the primary sequence.^{18a} In this study we demonstrate the ability of the peptide secondary structure to control self-assembly and hence relative positioning of the octahedral complexes, resulting in systematic tuning of the energy transfer properties of the system. The Ru(II) and Os(II) metal complexes are positioned near the midpoints of two

Received: March 30, 2012

Published: June 8, 2012

complementary peptide chains, each consisting of 28 residues (Figure 1). The primary sequence of each chain is chosen such

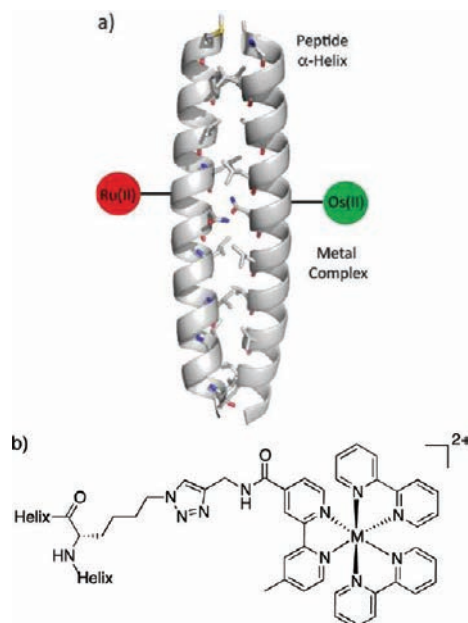


Figure 1. (a) Illustration of metalloprotein system containing the α -helical coiled-coil scaffold and metal complexes (coiled coil: pdb 2AHP). (b) Structure of the metal complex and its attachment to the α -helix.

that they adopt a dimeric supramolecular structure consisting of two α -helical coils, in which the hydrophobic residues are shielded from the aqueous environment and the hydrogen bonding and ionic interactions are maximized. Photoexcitation of the Ru(II) complex in the folded assembly results in energy transfer to the lower energy Os(II) acceptor on the opposing chain. Since the metal complexes are placed on different peptide chains, energy transfer is only possible if the two chains associate in solution, making this system particularly sensitive to the secondary and tertiary structure of the peptide scaffold.

The peptide structures studied here take advantage of two flexible synthetic methodologies: solid-phase peptide synthesis (SPPS) and the copper(I)-catalyzed azide–alkyne cycloaddition (CuAAC or “click reaction”). SPPS is advantageous as it allows for exact positioning of the chromophores in the primary sequence. The use of click chemistry as an orthogonal linkage strategy between the chromophores and the peptides has several advantages. First, it avoids issues with formation of statistical mixtures of species, as was obtained in the electron transfer coiled-coil systems developed by Ogawa, in which the chromophore linkage was accomplished via nonspecific coordination chemistry.¹⁵ Second, click chemistry provides advantages over the direct amide linkage used in the electron-transfer oligoprolin systems reported by Meyer, in which orthogonal protecting group strategies had to be employed.¹⁴

We have examined a series of peptide assemblies that systematically vary the placement of the complexes along the peptide backbone, results in predictable changes in the energy transfer rate, which are measured using time-resolved emission methods. Variation in the rate by almost an order of magnitude across the series, as well as denaturation studies, confirm that energy transfer is the direct result of folding into a well-defined tertiary structure. All-atom molecular dynamics simulations

provide insight into the microscopic environment, revealing an assembly with a dynamic, yet robust, tertiary structure that effectively controls the relative positioning of the two complexes.

II. RESULTS AND DISCUSSION

System Design. Since energy transfer between Ru(II) and Os(II) polypyridine complexes has not been previously studied using this type of chemical scaffold, a number of design elements were considered crucial for the proper development of such a system, as discussed below: (1) the design of the coiled-coil peptide scaffold, (2) the attachment chemistry including its utility, versatility, and compatibility with standard conditions for automated peptide synthesis, (3) the nature of the metal complexes including their chemical stability and photophysical properties, (4) the nature of the linking group and how it may affect coiled-coil secondary and quaternary structure, and (5) the positions for Ru(II) and Os(II) modification within the coiled-coil peptides.

Coiled-Coil Peptide Scaffold Design. The coiled-coil peptide scaffold was adopted from the heterodimeric self-assembling fiber (SAF) system originally reported by Woolfson and co-workers (Figure 2).¹⁸ Both 28-residue peptides contain

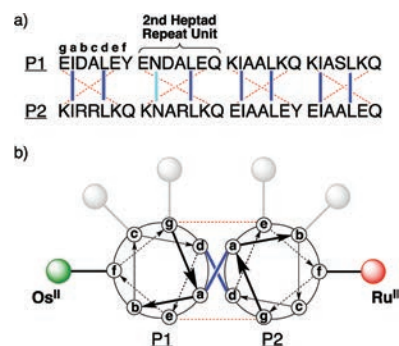


Figure 2. (a) Primary sequences of the P1 and P2 peptides using the single letter amino acid code (in capitals). Each 28-residue peptide has four heptad repeat units. The common letter designations for the heptad positions (*abcde*) are shown above the first heptad repeat unit for P1. The hydrophobic interactions are shown as blue lines, the hydrogen bonding interaction between Asn side chains is shown as a cyan line, and the complementary ionic interactions between the two peptides are shown as red dashed lines. (b) A helical-wheel diagram displaying the potential points for attachment when viewed down helix axis from the N-terminus. The P1 peptide is modified with Os(II) at the *f*, *c*, or *g* position within the second heptad. The P2 peptide is modified with Ru(II) at the *f*, *b*, or *e* position within the second heptad.

the canonical repeating heptad sequence (designated *abcde*) that most coiled-coil peptides display. The *a* and *d* sites are reserved for hydrophobic residues which provide the primary driving force for dimerization. Isoleucine and leucine residues were specifically chosen for the *a* and *d* sites, respectively, because they have been shown superior promoters for the desired parallel dimeric structure.^{18a,19} The *e* and *g* positions contain oppositely charged residues such as lysine and glutamate that provide complementary interactions only when the heterodimeric and parallel partnering is considered.^{19c,20} An asparagine residue is included at a single *a* position within each sequence. Polar residues included at these positions must satisfy their hydrogen bonding potential, and impart folding specificity

through mutual alignment to give a parallel coiled-coil exclusively.^{19,20b,21} Although the incorporation of two asparagine residues within the hydrophobic core of the parallel dimer interface is slightly destabilizing compared to more hydrophobic residues at these positions, their incorporation is more destabilizing within undesired structures including trimers, tetramers, antiparallel dimers, and misaligned dimers.^{19,20b,21} Thus, this sequence design provides parallel heterodimeric coiled-coils to the exclusion of other supramolecular architectures. Of significance for this study is the fact that the monomeric peptides with this type of sequence design typically do not fold into helical structures to any great extent. This is attributed to the fact that such a monomeric helix would display a large hydrophobic patch on one face of the helix, which is unfavorable in aqueous solution.

The majority of Woolfson's SAF peptides contain complementary interactions that promote a staggered heterodimer structure referred to as the "sticky-ends" design.^{18b} The P1 peptide sequence is a permutation which has been rearranged to discourage longitudinal association, and therefore fiber formation.^{18b} Natural coiled-coil peptides all share this "blunt" end assembly.²² The P2 apo-peptide sequence remains unchanged from several of Woolfson's reports.¹⁸

Synthesis of Metallopeptides Using CuAAC. A number of redox-active amino acids containing Ru(II) and Os(II) bipyridyl complexes have previously been reported.^{14,23} These amino acid derivatives are convenient because they can be incorporated into metallopeptides during traditional linear solid-phase peptide synthesis (SPPS), although they often include longer coupling times, more exotic coupling reagents, and decreased yields. We chose a convergent synthetic strategy because it would allow for the peptide, linker, and bipyridyl complexes to be easily varied for later optimization and investigation. The Cu(I)-catalyzed azide-alkyne 1,3-dipolar cycloaddition provides general and robust conditions for the conjugation of biomolecules.²⁴ Several alkynyl-functionalized Ru(II) and Os(II) complexes have been reported,^{10a-c,25} having previously been used for oligonucleotide modification with Sonogashira Pd(0) cross-coupling chemistry.²⁶ The Ru(II) and Os(II) bipyridyl complexes **1a** and **1b** (Figure 3) were selected,²⁵ as opposed to previously described phenanthroline complexes,^{10a-c} because the sp^3 -hybridized carbon within the propargyl amide group increases flexibility and electronically

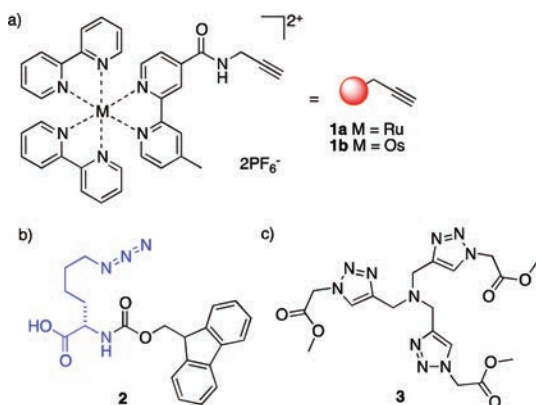


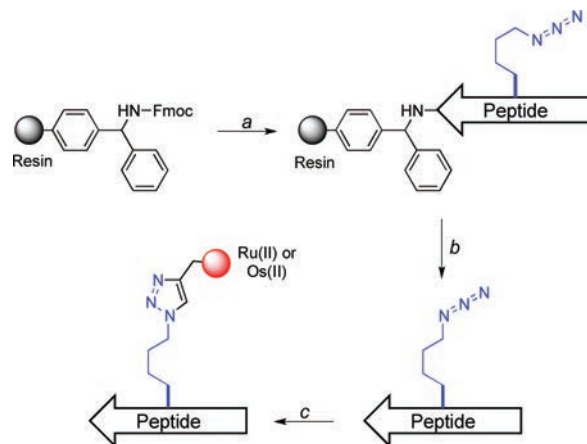
Figure 3. (a) Alkynyl-functionalized Ru(II) and Os(II) containing complexes **1a** and **1b**, respectively. (b) Fmoc-lysine- ϵ -azide **2** used in the synthesis of azidopeptides. (c) *tris*-(Triazolylmethyl)amine ligand **3** used to accelerate the CuAAC conjugation reaction.

decouples the metallobipyridine from the triazole ring formed during the CuAAC reaction.

Lysine ϵ -azide was selected to provide the tether for **1a** and **1b** since it contains four aliphatic methylene units, and was anticipated to be less destabilizing toward the coiled-coil peptide structure compared to shorter tether lengths (Figure 3).^{18f,27} The linker was also selected to be sufficiently flexible so as to allow rotational freedom for the metal complexes since orientation and angular relationships between donor and acceptor modules have a strong influence on energy transfer efficiencies.^{10c,d,13a}

Azidopeptides were synthesized by incorporating Fmoc-lysine ϵ -azide (**2**) at the desired point of (donor/acceptor) attachment during SPPS (Scheme 1). After the azidopeptides

Scheme 1. Synthesis of Metallopeptides Using CuAAC^a



^aConditions: (a) solid-phase peptide synthesis: Fmoc removal, piperidine/DMF (1:4); 2 × 15 min; coupling, 4 equiv of amino acid, 4 equiv of HBTU, 4 equiv of HOBT, 4 equiv of DIPEA, DMF; capping, Ac₂O/2,6-lutidine/DMF (5:6:89); (b) cleavage, TIPS/H₂O/TFA (2.5:2.5:95); purification, RP-HPLC (c) conjugation using the CuAAC reaction, 2 equiv of **1a** or **1b**, 1.5–2 equiv of [Cu(CH₃CN)₄]-PF₆, 1 equiv of **3**, DMF/buffer (1:1), buffer = 10 mM sodium phosphate buffer, pH 8.5.

were cleaved from the solid-phase support and purified using RP-HPLC, they were conjugated to **1a** or **1b** using the CuAAC reaction (Scheme 1). Reactions containing a *tris*-(triazolylmethyl)amine ligand (**3**) demonstrated shorter reaction times and increased yields compared to reactions lacking the ligand.²⁸ A more basic reaction medium (pH 8.5) provided shorter reaction times compared to lower pH media.^{24c} After conjugation was complete, the metallopeptides were purified using a combination of size-exclusion chromatography and RP-HPLC as described below.

Donor/Acceptor Placement in the Coiled-Coil. The coiled-coil peptide scaffold contains a multitude of possible positions for the attachment of polypyridyl donor/acceptor complexes. The positions selected for modification were chosen to provide a range of well-defined donor/acceptor distances in the self-assembled coiled-coil for measuring excited-state energy transfer. Substitutions on the first and last heptad repeat units of the peptides could potentially result in complications from end fraying near the termini, and were therefore avoided. Conjugation of **1b** (Os(II)) at the 2f, 2c, or 2g position within the P1 peptide sequence gave the excited state energy acceptor metallopeptides 2f-Os-P1, 2c-Os-P1, and 2g-Os-P1, respectively

(Table 1). Similarly, conjugation of **1a** (Ru(II)) at the *2f*, *2b*, or *2e* position within the P2 peptide sequence provided the donor

Table 1. Ru(II) and Os(II) Metallopeptide Sequences^a

Peptide	Sequence ^a
P1	EIDALEY-ENDALEQ-KIAALKQ-KIASLKQ
2f-Os-P1	EIDALEY-ENDALEX-KIAALKQ-KIASLKQ
2c-Os-P1	EIDALEY-ENDXLEQ-KIAALKQ-KIASLKQ
2g-Os-P1	EIDALEY-XNDALEX-KIAALKQ-KIASLKQ
P2	KIRRLKQ-KNARLKQ-EIAALEY-EIAALEQ
2f-Ru-P2	KIRRLKQ-KNARLX-EIAALEY-EIAALEQ
2b-Ru-P2	KIRRLKQ-KNXRLKQ-EIAALEY-EIAALEQ
2e-Ru-P2	KIRRLKQ-KNARLXQ-EIAALEY-EIAALEQ

^aThe primary sequences for the peptides synthesized and characterized in this study are given using the single letter amino acid code (in capitals). X represent the artificial amino acid lysine *ε*-azide used for the attachment of Os(II) (green) or Ru(II) (red) complexes.

metallopeptides *2f*-Ru-P2, *2b*-Ru-P2, and *2e*-Ru-P2, respectively (Table 1). Three specific pairs of metallopeptides were selected for structural analysis, photophysical characterization, and all-atom molecular dynamics simulation. The *2f*-Os/*2f*-Ru metallopeptide pair refers to the heterodimer formed by the *2f*-Os-P1 and *2f*-Ru-P2 metallopeptides and was expected to provide the largest donor/acceptor separation distance, based on the analysis of parallel dimeric coiled-coils with crystal structures reported in the protein database (PDB code: 3NM6, 1UIX, and 3M9B). The distance between the α -carbons of aligned f positions to 14.9 Å in these crystal structures. Similar analysis indicated that *b-c* separations were 12.7–13.5 Å, and *e-g* separations were 9.6–10.3 Å. Although these measurements do not account for the length or flexibility of the azidolysine linker, they qualitatively represent the general trends that may be expected for the rates of energy transfer in the *2f*-Os/*2f*-Ru, *2c*-Os/*2b*-Ru, and *2g*-Os/*2e*-Ru metallopeptide pairs.

Structural Characterization of the Metallopeptide Heterodimers by Circular Dichroism. Circular dichroism (CD) is a common technique for the characterization of peptide secondary structure.^{29a} A well-formed α -helix exhibits a maximum in the CD spectrum below 200 nm and minima at 208 and 222 nm. The CD spectra of the monomeric peptides each exhibit relatively weak minima at 208 and 222 nm, characteristic of a dynamic partially folded helical structure, as expected (Figure 4). Because peptide CD spectra are typically plotted with concentration-independent mean residue ellipticity on the *y*-axis, a 1:1 mixture of complementary peptides is expected to exhibit deeper minima at 208 and 222 nm if an α -helical coiled-coil structure is formed, whereas if dimerization does not occur, the spectrum of the mixture will be identical to the average of the spectra for the two individual peptides. The CD spectra for all three heterodimeric metallopeptide pairs indicate that they form coiled-coil structures when mixed in a 1:1 ratio in aqueous buffer at μ M concentrations (Figure 4).²⁹ The ellipticity at 222 nm is a quantitative measure of α -helicity and can be used to monitor coiled-coil dimerization. All three pairs display maximum α -helicity when equimolar mixtures are measured, indicating that heterodimeric coiled-coil structures are being formed (see Supporting Information). The *2f*-Os/*2f*-Ru peptide pair exhibits the largest negative signal at 222 nm, with an ellipticity ratio for the *2f*-Os/*2f*-Ru pair at 208 and 222 nm, $\theta_{222}/\theta_{208}$, equal to 1.00. Similarly, the *2c*-Os/*2b*-Ru and *2g*-Os/*2e*-Ru peptide pairs both have $\theta_{222}/\theta_{208}$ values equal to

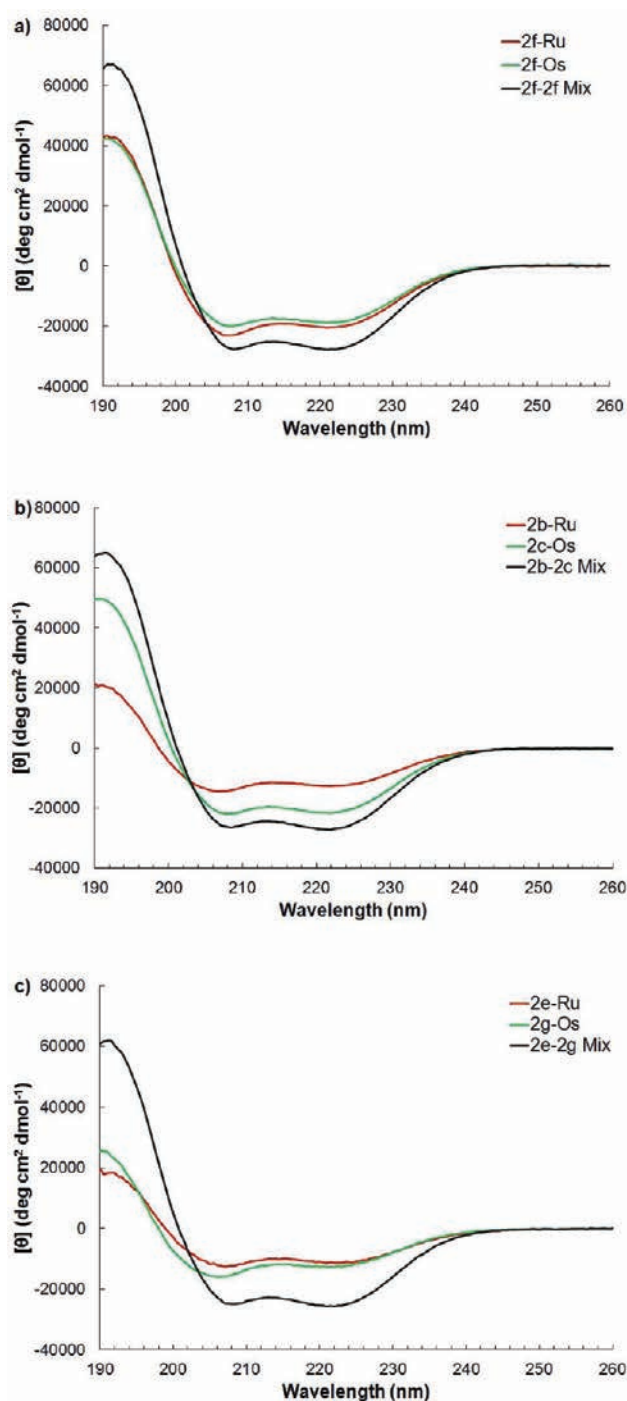


Figure 4. (a) Circular dichroism (CD) spectra of the individual *2f*-Os (green) and *2f*-Ru (red) peptides, both at a concentration of 50 μ M at 25 °C in 10 mM sodium phosphate buffer, pH 7.4. A 1:1 mixture of the two peptides (black, 50 μ M combined peptide concentration) shows a more intense negative signal at 222 nm indicating an increase in the α -helicity for the two peptides. (b) CD spectra of the *2c*-Os (green) and *2b*-Ru (red) peptides and the 1:1 mixture (black) under the same conditions as in (a). (c) CD spectra of the *2g*-Os (green) and *2e*-Ru (red) peptides and the 1:1 mixture (black) under the same conditions as in (a).

1.03. This ratio is characteristic of dimeric coiled-coil peptides, as single-stranded α -helices have values closer to 0.85.³⁰

Thermodynamic Stability Determined Using Guanidinium Denaturation. Chemical denaturation using guanidini-

niium chloride (GndHCl) provides a reliable tool for measuring coiled-coil dissociation constants.^{20c,31} The method has been used to compare small structural variations within families of similarly designed coiled-coils.^{20c} Gibbs free energy change of unfolding (ΔG_{unfold}) was measured for each of the metalloprotein dimers using the method of linear extrapolation (Figure 5).³¹ The different donor/acceptor modification points

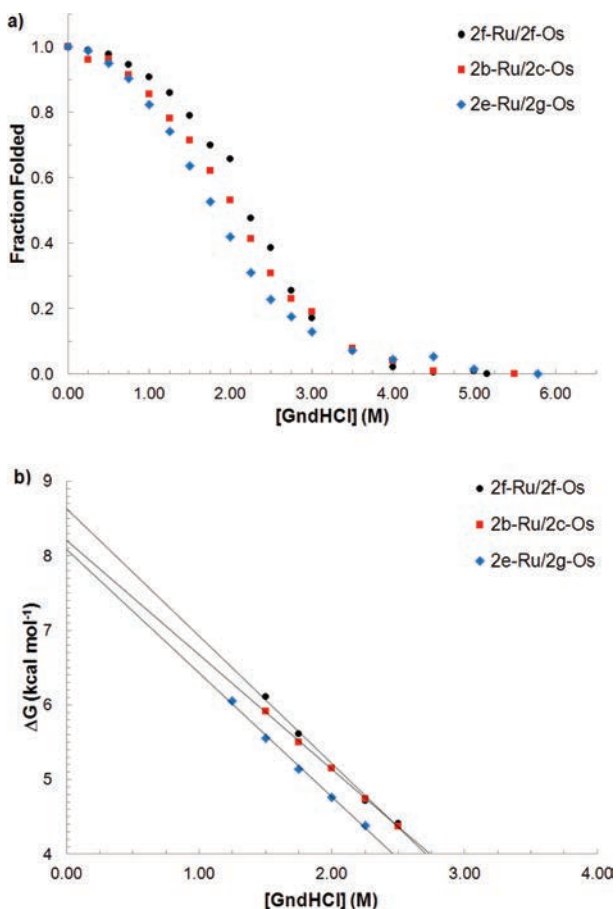


Figure 5. (a) Guanidinium chloride denaturation curves at 25 °C in 20 mM sodium phosphate buffer, 100 mM NaCl, pH 7.4. Data plotted for the 2*f*-Os/2*f*-Ru pair (black circles, 300 μM), the 2*c*-Os/2*b*-Ru pair (red squares, 200 μM), and the 2*g*-Os/2*e*-Ru pair (blue diamonds, 200 μM). The calculation of fraction folded is described within the experimental procedures section. (b) Gibbs free energy of unfolding is plotted as a function of guanidinium chloride concentration ($\Delta G = m[\text{GndHCl}] + \Delta G_{\text{unfold}}$). Linear extrapolation (Experimental Section) gives the value of ΔG_{unfold} at zero denaturant concentration. Data shown for the 2*f*-Os/2*f*-Ru pair (black circles, $m = -1.7$ kcal/mol·M, $R^2 = 0.997$), the 2*c*-Os/2*b*-Ru pair (red squares, $m = -1.5$ kcal/mol·M, $R^2 = 0.999$), and the 2*g*-Os/2*e*-Ru pair (blue diamonds, $m = -1.7$ kcal/mol·M, $R^2 = 0.997$).

for the metalloprotein pairs resulted in only subtle differences in structural stability. As may be expected, the 2*f*-Os/2*f*-Ru pair formed the most thermodynamically favorable heterodimer (Table 2). The value of ΔG_{unfold} measured for the 2*f*-Os/2*f*-Ru pair, 8.6 ± 0.10 kcal/mol, corresponds to a dissociation constant (K_d) equal to 0.49 ± 0.09 μM. The α -helicity of the fully folded 2*f*-Os/2*f*-Ru dimer was calculated to be 80%, based on molar ellipticity measurements at 222 nm ($-28,600 \pm 800$ deg·cm²·dmol⁻¹). The α -helical content determined for the 2*f*-Os/2*f*-Ru dimer falls within the range reported for similar

Table 2. Thermodynamic Stability of the Metallopeptide Heterodimers

peptide pair	ΔG_{unfold} (kcal/mol) ^a	K_d [μM] ^b	α -helicity ^c
2 <i>f</i> -Os/2 <i>f</i> -Ru	8.6	0.49 ± 0.09	80%
2 <i>c</i> -Os/2 <i>b</i> -Ru	8.2	0.97 ± 0.2	74%
2 <i>g</i> -Os/2 <i>e</i> -Ru	8.0	1.4 ± 0.3	72%

^aGibbs free energy of unfolding (ΔG_{unfold}) was measured for each peptide pair using the linear extrapolation method (Experimental Section). Error estimated to be ± 0.10 kcal/mol based on error due to linear extrapolation. ^bDissociation constants (K_d) were calculated using the equation $\Delta G_{\text{unfold}} = -RT \ln K_d$, using ΔG_{unfold} values obtained by the linear extrapolation method. ^cMaximum ellipticity values for each pair were measured using the CD signal at 222 nm for multiple trials. The predicted maximum molar ellipticity for a 28 residue helix (X_H^{28}) is calculated to be $-35,900$ deg·cm²·dmol⁻¹ using the equation: $X_H^n = X_H^\infty(1 - k/n)$, where X_H^∞ is the molar ellipticity for a helix of infinite length and is equal to $-39,500$ deg·cm²·dmol⁻¹, n is equal to 28 residues, and k is wavelength-dependent constant equal 2.57 at 222 nm.³³

sequences since values from 69 to 96% are common for three to five heptad-repeat coiled-coils.^{15,32} The fact that it is less than 100% helical likely arises from end-fraying.

The 2*c*-Os/2*b*-Ru peptide pair showed a minor destabilization when compared to the 2*f*-Os/2*f*-Ru pair. The difference in ΔG_{unfold} (8.2 ± 0.10 kcal/mol) for the 2*c*-Os/2*b*-Ru peptide pair corresponds to an increase in the extrapolated K_d (0.97 ± 0.20 μM). The maximum ellipticity for the 2*c*-Os/2*b*-Ru pair ($-26,400 \pm 700$ deg·cm²·dmol⁻¹) corresponds to 74% α -helicity, indicating slightly less α -helical character when compared to the 2*f*-Os/2*f*-Ru dimer. Not unexpectedly, the 2*g*-Os/2*e*-Ru peptide pair was found to be the least stable heterodimer, as this pair places the Ru(II) and Os(II) closest to the dimerization interface, although the magnitude of the destabilization was again quite minimal. The extrapolated ΔG_{unfold} (8.0 ± 0.10 kcal/mol) value for the 2*g*-Os/2*e*-Ru pair is within error of that reported for the 2*c*-Os/2*b*-Ru pair. The calculated K_d (1.4 ± 0.3 μM) value for 2*g*-Os/2*e*-Ru pair is therefore also within error. The maximum ellipticity ($-25,900 \pm 300$ deg·cm²·dmol⁻¹) for the 2*g*-Os/2*e*-Ru dimer corresponds to 72% α -helicity.

Although the thermodynamic parameters (ΔG_{unfold} , K_d , and % α -helicity) for the 2*b*-Ru/2*c*-Os and 2*e*-Ru/2*g*-Os metalloprotein pairs are within error, the GndHCl denaturation midpoints ($[\text{GndHCl}]_{1/2} = 2.0 \pm 0.05$ M for the 2*b*-Ru/2*c*-Os and 1.8 ± 0.05 M for the 2*e*-Ru/2*g*-Os) for the two pairs analyzed at the same total peptide concentrations are well outside of error. Chemical denaturation midpoints are often used to compare structurally similar peptide sequences since ΔG_{unfold} values are extrapolated and inherently prone to error.^{31,33} The difference in free energy of unfolding between the 2*b*-Ru/2*c*-Os and 2*e*-Ru/2*g*-Os metalloprotein pairs ($\Delta\Delta G_D$) was calculated to be 0.3 kcal·mol⁻¹ based on the difference between the $[\text{GndHCl}]_{1/2}$ values (see Experimental Section).^{31,33}

Solubility issues prevented full analysis of the parent sequences lacking Ru(II) or Os(II) complexes by GndHCl denaturation. On the basis of the relatively small degree of destabilization within the different metalloprotein pairs, it is expected that the 2*f*-Os/2*f*-Ru pair and the parent sequences would not be measurably different. Qualitative examination of CD spectra for the parent sequences also indicated a similar folding behavior (see Supporting Information). This conclusion

agrees with Ogawa's studies of de novo designed electron transfer metallopeptides, where very little destabilization was measured when large transition metal complexes were attached at *f* positions within the sequence.¹⁵ The ΔG_{unfold} and K_{d} values reported for the three metallopeptide dimers were similar to those reported by Ogawa,¹⁵ and other previously reported values corresponding to four-heptad coiled-coils,^{20c} taking into account that the two asparagine substitutions are expected to be slightly destabilizing.^{19,20b,21}

Subsequent photophysical measurements, including the appropriate control experiments, were conducted at concentrations well above the measured K_{d} values.

Photophysics. Steady-State Spectroscopy. The ground state absorption spectrum for the 2*g*-Os/2*e*-Ru metallopeptide pair exhibits a peak at 450 nm and a lower energy band that is centered at 650 nm (Figure 6). The peak centered at 450 nm is

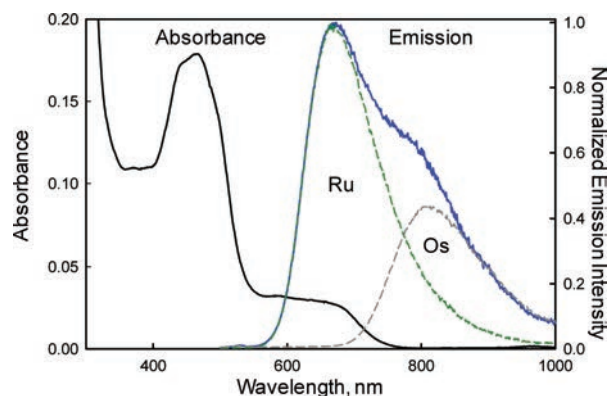


Figure 6. The UV-vis absorption (black: 25 μM 2*e*-Ru and 50 μM 2 *g*-Os) and steady state emission (blue: 25 μM 2*e*-Ru and 50 μM 2 *g*-Os) spectra of the 2*g*-Os/2*e*-Ru peptide coiled-coil in a 10 mM sodium phosphate buffer solution, pH 7, 25 °C. Also shown are the 2*e*-Ru(II) peptide (green dashed: 25 μM 2*e*-Ru) and 2*g*-Os(II) peptide emission spectra (gray dashed: 100 μM 2 *g*-Os). The excitation wavelength was 450 nm.

the singlet metal-to-ligand charge transfer (¹MLCT) for both the Ru(II) and Os(II) bipyridyl complexes, while the lower energy band corresponds to direct excitation of the ³MLCT in the Os(II) complex which is optically accessible because of large spin-orbit coupling. When excited at 450 nm, the steady state emission spectrum for the 2*g*-Os/2*e*-Ru peptide exhibits a higher energy band (λ_{max} at 660 nm) that corresponds to Ru(II) ³MLCT emission after fast intersystem crossing from the ¹MLCT, while the peak centered at 800 nm is Os(II) ³MLCT emission (Figure 6). The steady-state emission spectra show an increase in the Os(II) emission as the chromophores are moved closer to each other, providing direct evidence for Ru(II) to Os(II) energy transfer (see Supporting Information, Figure S3).

Time-Resolved Spectroscopy. Photoexcitation of the Ru(II) center at 450 nm is followed by rapid relaxation into the ³MLCT band, and potentially triplet-triplet energy transfer to the lower energy Os(II) site. In principle, energy transfer can be observed either through the quenching of Ru(II) emission at 660 nm or the appearance of the Os(II) emission at 800 nm. In practice, however, the Os(II) emission due to energy transfer is obscured by Ru(II) emission in the low energy tail and phosphorescence arising from the direct excitation of Os(II) at 450 nm. Both these contributions make a quantitative analysis

of the Os(II) emission difficult. While Ru(II) emission contaminates the emission of Os(II) at 800 nm, the converse is not true, and both the time-resolved and steady-state emission measurements show no detectable Os(II) emission at 660 nm. Thus, Ru(II) emission provides the cleanest window through which to view Ru-to-Os energy transfer.

The P1/2*e*-Ru coiled-coil was used as a control to measure the Ru lifetime in the absence of energy transfer (Figure 7a).

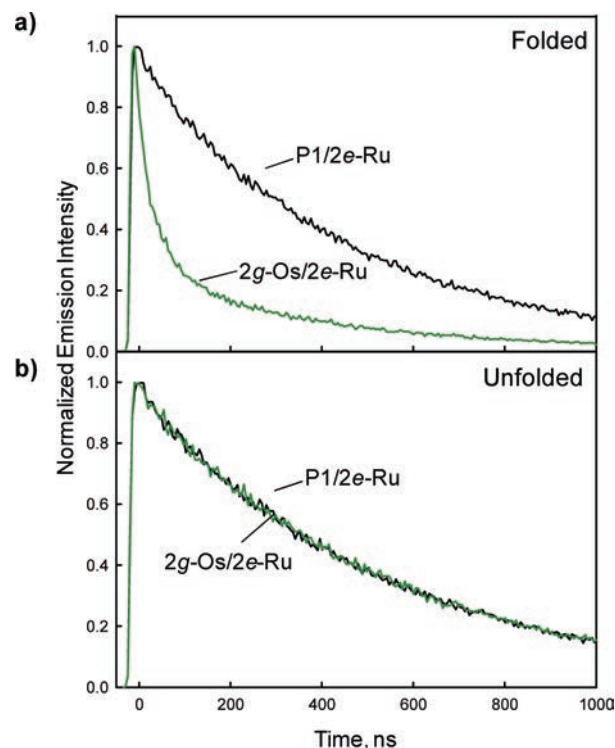


Figure 7. (a) Time-resolved emission of 2*e*-Ru peptide in the presence of the P1 peptide (black: 25 μM 2*e*-Ru and 50 μM P1) and the 2*g*-Os peptide (green: 25 μM 2*e*-Ru and 50 μM 2*g*-Os) in a 10 mM sodium phosphate buffer solution at pH 7 and 25 °C. (b) P1/2*e*-Ru peptide with chemical denaturant (black: 25 μM 2*e*-Ru, 50 μM P1 and 5 M guanidinium chloride, 20 mM sodium phosphate, and 100 mM sodium chloride buffer at pH 7 and 25 °C and 2*g*-Os/2*e*-Ru peptide pair with chemical denaturant (green: 25 μM 2*e*-Ru, 50 μM 2*g*-Os, and 5 M guanidinium chloride, 20 mM sodium phosphate, and 100 mM sodium chloride buffer at pH 7 and 25 °C). Ru(II) emission quenching by energy transfer is turned off in the presence of the chemical denaturant. The time-resolved emission data were collected at 660 nm with an excitation of 444 nm.

The decay is single exponential with a lifetime around 450 ns ($2.2 \times 10^6 \text{ s}^{-1}$), comparable to the lifetime of Ru(bpy)₃²⁺ in water.³⁴ Pairing of 2*e*-Ru with the 2*g*-Os peptide instead of the unmodified P1 results in quenched Ru(II) emission due to energy transfer (Figure 7a). The decay is biexponential with a fast component of 42 ns that is related to energy transfer and a slow component that matches the Ru(II) lifetime of 450 ns. The slow component is attributed to a small fraction of unassociated Ru(II) chains in solution that are present as a result of the ground state equilibrium between the peptide chains.

Influence of Folding on Energy Transfer. A comparison of the energy transfer dynamics in the folded and unfolded state can be achieved through denaturation of the peptide scaffold, which in principle can be accomplished by either heating or

chemical additives. Temperature induced denaturation is more problematic because of the high thermal stability of the coiled-coil peptides. The analysis would be further complicated by the fact that the Ru(II) ³MLCT excited state lifetime is diminished with increasing temperature because of the thermally accessible metal-centered (³dd) excited states that undergo rapid nonradiative decay. Chemical denaturation with GndHCl provides a viable alternative method for studying the denatured state at the same concentration used for time-resolved experiments.

The 660 nm decays for the P1/2*e*-Ru and 2*g*-Os/2*e*-Ru systems in the presence of guanidine denaturant were measured and compared to the nondenatured complex (Figure 7b). The excited state lifetime of the 2*e*-Ru peptide is slightly longer in the highly polar 5 M GndHCl denaturation medium ($\tau = 520$ ns compared to 450 ns in buffer), but is unaffected by the presence of up to 2 equiv (50 mM) of the 2*g*-Os peptide.

The ability of the chemical denaturant to turn off energy transfer confirms that the Ru(II) emission quenching arises from the folded coiled-coil peptide structure and not from nonspecific interactions between the peptide chains.

In addition, an Os(II) “control complex” (4, Figure 8) was designed to mimic the acceptor module, while lacking any

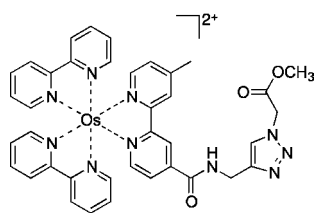


Figure 8. Os(II) complex (4) was used as a diagnostic for intermolecular energy transfer not mediated by the peptide scaffold.

molecular recognition elements that would allow for association with the partner peptide. When the control complex (4) was mixed with the 2*b*-Ru peptide, no change in the excited-state lifetime was observed with up to 2 equiv present. This differs from similar studies of Ru(II) and Os(II) modified oligonucleotides, which show that the addition of a non-covalently attached Os(II) complex ($[\text{Os}(\text{bpy})_2(\text{phen})]^{2+}$) to a Ru(II)-containing oligonucleotide solution results in some quenching (~8%) of the Ru(II) based phosphorescence, even at much lower Os(II) concentrations.^{10c} This observation could be a consequence of the difference in the net charge on the two scaffolds or intercalation.^{10e} The oligonucleotides used in that work are polyanionic molecules, and may have attractive charge–charge interactions with bipyridyl complexes that result in aggregation in solution. The 2*b*-Ru peptide on the other hand contains a net positive (+5) charge at pH 7, resulting in a repulsive charge–charge interactions with the control complex. In addition, weak intercalation of the bpy ligands into the DNA duplex may be responsible for the observed quenching in the DNA system, which is not possible in this peptide scaffold.^{10e}

The results of the two control experiments clearly demonstrate that energy transfer within the peptide system occurs between coiled-coil dimer partners, and requires the folded self-assembled peptide scaffold for structural organization.

Positional Variation and Energy Transfer. We compared the Ru(II) emission quenching for the three coiled-coil metallopeptide pairs: 2*f*-Os/2*f*-Ru, 2*c*-Os/2*b*-Ru, and 2*g*-Os/

2*e*-Ru (Figure 9), along with the transients from three coiled-coils containing the Ru(II) metallopeptides paired to the P1

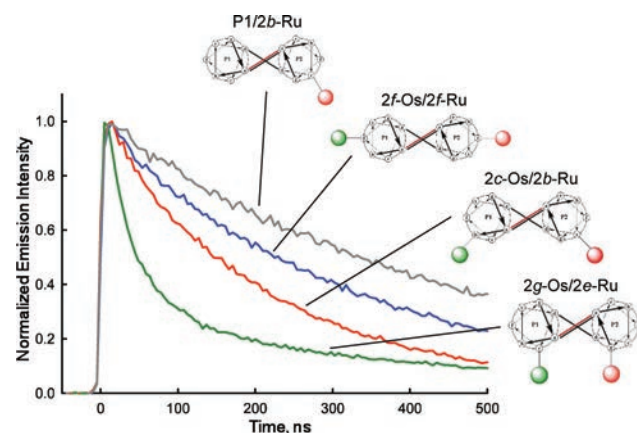


Figure 9. Time-resolved emission transients showing the distance dependence of the energy transfer rate for the 2*f*-Os/2*f*-Ru (blue: 25 μM 2*f*-Ru and 50 μM 2*f*-Os), 2*c*-Os/2*b*-Ru (red: 25 μM 2*b*-Ru and 50 μM 2*c*-Os), and 2*g*-Os/2*e*-Ru (green: 25 μM 2*e*-Ru and 50 μM 2*g*-Os) peptide pairs in 10 mM phosphate buffer solution at pH 7 and 25 °C. The P1/2*e*-Ru peptide (gray: 25 μM 2*e*-Ru and 50 μM P1) is shown for comparison. From the transients it is clear that the energy transfer rate is faster the closer the metal complexes are placed to one another. The time-resolved emission data were collected at 660 nm with an excitation wavelength of 444 nm.

apopeptide. All three of the P1/Ru(II) systems exhibit qualitatively similar monoexponential decay kinetics (Table 3). Each transient in the mixed Ru(II)/Os(II) systems is

Table 3. Results of the Global Analysis Showing the Dependence of the Energy Transfer Rate on the Position^a

	K_{D} , μM^{-1} (K_{D} , μM)	$k_{\text{Ru}} \times 10^6 \text{ s}^{-1}$ (lifetime, ns)	$k_{\text{ET}} \times 10^6 \text{ s}^{-1}$ (lifetime, ns)
2 <i>f</i> -Os/2 <i>f</i> -Ru	0.908 ± 0.005 (1.101 ± 0.006)	2.9 ± 0.002 (478.7 ± 0.5)	1.0 ± 0.02 (816 ± 14)
2 <i>c</i> -Os/2 <i>b</i> -Ru	0.919 ± 0.001 (1.088 ± 0.002)	2.2 ± 0.002 (450.0 ± 0.5)	3.0 ± 0.02 (304 ± 2)
2 <i>g</i> -Os/2 <i>e</i> -Ru	0.887 ± 0.001 (1.127 ± 0.001)	2.1 ± 0.002 (468.2 ± 0.4)	23 ± 0.1 (42.0 ± 0.2)

^aAll peptide samples contained 25 μM Ru peptide and 0 to 50 μM Os peptide in 10 mM sodium phosphate buffer at pH 7 and 25 °C. The error is from the global fitting analysis.

biexponential, where the slow component arises from the free Ru chains in solution and the fast component reflects Ru quenching due to energy transfer. The peptide pair that places the complexes the farthest apart, 2*f*-Os/2*f*-Ru (Figure 9 blue line), has the largest distance between alpha carbons (14.0–14.9 Å), and results in the slowest energy transfer. The 2*g*-Os/2*e*-Ru peptide pair (Figure 9, green line) places the complexes the closest to each other with an α -carbon distance of 9.6–10.3 Å, and has the fastest energy transfer. Lastly, the 2*c*-Os/2*b*-Ru peptide pair has an intermediate spacing (12.7–13.5 Å) and its energy transfer rate falls in the middle (Figure 9, red line). The trend of the quenching rates indicates that the peptide assembly influences the relative positions of the Ru(II) and Os(II) complexes, and thus their ability to undergo energy transfer, in a predictable manner.

Data Analysis. The emission decay was measured in a series of 2*g*-Os/2*e*-Ru samples in which the 2*e*-Ru peptide

concentration is kept constant at 25 μM and the 2*g*-Os peptide concentration is incrementally increased from 0 μM to 50 μM (Figure 10). As the 2*g*-Os peptide concentration is increased

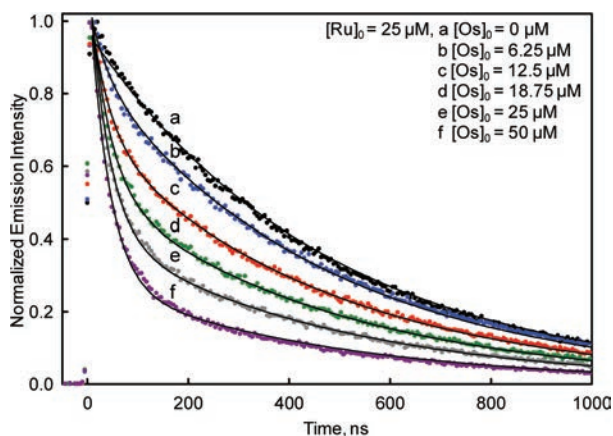


Figure 10. Time-resolved emission for P1/2*e*-Ru peptide (black: 25 μM 2*e*-Ru and 50 μM P1) and 2*g*-Os/2*e*-Ru peptide pair containing various amounts of the 2*g*-Os peptide (blue: 6.25 μM , red: 12.5 μM , green: 18.75 μM , gray: 25 μM , and purple: 50 μM with all containing 25 μM 2*e*-Ru) in a 10 mM phosphate buffer solution at pH 7 and 25 $^{\circ}\text{C}$. The increase in 2*g*-Os peptide concentration drives the equilibrium to heterodimer formation and thus greater Ru(II) emission quenching by energy transfer. The time-resolved emission data were collected at 660 nm with an excitation wavelength of 444 nm.

the slow component decreases in amplitude, consistent with a diminishing amount of free Ru(II). The relative amplitudes of the two kinetic components reflect the fractions of Ru(II)/Os(II) dimer (fast) and free Ru(II) peptide (slow), resulting in an intensity decay that can be expressed as

$$I(t) = \left(\frac{[\text{RuOs}]}{[\text{Ru}]_0} \right) e^{-(k_{\text{Ru}} + k_{\text{EnT}})t} + \left(\frac{[\text{Ru}]_0 - [\text{RuOs}]}{[\text{Ru}]_0} \right) e^{-k_{\text{Ru}}t} \quad (1)$$

where k_{EnT} is the energy transfer rate and k_{Ru} is the rate of Ru(II) excited state decay. The relative amplitudes of the two components are dependent on the concentration of associated heterodimers, $[\text{RuOs}]$, which is determined by the ground state equilibrium:



$$K_a = \frac{[\text{RuOs}]}{[\text{Ru}][\text{Os}]} = \frac{[\text{RuOs}]}{([\text{Ru}]_0 - [\text{RuOs}])([\text{Os}]_0 - [\text{RuOs}])} \quad (3)$$

where $[\text{Ru}]_0$ and $[\text{Os}]_0$ are the total concentrations of the two peptides and K_a is the equilibrium constant.

The solid lines in Figure 10 are the result of a global nonlinear least-squares fit of the series of decays obtained at different Os(II) concentrations to eqs 1–3 with k_{EnT} , k_{Ru} and K_a being adjustable parameters. Table 3 summarizes the fitting results for the three peptide pairs. The 2*g*-Os/2*e*-Ru peptide pair exhibits the fastest energy transfer with $k_{\text{EnT}} = 2.3 \times 10^7 \text{ s}^{-1}$ (42 ns) and the 2*f*-Os/2*f*-Ru peptide pair has the slowest with $k_{\text{EnT}} = 1.0 \times 10^6 \text{ s}^{-1}$ (816 ns), and the 2*c*-Os/2*b*-Ru pair fell in the middle at $3.0 \times 10^6 \text{ s}^{-1}$ (304 ns). The relatively slow energy transfer times in comparison with the lifetime of the Os(II) excited state (16 ns, $6.21 \times 10^7 \text{ s}^{-1}$) prevents a build-up of Os(II) excited state population. Hence a delayed rise in the Os

emission, which has been observed in other systems,^{6c} is not observed here. The long linker between the chromophore and the peptide scaffold will cause the attached chromophores to experience a variety of conformations that interconvert on the time scale of the excited state lifetime. Because energy transfer will be more favorable when the two chromophores are in close proximity, the observed rate will likely also reflect the time scale for structural fluctuations.

All-atom molecular dynamics simulations (discussed below) depict the bipyridyl complexes in the 2*g*-Os/2*e*-Ru and 2*c*-Os/2*b*-Ru systems in direct contact, and therefore the energy transfer occurs through Dexter energy transfer mechanism.³⁵ On the other hand the simulations show the complexes in the 2*f*-Os/2*f*-Ru system remaining at a significant metal–metal separation (3 nm). Therefore the energy transfer mechanism for the 2*f*-Os/2*f*-Ru system is unlikely to be through space Dexter energy transfer. Förster, energy transfer, which occurs through a dipole–dipole mechanism, can occur over larger donor–acceptor separations.³⁵ Although Förster energy transfer is formally forbidden for triplet–triplet energy transfer, the large spin–orbit coupling in these late transition metal complexes, particularly the Os(II), may provide it with some allowed character.³⁵ The presence of Förster energy transfer at longer separations is consistent with observations made in other Ru(II)/Os(II) energy transfer systems.^{6e,10a–c} Regardless of the mechanism, the coiled-coil peptide system is an effective scaffold for controlling the donor/acceptor placement and hence energy transfer rate in molecular assemblies.

All-Atom Molecular Dynamics Simulations. All atom molecular dynamics simulations were performed on each of the three coiled-coils to gain insight into the molecular level interactions in these systems. Since Ru(II) and Os(II), when enveloped by the bipyridyl ligands, are practically identical from a molecular dynamics perspective, Ru(II) was used as the central atom for simulation in both bipyridyl complexes. For the sake of concise comparisons with experiments, we retain the same nomenclature for the metallopeptide pairs. It is important to mention that since a single metal–metal distance can map into a variety of different conformational arrangements between two metal complexes, we present below detailed trajectory analysis, with supplementary movies providing additional structural information (see Supporting Information).

2*f*-Os/2*f*-Ru Heterodimer. Both bipyridyl complexes in the 2*f*-Os/2*f*-Ru system start from a distal position relative to the peptide backbone. During the equilibration phase the complexes were frequently found in the proximity of the coiled-coil peptide backbone, likely driven by favorable hydrophobic interactions. To overcome the bias of the deliberately chosen initial conditions, the first 250 ns of the simulation were not included when calculating the distance distributions. The subsequent data collection phase was run for approximately 500 ns. The dynamics of the bipyridyl complexes and their unnatural side chains can be described by two regimes. First, there are large-scale conformational rearrangements during which the tethered complexes escape from their states bound to the coiled-coil and are free to explore the phase space to find new collapsed conformations. Second, there are small-scale oscillations within these conformations, which occur on a much faster time scale, but do not result in significant displacement of the metal complexes. The attachment points for the bipyridyl complexes in the 2*f*-Os/2*f*-Ru system are far enough away from each other that the two complexes do not come into direct contact during the entire course of the

simulation. The corresponding metal-center displacement distributions and the trajectories from which they were derived are shown in Figure 11. The intermetal distance distribution is

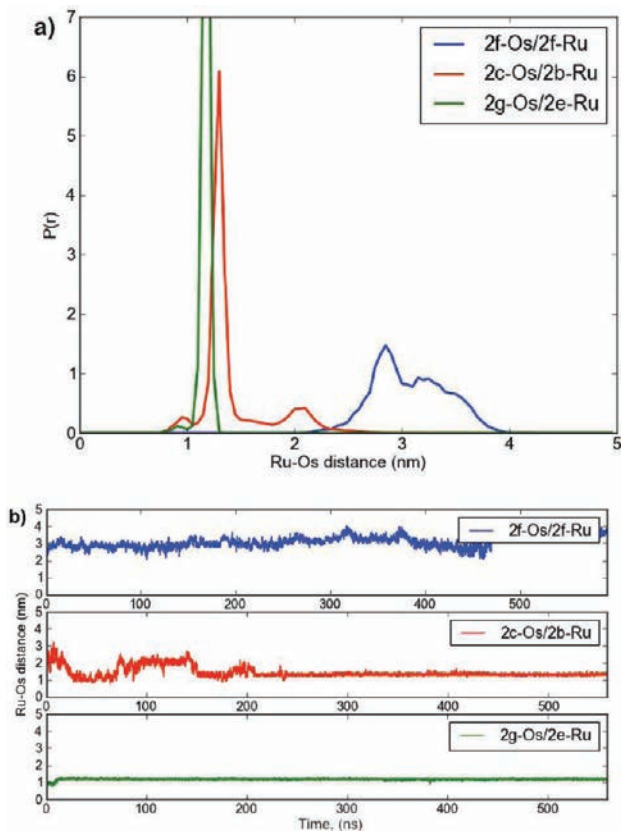


Figure 11. (a) Comparative plot of Ru–Os distance histograms (normalized) for different chromophore placements, including 2f-Os/2f-Ru, 2c-Os/2b-Ru, and 2g-Os/2e-Ru. (b) Ru–Os distance evolution in time for the 2f-Os/2f-Ru, 2c-Os/2b-Ru, and 2g-Os/2e-Ru metalloprotein pairs.

broad (over a 3 nm range) and non-Gaussian. Throughout the course of the simulation, the metal-center displacements observed for the 2f-Os/2f-Ru system are relatively large and would be expected to limit the efficiency of energy transfer. As discussed above, these simulations indicate that the Förster energy transfer mechanism may play an important role for this complex.

Interestingly, the bipyridyl complexes appear to influence the stability of the 2f-Os/2f-Ru coiled-coil structure as illustrated in the Supporting Information, Movie 6. α -Helical peptides have an increased propensity toward fraying near the termini, and when the metal complex and the 2f-Os/2f-Ru peptide terminus approach each other, the complex can entrain the ends of the peptides by providing competing hydrophobic interactions which result in further fraying. This partial folding and unfolding can be observed in the timeline plot of the helicity index α which is equal to the ratio of the number of residues in the α -helical conformation compared to the total number of residues in a sequence (see Figure 12 and Table 4). The implications of this observation are elaborated below.

2c-Os/2b-Ru Heterodimer. After extensive equilibration for approximately 300 ns, the initial conformation for the data collection corresponded to spatially separated bipyridyl complexes with relaxed linkers and a slightly perturbed

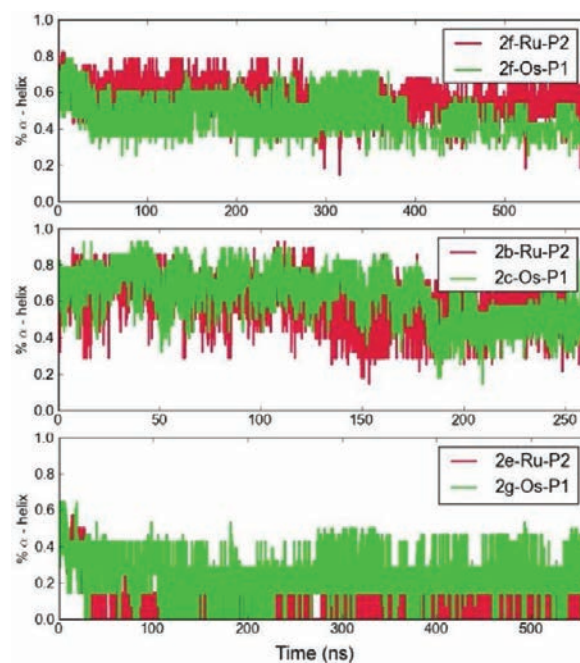


Figure 12. Fraction of α -helical content in each peptide as a function of time shown for the 2f-Os/2f-Ru (top), 2c-Os/2b-Ru (middle), and 2g-Os/2e-Ru (bottom) metalloprotein pairs. Each peptide actively explores its conformational space, while predominantly staying in an α -helical state. The exception is 2g-Os/2e-Ru system (see bottom graph), where an unfolding event is caught during MD. Visualization of the trajectory showed that peptide termini started interacting with the bipyridyl complexes and significantly disrupted the overall coiled-coil ternary and secondary structure.

Table 4. Dependence of the Coiled-Coil Secondary Structure and Metal-Center Displacement on Substitution Position

	helicity index α , X-Os-P1	helicity index α , Y-Ru-P2	Ru–Os average distance
X = 2f, Y = 2f	0.458 ± 0.097	0.559 ± 0.079	3.100 ± 0.336
X = 2c, Y = 2b	0.631 ± 0.139	0.593 ± 0.124	1.444 ± 0.319
X = 2g, Y = 2e	0.249 ± 0.097	0.070 ± 0.116	1.195 ± 0.048

structure for the coiled-coil scaffold. During the first 20 ns of the production run, the bipyridyl complexes do not form any stable close contact, with one complex actively exploring the surface of the peptide scaffold. At ~ 25 ns the two complexes contact each other and form a loose association, in which a single bipyridyl ring aligns with the triazole ring of the complementary peptide linker (see Figure 13c). This was followed by close packing of the metal complexes, and resulted in π - π stacking of bipyridine rings (see Figure 13b). The metal complexes showed relatively fast (~ 0.2 ns) conformational rearrangement of the bipyridine rings between them, often including a non-parallel, $\sim 45^\circ$ metastable π - π stacking (see Supporting Information, Movies 1 and 2).

The comparative graph of distance distributions in Figure 11 shows that 2c-Os/2b-Ru system has three main peaks dominated by the close-packed geometry at less than 1.5 nm. The timeline of Ru–Os distance has a feature of switching from one basin with more closely π - π stacked state(s), in which bipyridine rings align in a mostly parallel fashion (Figure 13b), to another, where the complexes are in close proximity to one

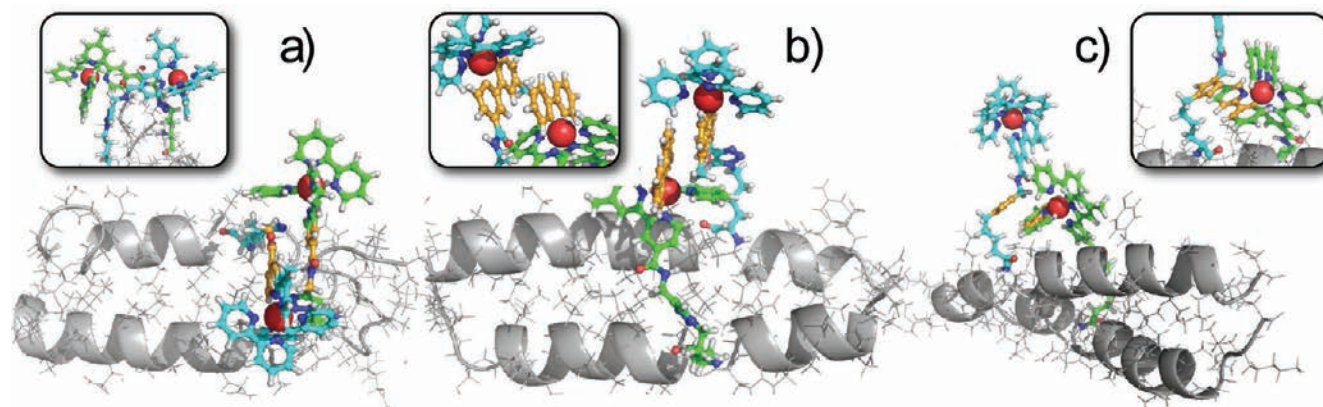


Figure 13. (a) Bipyridyl ligands arranged in a “neck” conformation, facing away from each other (1.2 nm feature). This conformation was only observed in the 2*g*-Os/2*e*-Ru system. (b) π – π stacking arrangement where bipyridyl rings of two complexes are in van der Waals contact and parallel to each other (\sim 1 nm feature). In our simulations π – π stacking was often shifted and was not stable for longer than \sim 10 ps. This tightly stacked conformation is observed consistently in 2*c*-Os/2*b*-Ru system and briefly in 2*g*-Os/2*e*-Ru system. (c) “Loose” packing arrangement of the bipyridyl complexes (\sim 2 nm feature) is a stable basin of conformations with characteristic π – π stacking of one of bipyridine rings of one chromophore and the triazole ring on the linker of the other. This stacking is stable in 2*c*-Os/2*b*-Ru system and transitory to closer intercomplex packing conformations in 2*g*-Os/2*e*-Ru system.

another, yet not in direct contact. These conformations correspond to the 2*c*-Os bipyridine ring π – π stacking with the triazole ring of 2*b*-Ru linker, as shown in Figure 13c. However the contribution from loose packing conformations is statistically larger, as can be illustrated by comparing the heights of the first peak at $<$ 1 nm (π – π stacking, see Figure 13b) and the second peak at approximately 1.2 nm (loose packing, see Figure 13c) in the Figure 11a.

In this system, we did not observe a similar perturbation of the peptide scaffold by the bipyridyl complexes as was seen in the 2*f*-Os/2*f*-Ru system. The peptide termini dynamically unfold and refold during the course of simulations (see Supporting Information, Movies 2 and 3), but not because of association with the bipyridyl complexes in this case. The helicity index of the 2*c*-Os-P1 and 2*b*-Ru-P2 peptides is shown in Figure 12. Interestingly, the standard deviation of the helicity index is approximately 2-fold higher for the 2*c*-Os/2*b*-Ru system, indicating that peptides are more dynamic and actively explore their phase space (see Table 4).

2*g*-Os/2*e*-Ru Heterodimer. In a manner very similar to the two previous systems, the bipyridyl complexes in the 2*g*-Os/2*e*-Ru system quickly collapsed onto the coiled-coil peptide scaffold during the equilibration phase \sim 250 ns. The two metal complexes came into van der Waals contact with each other in a conformation very similar to the intermediate chromophore packing arrangement that was observed in the 2*c*-Os/2*b*-Ru system (Figure 13c). For 30 ns the bipyridyl complexes fluctuate between the π – π stacking (see Figure 13b) and looser ligand arrangements, as shown in Figure 11b. Finally, we observe one more major conformational rearrangement where a tight “neck” stacking is achieved, which is characterized by the bipyridyl ring and a part of the connected linker of one complex aligning with the corresponding structural parts of the other. As a result, the complexes are facing away from each other (see Figure 13a and Supporting Information, Movie 4). This conformation, which was not observed in the 2*c*-Os/2*b*-Ru system, persists until the end of the simulation. As shown in Figure 13a and Supporting Information, Movie 5, the bipyridyl complexes in the 2*g*-Os/2*e*-Ru system also maintain a close proximity with the bipyridyl ligands spending most of their time in van der Waals contact.

This “neck” stacking creates a significant amount of strain for the peptide scaffold, as well as an additional hydrophobic surface consisting of the linker side chains pulled together. We show in Figure 13a and Supporting Information, Movie 5 that the peptide termini closest to the bipyridyl complex detach from the coiled-coil interface and bind to the groove between linkers or wrap around the bipyridyl complexes themselves, leading to more disruption of the coiled-coil structure, compared with the other two systems (see Figure 13). The analyses of the simulation data for all three systems suggest that the various placements of the complexes results in dissimilar complex-peptide interactions, where the latter influence the corresponding coiled-coil stabilities (see Table 4). Furthermore, although the trends predicted from the MD simulations are qualitatively consistent with the corresponding thermodynamic measurements, the quantitative extents of the coiled-coil disruption seen in simulations are likely overestimated. The following possibilities could have contributed to producing extra fraying in our MD simulations: (1) overestimating the metal-complex-peptide interactions, (2) underestimating the strength of the interpeptide bonding, or (3) preparing the initial coiled-coil conformations in an imperfect way, which did not allow tight enough packing of side-chains or accurate enough alignment of hydrophobic interactions (see the Experimental Section).

In summary, comparison of the dynamics for all three metalloprotein systems shows that the 2*g*-Os/2*e*-Ru pair has the narrowest Ru(II) to Os(II) distance distribution with the smallest probable separation (\sim 1 nm), and would therefore be the best promoter for energy transfer. A metal–metal distance of 1 nm suggests that the complexes are in close contact with each other and would imply efficient energy transfer, regardless of which mechanism is considered. This is in agreement with the photophysical measurements made on the metalloprotein systems, which also indicated the 2*g*-Os/2*e*-Ru pair to be the most efficient energy transfer promoter, as discussed above. Importantly, we have not observed unfolding of the coiled-coil near the linker attachment points for any of the three systems. This suggests that the dynamics of the bipyridyl complexes themselves do not impose a significant stress along the peptide backbone in our scaffold design. To gain deeper insights into

the mechanisms of energy transfer in these systems, subsequent quantum mechanical calculations can be carried out on selected structural snapshots of stable stacking conformations observed in the MD simulations. This, in turn, may help to improve the design of peptide scaffolds, allowing for more precise control over molecular components.

III. CONCLUSIONS

The ability to control the positioning and organization of molecular components is central to the design of functional molecular-based materials.³ However, architectures that rely solely on covalent bonding for structure (e.g., polymers, dendrimers) have limited control over the assembly geometry and higher-order spatial control. Using peptides as scaffolds, we have designed an artificial self-assembling system that utilizes weak forces to control the relative placement of Ru(II) and Os(II) complexes. The assemblies incorporate an α -helical coiled-coil peptide scaffold consisting of α -helical heterodimers in which each coil is functionalized with either a Ru(II)-containing energy donor or with an Os(II)-containing energy acceptor. This architecture differs from many other types of molecular assemblies in that it uses both intra- and intermolecular noncovalent interactions to adopt well-defined secondary and tertiary structures that control the placement of the energy transfer complexes. Moreover, the use of “click” chemistry allows for straightforward and well-defined control of the placement of the covalently linked chromophores.

Circular dichroism spectroscopy in conjunction with time-resolved emission spectroscopy confirms the importance of the heterodimeric α -helical coiled-coil structure for modulating energy transfer. Ru(II) to Os(II) energy transfer is only observed in the folded structures, and energy transfer rates measured across a series of supramolecular structures are consistent with a systematic variation of the metal complex separation. Chemical agents that denature the peptide scaffold also serve as an on-off switch, and completely disable energy transfer. Molecular dynamics simulations show Ru(II)–Os(II) distance distributions that are consistent with the order of the experimentally measured energy transfer rates. In addition, the simulations suggest that the assemblies maintain their α -helical character, but are dynamic in nature, with stable cores but multiple conformations interchanging on the nanosecond time scale. These studies demonstrate the sequence-structure-function paradigm found in natural proteins in a robust artificial self-assembling system and clearly establishes the essential role the supramolecular scaffold plays in controlling function. This system provides a promising new scaffold for functional materials that couples straightforward synthesis with fine control of three-dimensional structure that directly dictates function.

IV. EXPERIMENTAL SECTION

General Methods. Solvents were purchased from Fisher Scientific and were used as received unless noted otherwise. *cis*-Dichlorobis(2,2'-bipyridine)ruthenium(II) dihydrate was purchased from Strem Chemicals. All α -N-Fmoc-amino acids, including α -N-Fmoc-lysine, were purchased from Novabiochem. Tetrakis(acetonitrile)copper(I) hexafluorophosphate, 2,2'-bipyridine, 4,4'-dimethyl-2,2'-bipyridine, and tripropylamine were purchased from Aldrich. The compounds 4'-methyl-2,2'-bipyridine-4-carboxaldehyde, 4'-methyl-2,2'-bipyridine-4-carboxylic acid, and succinimidyl-4-carboxy-4'-methyl-2,2'-bipyridine were synthesized according to reported procedures.³⁶ *cis*-Dichlorobis(2,2'-bipyridine)osmium(II) was synthesized using the procedure reported by Meyer.³⁷ Deuterated solvents were purchased from

Cambridge Isotope Laboratories. ¹H and ¹³C NMR spectra were recorded at 400 and 100 MHz, respectively, on Bruker spectrometers. Chemical shifts were given in ppm relative to solvent peaks corresponding to residual protons for the deuterated solvents. These values were taken as δ 7.27, 1.93, and 5.32 for CDCl₃, CD₃CN, and CD₂Cl₂, respectively. Coupling constants are given in hertz. The details for peptide synthesis and purification are provided below. High-resolution and low-resolution mass spectra were obtained using a Bruker Biotof instrument. Milli-Q water was used for the preparation of all buffers and solutions.

Peptide Synthesis. Peptides were synthesized by standard automated SPPS using a Thuramed tetras synthesizer. Fmoc-protected amino acids were used along with a CLEAR-Amide resin from Peptides International, Inc. Amino acid residues were activated with HBTU, HOBt, and DIPEA in DMF. Amino acids were deprotected twice with 2% DBU and 2% piperidine in DMF for 15 min each step. Commercially available amino acids were coupled using double coupling cycles of 30–60 min each. The N-terminus of each peptide was acetylated using 5% acetic anhydride and 6% lutidine in DMF for 30 min. Cleavage of the peptides from the resin was performed in 95.0% TFA, 2.5% water, and 2.5% TIPS. TFA was evaporated with a stream of nitrogen and diethyl ether was added to precipitate the cleavage products. The peptides were extracted with water or collected as solids by centrifugation and lyophilized to dryness. Peptides were purified by RP-HPLC using an Atlantis Prep OBD dC-18 semi-preparative column, with a gradient of 0–100% solvent B over 40 min, where solvent A was 95:5 water/ACN, 0.1% TFA, and solvent B was 95:5 ACN/water, 0.1% TFA. Purified samples were lyophilized and the peptide sequence was confirmed by ESI-MS. M was calculated as 3212.73 (exact) for the **P1** parent sequence (C₁₄₂H₂₃₇N₃₇O₄₇). MS *m/z* observed: 1608.4 ([M + 2H]²⁺), 1072.6 ([M + 3H]³⁺), 804.7 ([M + 4H]⁴⁺); M was calculated as 3363.95 (exact) for the **P2** parent sequence (C₁₄₉H₂₅₈N₄₆O₄₂). MS *m/z* observed: 1123.0 ([M + 3H]³⁺), 842.5 ([M + 4H]⁴⁺), 674.0 ([M + 5H]⁵⁺).

Azidopeptide Synthesis. Peptides containing azidolysine residues at desired positions were synthesized using an automated synthesizer as described above. α -Fmoc- ϵ -azido-L-lysine **2** was synthesized by the reported procedure.^{18f,27} α -Fmoc- ϵ -azido-L-lysine **2** was injected manually, and a single 3 h coupling reaction was performed. The azidopeptides were cleaved from the resin, and purified in a fashion identical to the parent sequences. Azidopeptide identities were confirmed by ESI-MS. M was calculated as 3238.76 (exact) for **2f-N₃-P1** (C₁₄₃H₂₃₉N₃₉O₄₆). MS *m/z* observed: 1620.9 ([M + 2H]²⁺), 1081.0 ([M + 3H]³⁺), 811.0 ([M + 4H]⁴⁺); M was calculated as 3295.78 (exact) for **2c-N₃-P1** (C₁₄₅H₂₄₂N₄₀O₄₇). MS *m/z* observed: 1649.3 ([M + 2H]²⁺), 1099.9 ([M + 3H]³⁺), 825.2 ([M + 4H]⁴⁺); M was calculated as 3237.77 (exact) for **2g-N₃-P1** (C₁₄₃H₂₄₀N₄₀O₄₅). MS *m/z* observed: 1620.3 ([M + 2H]²⁺), 1080.6 ([M + 3H]³⁺), 810.7 ([M + 4H]⁴⁺); M was calculated as 3389.97 (exact) for **2f-N₃-P2** (C₁₅₀H₂₆₀N₄₈O₄₁). MS *m/z* observed: 1131.0 ([M + 3H]³⁺), 848.5 ([M + 4H]⁴⁺), 679.1 ([M + 5H]⁵⁺); M was calculated as 3447.00 (exact) for **2b-N₃-P2** (C₁₅₂H₂₆₃N₄₉O₄₂). MS *m/z* observed: 1150.3 ([M + 3H]³⁺), 863.0 ([M + 4H]⁴⁺), 690.6 ([M + 5H]⁵⁺); M was calculated as 3389.94 (exact) for **2e-N₃-P2** (C₁₄₉H₂₅₆N₄₈O₄₂). MS *m/z* observed: 1131.0 ([M + 3H]³⁺), 848.5 ([M + 4H]⁴⁺), 679.0 ([M + 5H]⁵⁺).

Metallopeptide Synthesis. In a typical procedure 8–15 mg (~2–4 μ mol) of azidopeptide would be partially dissolved in 1–3 mL of 50% (v/v) DMF in 10 mM sodium phosphate buffer, pH 8.5, that was deoxygenated with N₂ for 30 min. The azidopeptide was reacted with (2 equiv) of either the Ru(II) complex **1a** or the Os(II) complex **1b** in the presence of tetrakis(acetonitrile)copper(I) hexafluorophosphate (2 equiv), and tris-(triazolylmethyl)amine ligand (3, 1 equiv). The mixtures were allowed to stir overnight for 12–48 h, and then diluted with water (10 mL). The aqueous solutions were frozen and lyophilized. The fully lyophilized residue was dissolved in 0.1 M aqueous TFA and passed through a Pierce polyacrylamide desalting column. The conjugates traveled through the size-exclusion media more quickly than **1a** or **1b**, and provided the final metallopeptides after purification by reversed-phase HPLC using the conditions listed

above. Metallopeptide identities were confirmed by ESI-MS. M^{2+} was calculated as 3993.96 (exact) for **2f-Os-P1** ($C_{178}H_{268}N_{46}O_{47}Os$). MS m/z observed: 1997.0 ($[M^{2+}]^{2+}$), 1331.8 ($[M^{2+} + H^+]^{3+}$), 999.0 ($[M^{2+} + 2H^+]^{4+}$), 799.4 ($[M^{2+} + 3H^+]^{5+}$), 666.4 ($[M^{2+} + 4H^+]^{6+}$); M^{2+} was calculated as 4050.98 (exact) for **2c-Os-P1** ($C_{180}H_{271}N_{47}O_{48}Os$). MS m/z observed: 2025.8 ($[M^{2+}]^{2+}$), 1350.7 ($[M^{2+} + H^+]^{3+}$), 1013.2 ($[M^{2+} + 2H^+]^{4+}$), 810.8 ($[M^{2+} + 3H^+]^{5+}$), 679.5 ($[M^{2+} + 4H^+]^{6+}$); M^{2+} was calculated as 3992.98 (exact) for **2g-Os-P1** ($C_{178}H_{269}N_{47}O_{46}Os$). MS m/z observed: 1996.5 ($[M^{2+}]^{2+}$), 1131.3 ($[M^{2+} + H^+]^{3+}$), 998.7 ($[M^{2+} + 2H^+]^{4+}$), 799.2 ($[M^{2+} + 3H^+]^{5+}$), 666.2 ($[M^{2+} + 4H^+]^{6+}$); M^{2+} was calculated as 4055.12 (exact) for **2f-Ru-P2** ($C_{185}H_{289}N_{55}O_{42}Ru$). MS m/z observed: 1352.0 ($[M^{2+} + H^+]^{3+}$), 1014.1 ($[M^{2+} + 2H^+]^{4+}$), 811.6 ($[M^{2+} + 3H^+]^{5+}$), 676.5 ($[M^{2+} + 4H^+]^{6+}$), 580.0 ($[M^{2+} + 5H^+]^{7+}$); M^{2+} was calculated as 4112.14 (exact) for **2b-Ru-P2** ($C_{187}H_{292}N_{56}O_{43}Ru$); MS m/z observed: 1371.7 ($[M^{2+} + H^+]^{3+}$), 1029.0 ($[M^{2+} + 2H^+]^{4+}$), 823.6 ($[M^{2+} + 3H^+]^{5+}$); M^{2+} was calculated as 4055.09 (exact) for **2e-Ru-P2** ($C_{184}H_{285}N_{55}O_{43}Ru$). MS m/z observed: 1352.6 ($[M^{2+} + H^+]^{3+}$), 1014.5 ($[M^{2+} + 2H^+]^{4+}$).

Compound 1a. The propargyl amide derivatized Ru(II) complex was prepared according to the procedure reported by Khan and Grinstaff.^{25a}

Compound 1b. The propargyl amide derivatized Os(II) complex was prepared according to the procedure reported by Khan and Grinstaff.^{25a} A small round-bottom, equipped with a condenser, was charged with *cis*-dichlorobis(2,2'-bipyridine)osmium(II) (39.7 mg, 0.069 mmol), and 4'-methyl-2,2'-bipyridine-4-propargylamide (19.1 mg, 0.076 mmol, 1.1 equiv). The reagents were heated at reflux in 50% aqueous EtOH for 24 h, and then concentrated under vacuum. The residue was suspended in H₂O (100 mL), and filtered to remove unreacted *cis*-dichlorobis(2,2'-bipyridine)osmium(II). The aqueous filtrate was washed with DCM (2 × 100 mL). A portion of saturated NH₄PF₆ was added to the aqueous solution and a green precipitate formed. The precipitate was extracted into EtOAc and then concentrated to a solid under vacuum. The solid was partially dissolved in DCM, filtered, and then concentrated to provide the product as a dark green solid (18.4 mg, 26%). ¹H NMR (400 MHz, CD₂Cl₂): δ 8.80 (d, *J* = 1.2 Hz, 1H), δ 8.48 (s, 1H), δ 8.43–8.40 (m, 4H), δ 7.90–7.84 (m, 4H), δ 7.78 (t, *J* = 5.6 Hz, 1H), δ 7.70–7.65 (m, 4H), δ 7.63–7.59 (m, 4H), δ 7.41–7.34 (m, 4H), δ 7.44–7.41 (m, 4H), δ 7.21 (dd, *J* = 5.8, 1.0 Hz, 1H), δ 4.20 (dd, *J* = 5.6, 2.4 Hz, 2H), δ 2.69 (s, 3H), δ 2.28 (t, *J* = 2.4 Hz, 1H); UV–vis (CH₃CN) λ_{max} (ε): 247 (22,000), 291 (50,000), 485 (10,000), 593 (3,000); High-resolution ESI-MS: m/z calculated for C₃₃H₂₉N₇O₆ (M^{2+}), 337.6024; found 337.5952.

Compound 3. The *tris*-(triazolylmethyl)amine ligand was prepared according to the procedure reported by Chan and Fokin.^{28a,c} A solution of tripropargylamine (233.0 mg, 1.777 mmol), methyl azidoacetate (805.4 mg, 6.998 mmol, 3.94 equiv), and tetrakis-(acetonitrile)copper(I) hexafluorophosphate (21.9 mg, 58.8 μmol), and DIPEA (1 mL, 5.741 mmol, ~3 equiv to alkyne) in ACN (4 mL) was stirred under N₂ for 24 h. The reaction warmed considerably when DIPEA was added and was cooled in an ice bath. The reaction was concentrated in vacuo, and the residue was suspended in saturated aqueous NaHCO₃ (50 mL), extracted with CH₂Cl₂ (3 × 50 mL), dried over anhydrous Na₂SO₄, filtered, and concentrated. The product (**3**) was obtained as an off white solid after chromatography on silica gel using 5% (v/v) MeOH in CH₂Cl₂. Yield, 701 mg (83%). ¹H NMR (400 MHz, CDCl₃): δ 7.84 (s, 1H), δ 5.18 (s, 2H), δ 3.79 (s, 2H), δ 3.78 (s, 3H); ¹³C NMR (100 MHz, CDCl₃) δ 166.8, 144.6, 125.2, 52.9, 50.7, 47.4. High-resolution ESI-MS: m/z calculated for C₁₈H₂₄N₁₀O₆ ($M + Cs^+$), 609.0935; found 609.0920.

Compound 4. A solution of **1b** (6.95 mgs, 8 μmol), methyl azidoacetate (1.42 mg, 10 μmol, 1.7 equiv), and DIPEA (3 μL) in ACN (1.5 mL) was stirred in a round-bottom and cooled in an ice bath before tetrakis (acetonitrile)copper(I) hexafluorophosphate (0.56 mgs, 1.5 μmol, 20 mol %) was added. The solution was allowed to warm to room temperature slowly and stirred for 2 days under an inert atmosphere. The Os(II) complex was purified by RP-HPLC using methods identical to those described below for the metallopeptides.

ESI-MS: m/z calculated for C₃₈H₃₄N₁₀O₃Os (M^{2+}), 435.12; found 435.1.

Circular Dichroism. CD spectra were recorded on a chirascan circular dichroism spectrometer. CD spectra were recorded from 185 to 260 nm using 10 mM sodium phosphate buffer, pH 7. CD spectra taken for guanidinium denaturation experiments were taken from 200 to 260 nm. All spectra were recorded at 25 °C with an optical path length of 0.1 cm. The results are expressed as the mean molar residue ellipticity [θ] with the units of degrees-cm²-dmol⁻¹ and calculated as shown in eq 4:

$$[\theta] = \theta_{\text{obs}} / (10 \times l \times c \times n) \quad (4)$$

where θ_{obs} is the observed ellipticity in millidegrees, l is the optical path length in cm, c is the molar concentration of the peptide, and n is the number of residues for the peptide.

Guanidinium Chloride Denaturations. The GndHCl denaturation experiments were conducted by monitoring the ellipticity at 222 nm as a function of GndHCl concentration. Samples were prepared from stock peptide solutions, buffer (10 mM sodium phosphate, 100 mM sodium chloride, pH 7), and a solution of 8 M GndHCl in same buffer.

GndHCl denaturation curves were analyzed using a two-state folding/unfolding model. The fraction folded (F_F) was calculated using eq 5:

$$F_F = ([\theta] - [\theta]_D) / ([\theta]_F - [\theta]_D) \quad (5)$$

where $[\theta]$ is the observed molar ellipticity (eq 4), $[\theta]_F$ is the molar ellipticity of the fully folded state, and $[\theta]_D$ is the molar ellipticity of the denatured state. The fraction unfolded (F_U) was calculated using eq 6:

$$F_U = 1 - F_F \quad (6)$$

The free energy of unfolding was calculated using eq 7:

$$\Delta G = -RT \ln(2P_T F_U^2 / F_F) \quad (7)$$

where R is the molar gas constant, T is the temperature in Kelvin, and P_T is the total peptide concentration. The free energy of unfolding was then calculated via the method of linear extrapolation using eq 8:^{20c,31}

$$\Delta G = \Delta G_{\text{unfold}} - m[\text{GndHCl}] \quad (8)$$

where the points used for extrapolation were taken through the midpoint in the most linear portion of the denaturation curves. Dissociation constants (K_d) for all three metallopeptide pairs were determined using the ΔG_{unfold} values and eq 9:

$$K_d = \exp(\Delta G_{\text{unfold}} / RT) \times 10^6 \quad (9)$$

The difference in free energy of unfolding between the 2c-Os/2b-Ru and 2g-Os/2e-Ru metallopeptide pairs ($\Delta\Delta G_D$) was calculated based on the difference between their $[\text{GndHCl}]_{1/2}$ values using eq 10:⁸

$$\Delta\Delta G_D = ([\text{GndHCl}]_{1/2}^A - [\text{GndHCl}]_{1/2}^B)(m_A + m_B)(0.5) \quad (10)$$

where $[\text{GndHCl}]_{1/2}^A$ and $[\text{GndHCl}]_{1/2}^B$ are the GndHCl denaturation midpoints for two metallopeptide pairs, and m_A and m_B are the slope values from eq 8 applied to the Os/2b-Ru and 2g-Os/2e-Ru metallopeptide pairs, respectively.

Time-Resolved Emission. Ground state absorbance measurements were conducted with a Hewlett-Packard 8453 UV–vis–NIR absorption spectrophotometer. Steady state emission (SSE) data were collected using an Edinburgh Instruments FLS920 equipped with a 450 W xenon lamp and photomultiplier tube (Hamamatsu 2658P). SSE data were collected using a bandwidth no larger than 4.0 nm and, once collected, were corrected for the emission spectrophotometer's spectral response. The FLS920 was also used for time-resolved measurements by the time-correlated single photon counting (TCSPC) technique with an instrument response of <100 ps, using a 444.2 nm diode laser (Edinburgh Instruments EPL-445, 73 ps fwhm

pulsethickness) operated at 200 kHz. A 495 nm long pass color filter was used for emission experiments.

The samples were placed in a 2.0 mm cuvette and placed at 45 degree angle from the incident laser beam. Samples were purged in Argon for >25 min just prior to emission experiments. All experiments were performed with $Abs_{444\text{ nm}} < 0.2$ OD. The solvent for each sample was 10 μM phosphate buffer at pH 7.

Molecular Dynamic Modeling. Since no crystal structure was available for the system, the initial structure was generated using PyMOL,³⁸ which is a molecular visualization tool capable of constructing simple peptides. The P1 and P2 peptides were initially generated independently using PyMOL's helical parameters and were then manually aligned with care taken to avoid steric clashes and satisfy the hydrophobic interface. The ϵ -triazolo-L-lysine linker segment was constructed using Gaussview, part of the Gaussian 03 suite.³⁹ Ruthenium(II) and osmium(II) are very similar from an MD perspective. Since the primary focus of these simulations is peptide dynamics, ruthenium was used as the central atom in both complexes and osmium was not explicitly included. This is not expected to have any significant impact on the simulations, since the metal atoms are nearly completely shielded from the rest of the system by the bipyridyl ligands, and metal's formal charge, which is the same for Ru(II) and Os(II), plays the most important role. To examine the effect of linker positioning on the complexes, the following three systems were created: System 1, which corresponds to the 2f-Os/2f-Ru metallopeptide pair, System 2 which corresponds to the 2c-Os/2b-Ru metallopeptide pair, and System 3 which corresponds to the 2g-Os/2e-Ru metallopeptide pair.

The simulations were prepared using the AMBER⁴⁰ force field with the ff99SB⁴¹ parameter set. Since the AMBER libraries do not possess parameters for the artificial amino acids used as tethers, or for the chromophores themselves, these values needed to be collected from literature or obtained through quantum calculations. Partial charges for the linker and chromophores were obtained from Gaussian calculations using restricted B3LYP⁴² with the LANL2DZ⁴³ basis set. Charges derived using the restricted electrostatic potential (RESP) technique⁴⁴ gave spurious results for ruthenium and the chelating nitrogen atoms in the bipyridyl ligands. RESP has difficulty predicting the correct charge for buried atoms since the charges are assigned in an effort to reproduce the external electrostatic potential.⁴⁴ Because of this, Mulliken charges were used in lieu of RESP charges. In general, Mulliken charges tend to be slightly more exaggerated than RESP charges with an average difference in predicted charge of $0.1(\pm 0.1)e$ for all atoms excluding the ruthenium and those atoms immediately surrounding it. There was insufficient memory to compute partial charges for the entire linker and complex. To deal with this issue, the partial charges for the base of the peptide up to the γ -carbon of the side chain were extracted from the standard lysine amino acid residue. Force constants for Ru–N stretches, N–Ru–N (*cis/trans*) bends, C–C–N–Ru dihedrals, H–C–N–Ru dihedrals and van der Waals parameters were obtained from Brandt et al.⁴⁵ Since AMBER does not explicitly support Octahedral geometry, chelating nitrogen atoms were divided into three distinctly named but chemically identical types to establish different bending force constants for *cis* and *trans* positions. Each of the three simulations were performed with ~ 13000 explicit TIP3P water molecules in a box with the dimensions $\sim 75 \times 75 \times 75$ Å under periodic boundary conditions. The charge of each system was neutralized by the addition of sodium counterions, followed by the subsequent introduction of an additional 10 mM NaCl. Each system was held at constant volume, and the peptides were frozen in place while the water and ions were minimized for 200,000 steps. Subsequently, all constraints were removed from the systems, and they were minimized for an additional 200,000 steps. The systems were gradually heated via Langevin temperature control to 300 K in incremental steps of 5 K every 50 ps. The production runs proceeded under the constant pressure, moderated by Langevin piston (set to 1 atm), with 2 fs time steps using the SHAKE algorithm and Ewald summation for long-range interactions. Short-range nonbonded interactions were calculated at each step, long-range interactions were only calculated on even steps, and the pair list was updated every

10 steps. System coordinates were saved every 2000 steps (4 ps) for analysis for a total simulation length of 300 ns for each system.

■ ASSOCIATED CONTENT

■ Supporting Information

Figures containing the continuous variation experiments, additional circular dichroism spectra, denaturation of parent sequence, additional time-resolved emission transients, NMR spectra, and the complete ref 39 and 40. This material is available free of charge via the Internet at <http://pubs.acs.org>.

■ AUTHOR INFORMATION

Corresponding Author

*E-mail: mlwaters@email.unc.edu (M.L.W.), john_papanikolas@unc.edu (J.M.P.), gpaioian@umd.edu (G.A.P.).

Notes

The authors declare no competing financial interest.

■ ACKNOWLEDGMENTS

This material is based upon work wholly supported as part of the UNC EFRC: Center for Solar Fuels, an Energy Frontier Research Center funded by the U.S. Department of Energy, Office of Science, Office of Basic Energy Sciences under Award Number DE-SC0001011. Some of the instrumentation used in this project was housed in the UNC SERC "Solar Energy Research Center Instrumentation Facility" funded by the U.S. Department of Energy—Office of Energy Efficiency & Renewable Energy under Award Number DE-EE0003188.

■ REFERENCES

- (1) (a) Astruc, D.; Boisselier, E.; Ornelas, C. *Chem. Rev.* **2010**, *110*, 1857–1959. (b) Drain, C. M.; Varotto, A.; Radivojevic, I. *Chem. Rev.* **2009**, *109*, 1630–1658. (c) Szacilowski, K. *Chem. Rev.* **2008**, *108*, 3481–3548. (d) Hoebein, F. J. M.; Jonkheijm, P.; Meijer, E. W.; Schenning, A. *Chem. Rev.* **2005**, *105*, 1491–1546.
- (2) (a) Lakowicz, J. R. *Principles of Fluorescence Spectroscopy*, 3rd ed.; Springer: New York, 2006. (b) McDonagh, C.; Burke, C. S.; MacCraith, B. D. *Chem. Rev.* **2008**, *108*, 400–422.
- (3) (a) Meyer, T. J. *Acc. Chem. Res.* **1989**, *22*, 163–170. (b) Alstrum-Acevedo, J. H.; Brennaman, M. K.; Meyer, T. J. *Inorg. Chem.* **2005**, *44*, 6802–6827. (c) Gust, D.; Moore, T. A.; Moore, A. L. *Acc. Chem. Res.* **2009**, *42*, 1890–1898. (d) Gust, D.; Moore, T. A. *Science* **1989**, *244*, 35–41.
- (4) (a) Du, P. W.; Schneider, J.; Luo, G. G.; Brennessel, W. W.; Eisenberg, R. *Inorg. Chem.* **2009**, *48*, 4952–4962. (b) Youngblood, W. J.; Lee, S. H. A.; Maeda, K.; Mallouk, T. E. *Acc. Chem. Res.* **2009**, *42*, 1966–1973. (c) Bonchio, M.; Carofiglio, T.; Carraro, M.; Fornasier, R.; Tonellato, U. *Org. Lett.* **2002**, *4*, 4635–4637.
- (5) (a) Hsiao, J. S.; Krueger, B. P.; Wagner, R. W.; Johnson, T. E.; Delaney, J. K.; Mauzerall, D. C.; Fleming, G. R.; Lindsey, J. S.; Bocian, D. F.; Donohoe, R. J. *J. Am. Chem. Soc.* **1996**, *118*, 11181–11193. (b) Wagner, R. W.; Lindsey, J. S. *J. Am. Chem. Soc.* **1994**, *116*, 9759–9760. (c) Song, H.; Taniguchi, M.; Speckbacher, M.; Yu, L.; Bocian, D. F.; Lindsey, J. S.; Holten, D. *J. Phys. Chem. B* **2009**, *113*, 8011–8019. (d) Bellows, D.; Goudreau, T.; Aly, S. M.; Fortin, D.; Gros, C. P.; Barbe, J.-M.; Harvey, P. D. *Organometallics* **2010**, *29*, 317–325.
- (6) (a) Jones, W. E.; Baxter, S. M.; Strouse, G. F.; Meyer, T. J. *J. Am. Chem. Soc.* **1993**, *115*, 7363–7373. (b) Dupray, L. M.; Meyer, T. J. *Inorg. Chem.* **1996**, *35*, 6299–6307. (c) Dupray, L. M.; Devenney, M.; Striplin, D. R.; Meyer, T. J. *J. Am. Chem. Soc.* **1997**, *119*, 10243–10244. (d) Friesen, D. A.; Kajita, T.; Danielson, E.; Meyer, T. J. *Inorg. Chem.* **1998**, *37*, 2756–2762. (e) Fleming, C. N.; Maxwell, K. A.; DeSimone, J. M.; Meyer, T. J.; Papanikolas, J. M. *J. Am. Chem. Soc.* **2001**, *123*, 10336–10347. (f) Sowash, G. G.; Webber, S. E. *Macromolecules* **1988**, *21*, 1608–1611. (g) Webber, S. E. *Chem. Rev.* **1990**, *90*, 1469–1482.

- (7) (a) Marcaccio, M.; Paolucci, F.; Paradisi, C.; Roffia, S.; Fontanesi, C.; Yellowlees, L. J.; Serroni, S.; Campagna, S.; Denti, C.; Balzani, V. *J. Am. Chem. Soc.* **1999**, *121*, 10081–10091. (b) Campagna, S.; Denti, G.; Serroni, S.; Juris, A.; Venturi, M.; Ricevuto, V.; Balzani, V. *Chem.—Eur. J.* **1995**, *1*, 211–221. (c) Van Patten, P. G.; Shreve, A. P.; Lindsey, J. S.; Donohoe, R. J. *J. Phys. Chem. B* **1998**, *102*, 4209–4216. (d) Xu, Z. F.; Moore, J. S. *Acta Polym.* **1994**, *45*, 83–87. (e) Balzani, V.; Campagna, S.; Denti, G.; Juris, A.; Serroni, S.; Venturi, M. *Acc. Chem. Res.* **1998**, *31*, 26–34. (f) Tsukube, H.; Suzuki, Y.; Paul, D.; Kataoka, Y.; Shinoda, S. *Chem. Commun.* **2007**, 2533–2535. (g) Stapert, H. R.; Nishiyama, N.; Jiang, D. L.; Aida, T.; Kataoka, K. *Langmuir* **2000**, *16*, 8182–8188. (h) Ahn, T. S.; Thompson, A. L.; Bharathi, P.; Muller, A.; Bardeen, C. J. *J. Phys. Chem. B* **2006**, *110*, 19810–19819. (i) Nantalaksakul, A.; Reddy, D. R.; Bardeen, C. J.; Thayumanavan, S. *Photosynth. Res.* **2006**, *87*, 133–150. (j) Larsen, J.; Puntoriero, F.; Pascher, T.; McClenaghan, N.; Campagna, S.; Akesson, E.; Sundstrom, V. *ChemPhysChem* **2007**, *8*, 2643–2651. (k) Andersson, J.; Puntoriero, F.; Serroni, S.; Yartsev, A.; Pascher, T.; Polivka, T.; Campagna, S.; Sundstrom, V. *Faraday Discuss.* **2004**, *127*, 295–305. (l) Thomas, K. R. J.; Thompson, A. L.; Sivakumar, A. V.; Bardeen, C. J.; Thayumanavan, S. *J. Am. Chem. Soc.* **2005**, *127*, 373–383.
- (8) (a) Giansante, C.; Raffy, G.; Schaefer, C.; Rahma, H.; Kao, M.-T.; Olive, A. G. L.; Del Guizzo, A. *J. Am. Chem. Soc.* **2011**, *133*, 316–325. (b) Babu, S. S.; Kartha, K. K.; Ajayaghosh, A. *J. Phys. Chem. Lett.* **2010**, *1*, 3413–3424. (c) Ajayaghosh, A.; Praveen, V. K.; Vijayakumar, C. *Chem. Soc. Rev.* **2008**, *37*, 109–122. (d) Bhattacharya, S.; Samanta, S. K. *Langmuir* **2009**, *25*, 8378–8381.
- (9) Ferreira, K. N.; Iverson, T. M.; Maghlaoui, K.; Barber, J.; Iwata, S. *Science* **2004**, *303*, 1831–1838.
- (10) (a) Hurley, D. J.; Tor, Y. *J. Am. Chem. Soc.* **1998**, *120*, 2194–2195. (b) Hurley, D. J.; Tor, Y. *J. Am. Chem. Soc.* **2002**, *124*, 3749–3762. (c) Hurley, D. J.; Tor, Y. *J. Am. Chem. Soc.* **2002**, *124*, 13231–13241. (d) Lewis, F. D.; Zhang, L. G.; Zuo, X. B. *J. Am. Chem. Soc.* **2005**, *127*, 10002–10003. (e) Holmlin, R. E.; Tong, R. T.; Barton, J. K. *J. Am. Chem. Soc.* **1998**, *120*, 9724–9725.
- (11) Channon, K. J.; Devlin, G. L.; MacPhee, C. E. *J. Am. Chem. Soc.* **2009**, *131*, 12520–12521.
- (12) Nam, Y. S.; Shin, T.; Park, H.; Magyar, A. P.; Choi, K.; Fantner, G.; Nelson, K. A.; Belcher, A. M. *J. Am. Chem. Soc.* **2010**, *132*, 1462–1463.
- (13) (a) Stryer, L.; Haugland, R. P. *Proc. Natl. Acad. Sci.* **1967**, *58*, 719–726. (b) Pispisa, B.; Venanzi, M.; Palleschi, A.; Zanolli, G. *Macromolecules* **1994**, *27*, 7800–7808. (c) McGimpsey, W. G.; Chen, L.; Carraway, R.; Samaniego, W. N. *J. Phys. Chem. A* **1999**, *103*, 6082–6090. (d) Pispisa, B.; Stella, L.; Venanzi, M.; Palleschi, A.; Viappiani, C.; Polese, A.; Formaggio, F.; Toniolo, C. *Macromolecules* **2000**, *33*, 906–915. (e) Sahoo, H.; Roccatano, D.; Hennig, A.; Nau, W. M. *J. Am. Chem. Soc.* **2007**, *129*, 9762–9772.
- (14) Photoexcited-state electron transfer is a phenomenon closely related to energy transfer and has been extensively studied in a number of different peptide systems. (a) Mecklenburg, S. L.; Peek, B. M.; Erickson, B. W.; Meyer, T. J. *J. Am. Chem. Soc.* **1991**, *113*, 8540–8542. (b) Mecklenburg, S. L.; Peek, B. M.; Schoonover, J. R.; McCafferty, D. G.; Wall, C. G.; Erickson, B. W.; Meyer, T. J. *J. Am. Chem. Soc.* **1993**, *115*, 5479–5495. (c) Mecklenburg, S. L.; McCafferty, D. G.; Schoonover, J. R.; Peek, B. M.; Erickson, B. W.; Meyer, T. J. *Inorg. Chem.* **1994**, *33*, 2974–2983. (d) McCafferty, D. G.; Bishop, B. M.; Wall, C. G.; Hughes, S. G.; Mecklenburg, S. L.; Meyer, T. J.; Erickson, B. W. *Tetrahedron* **1995**, *51*, 1093–1106.
- (15) (a) Kozlov, G. V.; Ogawa, M. Y. *J. Am. Chem. Soc.* **1997**, *119*, 8377–8378. (b) Kornilova, A. Y.; Wishart, J. F.; Ogawa, M. Y. *Biochemistry* **2001**, *40*, 12186–12192. (c) Kornilova, A. Y.; Wishart, J. F.; Xiao, W. Z.; Lasey, R. C.; Fedorova, A.; Shin, Y. K.; Ogawa, M. Y. *J. Am. Chem. Soc.* **2000**, *122*, 7999–8006. (d) Fedorova, A.; Chaudhari, A.; Ogawa, M. Y. *J. Am. Chem. Soc.* **2003**, *125*, 357–362. (e) Fedorova, A.; Ogawa, M. Y. *Bioconjugate Chem.* **2002**, *13*, 150–154. (f) Hong, J.; Kharenko, O. A.; Ogawa, M. Y. *Inorg. Chem.* **2006**, *45*, 9974–9984.
- (16) Crick, F. H. C. *Nature* **1952**, *170*, 882–883.
- (17) (a) Talbot, J. A.; Hodges, R. S. *Acc. Chem. Res.* **1982**, *15*, 224–230. (b) Holtzer, A.; Holtzer, M. E. *Macromolecules* **1987**, *20*, 671–675.
- (18) (a) Woolfson, D. N. *Adv. Protein Chem.* **2005**, *70*, 79–112. (b) Pandya, M. J.; Spooner, G. M.; Sunde, M.; Thorpe, J. R.; Rodger, A.; Woolfson, D. N. *Biochemistry* **2000**, *39*, 8728–8734. (c) Ryadnov, M. G.; Woolfson, D. N. *Angew. Chem., Int. Ed.* **2003**, *42*, 3021–3023. (d) Ryadnov, M. G.; Woolfson, D. N. *Nat. Mater.* **2003**, *2*, 329–332. (e) Ryadnov, M. G.; Woolfson, D. N. *J. Am. Chem. Soc.* **2004**, *126*, 7454–7455. (f) Mahmoud, Z. N.; Gunnoo, S. B.; Thomson, A. R.; Fletcher, J. M.; Woolfson, D. N. *Biomaterials* **2011**, *32*, 3712–3720.
- (19) (a) Oshea, E. K.; Klemm, J. D.; Kim, P. S.; Alber, T. *Science* **1991**, *254*, 539–544. (b) Harbury, P. B.; Zhang, T.; Kim, P. S.; Alber, T. *Science* **1993**, *262*, 1401–1407. (c) Woolfson, D. N.; Alber, T. *Protein Sci.* **1995**, *4*, 1596–1607.
- (20) (a) Oshea, E. K.; Rutkowski, R.; Kim, P. S. *Cell* **1992**, *68*, 699–708. (b) Kohn, W. D.; Kay, C. M.; Hodges, R. S. *J. Mol. Biol.* **1998**, *283*, 993–1012. (c) Litowski, J. R.; Hodges, R. S. *J. Biol. Chem.* **2002**, *277*, 37272–37279. (d) Zhou, N. E.; Kay, C. M.; Hodges, R. S. *J. Mol. Biol.* **1994**, *247*, 500–512.
- (21) (a) Lumb, K. J.; Kim, P. S. *Biochemistry* **1995**, *34*, 8642–8648. (b) Oakley, M. G.; Kim, P. S. *Biochemistry* **1998**, *37*, 12603–12610. (c) Gonzalez, L.; Woolfson, D. N.; Alber, T. *Nat. Struct. Biol.* **1996**, *3*, 1011–1018.
- (22) (a) Lupas, A. *Trends Biochem. Sci.* **1996**, *21*, 375–382. (b) Marvin, D. A. *Curr. Opin. Struct. Biol.* **1998**, *8*, 150–158. (c) Herrmann, H.; Aebi, U. *Curr. Opin. Struct. Biol.* **1998**, *8*, 177–185. (d) Phillips, G. N.; Fillers, J. P.; Cohen, C. J. *Mol. Biol.* **1986**, *192*, 111–128. (e) McLachlan, A. D.; Karn, J. *J. Mol. Biol.* **1983**, *164*, 605–626.
- (23) (a) Geisser, B.; Ponce, A.; Alsfasser, R. *Inorg. Chem.* **1999**, *38*, 2030–2037. (b) Kise, K. J.; Bowler, B. E. *Inorg. Chem.* **2002**, *41*, 379–386. (c) Kise, K. J.; Bowler, B. E. *Inorg. Chem.* **2003**, *42*, 3891–3897. (d) McCafferty, D. G.; Friesen, D. A.; Danielson, E.; Wall, C. G.; Saderholm, M. J.; Erickson, B. W.; Meyer, T. J. *Proc. Natl. Acad. Sci. U.S.A.* **1996**, *93*, 8200–8204.
- (24) (a) Rostovtsev, V. V.; Green, L. G.; Fokin, V. V.; Sharpless, K. B. *Angew. Chem., Int. Ed.* **2002**, *41*, 2596–2599. (b) Tornoe, C. W.; Christensen, C.; Meldal, M. *J. Org. Chem.* **2002**, *67*, 3057–3064. (c) Meldal, M.; Tornoe, C. W. *Chem. Rev.* **2008**, *108*, 2952–3015.
- (25) (a) Khan, S. I.; Beilstein, A. E.; Grinstaff, M. W. *Inorg. Chem.* **1999**, *38*, 418–418. (b) Khan, S. I.; Beilstein, A. E.; Smith, G. D.; Sykora, M.; Grinstaff, M. W. *Inorg. Chem.* **1999**, *38*, 2411–2415. (c) Khan, S. I.; Grinstaff, M. W. *J. Am. Chem. Soc.* **1999**, *121*, 4704–4705. (d) Khan, S. I.; Beilstein, A. E.; Tierney, M. T.; Sykora, M.; Grinstaff, M. W. *Inorg. Chem.* **1999**, *38*, 5999–6002. (e) Tierney, M. T.; Sykora, M.; Khan, S. I.; Grinstaff, M. W. *J. Phys. Chem. B* **2000**, *104*, 7574–7576.
- (26) (a) Sonogashira, K.; Tohda, Y.; Hagihara, N. *Tetrahedron Lett.* **1975**, 4467–4470. (b) Chinchilla, R.; Najera, C. *Chem. Rev.* **2007**, *107*, 874–922. (c) Hobbs, F. W. *J. Org. Chem.* **1989**, *54*, 3420–3422.
- (27) (a) Isaad, A. L. C.; Barbetti, F.; Rovero, P.; D’Ursi, A. M.; Chelli, M.; Chorev, M.; Papini, A. M. *Eur. J. Org. Chem.* **2008**, 5308–5314. (b) Cantel, S.; Isaad, A. L. C.; Scrima, M.; Levy, J. J.; DiMarchi, R. D.; Rovero, P.; Halperin, J. A.; D’Ursi, A. M.; Papini, A. M.; Chorev, M. *J. Org. Chem.* **2008**, *73*, 5663–5674.
- (28) (a) Chan, T. R.; Hilgraf, R.; Sharpless, K. B.; Fokin, V. V. *Org. Lett.* **2004**, *6*, 2853–2855. (b) Lewis, W. G.; Magallon, F. G.; Fokin, V. V.; Finn, M. G. *J. Am. Chem. Soc.* **2004**, *126*, 9152–9153. (c) Juricek, M.; Stout, K.; Kouwer, P. H. J.; Rowan, A. E. *Org. Lett.* **2011**, *13*, 3494–3497.
- (29) (a) Woody, R. W. *Biochem. Spectrosc.* **1995**, *246*, 34–71. (b) Greenfield, N. J. *Nat. Protoc.* **2006**, *1*, 2876–2890. (c) Hodges, R. S. *Biochem. Cell Biol.* **1996**, *74*, 133–154. (d) Zhou, N. E.; Zhu, B. Y.; Kay, C. M.; Hodges, R. S. *Biopolymers* **1992**, *32*, 419–426.
- (30) (a) Zhou, N. E.; Kay, C. M.; Hodges, R. S. *Biochemistry* **1992**, *31*, 5739–5746. (b) Zhou, N. E.; Kay, C. M.; Hodges, R. S. *J. Biol. Chem.* **1992**, *267*, 2664–2670. (c) Su, J. Y.; Hodges, R. S.; Kay, C. M. *Biochemistry* **1994**, *33*, 15501–15510.

- (31) (a) Pace, C. N. In *Methods in Enzymology*; Hirs, C. H. W., Timasheff, S. E., Eds.; Academic Press: New York, 1986; Vol. 131. (b) DeFrancesco, R.; Pastore, A.; Vecchio, G.; Cortese, R. *Biochemistry* **1991**, *30*, 143–147.
- (32) (a) Chen, Y. H.; Yang, J. T.; Chau, K. H. *Biochemistry* **1974**, *13*, 3350–3359. (b) Scholtz, J. M.; Qian, H.; York, E. J.; Stewart, J. M.; Baldwin, R. L. *Biopolymers* **1991**, *31*, 1463–1470. (c) Wendt, H.; Berger, C.; Baici, A.; Thomas, R. M.; Bosshard, H. R. *Biochemistry* **1995**, *34*, 4097–4107.
- (33) (a) Kohn, W. D.; Kay, C. M.; Hodges, R. S. *Protein Sci.* **1995**, *4*, 237–250. (b) Serrano, L.; Horovitz, A.; Avron, B.; Bycroft, M.; Fersht, A. R. *Biochemistry* **1990**, *29*, 9343–9352.
- (34) Juris, A.; Balzani, V.; Barigelletti, F.; Campagna, S.; Belser, P.; Vonzelewsky, A. *Coord. Chem. Rev.* **1988**, *84*, 85–277.
- (35) (a) Dexter, D. L. *J. Chem. Phys.* **1953**, *21*, 836–850. (b) Förster, Th. *Discuss. Faraday Soc.* **1959**, *27*, 7–17. (c) Murtaza, Z.; Graff, D. K.; Zipp, A. P.; Worl, L. A.; Jones, W. E.; Bates, W. D.; Meyer, T. J. *J. Phys. Chem.* **1994**, *98*, 10504–10513.
- (36) (a) Wang, G. Y.; Bergstrom, D. E. *Synlett* **1992**, 422–424. (b) Peek, B. M.; Ross, G. T.; Edwards, S. W.; Meyer, G. J.; Meyer, T. J.; Erickson, B. W. *Int. J. Pept. Protein Res.* **1991**, *38*, 114–123. (c) Telser, J.; Cruickshank, K. A.; Schanze, K. S.; Netzel, T. L. *J. Am. Chem. Soc.* **1989**, *111*, 7221–7226.
- (37) Johnson, S. R.; Westmoreland, T. D.; Caspar, J. V.; Barqawi, K. R.; Meyer, T. J. *Inorg. Chem.* **1988**, *27*, 3195–3200.
- (38) *The PyMOL Molecular Graphics System*, 1.2r3pre ed.; Schrödinger, LLC: New York.
- (39) Frisch, M. J.; et al. *Gaussian 03*, Revision C.02; Gaussian, Inc.: Wallingford, CT, 2004.
- (40) Case, D. A.; et al. *AMBER 11*; University of California: San Francisco, CA, 2010.
- (41) Hornak, V.; Abel, R.; Okur, A.; Strockbine, B.; Roitberg, A.; Simmerling, C. *Proteins: Struct., Funct., Bioinf.* **2006**, *65*, 712–725.
- (42) Lee, C. T.; Yang, W. T.; Parr, R. G. *Phys. Rev. B* **1988**, *37*, 785–789.
- (43) (a) Hay, P. J.; Wadt, W. R. *J. Chem. Phys.* **1985**, *82*, 270–283. (b) Hay, P. J.; Wadt, W. R. *J. Chem. Phys.* **1985**, *82*, 299–310. (c) Wadt, W. R.; Hay, P. J. *J. Chem. Phys.* **1985**, *82*, 284–298.
- (44) Bayly, C. I.; Cieplak, P.; Cornell, W. D.; Kollman, P. A. *J. Phys. Chem.* **1993**, *97*, 10269–10280.
- (45) Brandt, P.; Norrby, T.; Akermark, E.; Norrby, P. O. *Inorg. Chem.* **1998**, *37*, 4120–4127.

Energy Migration Dynamics in a Ru(II)- and Os(II)-Based Antenna Polymer Embedded in a Disordered, Rigid Medium

Cavan N. Fleming, Paul Jang, Thomas J. Meyer,* and John M. Papanikolas*[†]

Department of Chemistry, Venable and Kenan Laboratories, University of North Carolina at Chapel Hill, Chapel Hill, North Carolina 27599-3290

Received: August 25, 2003

The energy migration dynamics have been studied in multi-centered assemblies embedded in poly(methyl methacrylate) (PMMA) films using steady-state and time-resolved emission techniques. The assemblies consist of twenty Ru(II) and Os(II) polypyridyl coordination complexes linked through a polystyrene backbone. Energy migration is initiated by photoexcitation of one of the Ru(II) sites and terminated upon sensitization of a low-energy Os trap. The inhomogeneous environment of the assembly results in a distribution of excited-state energies, which is frozen in time due to the rigidity of the PMMA film. Energy migration proceeds toward the lower energy sites, resulting in a time-dependent red-shift in the polymer emission band.

I. Introduction

The ability of polymers to conduct excited-state energy is well documented.^{1–11} There are many examples of multi-centered systems in which photoexcitation initially produces a localized excited state that then migrates between pendent chromophores by Dexter or Forster energy transfer. In fluid solution, the presence of fast solvent relaxation and a homogeneous environment leads to energy migration between chromophores that are thermally equilibrated and, if chemically identical, isoenergetic.

We have recently published results on the excited-state energy migration dynamics within a supramolecular assembly containing polypyridyl Ru(II) and Os(II) chromophores.¹¹ The chromophores are linked through a polystyrene backbone to yield assemblies with approximately 20 coordination complexes (17 Ru^{II} and 3 Os^{II}) per chain. The chemical structures of the polymer and monomer constituents are shown in Figure 1. Energy migration is initiated upon photoexcitation of the metal-to-ligand charge-transfer transition (MLCT) of one of the Ru sites, which then leads to efficient energy transport to a lower energy Os trap through a series of Ru* → Ru energy hops. The macromolecular structure of the assembly plays an important role in its energy transport properties. Figure 1 depicts a structure calculated using Monte Carlo simulation methods. Here, the larger spheres are the Ru^{II} or Os^{II} chromophores and the smaller spheres are the PF₆⁻ counterions that surround the polymer whose overall charge is +40. The polymer adopts a twisted backbone and extended rodlike structure that attempts to alleviate the steric and Coulombic repulsions between adjacent chromophores, and the result is a densely packed structure in which the average distance between the peripheries of adjacent chromophores is 2–3 Å. Our previous work¹¹ shows efficient energy transport along the polymer chain, which is facilitated by the close proximity of the pendent groups.

We report here results on the incorporation of these supramolecular assemblies into room-temperature solid solutions. Like its fluid solution counterpart, steady-state and time-resolved

emission studies indicate that this antenna polymer is capable of energy transport, even when it is embedded in poly(methyl methacrylate) (PMMA) films. This paper explores the effect of the rigid environment on the energy transport process.

One benchmark for comparison is electron transfer reactions, which are sensitive to the dynamical response of the surrounding medium. Solvent molecules reorient in response to the changing charge distribution between the donor and acceptor. In rigid media, where solvent motion is restricted, the energetics and dynamics of electron transfer reactions are significantly effected, often to the point where the reaction is shut down.^{12,13} Unlike electron transfer, the nature of the solvent should play a less prominent role for energy transfer, since energy transfer involves the motion of a dipole, as opposed to individual charges. This role is not necessarily negligible, however, given the sensitivity of the energetics of charge-transfer excited states toward the solvent environment.

Our results point to additional complexities arising from this solid surroundings. These complexities are manifested as (1) nonexponential decay kinetics in the monomers and homopolymers (PS–Ru₂₀ and PS–Os₂₀), (2) spectroscopic differences between the monomers and their corresponding homopolymers, and (3) time-dependent spectral shifts in the emission spectra of the polymers. All of these are qualitatively different from our observations in fluid solutions, and stem from a combination of two factors: a lifting of degeneracy of adjacent excited states due to inhomogeneities in the local electrostatic field and the rigid molecular environment. As a result, excited states migrate toward lower energy sites and can become trapped at electrostatic minima. Although inhomogeneities are also present in fluid solution, the motion of adjacent sites relative to each other causes the energy of a particular site to fluctuate, and this prevents trapping. Our conclusions have implications for describing energy transport in fluid solutions. In particular, it suggests that the efficient energy migration observed in fluid solution might arise (at least in part) from a trapeze-like motion of the side chains that brings adjacent sites into close physical contact, thus enhancing the overlap of donor and acceptor wave functions. If this is the case, then inter-site motion and flexibility

* Authors to whom correspondence should be addressed.

[†] E-mail: John_Papanikolas@unc.edu.

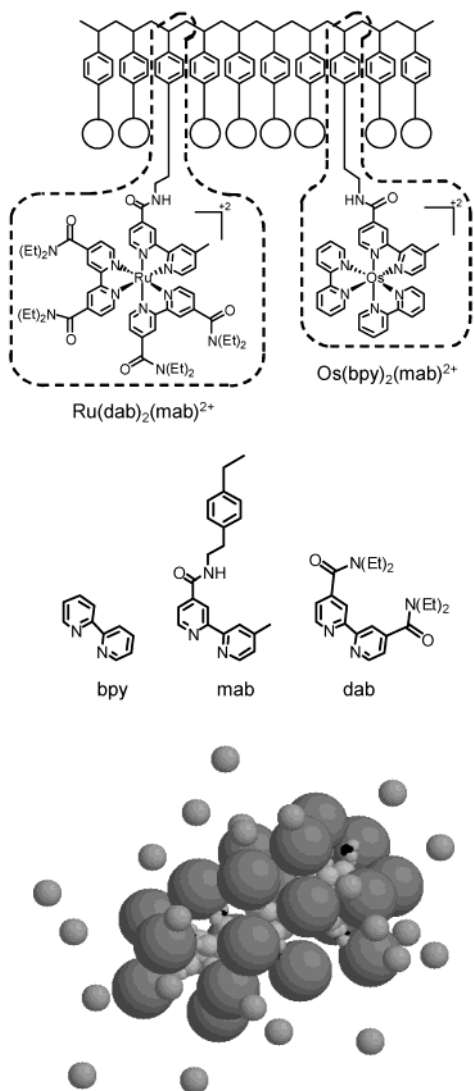


Figure 1. Chemical structures of the monomer and polymer systems discussed in this work (top) and a three-dimensional view of the polymer system obtained from Monte Carlo simulation (bottom), ref 11.

would be an important architectural feature that is needed to design efficient nanoscale materials for energy transport.

II. Experimental Section

Preparation of Polymer Films. An amount of 0.6 g of PMMA was dissolved in 5 mL of chloroform. Dissolution occurred over a period of ~30 min with constant stirring and mild heat (~40 °C) applied. The PF₆⁻ salt of the complex or polymer array was dissolved in chloroform or acetonitrile, depending upon its solubility, and its concentration was adjusted to achieve an OD of ~0.6 at the MLCT maximum. An amount of 1 mL of the complex solution was added to the polymer solution, stirred, and poured into a Teflon mold. The solvent was allowed to evaporate slowly over a period of 2–3 days in an open-air desiccator. The resulting film was then placed in a vacuum desiccator for 2 days prior to making measurements. The films produced were 4 cm in length and 1 cm in width, and had a fairly uniform thickness of ~1 mm.

Measurements. UV–visible spectra were recorded on a diode array spectrometer with 2 nm resolution. The spectroscopic grade acetonitrile used in the photophysical measurements was either used as received or distilled over CaH₂. Steady-state

emission spectra were recorded on a photon counting spectrofluorimeter and were corrected for the instrument response. Optically dilute samples (less than 0.12 OD at the excitation wavelength) were argon sparged for 40 min prior to use. Measurements in rigid media were performed in open atmosphere. Emission quantum yields were calculated by relative actinometry using eq 1.

$$\Phi_{\text{sam}} = \Phi_{\text{ref}} \left(\frac{I_{\text{sam}}}{I_{\text{ref}}} \right) \left(\frac{n_{\text{sam}}}{n_{\text{ref}}} \right)^2 \left(\frac{A_{\text{ref}}}{A_{\text{sam}}} \right) \quad (1)$$

In this equation, Φ_{sam} is the emission quantum yield of either the sample or the reference compound, I is the integrated emission profile, n is the refractive index of the solvent, and A is the absorbance of the sample in a 1 cm quartz cuvette or in ~1 mm PMMA films drip-coated onto a quartz plate. For fluid solution measurements, the reference was either [Ru(bpy)₃](PF₆)₂ for which $\Phi_{\text{ref}} = 0.062$ or [Os(bpy)₃](PF₆)₂ for which $\Phi_{\text{ref}} = 0.005$ in acetonitrile at 298 K. The reference used for measurements in PMMA is [Rhodamine 6G](Cl) in PMMA at 298 K for which $\Phi_{\text{ref}} = 0.77$. The reference quantum yield used here is the average of two published values.^{14,15}

Time-resolved measurements were conducted by time-correlated single-photon counting (TCSPC). The apparatus consists of a commercially available mode-locked Nd:YAG laser whose frequency-tripled output is used to synchronously pump a single jet dye laser with Stilbene 3. The dye laser output at 430 nm is cavity dumped to produce ~10 ps pulses with ~6 nJ/pulse energies. The repetition rate of the dye laser was selected to be roughly 5 times the natural lifetime of the sample (475 kHz for measurements at 780 nm or 190 kHz for measurements at 640 nm at room temperature). The beam is passed through an iris and illuminated without focusing a 10 mm quartz cuvette. The intensity of the detected luminescence is varied by use of ND filters mounted before the monochromator. For luminescence measurements the emitted light is collected at 90° and focused onto the slit of a 240 mm focal length, single grating monochromator and subsequently delivered to a cooled, multichannel plate-photomultiplier tube (MCP-PMT) with a 170 ps rise time. The signal from the MCP is amplified prior to sending it into a 200 MHz constant fraction discriminator (CFD) whose output served as the start pulse for the time-to-amplitude converter (TAC). The stop pulse in the timing scheme is obtained by splitting off 10% of the excitation beam and focusing it onto a photodiode. The photodiode pulse is sent into a variable delay box, then to the CFD, and finally to the TAC. The TAC's output is processed by a multichannel analyzer that is interfaced to a PC. The time-resolution of the apparatus is ~100 ps.

III. Results and Discussion

In a previous report on the energy transfer dynamics in room-temperature CH₃CN,¹¹ we combined steady-state and time-resolved spectroscopy with Monte Carlo simulations to obtain a detailed look at the polymer structure and its relationship to the energy transfer dynamics in PS–Ru₁₇Os₃. In this paper we extend the fluid solution work to an amorphous solid, PMMA.

As with the fluid solution, the energy transport properties will be closely linked to the macromolecular structure of the polymer array. Given the dense loading of complexes, we expect that the polymer array will adopt a similar extended rodlike structure in PMMA as it does in CH₃CN. However, some differences may exist. In the low dielectric environment of PMMA ($D_s = 3.6$) the counterions are more closely associated with the assembly. Furthermore, in the absence of a small, highly

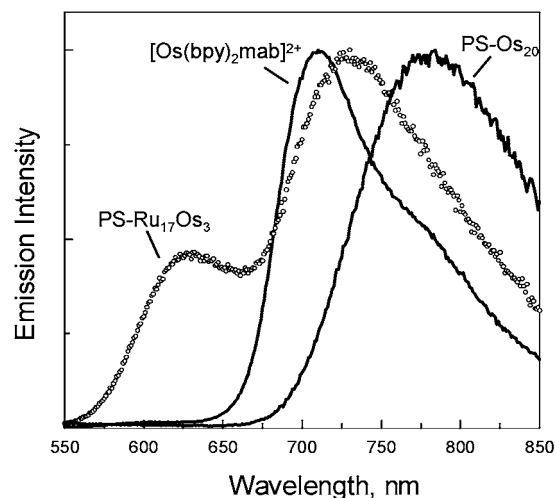


Figure 2. Steady-state emission spectra of $[\text{Os}(\text{bpy})_2(\text{mab})]^{2+}$, PS-Ru₁₇Os₃, and PS-Os₂₀ in room-temperature PMMA. Excitation was at 423 nm.

polar solvent such as CH₃CN, the electrostatic interactions between adjacent complexes could be greater, and this would increase the average periphery-periphery distance. Beyond these small differences, the polymer arrays can be accurately described as a densely loaded system in which each site is in close proximity to multiple neighbor sites.

The discussion of our spectroscopic results is divided into two sections. Section A describes our steady-state results, while time-resolved results are presented in Section B.

A. Steady-State Emission. Steady-state emission spectra of $[\text{Os}(\text{bpy})_2(\text{mab})]^{2+}$, PS-Os₂₀, and PS-Ru₁₇Os₃ embedded in room-temperature PMMA are displayed in Figure 2. These spectra differ from their fluid solution counterparts in several regards.

The changes observed for the monomer complexes are consistent with trends expected for rigid media. The emission band of $[\text{Os}(\text{bpy})_2(\text{mab})]^{2+}$, which peaks at 715 nm, is shifted to higher energy in rigid polymeric media relative to its value in CH₃CN where $\lambda_{\text{max}} = 780$ nm. Furthermore, the band is not as broad and has more structure than it does in fluid solution; vibronic structure appears at ~ 775 nm in PMMA. These observations are typical for emissive MLCT excited states in rigid environments.^{16,17} The origin of this blue shift is also well understood. In fluid solution, the solvent dipoles reorient to configurations appropriate to the electronic configuration of the excited state, stabilizing the excited state, and leading to a red-shifted emission band. In rigid solvents, the medium is at least partially frozen on the time scale for excited-state decay; emission then occurs with the surrounding solvent dipole orientations more like those surrounding the ground state and the emission appears at higher energy. Emission quantum yields are also consistent with this picture (Table 1). The quantum yields of both Ru and Os complexes *increase* upon incorporation into PMMA, consistent with the higher excited-state energy, as predicted by the energy gap law.

While the monomer emission is consistent with other observations in rigid environments, the polymer emission is not. In fluid solution, the homopolymers (PS-Ru₂₀ and PS-Os₂₀) are spectroscopically equivalent to their corresponding monomer complexes. However, in PMMA there are stark differences between the two. PS-Os₂₀ in PMMA has an emission band typical of fluid acetonitrile, and the Os* emission from PS-Ru₁₇Os₃ is intermediate between these two cases (Figure 2). In addition, the increase in quantum yield observed upon incor-

TABLE 1: Summary of Room Temperature Lifetimes (τ) and Emission Quantum Yields (Φ_{em}) in PMMA and CH₃CN

complex	CH ₃ CN ^c		PMMA ^c	
	Φ_{em}	τ (ns)	Φ_{em}	τ (ns)
$[\text{Ru}(\text{dab})_2(\text{mab})]^{2+}$	0.11	1100 ^a	0.21	1490 ^a
PS-Ru ₂₀	0.10	1000 ^a	0.050	1200 ^b
$[\text{Os}(\text{bpy})_2(\text{mab})]^{2+}$	0.0030	56 ^a	0.030	140 ^a
PS-Os ₂₀	0.0032	49 ^a	0.0027	40 ^b

^a A sum of two exponential functions was used to fit the decays. The results are as follows: $\tau_1 = 87$ ns (0.42), $\tau_2 = 182$ ns (0.55) for $[\text{Os}(\text{bpy})_2(\text{mab})]^{2+}$; $\tau_1 = 650$ ns (0.30), $\tau_2 = 1850$ ns (0.70) for $[\text{Ru}(\text{dab})_2(\text{mab})]^{2+}$. Average lifetimes are reported. Monitoring occurred at the emission band maximum. ^b A sum of three exponential functions was used to fit the decays. The results are as follows: $\tau_1 = 2$ ns (0.20), $\tau_2 = 13$ ns (0.40), $\tau_3 = 40$ ns (0.35) for PS-Os₂₀; $\tau_1 = 20$ ns (0.15), $\tau_2 = 225$ ns (0.20), $\tau_3 = 1200$ ns (0.60) for PS-Ru₂₀. Slow component is tabulated for two polymers samples. Spectral evolution is observed on the 1–10 ns time scale which is partly responsible for the nonexponential behavior observed in the PS-Os₂₀ and PS-Ru₂₀. This evolution does not reflect the emissive properties of the complexes, but rather energy migration among complexes with an inhomogeneous distribution of excited-state energies. Monitoring occurred at the emission band maximum. ^c Care must be taken in making quantitative comparisons between the two different solvents (PMMA versus CH₃CN) because different references were used, and each reference is most likely known to differing degrees of certainty.

poration of the monomer into the rigid environment is not observed for the polymers. On the whole, comparison between the PMMA and CH₃CN results suggest that while the spectroscopic properties of the monomer change upon incorporation into the PMMA matrix, consistent with known rigid media effects, the polymer arrays have spectroscopic properties that remain more akin to those observed in fluid solution. These observations can be explained by a dispersion in the Os* excited-state energies, which is discussed in more detail in Section B.

B. Time-Resolved Emission. This project examines the time-resolved emission from the mixed loaded polymer, PS-Ru₁₇Os₃, the homopolymers, PS-Ru₂₀ and PS-Os₂₀, and the corresponding monomers, $[\text{Os}(\text{bpy})_2(\text{mab})]^{2+}$ and $[\text{Ru}(\text{dab})_2(\text{mab})]^{2+}$ in room-temperature PMMA. The monomers and homopolymers serve as model systems for the mixed loaded system.

Energy transport along the polymer backbone is evident in the time-resolved emission data obtained from the PS-Ru₁₇Os₃/PMMA samples. Figure 3 shows the growth and decay of Os emission (observed at 780 nm) and the decay of the Ru emission (observed at 640 nm) as a function of time after photoexcitation of the Ru sites in PS-Ru₁₇Os₃. The delayed growth in the Os emission, and its correlation with the Ru decay, is a clear indication of Os sensitization by Ru excited states. The time scale associated with the growth of the Os emission reflects both the rates of individual Ru* \rightarrow Ru energy transfer events and the number of steps needed to reach the Os trap. Qualitatively the Os* rise kinetics are similar in PMMA and acetonitrile. In acetonitrile a fast, instrument response limited rise comprises $\sim 55\%$ of the signal. The fast rise has contributions from both direct Os excitation and Ru emission (detected as a result of the overlapping emission bands at 780 nm) as previously discussed.¹¹ In PMMA the fast rise appears to be a larger fraction of the signal, 60–70%. This could be indicative of a lower efficiency for energy transport compared with fluid solution; however, a quantitative measure based on the time-resolved data was not possible.

In our fluid solution studies, we were able to determine the contribution of direct Os excitation and Ru emission to the fast

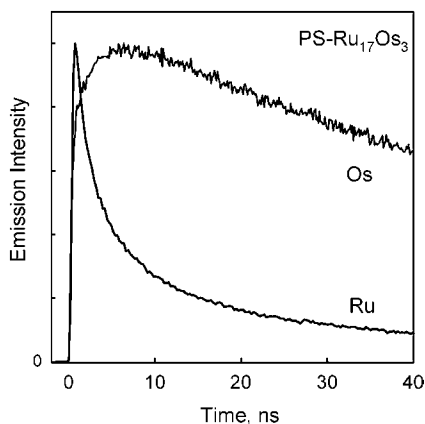


Figure 3. Time-resolved emission detected from PS-Ru₁₇Os₃ in room temperature PMMA while monitoring at 730 nm. The transient shown is an average of three measurements made from three different samples. In all cases we observe sensitized Os emission, but the exact kinetics of the rise vary slightly between samples, unlike our observations in fluid solution.

rise and use this information to assess the energy transfer efficiency in CH₃CN. This was possible in part because in fluid solution the monomer complexes, [Ru(dab)₂(mab)]²⁺ and [Os(bpy)₂(mab)]²⁺, are spectroscopically equivalent to their corresponding homopolymers, PS-Ru₂₀ and PS-Os₂₀. This is not the case in the rigid polymeric media where the excited-state energies, lifetimes, and emission quantum yields for Os emission in PS-Os₂₀, the mixed polymer PS-Ru₁₇Os₃, and [Os(bpy)₂(mab)]²⁺ are all different (Table 1).

While there are qualitative similarities in the kinetics found in fluid solution versus PMMA, there are some significant differences. In fluid solution, both the monomers and homopolymers show nearly identical spectroscopic signatures. Both exhibit single-exponential decay kinetics with similar decay rates, and the emission spectra decay without a change in shape (i.e., kinetics are independent of monitoring wavelength). In PMMA, on the other hand, the correspondence between the monomer and its corresponding homopolymer is lost.

Both the monomers, [Os(bpy)₂(mab)]²⁺ and [Ru(dab)₂(mab)]²⁺, and homopolymers, PS-Os₂₀ and PS-Ru₂₀, display nonexponential kinetics in PMMA, although the degree of nonexponential behavior is significantly less in the monomers. Nonexponential decay kinetics are a common feature for polypyridyl complexes in a variety of rigid media where it has been attributed to the heterogeneity of the solvent.¹⁸ In short, the distribution of solvent microenvironments leads to a distribution of excited-state lifetimes. Here it appears that in the case of the polymers, solvent heterogeneity plays only part of the role in the observed nonexponential kinetics.

In PMMA, the emission spectra for the PS-Ru₂₀ or PS-Os₂₀ polymers change with time after photoexcitation. When monitored on the low energy side of emission band, the Os* emission from PS-Os₂₀ is single exponential and similar to fluid CH₃CN. Nonexponential decay kinetics becomes prominent at the emission band maximum and to the high energy side. Reconstruction of the emission band from the single wavelength kinetic traces reveals a spectral shift as a function of time (Figure 4). The band maximum shifts ~50 nm to the red, reaching its final form by about 10 ns. No monitoring wavelength dependence is observed for [Os(bpy)₂(mab)]²⁺ in PMMA, i.e., the emission band decays uniformly with time (Figure 5).

The absence of a spectral shift for [Os(bpy)₂(mab)]²⁺ in PMMA is telling. At the low concentration of monomer doping, the probability that multiple complexes occupy the same site is

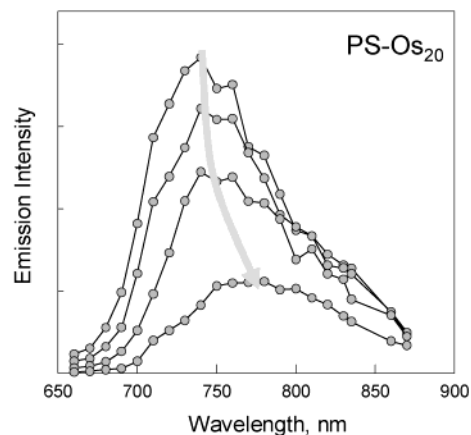


Figure 4. Time-resolved emission spectra of PS-Os₂₀ in room-temperature PMMA. Spectra have been corrected for the instrument response. Spectra measured at $t = 110$ ps, 510 ps, 2 ns, and 10 ns (from top to bottom).

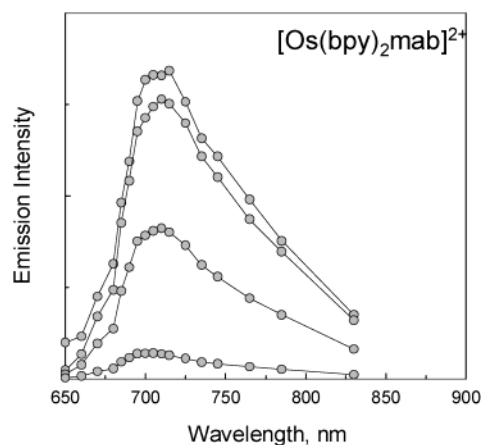


Figure 5. Time-resolved emission spectra of [Os(bpy)₂(mab)]²⁺ in room-temperature PMMA. Spectra have been corrected for the instrument response. Spectra measured at $t = 0$, 10, 100, and 400 ns (from top to bottom).

negligible. The polymer arrays, on the other hand, have a high *local* concentration of chromophores. One of the consequences of this high concentration is already known; close contact of adjacent sites leads to weak electronic coupling and enables Os* → Os energy transfer even in the rigid, low dielectric environment of PMMA. Another consequence is that an MLCT excited state experiences an electrostatic interaction with surrounding metal dications, counterions, in addition to the surrounding PMMA matrix. The presence of the nearby ions can significantly affect the energetics of the MLCT excited state in a way not present in monomer doped films. Because the distance between nearest neighbors and the number of metal complexes that exist in close contact varies along the chain, there is a dispersion in Os* excited-state energies.

The combination of facile energy transfer and energetic disorder leads to a situation where excited-state energy can relax from higher energy sites to lower ones as the energy migrates spatially along the polymer array (Figure 6). In the case of the PS-Os₂₀, MLCT photoexcitation of Os is followed by multiple Os* → Os energy transfer events whereby energy cascades to lower energy sites. In PS-Os₂₀, the lowest energy sites can be accessed. In the mixed polymer PS-Ru₁₇Os₃ the Os are deep traps, surrounded by Ru. Thus, energy transfer from Ru* → Os is irreversible and many low-energy Os sites are not reached. Correspondingly, the emission max is to higher energy.

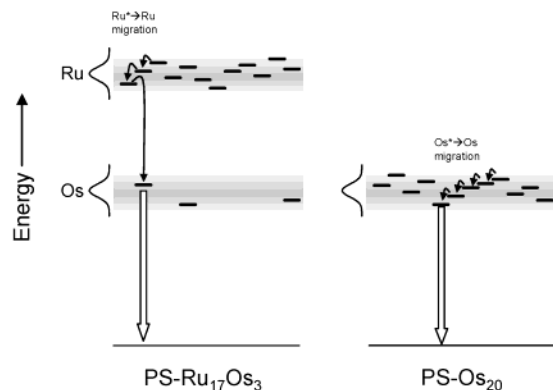


Figure 6. Schematic diagram depicting the energetic disorder contained in the PS-Ru₁₇Os₃ and PS-Os₂₀ polymer systems. In the mixed loaded system, energy migration among the Ru sites occurs until energy transfer to an Os trap, whose excited-state energy can be anywhere within the broad Os* energy distribution. In the PS-Os₂₀ system energy migration among the Os sites funnels the excited states toward lower energy sites.

Energetic disorder and excitation dependent kinetics are characteristic features of amorphous polymer media. This behavior has been observed in both singlet and triplet energy transfer in polymer films with pendant aromatic chromophores. Fayer et al.¹⁹ studied the excitation wavelength-dependent fluorescence depolarization in the 2-vinylnaphthalene/methyl methacrylate copolymer and attributed the observed wavelength dependence to site inhomogeneity. Time-resolved phosphorescence spectra have also revealed similar information.²⁰

Dynamical solvent effects involving structural reorganization of the environment in response to the excited-state charge distribution could also contribute to the spectral shift. It is possible that if the excited state were fixed (i.e., no energy migration) than a spectral shift could still be observed as a result of solvation dynamics that occur on a time scale comparable to excited-state decay. These could come in two forms, either relaxation of the surrounding PMMA shell or mobility of the polymer array. In the case of rigid, polymeric solvents such as PMMA, large amplitude motion of the polymer backbone is most likely frozen on the time scale of excited-state decay and will not participate in a solvation process involving rotation or translation. The primary glass transition temperature for the PMMA used in this study is 120 °C. However, PMMA has a

very broad secondary phase transition involving motion of the ester side chain centered at room temperature. Orientational freedom of the ester group could participate in the solvation dynamics and lead to the observed time dependence. The absence of spectral shift in [Os(bpy)₂(mab)]²⁺ suggests that the PMMA motion is fast (<100 ps) and not contributing to the observed dynamics which take place on a nanosecond time scale in the PS-Os₂₀ system. The mobility of the polymer array is, on the other hand, still an open question. Direct excitation of the Os sites (at 700 nm) in PS-Ru₁₇Os₃ could provide insight into this issue.

Acknowledgment. Funding for this project was provided by The Research Corporation (RI0048), the Petroleum Research Fund (36385-G6), the United States Department of Energy, and the National Science Foundation (CHE-0301266).

References and Notes

- (1) Webber, S. E. *Chem. Rev.* **1990**, *90*, 1469–1482.
- (2) Holden, D. A.; Guillet, J. E. *Macromolecules* **1980**, *13*, 289.
- (3) Ng, D.; Guillet, J. E. *Macromolecules* **1982**, *15*, 724.
- (4) Watkins, D. M.; Fox, M. A. *J. Am. Chem. Soc.* **1996**, *118*, 4344–4353.
- (5) Clements, J. H.; Webber, S. E. *J. Phys. Chem. B* **1999**, *103*, 9366.
- (6) Clements, J. H.; Webber, S. E. *J. Phys. Chem. A* **1999**, *103*, 2513–2523.
- (7) Jones, W. E.; Baxter, S. M.; Strouse, G. F.; Meyer, T. J. *J. Am. Chem. Soc.* **1993**, *115*, 7363–7373.
- (8) Yekta, A.; Spiro, J. G.; Winnik, M. A. *J. Phys. Chem. B* **1998**, *102*, 7960–7970.
- (9) Schillén, K.; Yekta, A.; Ni, S.; Winnik, M. A. *Macromolecules* **1998**, *31*, 210–212.
- (10) Rharbi, Y.; Yekta, A.; Winnik, M. A.; DeVoe, R. J.; Barrera, D. *Macromolecules* **1999**, *32*, 3241–3248.
- (11) Fleming, C. N.; Maxwell, K. A.; Meyer, T. J.; Papanikolas, J. M. *J. Am. Chem. Soc.* **2001**, *123*, 10336–10347.
- (12) Gaines, G. L.; O'Neil, M. P.; Svec, W. A.; Niemczyk, M. P.; Wasielewski, M. R. *J. Am. Chem. Soc.* **1991**, *113*, 719–721.
- (13) Chen, P.; Meyer, T. J. *Inorg. Chem.* **1996**, *35*, 5520–5524.
- (14) Reisfeld, R.; Zusman, R.; Cohen, Y.; Eyal, M. *Chem. Phys. Lett.* **1988**, *147*, 142–147.
- (15) Deshpande, A. V.; Namdas, E. B. *J. Lumin.* **2000**, *91*, 25–31.
- (16) Chen, P.; Meyer, T. J. *Chem. Rev.* **1998**, *98*, 1439–1477.
- (17) Wrighton, M. S.; Morse, D. L. *J. Am. Chem. Soc.* **1974**, *96*, 998.
- (18) Maruszewski, K.; Strommen, D. P.; Kincaid, J. R. *J. Am. Chem. Soc.* **1993**, *115*, 8345.
- (19) Stein, A. D.; Peterson, K. A.; Fayer, M. D. *J. Chem. Phys.* **1990**, *92*, 5622–5635.
- (20) Hisada, K.; Ito, S.; Yamamoto, M. *J. Phys. Chem. B* **1997**, *101*, 6827–6833.

Triplet–Triplet Annihilation of Excited States of Polypyridyl Ru(II) Complexes Bound to Polystyrene

George B. Shaw and John M. Papanikolas*

Department of Chemistry, Venable and Kenan Laboratories, The University of North Carolina at Chapel Hill, Chapel Hill, North Carolina 27599-3290

Received: December 12, 2001; In Final Form: March 14, 2002

Femtosecond transient absorption spectroscopy is used to study the triplet–triplet annihilation (TTA) interaction between the metal-to-ligand charge-transfer (MLCT) excited states of Ru(II) polypyridyl complexes bound to a polystyrene backbone. The polymer chains have, on average, 20 repeat units, each functionalized with a transition metal complex. Spectroscopic experiments are performed on assemblies dissolved in acetonitrile at room temperature. The time-resolved spectra show kinetics that depend on the intensity of the excitation laser. These effects are attributed to the interaction between multiple excited states formed on a single chain. Fast and slow (intensity-dependent) kinetic components are observed. The fast (3 ps) component is assigned to the TTA of MLCT excited states formed at adjacent sites within the assembly, while the slow component is attributed to TTA between excited states that must undergo energy migration prior to annihilation. Femtosecond experiments are also performed on Ru(bpy)₃²⁺ (bpy = 2,2'-bipyridine) and a mixed-ligand Ru(II) complex that serves as a reference system for the polymer.

I. Introduction

During the past decade, there has been an intense interest in the development of molecular-based materials that are capable of performing complex functions.^{1–12} The ability to control the spatial arrangement of the molecular components is critical to the success of this endeavor, especially if intermolecular energy- and charge-transfer processes are at the core of the material's function. Derivatized polymers provide an attractive approach for arranging molecular components because they offer simplicity and flexibility in the design of molecular assemblies. The Meyer group has exploited this in their work on derivatized polystyrene,^{13–20} and the controlled positioning of chromophores and other components along a polymer backbone has been demonstrated by other groups as well.^{21–33} We are using ultrafast spectroscopic techniques to characterize the functional properties of the molecular assemblies synthesized in the Meyer group. These systems are composed of a polystyrene (PS) backbone derivatized with polypyridyl Ru(II)- or Os(II)-based chromophores or both. The chemical structure of a typical system, and the one that is studied in this work, is displayed in Figure 1.

The polymer chains consist of, on average, 20 repeat units, each one functionalized with a polypyridyl transition metal complex. The three-dimensional structure is greatly influenced by the large (14 Å diameter) metal dication monomer units. This is clearly evident in the structures calculated by molecular modeling,³⁴ one of which is depicted in Figure 2. The larger spheres are the transition-metal chromophores and the smaller spheres are the PF₆⁻ counter ions that surround the polymer of which the overall charge is +40. The densely loaded polymer adopts a twisted backbone and extended rodlike structure to alleviate the steric and Coulombic repulsions between adjacent complexes. One consequence of the dense loading is that the average distance between the peripheries of adjacent chromophores is 2–3 Å. It is this small spacing that makes efficient

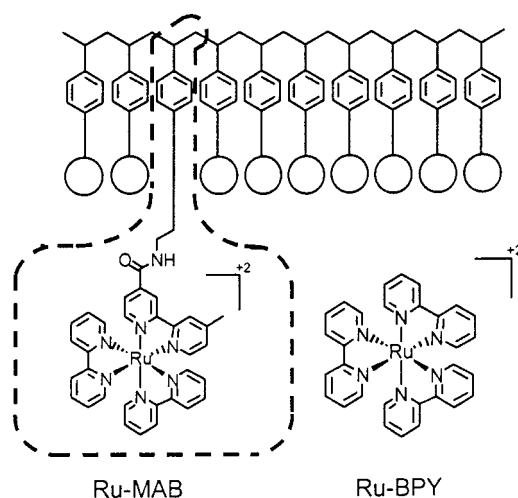


Figure 1. Chemical structures of the polymer assembly and two transition-metal complexes discussed in the text. Each polymer chain contains, on average, 20 repeat units. The open circles in the structure represent other transition-metal complexes that are not shown for clarity. The notation MAB in Ru-MAB refers to the presence of the monoamide functionalized ligand, while BPY denotes that all three ligands are 2,2'-bipyridine.

energy transport possible. The main role of the polymer backbone is thus to provide a structural support for holding the complexes in close proximity.

Photoexcitation of one of the Ru monomer units in the vicinity of 450 nm promotes the complex to a singlet metal-to-ligand charge-transfer (¹MLCT) excited state, which efficiently decays into a triplet state within a matter of a few hundred femtoseconds. The ³MLCT state has a lifetime of about 1 μs, providing adequate time for excited-state energy transfer to other members of the assembly.

In a recent paper, we presented a detailed study of the excited-state energy migration dynamics.³⁴ Although that work was performed on a slightly different polymer system than the one

* To whom correspondence should be addressed. E-mail: John_Papanikolas@unc.edu.

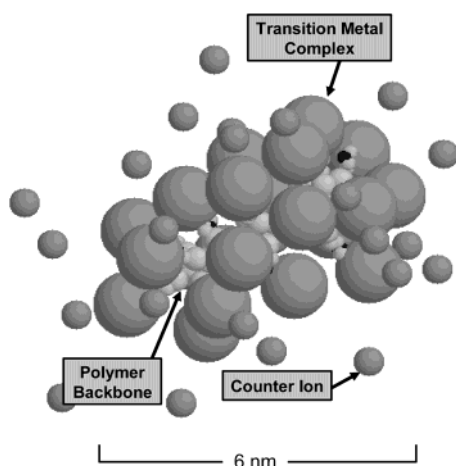


Figure 2. Structure of a polymer assembly containing 20 transition-metal complexes calculated by Monte Carlo simulations. Large spheres represent the metal complexes, and the small spheres are the PF_6^- counter ions.

described here, it revealed the presence of efficient energy migration along the polymer backbone, suggesting that these assemblies could perform light-harvesting functions in future molecular-scale solar energy conversion devices. Those energy migration studies were performed at low excitation irradiances to ensure that each chain had at most a single excited state.

At higher irradiance, multiple excited states can be formed on a single chain. These excited states can interact with each other, leading to additional deactivation pathways that could ultimately limit the polymer's light-harvesting capabilities. In this paper, we explore this triplet–triplet annihilation (TTA) process using femtosecond transient absorption spectroscopy. Our experiments provide the first definitive measure of a time scale for this process. They suggest that when two excited states are created next to each other, TTA occurs within just a few picoseconds. This deactivation process is not unique to our polymer but has been observed in a number of systems in which Ru(II) complexes are found in close proximity to each other.^{35–39}

II. Experimental Section

A complete description of the experimental apparatus has been provided elsewhere, so only a brief description will given here.⁴⁰ The transient absorption spectrometer is based on a commercially available ultrafast laser system (Clark CPA-2001), consisting of an erbium-doped fiber ring oscillator and a chirped pulse Ti:sapphire regenerative amplifier that is pumped by a frequency-doubled, mode-locked, Q-switched Nd:YAG laser. The amplifier produces 120 fs laser pulses at 775 nm at 1 kHz with pulse energies of approximately 950 $\mu\text{J}/\text{pulse}$. The amplified output is split into two beams by an uncoated glass window.

The larger, transmitted fraction (96%) pumps an optical parametric amplifier (OPA), which generates tunable femtosecond laser pulses used to excite the sample. For the experiments described here, the fourth harmonic of the OPA output is tuned to 442 nm. This is the pump beam used to excite the polymer sample. It is focused to a spot size of $\sim 500 \mu\text{m}$ at the sample. After passing through the sample, the pump beam is then directed into a photodiode for normalization of the transient absorption signal to changes in laser power.

The weak (4%) reflection from the front surface of the uncoated optic is used to generate the probe beam. This beam is directed into a computer-controlled translation stage that is used to vary the optical delay between pump and probe pulses. The resolution of the translation stage is 1 μm . After passing

through the delay stage, it is focused with a 150 mm focal-length lens into a 6 mm thick CaF_2 window to generate a white light continuum, which is then collimated with an 80 mm focal length achromatic lens. The white light is split into two weaker beams of nearly equal intensity by taking the reflections off the front and rear surfaces of a 2.5 cm thick quartz window. The front surface reflection, denoted the signal beam, is used for the probe pulse. The rear surface reflection is used as the reference beam in the transient absorption measurement. The signal and reference beams are focused to a spot size of $\sim 150 \mu\text{m}$ at the sample. While both beams are directed through the sample, only the signal is spatially overlapped with the pump beam. The signal and reference beams are simultaneously directed into a 0.27 m monochromator, dispersed with a 1200 line/mm holographic grating, and detected with a two-dimensional 1028×256 pixel liquid-nitrogen-cooled CCD array. This apparatus is capable of measuring a 77 nm segment of the transient absorption spectrum centered anywhere between 350 and 1000 nm with a sensitivity of better than 1 mOD.

The excited-state dynamics are followed through the evolution of the transient absorption spectra obtained at a series of pump–probe delay times. A typical data collection session consists of measuring transient absorption spectra at a series of 96 different pump–probe delay positions. First, the transient absorption spectrum at a given delay is measured. Ten exposures of the CCD camera are performed, and the spectra from each are averaged together before moving on to the next pump–probe delay position. The entire set of pump–probe delay positions is repeated at least three times, and the spectra obtained at like delays are averaged together. In some cases, the final spectrum represents a compilation of several different data collection sessions. Thus, each transient absorption spectrum represents an average over at least 24 000 (and in some instances as many as 150 000) laser pulses.

The PS–Ru₂₀ polymer and Ru-MAB monomer were obtained as PF_6^- salts as gifts from Thomas J. Meyer and used without further purification. The synthesis of these materials has been described elsewhere.^{14,41} Spectroscopy-grade acetonitrile was used as obtained from the vendor (Burdick and Jackson). All experiments were performed on room-temperature solutions of which the concentrations were adjusted to give an optical density of ~ 0.25 at 450 nm in a 2 mm path length cell.

III. Results and Discussion

The experiments discussed in this paper focus on the PS–Ru₂₀ homopolymer and the Ru-MAB complex, which serves as a reference system for the polymer. The ground-state absorption spectra of PS–Ru₂₀ and its corresponding monomer complex are displayed in Figure 3. The two spectra are remarkably similar, each showing a strong absorption centered at 450 nm. The similarities between the polymer and monomer spectra indicate that the polymer chains are well described as a collection of independent chromophores. This view is further supported by steady-state and time-resolved emission measurements, which yield nearly identical spectroscopic signatures for both the monomer and polymer, at least at low excitation intensities.³⁴ Together these observations justify the comparison between the monomer and the homopolymer.

To gain insight into Ru-MAB dynamics, we have also examined Ru(bpy)₃²⁺ (denoted Ru-BPY). While the Ru-MAB and Ru-BPY complexes are quite similar, the ligand asymmetry present in the Ru-MAB complex introduces some differences. The amide substituent used to link the complexes to the polymer

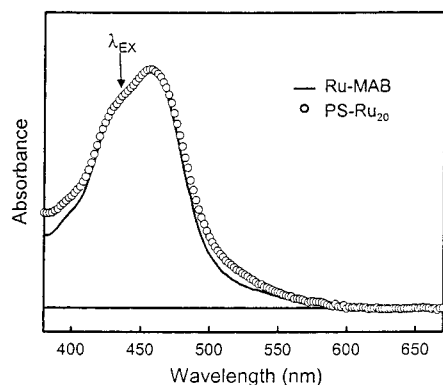


Figure 3. Comparison of the ground-state absorption spectra for PS-Ru₂₀ and its monomer complex, Ru-MAB. The arrow indicates the wavelength used to excite the samples.

increases the π network of the mab ligand orbitals, lowering their energy relative to the unfunctionalized bipyridine (bpy) ligand by about 700 cm^{-1} . Transient infrared experiments confirm this state ordering, showing that the photoexcited electron in Ru-MAB ultimately resides on the mab ligand.⁴² Despite the difference in energy, selective photoexcitation of a particular ligand is not possible, and thus the transfer of the MLCT excitation to the lowest energy ligand is an important relaxation pathway.

The excited-state spectra exhibited by the polymer will show kinetic evolution arising from processes that are intrinsic to the monomer as well as the polymer. In section A, we present the results of experiments performed on the monomer. These experiments enable us to identify the spectroscopic signatures of the monomer and at the same time provide insight into the excited-state dynamics of mixed-ligand polypyridyl complexes. Transient absorption experiments performed on the polymer are discussed in section B. These experiments complement our previously published energy migration studies.³⁴

A. Monomer Dynamics. The transient absorption spectra observed at 0.4 and 400 ps following photoexcitation of the Ru-MAB complex are displayed in Figure 4. These transient spectra are typical of those exhibited by ruthenium polypyridyl complexes, showing a strong ground-state bleach to the blue of $\sim 490\text{ nm}$ and a weak excited-state absorption to the red. A comparison of the early and late spectra shows that there is an overall increase of the transient absorbance during the first 400 ps. The kinetics of the growth is depicted in Figure 5, which shows the transient absorption signal at 475 nm as a function of pump-probe delay. The spectral changes occur with an *average* time constant of 3.9 ps. Closer inspection reveals biphasic kinetics with fast and slow time constants of 2 and 12 ps, respectively.

Generally speaking, transient absorption spectra are a superposition of signals that arise from the ground-state bleach, excited-state absorption, and stimulated emission. The ground-state bleach and stimulated emission contributions are both negative, while the contribution from excited-state absorption is positive. The observed increase in the transient absorption signal could be due to changes in any of these contributions.

Excited-state decay is one possibility. Relaxation back to the ground state would decrease the magnitude of both the absorption and bleach contributions, causing the transient absorption signal to decrease in magnitude. However, this process is dismissed because the lifetime of the lowest-energy MLCT state is on the order of $1\ \mu\text{s}$, and thus, there is essentially no ground-state recovery on the picosecond time scale. Another possibility is that the observed spectral changes reflect changes in

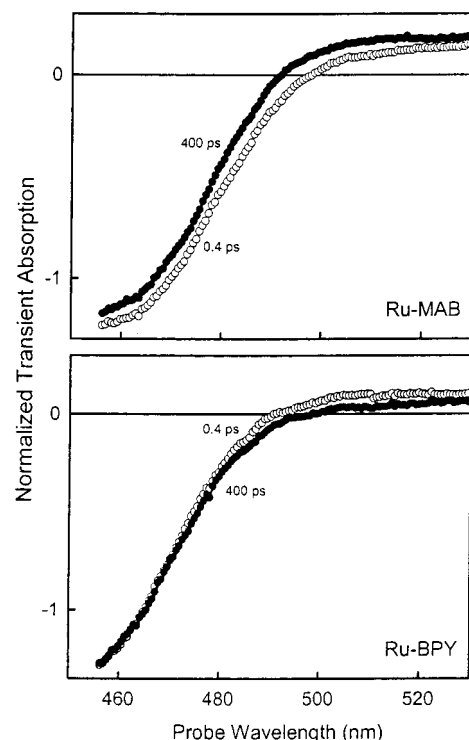


Figure 4. Transient absorption spectra for Ru-MAB (top panel) and Ru-BPY (bottom panel) observed following photoexcitation at 440 nm . Open (\circ) and filled (\bullet) circles correspond to spectra obtained at 0.4 and 400 ps after photoexcitation, respectively.

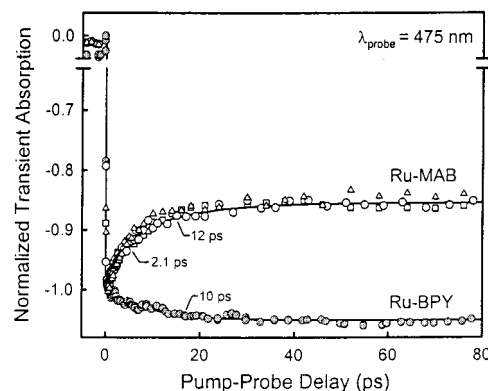


Figure 5. Transient absorption kinetics observed at a probe wavelength of 475 nm for both Ru-BPY and Ru-MAB. Three transients are shown for the Ru-MAB complex, which were obtained at different pump pulse energies: (\square) 0.25 ; (\circ) 0.6 ; (\triangle) $1.20\ \mu\text{J/pulse}$. For display purposes, all transients were scaled to have a value of -1 at zero pump-probe delay.

stimulated emission intensity. If this were the source of the spectral reshaping, then the growth amplitude should increase with increasing probe wavelength, because the luminescence peaks further to the red at 620 nm . This is not observed. The difference between the 0.4 and 400 ps transient spectra (Figure 6) shows that the maximum change in the transient absorption signal occurs in neighborhood of 480 nm . All in all, our observations suggest that the spectral reshaping in the monomer is due solely to a shift in the excited-state absorption rather than a change in the bleach or stimulated emission contributions.

In addition to single-photon dynamics, the evolution of the excited-state spectrum could result from processes initiated by the absorption of multiple photons. A power dependence study of the transient absorption spectra obtained from the Ru-MAB complex allows us to rule out effects due to multiphoton

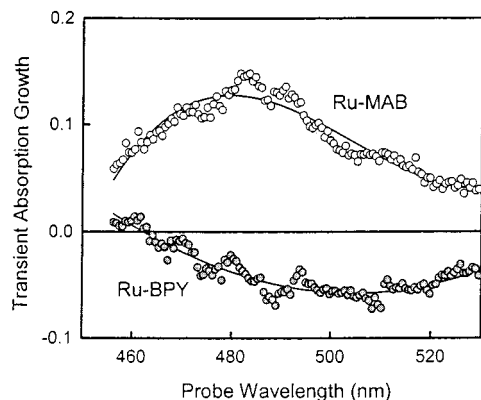


Figure 6. Growth in the transient absorption signal displayed as a function of probe wavelength. The individual points are obtained by taking the difference between the 0.4 and 400 ps spectra shown in Figure 4. Open (○) and filled (●) circles represent changes in the Ru-MAB and Ru-BPY spectra, respectively.

absorption. Shown in Figure 5 are the 475 nm transients obtained from Ru-MAB at a range of pump-pulse powers. Each transient is normalized to have a value of -1 at zero pump-probe delay. By normalizing the transients, we are in effect presenting the transient absorption *per excited state*. In this “normalized” format, the growth/decay kinetics that arise from single-photon processes will always appear the same (i.e., have the same shape), regardless of the excitation intensity. This is the case for the Ru-MAB data presented in Figure 5, indicating that the observed spectral changes stem from single-photon processes. Although we do not observe multiphoton effects, recent spectroscopic experiments on Ru-BPY performed under intense laser irradiation have shown that such processes are possible.⁴³ However, in those experiments, the laser intensities were more than 2 orders of magnitude larger than those used here.

Linking observed spectral changes to specific relaxation processes requires the assignment of the excited-state absorption feature(s). Spectroelectrochemical measurements performed by McCusker and co-workers⁴⁴ on similar Ru polypyridyl complexes suggest that the excited-state absorption is actually a superposition of two absorption features. One contribution comes from a $\pi\pi^*$ transition localized on the reduced polypyridyl ligand that is present in the MLCT excited state. This transition, which peaks at ~ 500 nm and has a long tail that extends to the red, should be sensitive to the substituents that are present on the polypyridyl ligand and could thus be a good spectral indicator of the location of the photoexcited electron. The second contribution to the excited-state absorption is suggested to come from a ligand-to-metal charge-transfer (LMCT) transition that is centered to the red of the $\pi\pi^*$ absorption. This excitation involves the promotion of an electron from one of the *neutral* polypyridyl ligands to the formally oxidized metal center. Thus, the blue edge of the excited-state absorption feature is most likely $\pi\pi^*$ in nature, whereas the red edge could contain contributions from both $\pi\pi^*$ and LMCT transitions. Our analysis of the transient spectra focuses primarily on probe wavelengths to the blue of the zero crossing, where the contribution from the LMCT transition is minimized.

As a benchmark for comparison, we have performed a similar set of experiments on the symmetric Ru-BPY complex under identical experimental conditions. The transient absorption spectra for Ru-BPY also show a strong bleach to the blue of 500 nm and a weak excited-state absorption to the red (Figure 4). In this respect, they are qualitatively similar to those observed for the asymmetric complex. The spectral reshaping that takes place in the Ru-BPY spectra is qualitatively different, however.

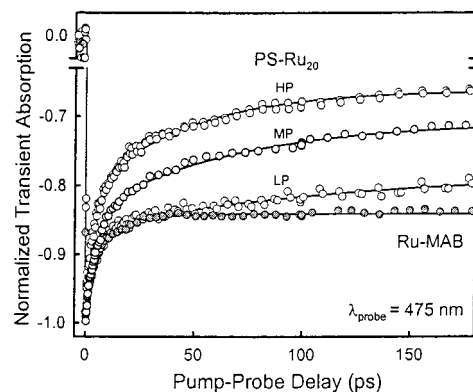


Figure 7. Transient absorption signal observed at 475 nm as a function of pump-probe delay. Open circles (○) represent data collected from PS-Ru₂₀ dissolved in CH₃CN. Three transients corresponding to high, medium, and low excitation irradiance conditions (HP, MP, and LP, respectively) are displayed for the polymer. The filled circles (●) are the data for the monomer complex, Ru-MAB. All four transients were scaled such that they had a value of unity at zero delay.

For probe wavelengths to the blue of 470 nm, the transient absorbance does not change after about 200 fs, consistent with ultrafast measurements performed in other laboratories. To the red of 470 nm, there is an overall *decrease* in the transient absorption. The kinetics at 475 nm are displayed in Figure 5 along with the mixed-ligand data. The decrease is well-described by a single exponential with a 10–12 ps time constant. This is similar to the slow time component observed in the asymmetric complex, suggesting that this dynamical process occurs in both systems. The slow time component could correspond to vibrational cooling or relaxation through the manifold of low-lying triplet states or both. It is interesting to note that if the same dynamical process is responsible for the slow spectral changes in both complexes, then it acts to increase the intensity of the excited-state absorption in the asymmetric complex and decrease it in Ru-BPY.

Unlike the mixed-ligand complex, Ru-BPY shows no evidence of a fast time component. This suggests that the dynamical process that gives rise to the 2 ps reshaping in Ru-MAB involves the mab ligand. One possibility is that it corresponds to the transfer of the MLCT excitation from one of the bpy ligands to the lower energy mab ligand in what amounts to interligand electron transfer (ILET). Measurements performed in our laboratory on the Os-MAB complex yield an ILET time of 1.5 ps, which is similar to the time constant observed here.⁴⁰ However, that assignment was made on the basis of polarization anisotropy data not spectral changes. Because evolution in the transient absorption spectra could result from a number of potential processes, including solvent reorganization and vibrational relaxation, a definitive conclusion cannot be reached on the basis of the available experimental data.

B. Polymer Dynamics. Transient absorption data has also been collected for the PS-Ru₂₀ polymer dissolved in acetonitrile under similar experimental conditions. The transient spectra observed for the polymer (not shown) have a qualitatively similar shape to those observed for the monomer complex. Furthermore, like the monomer, there is an overall increase in the *magnitude* of the transient absorption signal at later times; however, the kinetics of this growth are different. Shown in Figure 7 is the transient absorption signal at 475 nm as a function of pump-probe delay for both the polymer and monomer systems. The figure shows three polymer transients that correspond to low (0.2 μ J/pulse), medium (0.6 μ J/pulse), and high (1.2 μ J/pulse) power excitation conditions (denoted LP, MP,

TABLE 1: Summary of Parameters Obtained from Nonlinear Least Squares Analysis of the Polymer Transients Shown in Figure 7^a

	fit parameters				annihilation contribution	
	time constants (ps)		amplitudes		fast	total
	τ_f	τ_s	c_f	c_s	$c_f - c_f^{\text{LP}}$	$[c_f - c_f^{\text{LP}}] + c_s$
LP	4.3	105	0.14	0.08	0.00	0.08
MP	5.3	64	0.16	0.13	0.02	0.15
HP	3.5	44	0.19	0.15	0.05	0.20

^a The amplitudes for the annihilation contribution were obtained by assuming that the entire fast component observed in the low-power (LP) case is due to dynamics that take place within the monomer complex.

and HP, respectively). Each transient has been normalized to a value of -1 at zero delay. The most notable difference is that the growth in the transient absorption signal for the polymer depends on the intensity of the excitation laser, suggesting that a portion of the transient originates from a multiphoton process. Because multiphoton processes are not observed in the monomer complexes themselves, we attribute the power-dependent kinetics observed in the polymer to a triplet–triplet annihilation (TTA) process involving multiple excited states formed on a single chain.

As with the monomer spectra, the spectral changes stemming from the TTA process could arise from the ground-state bleach, excited-state absorption, or a combination of the two. An analysis of the transient spectra (discussed in more detail below) suggests that these changes result from the replenishment of the ground-state population. That is, TTA results in the simultaneous decay of both the absorption and the bleach.

To quantify the transient absorption changes, we have fit each of the polymer decays to a sum of two exponentials,

$$A(t) = c_f \exp\left(-\frac{t}{\tau_f}\right) + c_s \exp\left(-\frac{t}{\tau_s}\right) \quad (1)$$

where τ_f and τ_s are the time constants of the fast and slow components, respectively, and c_f and c_s are their corresponding amplitudes. The results are provided in Table 1. The use of a biexponential model is not meant to imply that the polymer should be viewed as a two-state system, which it most certainly is not, but rather to provide a quantitative description of the temporal kinetics.

At low excitation intensities, the polymer's fast component (4.3 ps) has a time constant that is very close to average time constant observed in the monomer (3.9 ps). The amplitude of this component is similar to that observed in the monomer, representing 14–16% of the total signal in both cases. The similarity between the LP polymer and the monomer data at early times suggests that these spectral changes arise almost entirely from the individual monomer complexes. In addition to the fast evolution, the polymer also exhibits a slow (105 ps) annihilation component.

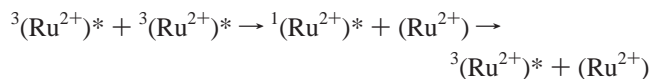
At the higher excitation intensities (MP and HP), the differences between the polymer and monomer transients become more pronounced. The first difference is that there is an overall increase in the total amplitude of the annihilation component at the higher laser powers. Whereas at low powers this amplitude is approximately 8%, at the higher excitation intensities it is closer to 20% (Table 1). The second difference is that the annihilation kinetics at the higher excitation irradiances cannot be described by a single rate constant. The high-power (HP) transient shows clear evidence of this, and the nonlinear least-squares analysis extracts both a fast (3–4 ps)

and a slow (40–50 ps) component. The time constant of the fast component appears to be independent of the excitation intensity (Table 1). This is not true of the slow component, however, which varies from 105 ps at the lowest power studied to about 44 ps at the highest. The amplitudes of both components increase with increasing excitation intensity.

We assign the fast (3–5 ps) time component to the time scale for TTA when the two excited states are formed at sites adjacent to each other. The amplitude of this component in the *normalized* transient corresponds roughly to the number of adjacent excited-state pairs that are formed in the photoexcitation process divided by the total number of excited states, that is, $N_{\text{PAIRS}}/N_{\text{ES}}$. Because N_{PAIRS} scales with the square of the laser power and N_{ES} scales linearly, the fast amplitude is only expected to exhibit linear power dependence. The fast annihilation amplitudes presented in Table 1 are consistent with this expectation. Namely, this amplitude in the HP (1.2 $\mu\text{J}/\text{pulse}$) transient is about double that observed in the MP (0.6 $\mu\text{J}/\text{pulse}$) case. Our assignment of the fast component to the TTA of adjacent pairs indicates that the Ru^*-Ru^* annihilation time is in the vicinity of 3–5 ps. Ultrafast TTA of Ru(II) excited states has been observed in other systems as well; however, in those studies, the instrumental time resolution prevented the measurement of a definitive TTA time scale.^{36,39}

The slow component is assigned to excited-state pairs that must undergo energy migration prior to deactivation. Although we have not examined the energy migration in this polymer system, we have investigated the $\text{Ru}^* \rightarrow \text{Ru}$ energy transfer in a slightly different polymer.³⁴ Those experiments suggest transfer times in the range of 1–4 ns. The time scale for the formation of an excited-state pair and the energy-transfer time, while related to each other, are not numerically equivalent. For example, in the simple case of a linear trimer with two excited states (i.e., $\text{Ru}^*-\text{Ru}-\text{Ru}^*$), pair formation can be achieved via energy transfer of either complex to give $\text{Ru}-\text{Ru}^*-\text{Ru}^*$ or $\text{Ru}^*-\text{Ru}^*-\text{Ru}$. In this situation, the pair would be formed on a time scale that is half of the energy-transfer time. In reality, the number of pathways will depend on the number of nearest neighbors, as well as the number of excited states created per chain. For a given distribution of excited states, the pair-formation time is reduced from the energy-transfer time by the number of possible ways that pair can be formed. Monte Carlo simulations suggest that each complex has approximately 4–5 nearest neighbors. As a result, the reduction from the energy-transfer time could be substantial and account for our observations. In principle, an analysis of the slow component could yield information about the energy migration/TTA process. However, the slow component reflects a combination of both excited-state energy migration and TTA, and definitive information regarding energy transfer in this polymer is not currently available. Furthermore, we only observe the first 200 ps of this process, which probably represents the very beginning of a multiexponential decay that may continue for nanoseconds. For these reasons, we have opted not to pursue such an analysis at this time.

Annihilation Mechanism. There are two triplet–triplet deactivation mechanisms that could lead to the observed power-dependent signals. Annihilation via energy transfer is one possibility,



where the singlet state formed in the first step decays rapidly

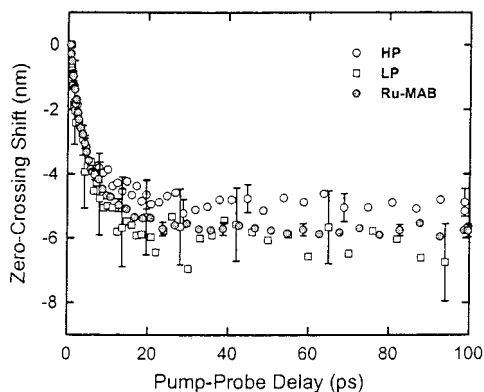
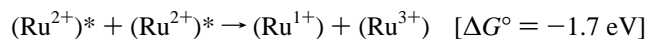


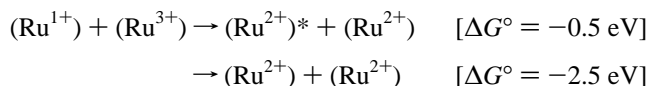
Figure 8. Plot of the shift in the transient absorption zero-crossing point as a function of pump-probe delay. The filled circles (●) represent the Ru-MAB monomer data and the open squares (□) and circles (○) are obtained from the low- and high-power polymer spectra, respectively. In all cases, the zero-crossing starts at about 501 nm and shifts by approximately 5–6 nm to the blue.

(~200 fs) to the triplet in the second.⁴⁴ Because the second step is so rapid, the net result observed in the experiment is the replenishment of the ground-state population. (In this notation, the (Ru²⁺) refers to a single Ru(II) coordination complex within the array.)

Electron-transfer between *two* photoexcited complexes is another possible mechanism,



This reaction amounts to the transfer of an electron from the bpy⁻ of one (Ru²⁺)^{*} complex to the metal center of the other. The oxidized and reduced species are present only transiently and are returned to their original charge states via a back electron-transfer reaction,



The first reaction produces a single excited state, while the second yields two ground-state species. Both are energetically downhill, but the large driving force of the second puts it far into the inverted regime. As a result ground-state production via the second reaction is not an important pathway.⁴⁵

These two annihilation mechanisms should have different signatures in the transient absorption spectra. Annihilation via energy transfer will uniformly decrease the magnitude of the transient spectra but not alter their shape. In contrast, annihilation through electron transfer will lead to the formation of charge-transfer products, which will not have the same absorption spectrum as the (Ru²⁺)^{*} species. The (Ru³⁺) complex absorbs only weakly in this spectral region. The (Ru¹⁺) complex, on the other hand, has a strong MLCT absorption band centered at 500 nm.^{46–48} If back electron transfer were slow, then there should be a significant build-up in the charge-transfer product, which would change the shape of the transient spectra.

To determine whether there is a shape change in the polymer spectra, beyond that introduced by the monomer, we have examined the location of the transient absorption zero crossing as a function of pump–probe delay. This is displayed for the monomer and the HP and LP data sets of the polymer in Figure 8. The zero crossing for the monomer appears at 495 nm and then during the first few picoseconds shifts by about 5–6 nm to the blue. Within experimental error, the shifts exhibited by polymer are identical to that of the monomer, at both excitation

intensities. This indicates that either TTA proceeds through an energy-transfer mechanism or the rate of back electron transfer in the charge separation pathway is sufficiently fast that there is no appreciable build-up of the charge-transfer product.

Triplet–triplet annihilation has been observed in other systems as well. Work on dye-functionalized TiO₂ films³⁵ showed intensity-dependent signals that were attributed to fast ($k > 10^8 \text{ s}^{-1}$) TTA among the densely packed Ru(II) complexes in the mesoporous film. As in our experiments, no charge-separated products were observed; however, it was pointed out that this might just be the result of a fast back electron-transfer reaction. Some evidence for the formation of charge-separated products does exist in the literature.^{36,39} The presence of charge separation in single crystals of Ru-BPY was concluded on the basis of a 500 nm feature that appeared in the transient absorption spectra shortly after photoexcitation. The absorption feature emerged within 40 ps (limited by the time resolution of the instrument) and decayed away within several hundred picoseconds. Similar results have been reported for Ru(II)–Ru(II) dimers.³⁹

IV. Conclusions

The triplet–triplet annihilation (TTA) process between MLCT excited states of Ru(II) polypyridyl complexes bound to polystyrene is studied using femtosecond transient absorption spectroscopy. The polymers show clear power-dependent signals on a 3–5 ps time scale that are attributed to TTA between excited states formed adjacent to each other on the polymer chain. Decay on slower time scales is also observed, which could result from excited-state pairs that undergo energy migration prior to deactivation.

The transient spectra show no clear evidence of an additional change in spectral shape, beyond that introduced by the monomer complex. This suggests that TTA proceeds either through an energy-transfer mechanism or through an electron-transfer process to give charge-separated products that then rapidly undergo back electron transfer.

Acknowledgment. Funding for this project was provided by the Research Corporation (RI0048), the Petroleum Research Fund administered by the ACS, and the University of North Carolina at Chapel Hill.

References and Notes

- (1) Alivisatos, A. P.; Barbara, P. F.; Castleman, A. W.; Chang, J.; Dixon, D. A.; Klein, M. L.; McLendon, G. L.; Miller, J. S.; Ratner, M. A.; Rossky, P. J.; Stupp, S. I.; Thompson, M. E. *Adv. Mater.* **1998**, *10*, 1297–1336.
- (2) Balzani, V.; Gomez-Lopez, M.; Stoddart, J. F. *Acc. Chem. Res.* **1998**, *31*, 405–414.
- (3) Balzani, V.; Juris, A.; Venturi, M.; Campagna, S.; Serroni, S. *Chem. Rev.* **1996**, *96*, 759–833.
- (4) Collier, C. P.; Mattersteig, G.; Wong, E. W.; Luo, Y.; Beverly, K.; Sampaio, J.; Raymo, F. M.; Stoddart, J. F.; Heath, J. R. *Science* **2000**, *289*, 1172–1175.
- (5) Heath, J. R. *Acc. Chem. Res.* **1999**, *32*, 388.
- (6) Piotrowiak, P. *Chem. Soc. Rev.* **1999**, *28*, 143–150.
- (7) Fabbri, L.; Licchelli, M.; Pallavicini, P. *Acc. Chem. Res.* **1999**, *32*, 846–853.
- (8) Ward, M. D. *Chem. Soc. Rev.* **1997**, *26*, 364–375.
- (9) Benniston, A. C. *Chem. Soc. Rev.* **1996**, *25*, 427–435.
- (10) Reimers, J. R.; Lu, T. X.; Crossley, M. J.; Hush, N. S. *Nanotechnology* **1996**, *7*, 424–429.
- (11) Krusche, M. J.; Lehn, J. M. The Utilization of Persistent H-Bonding Motifs in the Self-Assembly of Supramolecular Architectures. In *Molecular self-assembly: organic versus inorganic approaches*; Fujita, M., Ed.; Springer: Berlin, 2000; Vol. 96, pp 3–29.
- (12) Ziener, U.; Breuning, E.; Lehn, J. M.; Wegelius, E.; Rissanen, K.; Baum, G.; Fenske, D.; Vaughan, G. *Chem.—Eur. J.* **2000**, *6*, 4132–4139.

- (13) Worl, L. A.; Jones, W. E.; Strouse, G. F.; Younathan, J. N.; Danielson, E.; Maxwell, K. A.; Sykora, M.; Meyer, T. J. *Inorg. Chem.* **1999**, *38*, 2705–2708.
- (14) Friesen, D. A.; Kajita, T.; Danielson, E.; Meyer, T. J. *Inorg. Chem.* **1998**, *37*, 2756–2762.
- (15) Maxwell, K. A.; Dupray, L. M.; Meyer, T. J. *Polym. Prepr. (Am. Chem. Soc., Div. Polym. Chem.)* **1997**, *38*, 329–330.
- (16) Dupray, L. M.; Meyer, T. J. *Inorg. Chem.* **1996**, *35*, 6299–6307.
- (17) Jones, W. E.; Baxter, S. M.; Strouse, G. F.; Meyer, T. J. *J. Am. Chem. Soc.* **1993**, *115*, 7363–7373.
- (18) Dupray, L. M.; Devenney, M.; Striplin, D. R.; Meyer, T. J. *J. Am. Chem. Soc.* **1997**, *119*, 10243–10244.
- (19) Peters, M. A.; Belu, A. M.; Linton, R. W.; Dupray, L. M.; Meyer, T. J.; DeSimone, J. M. *J. Am. Chem. Soc.* **1995**, *117*, 3380–3388.
- (20) Sykora, M.; Maxwell, K. A.; DeSimone, J. M.; Meyer, T. J. *Proc. Natl. Acad. Sci. U.S.A.* **2000**, *97*, 7687–7691.
- (21) Wong, K. T.; Lehn, J. M.; Peng, S. M.; Lee, G. H. *Chem. Commun.* **2000**, 2259–2260.
- (22) Galoppini, E.; Fox, M. A. *J. Am. Chem. Soc.* **1996**, *118*, 2299–2300.
- (23) Clements, J. H.; Webber, S. E. *J. Phys. Chem. B* **1999**, *103*, 9366.
- (24) Clements, J. H.; Webber, S. E. *J. Phys. Chem. A* **1999**, *103*, 2513–2523.
- (25) Schillén, K.; Yekta, A.; Ni, S.; Farinha, J. P. S.; Winnik, M. A. *J. Phys. Chem. B* **1999**, *103*, 9090–9103.
- (26) Rharbi, Y.; Yekta, A.; Winnik, M. A.; DeVoe, R. J.; Barrera, D. *Macromolecules* **1999**, *32*, 3241–3248.
- (27) Walters, K. A.; Trouillet, L.; Guillerez, S.; Schanze, K. S. *Inorg. Chem.* **2000**, *39*, 5496–5509.
- (28) Walters, K. A.; Ley, K. D.; Schanze, K. S. *Langmuir* **1999**, *15*, 5676–5680.
- (29) Mcquade, D. T.; Pullen, A. E.; Swager, T. M. *Chem. Rev.* **2000**, *100*, 2537–2574.
- (30) Swager, T. M. *Acc. Chem. Res.* **1998**, *31*, 201–207.
- (31) Chen, L. X.; Jäger, W. J. H.; Gosztola, D. J.; Niemczyk, M. P.; Wasielewski, M. R. *J. Phys. Chem. B* **2000**, *104*, 1950–1960.
- (32) Chen, L. X.; Jäger, W. J. H.; Niemczyk, M. P.; Wasielewski, M. R. *J. Phys. Chem. A* **1999**, *103*, 4341–4351.
- (33) Wolcan, E.; Ferraudi, G. *J. Phys. Chem. A* **2000**, *104*, 9281–9286.
- (34) Fleming, C. N.; Maxwell, K. A.; Meyer, T. J.; Papanikolas, J. M. *J. Am. Chem. Soc.* **2001**, 10336–10347.
- (35) Kelly, C. A.; Farzad, F.; Thompson, D. W.; Meyer, G. J. *Langmuir* **1999**, *15*, 731–737.
- (36) Ikeda, N.; Yoshimura, A.; Tsushima, M.; Ohno, T. *J. Phys. Chem. A* **2000**, *104*, 6158–6164.
- (37) Sykora, M.; Kincaid, J. R.; Dutta, P. K.; Castagnola, N. B. *J. Phys. Chem. B* **1999**, *103*, 309–320.
- (38) Milosavijevic, B. H.; Thomas, J. K. *J. Phys. Chem.* **1983**, *87*, 616–621.
- (39) Nozaki, K.; Ikeda, N.; Ohno, T. *New J. Chem.* **1996**, *20*, 739–748.
- (40) Shaw, G. B.; Brown, C. L.; Papanikolas, J. M. *J. Phys. Chem. A* **2002**, *106*, 1483–1495.
- (41) Maxwell, K. A. Doctoral Dissertation, University of North Carolina at Chapel Hill, 1999.
- (42) Smith, G. D.; Maxwell, K. A.; Desimone, J. M.; Meyer, T. J.; Palmer, R. A. *Inorg. Chem.* **2000**, *39*, 893–898.
- (43) Thompson, D. W.; Wishart, J. F.; Brunshwig, B. S.; Sutin, N. *J. Phys. Chem. A* **2001**, *105*, 8117–8122.
- (44) Damrauer, N. H.; Cerullo, G.; Yeh, A.; Boussie, T. R.; Shank, C. V.; McCusker, J. K. *Science* **1997**, *275*, 54–57.
- (45) Wallace, W. L.; Bard, A. J. *J. Phys. Chem.* **1979**, *83*, 1350–1357.
- (46) Coombe, V. T.; Heath, G. A.; MacKenzie, A. J.; Yellowlees, L. J. *Inorg. Chem.* **1984**, *23*, 3423–3425.
- (47) Heath, G. A.; Yellowlees, L. J.; Braterman, P. S. *Chem. Commun.* **1981**, 287–289.
- (48) Anderson, C. P.; Salmon, D. J.; Meyer, T. J.; Young, R. C. *J. Am. Chem. Soc.* **1977**, *99*, 1980–1982.

Ultrafast Excited-State Energy Migration Dynamics in an Efficient Light-Harvesting Antenna Polymer Based on Ru(II) and Os(II) Polypyridyl Complexes

Cavan N. Fleming, Kimberly A. Maxwell, Joseph M. DeSimone, Thomas J. Meyer,[†] and John M. Papanikolas*

Contribution from the Department of Chemistry, Venable and Kenan Laboratories, The University of North Carolina at Chapel Hill, Chapel Hill, North Carolina 27599-3290

Received May 29, 2001

Abstract: A detailed study of the excited state energy migration dynamics that take place within an assembly of Ru(II) and Os(II) polypyridyl complexes linked together through a polymer backbone is presented. The energy migration process is initiated by the photoexcitation of the metal-to-ligand charge transfer (MLCT) transition in one of the Ru(II) complexes and terminated by energy transfer to a lower energy Os(II) trap. Energy transfer sensitization of Os(II) can occur in a single step if the excited state is formed adjacent to a trap, or after a series of hops between isoenergetic rutheniums prior to reaching a trap. The dynamics of the energy transfer process are followed by monitoring the growth of Os(II)* luminescence at 780 nm. The kinetics of the growth are complex and can be fit by a sum of two exponentials. This kinetic complexity arises both from the presence of a distribution of donor–acceptor distances and the variety of time scales by which Os(II)* can be formed. We have augmented the time-resolved experiments with Monte Carlo simulations, which provide insight into the polymer array's structure and at the same time form the basis of a molecular-level description of the energy migration dynamics. The simulations indicate that the most probable Ru*→Os energy transfer time is ~400 ps while the time scale for Ru*→Ru hopping is approximately 1–4 ns. The time scale for Ru*→Ru hopping relative to its natural lifetime (1000 ns) suggests that this polymer system could be extended to considerably longer dimensions without an appreciable loss in its overall efficiency.

I. Introduction

One strategy for designing functional nanoscale materials is to organize molecular constituents into assemblies that perform complex functions.^{1–12} A critical factor in the development of such materials is the ability to control the spatial arrangement of the molecular components, especially if intermolecular energy- and charge-transfer processes are at the core of the material's function. Spatial organization can be achieved through the design of covalently bonded supramolecules in which

molecular subunits are linked together so that their relative geometries (i.e. separations and orientations) are well defined.^{13–19} Structures of this kind are demanding to synthesize, but offer the greatest amount of control over structural parameters. An alternative method utilizes disordered supports to organize the necessary components.^{20–38} Derivatized polymers are attractive for the positioning of molecular constituents because they offer

[†] Present address: Los Alamos National Laboratory MS A127, Los Alamos, NM 87545.

(1) Alivisatos, A. P.; Barbara, P. F.; Castleman, A. W.; Chang, J.; Dixon, D. A.; Klein, M. L.; McLendon, G. L.; Miller, J. S.; Ratner, M. A.; Rosky, P. J.; Stupp, S. I.; Thompson, M. E. *Adv. Mater.* **1998**, *10* (16), 1297–1336.

(2) Balzani, V.; Gomez-Lopez, M.; Stoddart, J. F. *Acc. Chem. Res.* **1998**, *31*, 405–414.

(3) Balzani, V.; Juris, A.; Venturi, M.; Campagna, S.; Serroni, S. *Chem. Rev.* **1996**, *96*, 759–833.

(4) Collier, C. P.; Mattersteig, G.; Wong, E. W.; Luo, Y.; Beverly, K.; Sampaio, J.; Raymo, F. M.; Stoddart, J. F.; Heath, J. R. *Science* **2000**, *289* (5482), 1172–1175.

(5) Heath, J. R. *Acc. Chem. Res.* **1999**, *32* (5), 388.

(6) Piotrowiak, P. *Chem. Soc. Rev.* **1999**, *28*, 143–150.

(7) Fabbri, L.; Licchelli, M.; Pallavicini, P. *Acc. Chem. Res.* **1999**, *32*, 846–853.

(8) Ward, M. D. *Chem. Soc. Rev.* **1997**, *26*, 364–375.

(9) Benniston, A. C. *Chem. Soc. Rev.* **1996**, 427–435.

(10) Reimers, J. R.; Lu, T. X.; Crossley, M. J.; Hush, N. S. *Nanotechnology* **1996**, *7*, 424–429.

(11) Krische, M. J.; Lehn, J. M. *Struct. Bonding* **2000**, *96*, pp 3–29.

(12) Ziener, U.; Breuning, E.; Lehn, J. M.; Wegelius, E.; Rissanen, K.; Baum, G.; Fenske, D.; Vaughan, G. *Chem. Eur. J.* **2000**, *6* (22), 4132–4139.

(13) Kleverlaan, C. J.; Indelli, M. T.; Bignozzi, C. A.; Pavanin, L.; Scandola, F.; Hasselman, G. M.; Meyer, G. J. *J. Am. Chem. Soc.* **2000**, *122* (12), 2840–2849.

(14) Bignozzi, C. A.; Argazzi, R.; Kleverlaan, C. J. *Chem. Soc. Rev.* **2000**, *29* (2), 87–96.

(15) Bignozzi, C. A.; Schoonover, J. R.; Scandola, F. *Prog. Inorg. Chem.* **1997**, *44*, 1–95.

(16) Gust, D.; Moore, T. A.; Moore, A. L. *J. Photochem. Photobiol., B* **2000**, *58* (2–3), 63–71.

(17) Gust, D.; Moore, T. A.; Moore, A. L. *Acc. Chem. Res.* **2001**, *34* (1), 40–48.

(18) Hissler, M.; McGarrah, J. E.; Connick, W. B.; Geiger, D. K.; Cummings, S. D.; Eisenberg, R. *Coord. Chem. Rev.* **2000**, *208*, 115–137.

(19) Slate, C. A.; Striplin, D. R.; Moss, J. A.; Chen, P.; Erickson, B. W.; Meyer, T. J. *J. Am. Chem. Soc.* **1998**, *120*, 4885–4886.

(20) Mallouk, T. E.; Gavin, J. A. *Acc. Chem. Res.* **1998**, *31*, 209–217.

(21) Kaschak, D. M.; Lean, J. T.; Waraksa, C. C.; Saupe, G. B.; Usami, H.; Mallouk, T. E. *J. Am. Chem. Soc.* **1999**, *121*, 3435–3445.

(22) Kaschak, D. M.; Johnson, S. A.; Waraksa, C. C.; Pogue, J.; Mallouk, T. E. *Coord. Chem. Rev.* **1999**, *186*, 403–416.

(23) Kincaid, J. R. *Chem. Eur. J.* **2000**, *6* (22), 4055–4061.

(24) Wu, A.; Yoo, D.; Lee, J. K.; Rubner, M. F. *J. Am. Chem. Soc.* **1999**, *121* (20), 4883–4891.

(25) Mattoussi, H.; Rubner, M. F.; Zhou, F.; Kumar, J.; Tripathy, S. K.; Chiang, L. Y. *Appl. Phys. Lett.* **2000**, *77* (10), 1540–1542.

(26) Baur, J. W.; Rubner, M. F.; Reynolds, J. R.; Kim, S. *Langmuir* **1999**, *15* (19), 6460–6469.

(27) Lee, J. K.; Yoo, D.; Rubner, M. F. *Chem. Mater.* **1997**, *9* (8), 1710.

flexibility and simplicity in the design of multicomponent assemblies. The Meyer group has explored this approach in their work on derivatized polystyrene,^{39–46} and the controlled positioning of chromophores and other components along a polymer backbone has been demonstrated by other groups as well.^{47–59} In this paper we describe ultrafast spectroscopic experiments that are aimed at characterizing the light-harvesting function of a polymer derivatized with Ru(II) and Os(II) chromophores.

The functional capabilities of light-harvesting systems can be quantified on the basis of the efficiency with which they conduct excited-state energy. For efficient conduction to occur, the time scale for energy transfer must be fast compared to the lifetime of the excited state. For example, if the time scale for an excited state to hop to an adjacent site is 10 times faster than its lifetime, energy transfer will occur with 90% efficiency.

(28) Shortreed, M. R.; Swallen, S. F.; Shi, Z.; Tan, W.; Xu, Z.; Devadoss, C.; Moore, J. S.; Kopelman, R. *J. Phys. Chem. B* **1997**, *101*, 6318.

(29) Devadoss, C.; Bharathi, P.; Moore, J. S. *J. Am. Chem. Soc.* **1996**, *118*, 9635.

(30) Balzani, V.; Campagna, S.; Denti, G.; Juris, A.; Serroni, S.; Venturi, M. *Acc. Chem. Res.* **1998**, *31*, 26–34.

(31) Jiang, D.; Aida, T. *J. Am. Chem. Soc.* **1998**, *120*, 10895.

(32) Adronov, A.; Gilat, S. L.; Fréchet, J. M. J.; Ohta, K.; Neuwahl, F. V. R.; Fleming, G. R. *J. Am. Chem. Soc.* **2000**, *122* (6), 1175–1185.

(33) Neuwahl, F. V. R.; Righini, R.; Adronov, A.; Malenfant, P. R. L.; Fréchet, J. M. J. *J. Phys. Chem. B* **2001**, *105*, 1307.

(34) Vögtle, F.; Plevovets, M.; Nieger, M.; Azzellini, G. C.; Credi, A.; Cola, L. D.; Marchis, V. D.; Venturi, M.; Balzani, V. *J. Am. Chem. Soc.* **1999**, *121*, 6290–6298.

(35) Newkome, G. R.; He, E.; Moorefield, C. N. *Chem. Rev.* **1999**, *99*, 1689–1746.

(36) Stewart, G. M.; Fox, M. A. *Chem. Mater.* **1998**, *10*, 860.

(37) Storrier, G. D.; Takada, K.; Abruña, H. D. *Langmuir* **1999**, *15*, 872–884.

(38) Yeow, E. K. L.; Ghiggino, K. P.; Reek, J. N. H.; Crossley, M. J.; Bosman, A. W.; Schenning, A. P. H. J.; Meijer, E. W. *J. Phys. Chem. B* **2000**, *104* (12), 2596–2606.

(39) Worl, L. A.; Jones, W. E.; Strouse, G. F.; Younathan, J. N.; Danielson, E.; Maxwell, K. A.; Sykora, M.; Meyer, T. J. *Inorg. Chem.* **1999**, *38* (11), 2705–2708.

(40) Friesen, D. A.; Kajita, T.; Danielson, E.; Meyer, T. J. *Inorg. Chem.* **1998**, *37* (11), 2756–2762.

(41) Maxwell, K. A.; Dupray, L. M.; Meyer, T. J. *Polym. Prepr. (Am. Chem. Soc., Div. Polym. Chem.)* **1997**, *38*, 329–330.

(42) Dupray, L. M.; Meyer, T. J. *Inorg. Chem.* **1996**, *35* (21), 6299–6307.

(43) Jones, W. E.; Baxter, S. M.; Strouse, G. F.; Meyer, T. J. *J. Am. Chem. Soc.* **1993**, *115* (16), 7363–7373.

(44) Dupray, L. M.; Devenney, M.; Striplin, D. R.; Meyer, T. J. *J. Am. Chem. Soc.* **1997**, *119* (42), 10243–10244.

(45) Peters, M. A.; Belu, A. M.; Linton, R. W.; Dupray, L. M.; Meyer, T. J.; DeSimone, J. M. *J. Am. Chem. Soc.* **1995**, *117* (12), 3380–3388.

(46) Sykora, M.; Maxwell, K. A.; DeSimone, J. M.; Meyer, T. J. *Proc. Natl. Acad. Sci. U.S.A.* **2000**, *97* (14), 7687–7691.

(47) Wong, K. T.; Lehn, J. M.; Peng, S. M.; Lee, G. H. *Chem. Commun.* **2000**, *22*, 2259–2260.

(48) Galoppini, E.; Fox, M. A. *J. Am. Chem. Soc.* **1996**, *118* (9), 2299–2300.

(49) Clements, J. H.; Webber, S. E. *J. Phys. Chem. B* **1999**, *103*, 9366.

(50) Clements, J. H.; Webber, S. E. *J. Phys. Chem. A* **1999**, *103*, 2513–2523.

(51) Schillén, K.; Yekta, A.; Ni, S.; Farinha, J. P. S.; Winnik, M. A. *J. Phys. Chem. B* **1999**, *103*, 9090–9103.

(52) Rharbi, Y.; Yekta, A.; Winnik, M. A.; DeVoe, R. J.; Barrera, D. *Macromolecules* **1999**, *32*, 3241–3248.

(53) Walters, K. A.; Trouillet, L.; Guillerez, S.; Schanze, K. S. *Inorg. Chem.* **2000**, *39* (24), 5496–5509.

(54) Walters, K. A.; Ley, K. D.; Schanze, K. S. *Langmuir* **1999**, *15* (17), 5676–5680.

(55) Mcquade, D. T.; Pullen, A. E.; Swager, T. M. *Chem. Rev.* **2000**, *100* (7), 2537–2574.

(56) Swager, T. M. *Acc. Chem. Res.* **1998**, *31* (5), 201–207.

(57) Chen, L. X.; Jäger, W. J. H.; Gosztola, D. J.; Niemczyk, M. P.; Wasielewski, M. R. *J. Phys. Chem. B* **2000**, *104* (9), 1950–1960.

(58) Chen, L. X.; Jäger, W. J. H.; Niemczyk, M. P.; Wasielewski, M. R. *J. Phys. Chem. A* **1999**, *103* (22), 4341–4351.

(59) Wolcan, E.; Ferraudi, G. *J. Phys. Chem. A* **2000**, *104* (41), 9281–9286.

Thus efficient energy migration is best achieved by combining fast energy transfer between monomer units with long-lived excited states.

A number of attempts have been made to mimic the energy transfer capabilities of biological photosynthetic systems. Early efforts focused on methacrylate polymers functionalized with naphthalene- and anthracene-based chromophores.^{60–62} Following photoexcitation, the naphthalene excited state migrates along the polymer backbone until it is quenched by energy transfer to an anthracene trap that exists in low concentrations (~1%). A wide range of efficiencies has been reported for different systems; however, in general the efficiencies are much less than unity, ranging from 30 to 80%. Fox and co-workers^{63–66} investigated a series of diblock and triblock copolymer systems that couple energy migration with electron transfer. In these systems, the rate of energy migration ($\tau \sim 300$ ps) is comparable to the lifetime of the photoexcited donor ($\tau \sim 4$ ns).

Efficient energy conduction has also been observed in porphyrin arrays, and a great deal has been learned about the energy transfer dynamics in these multicentered systems.^{67–73} In the case of a Zn/free-base porphyrin dimer, energy transfer to the free base subunit occurs with an efficiency of greater than 95%. When the system is extended to a trimer with two isoenergetic Zn porphyrin donors, the energy hopping between donors occurs with a time constant of ≈ 50 ps, or 40 times faster than the natural lifetime of the monomer. One consequence of the intrinsically short excited-state lifetime is that energy hopping competes with the decay of the excited state, limiting the energy transfer efficiency. This effect is magnified when there are multiple energy transfer steps. The reported efficiency⁷³ for donor and acceptor separated by three isoenergetic Zn porphyrins is 76% and calculations indicate that this drops to 13% when the array is extended to 20 monomer units.⁷¹

In this paper we describe an ultrafast spectroscopic investigation of the photoinduced energy migration dynamics that take place within a supramolecular assembly consisting of 20 Ru(II) and/or Os(II) polypyridyl coordination complexes linked together through a polystyrene backbone (Figure 1). Our experiments are performed on a solution of polymer chains dissolved in acetonitrile, and thus probe the dynamics that occur within individual assemblies. Energy migration is initiated by photoexcitation of one of the Ru(II) complexes and terminated upon energy transfer to a lower energy Os(II) trap. We find that when there is an average of three Os complexes per

(60) Webber, S. E. *Chem. Rev.* **1990**, *90*, 1469–1482.

(61) Holden, D. A.; Guillet, J. E. *Macromolecules* **1980**, *13*, 289.

(62) Ng, D.; Guillet, J. E. *Macromolecules* **1982**, *15*, 724.

(63) Fox, M. A. *Acc. Chem. Res.* **1999**, *32*, 201–207.

(64) Watkins, D. M.; Fox, M. A. *J. Am. Chem. Soc.* **1996**, *118*, 4344–4353.

(65) Whitesell, J. K.; Chang, H. K.; Fox, M. A.; Galoppini, E.; Watkins, D. M.; Fox, H.; Hong, B. *Pure Appl. Chem.* **1996**, *68*, 1469–1774.

(66) Fox, M. A. *Macromol. Symp.* **1996**, *101*, 219–226.

(67) Li, J.; Lindsey, J. S. *J. Org. Chem.* **1999**, *64* (25), 9101–9108.

(68) Li, J.; Ambrose, A.; Yang, S. I.; Diers, J. R.; Seth, J.; Wack, C. R.; Bocian, D. F.; Holten, D.; Lindsey, J. S. *J. Am. Chem. Soc.* **1999**, *121* (38), 8927–8940.

(69) Kuciauskas, D.; Liddell, P. A.; Lin, S.; Johnson, T. E.; Weghorn, S. J.; Lindsey, J. S.; Moore, A. L.; Moore, T. A.; Gust, D. *J. Am. Chem. Soc.* **1999**, *121* (37), 8604–8614.

(70) Li, F.; Yang, S. I.; Ciringh, Y.; Seth, J.; Martin, C. H.; Singh, D. L.; Kim, D.; Birge, R. R.; Bocian, D. F.; Holten, D.; Lindsey, J. S. *J. Am. Chem. Soc.* **1998**, *120* (39), 10001–10017.

(71) Van Patten, P. G.; Shreve, A. P.; Lindsey, J. S.; Donohoe, R. J. *J. Phys. Chem. B* **1998**, *102*, 4209.

(72) Cho, H. S.; Song, N. W.; Kim, Y. H.; Jeoung, S. C.; Hahn, S.; Kim, D.; Kim, S. K.; Yoshida, N.; Osuka, A. *J. Phys. Chem. A* **2000**, *104* (15), 3287–3298.

(73) Wagner, R. W.; Lindsey, J. S. *J. Am. Chem. Soc.* **1994**, *116*, 9759.

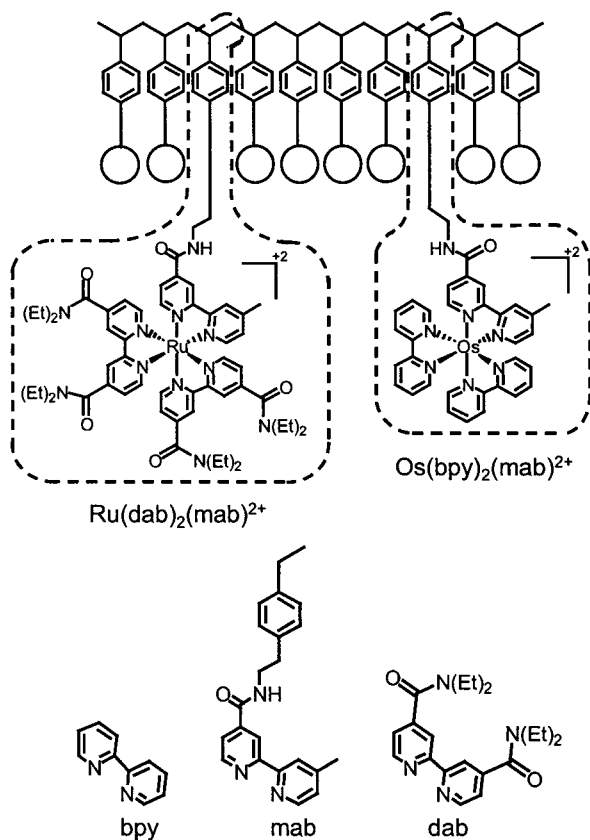


Figure 1. Schematic diagram depicting the structure of the polymeric assembly. Ru(II) and Os(II) complexes are covalently linked to a polystyrene backbone. Open circles in the diagram represent other transition metal complexes that are not shown for clarity. The structures of the two monomer complexes, Ru(dab)₂(mab)²⁺ and Os(bpy)₂(mab)²⁺, are identified by the dashed lines. Our experiments were performed on polymer chains dissolved in CH₃CN. At the bottom of the figure are the chemical structures of the three ligands (bpy, mab, and dab) referred to in the text.

chain the sensitization efficiency of the Os sites by photoexcited Ru complexes is near unity ($\approx 95\%$). Although this efficiency is an indicator of its light-harvesting potential, its value depends on the degree of Os loading, and thus does not provide a window through which to view the microscopic dynamics.

To gain a better understanding of the *intrinsic* properties of the energy migration process we have augmented our time-resolved experiments with Monte Carlo simulations. These provide insight into the polymer array's structure and at the same time form the basis of a molecular-level description of the energy migration dynamics. Our simulations suggest that the Ru^{*}→Ru energy transfer times are in the range between 1 and 4 ns, or about 250–1000 times faster than the natural lifetime of the Ru excited state (1000 ns). This implies a single-step energy transfer efficiency of 99.6 to 99.9%. The fast excited state hopping relative to the Ru excited state lifetime suggests that an excited state could make a large number of hops, and thus transport excited state energy over long distances with relatively high efficiency.

II. Experimental Section

A. Synthesis and Materials. The primary focus of our spectroscopic experiments is on the polymeric system with mixed Ru(II)/Os(II) loading, PS-Ru₁₇Os₃. The synthesis of this system is described fully elsewhere^{40,74} and so only a brief description is given here. The synthesis of the polystyrene backbone, PS-CH₂CH₂NH₂, is accomplished via a living anionic polymerization of a vinyl monomer with a protected

amine group. The living anionic method offers the advantage of decreased molecular weight polydispersity compared to free radical techniques (PDI = 1.08). In the present work, the polymerization was terminated at 20 repeat units. The loading of the polystyrene backbone is accomplished by amide coupling of the deprotected amine with carboxylic acid derivatized Ru and Os complexes. In the case of the mixed-loaded polymers, the minority species is loaded first by reacting the deprotected polymer with 3 equiv of Os(II) complex per polymer chain. The remaining sites are then loaded with Ru(II) complexes via reaction with an excess of the acid functionalized Ru(II) compound. The degree of metal site vacancies (i.e. binding sites with no attached complex) was assessed by using ¹H NMR.⁴¹ The 17:3 Ru/Os loading ratio was confirmed by ¹H NMR and UV–vis absorption measurements. Spectroscopic experiments are performed on polymer chains dissolved in room temperature acetonitrile.

B. Steady-State Methods. UV–visible spectra were recorded on a diode array spectrometer with 2 nm resolution. The spectroscopic grade acetonitrile used in the photophysical measurements was either used as received or distilled over CaH₂. Steady state emission spectra were recorded on a photon counting spectrofluorimeter and were corrected for the instrument response. Optically dilute samples (less than 0.12 OD at the excitation wavelength) were Argon sparged for 40 min prior to use. Emission quantum yields were determined by relative actinometry.⁷⁵ The procedure involves the measurement of the integrated emission profile (*I*) and absorbance (*A*) of an unknown sample and a reference compound. The quantum yield of the sample (Φ) is then determined by using

$$\Phi = \Phi_R \left(\frac{I}{I_R} \right) \left(\frac{n}{n_R} \right)^2 \left(\frac{A_R}{A} \right) \quad (1)$$

where *n* is the refractive index of the solvent, and Φ_R , *A_R*, and *n_R* all refer to the reference compound. The reference used in this work was either [Ru(bpy)₃](PF₆)₂, for which $\Phi_{em} = 0.062$,⁷⁶ or [Os(bpy)₃](PF₆)₂, for which $\Phi_{em} = 0.005$,⁷⁷ in acetonitrile at 298 K.

C. Time-Resolved Emission Methods. Time-resolved measurements were conducted by time-correlated single photon counting (TCSPC). The apparatus consists of a mode-locked Nd:YAG laser (Coherent Antares) whose frequency tripled output is used to synchronously pump a single jet dye laser with Stilbene 3. The dye laser output at 430 nm is cavity dumped to produce ~ 10 ps pulses with a pulse energy of ~ 6 nJ/pulse. The repetition rate of the dye laser was selected to be at least 5 times the natural lifetime of the sample (475 kHz for measurements at 780 nm or 190 kHz for measurements at 640 nm). The beam passes through an iris and illuminates, without focusing, a 10 mm quartz cuvette containing the sample. The emitted light is collected at 90° and focused onto the slit of a 240 mm focal length, single grating monochromator and subsequently delivered to a cooled, multichannel plate-photomultiplier tube (MCP, Hamamatsu R3809U-51). The intensity of the detected luminescence is varied by use of neutral density filters mounted before the monochromator. The signal from the MCP is amplified prior to sending it into a 200 MHz constant fraction discriminator (CFD, Tennelec 454) whose output serves as the start pulse for a time-to-amplitude converter (TAC, Tennelec 864). The stop pulse is obtained by focusing 10% of the excitation beam onto a Si:PIN photodiode, whose output is sent into a variable delay box, then to a CFD, and finally to the TAC. The TAC's output is sent to a multichannel analyzer that is interfaced to a PC. The instrument response of the apparatus is 80 ps at the fwhm.

III. Results and Discussion

The energy migration process is initiated by photoexcitation of one of the Ru monomers to a singlet metal-to-ligand charge transfer (¹MLCT) state, which is followed by efficient inter-

(74) Maxwell, K. A. Doctoral Dissertation, University of North Carolina at Chapel Hill, Chapel Hill, NC, 1999.

(75) Demas, J. N.; Crosby, G. A. *J. Phys. Chem.* **1971**, *75*, 991.

(76) Casper, J. V.; Meyer, T. J. *J. Am. Chem. Soc.* **1983**, *105*, 5583.

(77) Casper, J. V.; Kober, E. M.; Sullivan, B. P.; Meyer, T. J. *J. Am. Chem. Soc.* **1982**, *104*, 630.

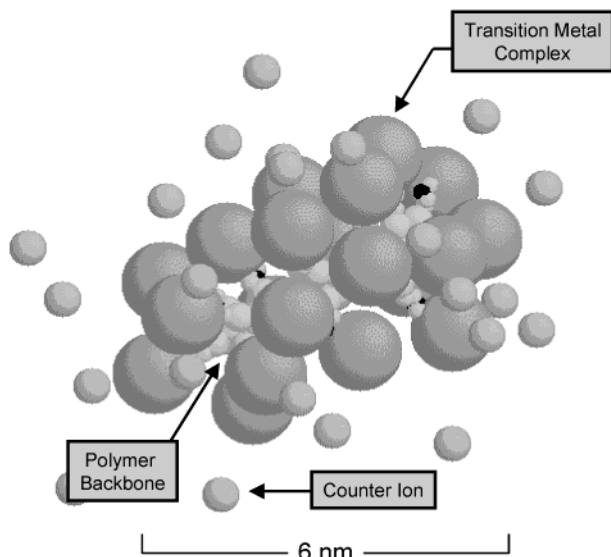


Figure 2. Structure of a polymer assembly containing 20 transition metal complexes calculated by Monte Carlo simulations (see text). Large spheres represent the metal complexes and small spheres are the PF_6^- counterions.

system crossing to a $^3\text{MLCT}$ state in a matter of several hundred femtoseconds.^{78,79} The lifetime of this low-lying triplet state is about 1000 ns, and as a result there is sufficient time for the excited state to either transfer to an adjacent Ru complex or be quenched by direct energy transfer to a lower energy Os site before relaxation back to the ground state. Because the Os excited state lies approximately 0.34 eV below the Ru excited state, the Os sites are considered to be deep traps that terminate the energy migration process.

This work focuses on polymers with mixed Ru/Os loading ($\text{PS-Ru}_{17}\text{Os}_3$), their corresponding ruthenium and osmium homopolymers (PS-Ru_{20} and PS-Os_{20}), and the two monomer complexes, $\text{Ru}(\text{dab})_2(\text{mab})^{2+}$ and $\text{Os}(\text{bpy})_2(\text{mab})^{2+}$. The homopolymers and monomer complexes serve as reference systems.⁸⁰ This approach is justified by a series of spectroscopic experiments that indicate the polymers are well described as a collection of chromophores whose excited states remain intact upon incorporation into the array. Thus, the polymer backbone is primarily a structural support that holds complexes in close proximity.

The outline of this section is as follows. In Section A we address some of the issues associated with the polymer structure and the arrangement of the metal complexes. These concepts are central to the interpretation of the spectroscopic data, and thus the salient details are presented early in the discussion. The steady-state spectroscopy is discussed in Section B and the time-resolved experiments are presented in Section C. In that section we discuss the kinetics of the energy transfer process, measurements of the sensitization efficiency, and the energy transfer mechanism. Finally in Section D we describe the Monte Carlo simulations that are used to model the polymer structure and gain insight into the intrinsic properties of the energy migration dynamics.

(78) Demas, J. N.; Crosby, G. A. *J. Am. Chem. Soc.* **1971**, *93*, 2841.

(79) Damrauer, N. H.; Cerullo G.; Yeh, A.; Bousie, T. R.; Shank, C. V.; McCusker, J. K. *Science* **1997**, *275*, 54–57.

(80) Other possible choices for the homopolymer systems are PS-Ru_{17} and PS-Os_3 . However, the macromolecular structure is strongly influenced by the number of metal complexes, and therefore these systems (PS-Os_3 in particular) will more than likely have very different structures when compared to their $\text{PS-Ru}_{17}\text{Os}_3$ parent. This would make them poor mimics for the mixed-loaded polymer.

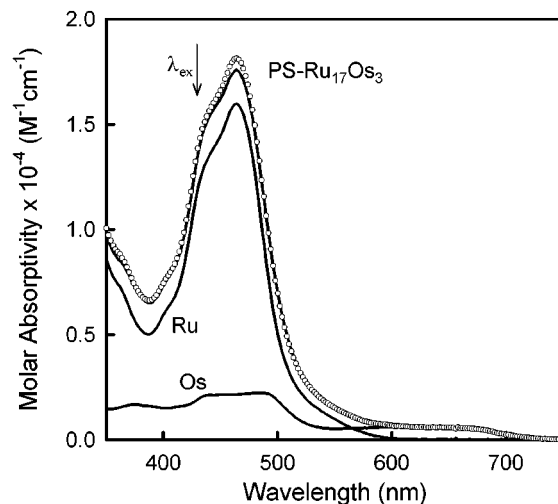


Figure 3. Absorption spectra of the $\text{PS-Ru}_{17}\text{Os}_3$ polymer assembly and Ru and Os monomer complexes, $\text{Ru}(\text{dab})_2(\text{mab})^{2+}$ and $\text{Os}(\text{bpy})_2(\text{mab})^{2+}$, in room temperature CH_3CN . The monomer spectra are scaled by 17/20 and 3/20, respectively, to reflect their contributions to the polymer sample. The solid lines are the experimental observation; the individual points are obtained by the addition of the two monomer spectra. The arrow identifies the excitation wavelength used for the time-resolved experiments discussed later in the text.

A. Supramolecular Structure and Metal Complex Loading. The microscopic details of the energy transfer dynamics will depend on the polymer structure and this is greatly influenced by the large (14 Å diameter) metal dication monomer units. A typical structure calculated from molecular modeling is depicted in Figure 2 (the details of these calculations are described later). The larger spheres are the Ru(II) or Os(II) chromophores and the smaller spheres are the PF_6^- counterions that surround the polymer whose overall charge is +40. The densely loaded polymer adopts a twisted backbone and extended rodlike structure to alleviate the steric and Coulombic repulsions between adjacent chromophores. One consequence of the dense loading is that the average distance between the peripheries of adjacent chromophores is 2–3 Å. It is this close proximity of the complexes that is partly responsible for the efficient energy transfer that is observed.

The arrangement of the Ru and Os complexes on the polymer chain plays an integral role in the description of the migration dynamics. The mixed polymer is loaded with (on average) 17 Ru and 3 Os complexes. The average, however, is over the entire sample not an individual chain. And furthermore, the loading is random, allowing for a certain fraction of chains to have more or less Os complexes in a number of possible configurations. The probability that a chain will have n Os sites is given by,

$$P_n = \frac{N!}{(N-n)!n!} \cdot P_{\text{Ru}}^{(N-n)} \cdot P_{\text{Os}}^n \quad (2)$$

where P_{Ru} (17/20) and P_{Os} (3/20) are the probability that a given site is Ru or Os, respectively, and N is the total number of complexes. For our samples there is a narrow distribution of chain lengths (PDI = 1.08) centered at $N = 20$. Statistically we expect 24% of the chains to have three Os with 35% of the chains having more than three and 41% having less; 4% of the chains are expected to be Ru homopolymer (i.e. $n = 0$).

B. Steady-State Spectra. The ground-state absorption spectrum of the $\text{PS-Ru}_{17}\text{Os}_3$ polymer is displayed in Figure 3. The spectrum shows an intense band centered at 450 nm and a

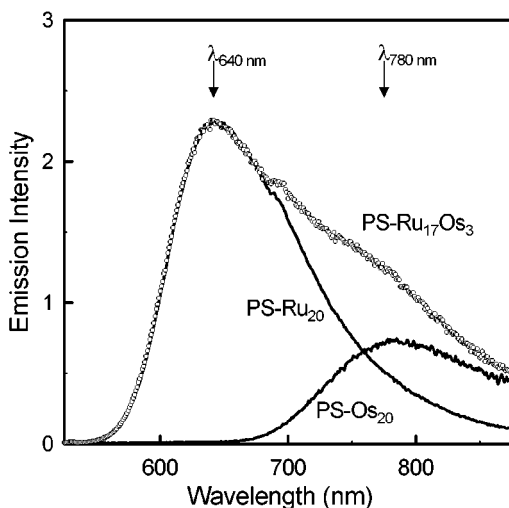


Figure 4. Emission spectra of PS-Ru₁₇Os₃ (open circles) and its Ru and Os homopolymer counterparts (solid lines). The arrows indicate the two monitoring wavelengths used in the time-resolved experiments. Emission monitored at 640 nm arises entirely from Ru(II) luminescence, while the emission monitored at 780 nm has both Ru(II) and Os(II) contributions (see text).

weaker absorption that extends out to about 700 nm. The polymer spectrum can be understood in terms of the absorption spectra of the two monomer complexes, Ru(dab)₂(mab)²⁺ and Os(bpy)₂(mab)²⁺. These spectra are also shown in the figure, but their absorptivities are weighted by 17/20 and 3/20, respectively, to reflect their relative abundances within the polymer sample.

The broad absorption band centered near 450 nm (for both Ru and Os) is a metal-to-ligand charge transfer (MLCT) transition that involves the promotion of a metal $d\pi$ electron to a π^* orbital on one of the polypyridyl ligands. Any of the three ligands could receive the electron in the optical excitation process, but at long times the photoexcited electron resides on the lowest energy ligand, i.e. one of the two *dab* ligands.

On a per molecule basis, the absorption cross-section for excitation of the Ru complex at 430 nm (the excitation wavelength used in these experiments) is comparable to that of Os. As a result, the relative probability for Ru or Os excitation is determined by their mole fractions in the sample. In addition to the 450 nm band, the Os complex has a weak absorption feature centered around 630 nm. This transition corresponds to direct excitation to a ³MLCT state. Although this is formally a spin-forbidden transition, its intensity becomes appreciable in Os as a result of the large spin-orbit coupling in the heavier metal.

The absorption spectrum of the polymer can be reproduced by a superposition of the weighted monomer spectra. This suggests that the polymer can be described as an array of weakly coupled chromophores whose electronic structures remain essentially intact upon loading onto the polymer backbone. This conclusion is also supported by other general observations. At low excitation energies, the spectroscopic signatures (i.e. absorption spectra, emission spectra, and excited-state lifetimes) exhibited by the Ru and Os homopolymers are almost identical to their monomer counterparts.

Displayed in Figure 4 is the emission spectrum of PS-Ru₁₇Os₃ in room temperature CH₃CN. The spectrum shows two features: a high-energy band with a maximum at 640 nm, and a low-energy shoulder in the vicinity of 750–800 nm. These features are assigned to Ru- and Os-complex emission,

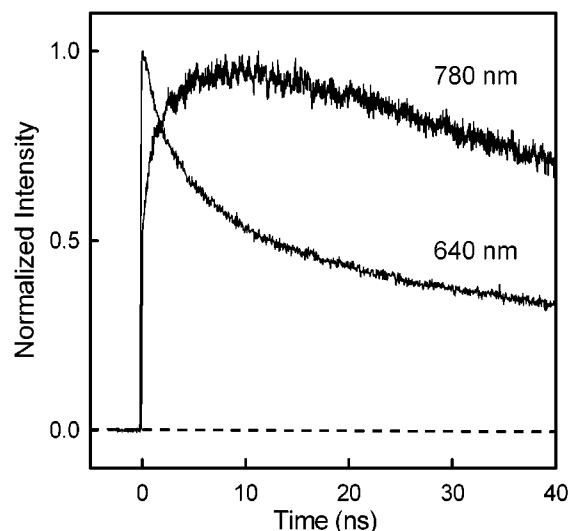


Figure 5. Time-resolved emission from PS-Ru₁₇Os₃ detected at 640 nm (entirely Ru(II)) and 780 nm (primarily Os(II)). Excitation was at 430 nm. Both transients are normalized such that their maximum intensity is equal to unity.

respectively. The emission spectra of the two homopolymers are also displayed in the figure, with their intensities scaled to reflect their relative contributions to the PS-Ru₁₇Os₃ emission.

The relative intensities of Ru and Os emission offer evidence of extensive quenching of the Ru excited state. The ratio of the two emission intensities is determined by the number of Ru excited states, the number of Os excited states (created by either direct excitation or Ru* \rightarrow Os energy transfer), and the relative luminescence quantum yields. The steady-state emission spectrum shows that Ru emission is about 3 times more intense than that of Os. However, the quantum yield for Ru emission is $\approx 10\%$, or about 30 times larger than that of Os ($\Phi = 0.32\%$). Once adjusted for the difference in quantum yields, the relative intensities suggest that the Os excited states outnumber the Ru excited states by a factor of 10. Since there are 5–6 times more Ru excited states produced by photoexcitation, the presence of a larger number of excited Os complexes points to an efficient Ru* \rightarrow Os energy transfer process. Measurements of the energy transfer efficiency (Section C-2) support this conclusion. In fact, the majority of the Ru complex emission observed in the PS-Ru₁₇Os₃ spectrum is attributed to polymer chains that have zero Os complexes, i.e. Ru homopolymers. Statistically, such chains are expected to constitute 4% of the polymer sample.

C. Energy Transfer Dynamics. Photoinduced energy migration is followed through the time-resolved luminescence detected at 640 and 780 nm, both of which are displayed in Figure 5. At 640 nm Ru is the sole emitter. The emission at this wavelength decays on multiple time scales, ranging from 2 to 980 ns. The emission detected at 780 nm reflects the appearance of Os(II) excited states. The growth in emission at this wavelength shows a rapid rise followed by a slower rise to the maximum at 5–10 ns. The rapid rise accounts for 56% of the maximum intensity and lies within the instrument response of the apparatus (80 ps). The slower rise coincides with the fastest decay component in the Ru emission, implying that the slower growth arises from the production of Os excited states by Ru* \rightarrow Os energy transfer. The decay of the luminescence after the maximum is nonexponential. This differs from PS-Os₂₀, which decays with single exponential kinetics and a 49 ns lifetime. The nonexponential behavior observed in the decay of the 780 nm emission is

probably the result of photosensitization events that are delayed due to $\text{Ru}^* \rightarrow \text{Ru}$ energy migration.

The Ru emission past 500 ns decays with a lifetime of 980 ns, which is characteristic of the PS-Ru₂₀ homopolymer (1000 ns). One possible explanation of this is that the Ru excited state gets trapped within a subset of complexes and is not able to fully explore the entire polymer. Although such a scenario cannot be entirely ruled out, our simulations of the energy migration dynamics (Section D) do not support its presence. Instead we attribute the long tail in the Ru luminescence to emission from the subset of polymer chains that do not have any Os complexes, i.e. Ru homopolymer, which is present in the mixed polymer sample due to the statistical nature of the metal complex loading.

The deviation from single-exponential kinetics in both the Ru and Os data is a result of a complex energy transfer process where the number of $\text{Ru}^* \rightarrow \text{Ru}$ migration steps that precede $\text{Ru}^* \rightarrow \text{Os}$ trapping varies from one excitation event to the next. As mentioned earlier, the average ratio of Ru to Os over the ensemble of chains is 17:3 but the loading on an individual chain is random. This results in a distribution in the degree of Os loading and a large number of possible chromophore configurations. Furthermore, since an energy gradient toward the trapping site does not exist, the propagation of the excited state from one Ru to the next is a series of uncorrelated hopping events. As a result, even if two polymer chains have exactly the same arrangement of chromophores and the same initial location of the excited state, the random walk behavior could cause the path that one excited state takes to the trap to be different from another.

The growth in the Os emission intensity and the concomitant decay in the Ru emission most certainly reflect the rates of excited state energy transfer. However, because the observed time scales are closely linked to the degree of Os loading they do not provide a direct measure of the energy transfer times. For example, a chain with a 16:4 Ru to Os loading would show a faster growth rate in the Os emission simply because a Ru excited state would make on average fewer steps to the Os trap. Since the $\text{Ru}^* \rightarrow \text{Ru}$ energy transfer time should be independent of the number of Os complexes on a given chain, the growth and decay times extracted directly from the data can, at best, provide only a qualitative description of the energy migration process. In the sections that follow, we present a more thorough analysis of the spectroscopic data, and develop a fundamental picture of the energy migration dynamics.

1. Time-Resolved Data—A Closer Look. There are two contributions to the luminescence at 780 nm that do not arise from Os sensitization. These are (1) emission originating from Os centers directly excited by the laser, and (2) Ru luminescence that is also detected due to the overlap of Ru and Os emission bands. The question therefore arises as to which features of the 780 nm transient are due to energy migration and which aspects are not.

The contributions to the transient emission that do not arise from sensitized emission are easily determined. The contribution from direct Os excitation is assessed by comparing the PS-Ru₁₇-Os₃ transient at 780 nm with that of PS-Os₂₀ under the exact same conditions of concentration and integrated irradiance. The Ru contribution is determined by exploiting the difference in Ru and Os emission lifetimes. PS-Ru₂₀ has an emission lifetime of 1000 ns, which is substantially longer than the 49 ns lifetime observed for PS-Os₂₀. Thus, the 780 nm luminescence observed at very long times (i.e. >500 ns) is due solely to Ru. Its contribution is determined by scaling the emission transient

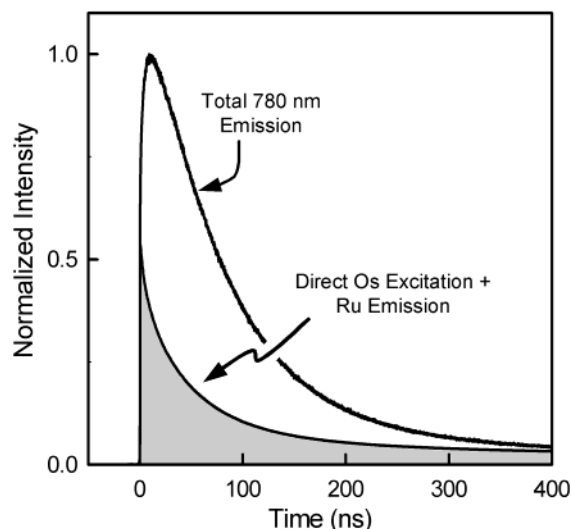


Figure 6. Contributions from direct Os excitation and Ru emission to the total PS-Ru₁₇Os₃ emission detected at 780 nm. The total emission at 780 nm is the same as that displayed in Figure 5, only on a longer time scale.

observed at 640 nm to match the 780 nm data at times greater than 500 ns. This assumes that the decay of the Ru emission detected at 780 nm has the same shape as that at 640 nm (where Ru is the sole emitter). This assumption is supported by time-resolved emission experiments performed on PS-Ru₂₀ that show no spectral shifts in the decay of the Ru emission band, indicating that it decays uniformly. The sum of these two contributions is displayed along with the total emission detected at 780 nm in Figure 6.

The sensitized Os emission is determined simply by subtracting out the direct Os excitation and Ru contamination contributions from the total emission. It represents a substantial fraction ($\approx 60\%$) of the total luminescence detected at 780 nm. In the next section, we will use this to determine the efficiency of Os sensitization.

The rise in the *sensitized* emission is displayed in the top panel of Figure 7. This portion of the transient cannot be fit by a single-exponential model, which is evidenced by the residuals (Figure 7). The rise is well described, on the other hand, by a biexponential function of the form,

$$I(t) = A_1 \left(1 - \exp\left(-\frac{t}{\tau_1}\right) \right) + A_2 \left(1 - \exp\left(-\frac{t}{\tau_2}\right) \right) \quad (3)$$

The fit to this function is displayed as the solid line in the top panel of Figure 7. The rise is comprised of a fast, 400 ps component, which accounts for about 25–30% of the maximum amplitude, and a slower component with a 3.6 ns time constant. The fit to a biexponential function is not meant to imply that the polymer system should be viewed as a two-state system, which it most certainly is not. Nevertheless, the presence of two kinetic components suggests that there are two qualitatively distinct dynamical processes occurring on different time scales. The 400 ps component is attributed to the prompt $\text{Ru}^* \rightarrow \text{Os}$ energy transfer that occurs when the Ru excited state is formed at a site directly adjacent to the Os trap. As mentioned earlier, the $\text{Ru}^* \rightarrow \text{Os}$ energy transfer will take place on a range of time scales. The fast time component observed here probably represents the fastest portion of the distribution, since it is these energy transfer events that will give rise to prompt sensitization.

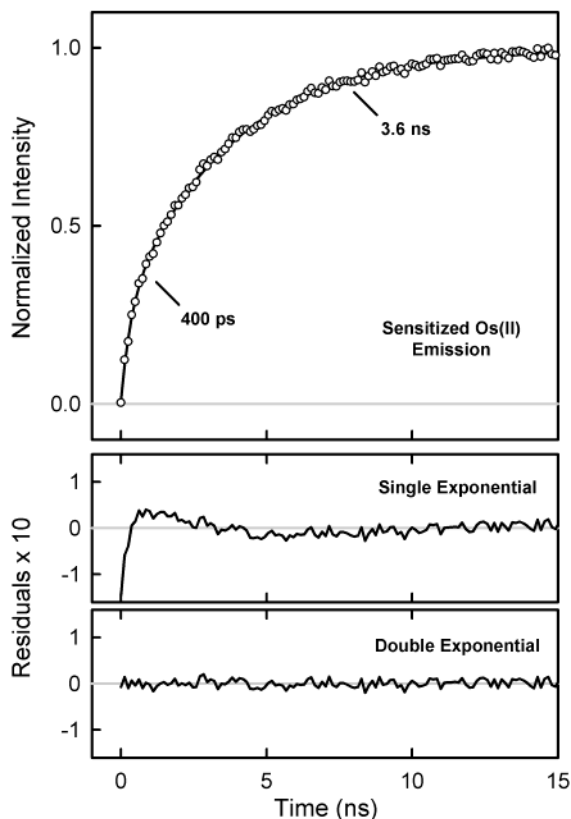


Figure 7. The upper panel shows rise in sensitized Os(II) emission from PS-Ru₁₇Os₃ detected at 780 nm. The individual points are the experimental data and the solid line is the result of a nonlinear least-squares fit to a biexponential function. Attempts were made to fit the rise to a single-exponential function. The residuals from this fit (middle panel) show clear deviation from single-exponential behavior. The residuals displayed in the lowest panel are for the biexponential fit. The sum-of-squared residuals are 0.06 and 0.01 for the single exponential and biexponential fits, respectively.

The rest of the rise is attributed to emission from sensitized Os complexes that are formed after one or more Ru* \rightarrow Ru hops. A more realistic model of the energy migration dynamics is incorporated into our Monte Carlo simulations, which are discussed in Section D.

2. Efficiency of Sensitizing Os Traps. Energy transfer competes with the intrinsic radiative (k_r) and nonradiative (k_{nr}) pathways in depopulating the excited state of the donor. The quantum yield, or efficiency (χ_{EN}), of sensitizing the Os(II) sites can be defined as,

$$\chi_{EN} = \frac{k_{EN}}{k_{EN} + k_r + k_{nr}} = 1 - \frac{\Phi_D}{\Phi_D^o} = 1 - \frac{\tau_D}{\tau_D^o} \quad (4)$$

Thus, quantum yield (Φ) or lifetime (τ) measurements of the donor in the presence (Φ_D or τ_D) and absence (Φ_D^o or τ_D^o) of the acceptor can be used to calculate χ_{EN} . The quantum yields for Ru emission from PS-Ru₁₇Os₃ and PS-Ru₂₀ polymers are 0.019 and 0.1, respectively, implying a sensitization efficiency of $80 \pm 10\%$.

Alternatively, the efficiency can be defined as the ratio of the number of sensitized acceptors, denoted $N(\text{Os}_{EN})$, to the number of excited donors, i.e.

$$\chi_{EN} = \frac{N(\text{Os}_{EN})}{N(\text{Ru}^*)} \quad (5)$$

Both of these quantities can be determined by using the luminescence decay data of the acceptor.

The first quantity needed is $N(\text{Os}_{EN})$, the number of Os excited states formed via sensitization. This is given by,

$$N(\text{Os}_{EN}) = \frac{G}{\Phi_{Os}} \left(\eta_S - \eta_R \cdot \frac{[S]}{[R]} \cdot P_{Os} \right) \quad (6a)$$

where η is an integrated intensity obtained from the emission transient, i.e., $\eta = \int I(t) dt$. η_S and η_R are the total number of photons observed at 780 nm from PS-Ru₁₇Os₃ (sample) and PS-Os₂₀ (reference), respectively. (The Ru contribution is removed from the mixed polymer emission prior to performing this analysis.) Φ_{Os} is the emission quantum yield of PS-Os₂₀ in CH₃CN, P_{Os} is the mole fraction of Os in the sample (3/20), and G is a geometrical factor that reflects the photon collection efficiency of our apparatus at 780 nm. The ratio $[S]/[R]$ accounts for differences in polymer chain concentration between the sample and reference: this is determined from absorption measurements on the two separate samples. The first term in eq 6a is the total number of Os excited states produced by either sensitization or direct excitation, while the second term reflects the number of Os excited states resulting from direct excitation alone.

The second quantity needed is $N(\text{Ru}^*)$, the number of directly excited donors. This is determined from the PS-Os₂₀ reference by using the following expression,

$$N(\text{Ru}^*) = G \left(\frac{\eta_R}{\Phi_{Os}} \cdot \frac{\epsilon_{Ru}}{\epsilon_{Os}} \cdot \frac{[S]}{[R]} \cdot P_{Ru} \right), \quad (6b)$$

where ϵ is the molar absorptivity at the excitation wavelength for Ru and Os, and P_{Ru} is the mole fraction of Ru in the sample (17/20). The ratio of absorptivities is included to take into account the difference in excitation probabilities of the Ru and Os complexes. In essence, the Os homopolymer is used as a quantum counter. In principle the Ru emission could be used, but this would introduce the Ru quantum yield into the analysis as well as the photon collection efficiency at 640 nm. Not only is this avoided by using the Os emission, but since Φ_{Os} and G appear in both eqs 6a and 6b, they do not appear in the final expression for the efficiency (eq 5). The efficiency of Os sensitization in the PS-Ru₁₇Os₃ polymer at room temperature in CH₃CN is calculated in this manner to be $88 \pm 12\%$.

On the basis of these two methods we estimate the overall efficiency for the sensitization of the Os traps to be approximately 85%. We point out, however, that this represents an average efficiency over the entire sample, including those chains that do not have any Os complexes and hence remain unquenched. Depending upon the fraction of PS-Ru₂₀ homopolymer in the sample, the sensitization efficiency for the subset of chains with at least one Os complex could be substantially higher.

The presence of PS-Ru₂₀ in the sample is expected, and due in part to the statistical nature of the loading. Statistical arguments predict a 4% fraction of homopolymer. However, the actual fraction appears greater than this. The homopolymer contribution is seen most clearly in the long time decay of the 640 nm emission, Figure 8. The longest time component is assigned to emission from the homopolymer fraction. Extrapolating this emission tail back to $t = 0$ we find that 85% of the integrated emission at 640 nm can be attributed to Ru homopolymer. The fraction of homopolymer

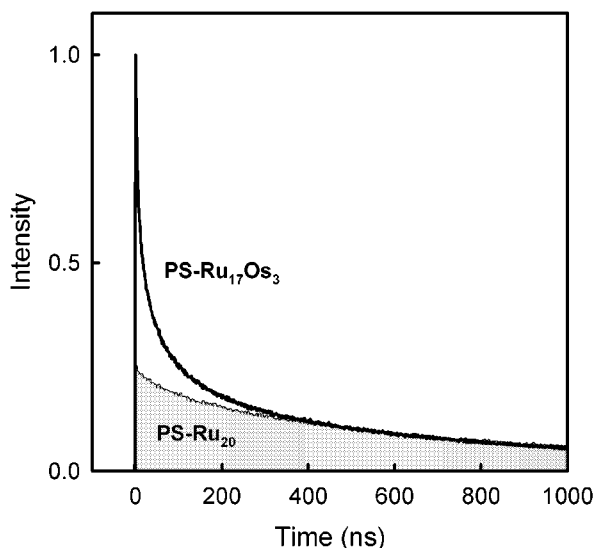


Figure 8. Time-resolved emission from PS-Ru₁₇Os₃ detected at 640 nm. The shaded area depicts the contribution from the Ru homopolymer.

chains (F_H) is given by

$$F_H = \frac{N_H}{N_T} = \left(\frac{\eta_H}{\eta_T} \right) (1 - \chi_{EN}) \quad (7)$$

where N_H and N_T are the number of homopolymer chains and the total number of chains, respectively, and η_H and η_T represent the integrated emission intensities. The ratio η_H/η_T is the fraction of the total emission that emanates from the homopolymer chains, 85%. The homopolymer fraction thus calculated is 10–12%. It is unclear why there is a larger fraction than statistically predicted. It is perhaps due to an artifact of the synthetic procedure, arising from the limited solubility of the amine-derivatized polymer precursor. The implication is that the sensitization efficiency averaged over the entire sample can be at most 90%, and thus the efficiency of those polymer chains that have at least one Os complex is in fact closer to 95%. We point out that deviation from the statistics of eq 2 does not affect any of the numerical results achieved thus far. The analysis of the steady-state spectra and the efficiency of energy transfer depend only upon the relative amounts of Ru(II) and Os(II) complexes in the sample, not on how they are distributed among the chains.

3. Energy Transfer Mechanism. The energy transfer rate constant can be cast in a “golden-rule” expression in which k_{EN} is proportional to the square of an electronic coupling matrix element, H_{DA} .^{15,81} This two-electron matrix element involves the molecular orbitals on both the donor and acceptor. The electronic factor can be split into a Coulombic term and an exchange term, which give rise to Förster and Dexter energy transfer mechanisms, respectively.

The Förster mechanism describes energy transfer through a dipole–dipole coupling term. As a result, the rate constant has a gradual dependence ($1/R^6$) on the donor–acceptor separation, and energy transfer is capable of occurring over large distances. The Förster mechanism is most efficient when the optical transitions connecting the ground and excited states in both partners are electric-dipole allowed.⁸² On the surface this would seem to exclude the Förster mechanism for energy transfer involving Ru and Os metal complexes, where optical transitions to the lowest excited state are spin-forbidden. However, because

of the large spin–orbit coupling, this selection rule may not be absolute. Spin–orbit coupling introduces some singlet character into the emitting states. The fraction is estimated to be less than 11% in Ru(bpy)₃²⁺, and in Os(bpy)₃²⁺ it is probably around 30%.⁸³ Although we cannot completely rule out the Förster mechanism, the small percentage of singlet character in the donor and acceptor complexes suggests that it may not be the dominant pathway.

The Dexter mechanism, on the other hand, involves the exchange of donor and acceptor electrons, and is therefore expected to operate only at short distances where the electron clouds can interpenetrate. Because this interaction requires overlap between the orbitals, the energy transfer rate constant in the Dexter formulation falls off exponentially with increasing separation. The distance over which energy transfer occurs can be extended, however, when the donor and acceptor are connected through a series of covalent bonds. In these cases the orbitals can indirectly mix via a superexchange type interaction that involves molecular orbitals on the intervening bonds. The polymer backbone in PS-Ru₁₇Os₃ is in essence a bridging ligand between adjacent complexes, and hence there is the potential for a through-bond pathway. Thus the question is whether the coupling between the sites arises from a direct overlap of wave functions or a bridge-mediated superexchange pathway.

There are clear examples in the literature of efficient through bond coupling in Ru/Os dimers. Harriman and co-workers⁸⁴ report an energy transfer time of 6 ps for the complex [(bpy)₂Ru-(bpy-C≡C-bpy)Os(bpy)₂](PF₆)₄. Although the observation is interesting, the short bridging length and high degree of conjugation make comparisons to this system irrelevant. For energy transfer to proceed through bond in our system, efficient coupling would need to occur across a network consisting of 18 σ and π bonds. Reports of Ru*→Os energy transfer in systems involving extended bridges have also appeared in the literature. Balzani et al.⁸⁵ observe a 1.5 ns energy transfer time for [(bpy)₂Ru(bpy-(ph)₃-bpy)Os(bpy)₂]⁴⁺, where the bridge is 11 Å and 13 bonds in length. Here energy transfer is attributed to a through-bond-type mechanism, which is probably enhanced by the high degree of conjugation in the phenylene spacers. This is in contrast to the [(bpy)₂Ru(bpy-S-bpy)Os(bpy)₂]⁴⁺ dimer, where S consists of a bicyclooctane component linked to two ethylene components.⁸⁶ This bridging ligand is roughly 9 Å in length, and unlike the previous case, the bicyclooctane bridge contains no conjugated bonds. The saturated bonds substantially diminish the electronic communication between metal centers, leading to a longer time scale for energy transfer compared to the phenylene bridge, despite its physically shorter length. The range of energy transfer rate constants observed in various dimers reflects the differences between bridging ligands in their ability to mediate electronic communication between the donor and acceptor. Thus, the most germane comparisons will be those that have similar bonding networks between the metal centers.

Schmehl and co-workers⁸⁷ provide an example of a bridging ligand that more closely resembles the combination of σ and π bonds found in our polymer. They report an energy transfer time of about 10 ns in [(dmb)₂Ru(bpy-etphet-bpy)Os(dmb)₂]⁴⁺

(83) Kober, E. M.; Meyer, T. J. *Inorg. Chem.* **1984**, *23*, 3877–3886.

(84) Harriman, A.; Romero, F. M.; Ziessel, R.; Benniston, A. C. *J. Phys. Chem. A* **1999**, *103* (28), 5399–5408.

(85) Schlicke B.; Belsler, P.; Cola, L. D.; Sabbioni, E.; Balzani, V. *J. Am. Chem. Soc.* **1999**, *121* (17), 4207–4214.

(86) De Cola, L.; Balzani, V.; Barigelletti, F.; Flamigni, L.; Zelewsky, A.; Frank, M.; Vögtle, F. *Inorg. Chem.* **1993**, *32*, 5228.

(87) Shaw, J. R.; Sadler, G. S.; Wacholtz, W. F.; Ryu, C. K.; Schmehl, R. H. *New J. Chem.* **1996**, *20*, 749–758.

(81) Speiser, S. *Chem. Rev.* **1996**, *96*, 1953–1976.

(82) Förster, T. *J. Chem. Soc., Faraday Trans.* **1959**, *27*, 7.

where the bridge spans roughly 12 Å and 9 bonds. The Ru*→Os energy transfer observed in this system is slower than that found in our polymer (~400 ps), despite the fact that there are fewer bonds in its bridging network. This trend is inconsistent with a through-bond-type mechanism.

It is consistent with an energy transfer mechanism that arises from a direct overlap of the donor and acceptor wave functions. The distance between Ru and Os complexes in the dimer will be very different than that found in the polymer. The dimer will probably adopt an extended structure that minimizes the Coulombic repulsions between the metal complexes. In contrast, our Monte Carlo simulations (Section D) suggest that the dense loading of the polymer leads to Ru and Os complexes that are in much closer proximity, despite the longer bridging network between them. This suggests that energy transfer in the polymer is due, at least in part, to an effective coupling between adjacent chromophores that does not involve the orbitals on the bridging network. While this tends to rule out coupling through the polymer backbone, there is also the possibility of a superexchange pathway involving the intervening solvent. Solvent-mediated superexchange has been discussed in relation to energy transfer in other systems.⁸¹

D. Monte Carlo Simulation of Energy Migration. The energy transfer time will be characterized not by a single rate constant but rather a distribution of rate constants that reflects a range of separations between metal complexes. Thus, to determine the time scale for Ru*→Ru and Ru*→Os energy transfer, the physical model must incorporate a microscopic description of the polymer's structure. The kinetic model used here combines a Monte Carlo simulation that yields structural information with a stochastic simulation of the energy migration. Together with the time-resolved measurements these calculations provide insight into the structure and dynamics at the molecular level.

1. Polymer Structure. The polymer structure is calculated by using a Metropolis Monte Carlo algorithm. The potential energy function that describes the assembly represents each metal complex as a hard 14 Å diameter sphere with a +2 charge placed at its center. The polystyrene backbone is modeled as a flexible chain that is free to rotate about the C–C single bonds (whose lengths are held constant). The surrounding solvent is treated as a dielectric continuum and the PF₆⁻ counterions are represented by hard spheres (6.3 Å diameter) with a -1 charge located at their centers. Our calculations are performed on polymer chains in which every binding site is occupied by a metal complex. This is consistent with ¹H NMR measurements that indicate complete loading of the polymer chains.

The initial structure is constructed by placing the metal complexes on the side chains of an extended polystyrene chain. Because polystyrene is considered to have an atactic structure, the handedness of the chiral carbons in the backbone is chosen at random such that right- and left-handed sites are equally likely. Starting with this structure, one C–C bond in the polymer backbone is chosen at random. The array structure is altered by rotation about this bond and the change in energy, Δ*E*, between the old and the new configurations is calculated. If the energy of the new structure is lower, the move is accepted. If the potential energy is increased, the new configuration is accepted only if the quantity exp(-Δ*E*/*k*_B*T*) is less than a random number chosen on the interval (0,1). The structure is annealed during the course of generating 5 × 10⁵ configurations. After this annealing period an additional 10⁶ structures are generated, from which 20 are selected. This is repeated 20 times to produce an ensemble of 400 structures.

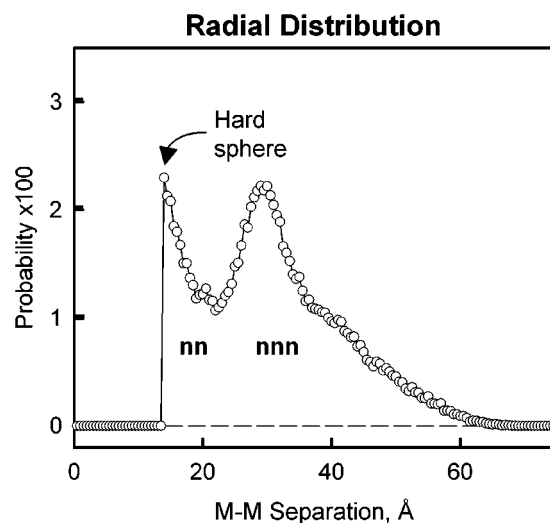


Figure 9. Metal–metal pair distribution function calculated from Monte Carlo simulations of the polymer structure. nn and nnn refer to the nearest neighbors and next nearest neighbors, respectively.

A typical structure is shown in Figure 1. The large spheres represent the transition metal complexes while the smaller spheres represent the PF₆⁻ counterions. The carbon backbone undergoes significant twisting to relieve the steric and Coulombic repulsion between the large transition metal complexes. The result is a structure in which one complex is in close proximity to several others within the array. In addition, the nearest neighbor through space is not necessarily the same as the nearest neighbor through bond.

The metal–metal (MM) pair distribution function obtained from analyzing 400 different chain structures is displayed in Figure 9. The largest MM separation with nonzero probability is around 6 nm, reflecting the average length of the polymer chain. The oscillations in the probability distribution indicate the presence of structural organization that is analogous to the level of order found in other ostensibly disordered systems such as molecular liquids. Each oscillation in the pair distribution corresponds to a “chromophore shell” that surrounds the metal complex of interest. There are two distinct shells observed in the distribution, one centered at 14 Å and the other at 29 Å. These two peaks correspond to the distribution of nearest neighbors (nn) and next-nearest neighbors (nnn), respectively. From the integrated area of the nearest neighbor (nn) peak, we estimate that each complex has between 4 and 5 nearest neighbors and that in more than half of the nearest neighbor pairs the peripheries of the complexes are separated by less than 2 Å.

2. Simulation of Energy Migration Dynamics. We have extended our Monte Carlo simulations of the polymer structure to model the excited-state energy migration dynamics. Similar methods have been implemented to simulate energy migration in other systems.^{38,88} The output of the computer model is an emission transient that is directly comparable to our experimental data, and thus there is a direct link between the simulations, which provide insight into the dynamics at the molecular level, and the experimental observations. The simulations start with a structure selected at random from a 300 K thermal ensemble generated by the Monte Carlo simulation. Each site is randomly assigned to be either a Ru or Os complex with a probability of 17/20 and 3/20, respectively. To be consistent with the experiment, the PS–Ru₂₀ homopolymer fraction is set to be 10%.

(88) Hisada, K.; Ito, S.; Yamamoto, M. *Langmuir* **1996**, *12*, 3682–3687.

The macro structure of the polymers is such that there is a range of separations between adjacent complexes, and thus the Ru*→Ru and Ru*→Os energy transfer steps are not described by a single rate constant, but rather a distribution of rate constants. For a given polymer structure and Ru/Os loading configuration, the rate constants for energy transfer between pairs of metal centers are calculated based on the physical separation between the complexes, i.e.

$$k_{ij}^{\text{Ru}}(R_{ij}) = k_0^{\text{Ru}} \exp(-\beta_{\text{Ru}} R_{ij}) \quad (8a)$$

$$k_{ij}^{\text{Os}}(R_{ij}) = k_0^{\text{Os}} \exp(-\beta_{\text{Os}} R_{ij}) \quad (8b)$$

where the first and second expressions apply to Ru*→Ru and Ru*→Os energy transfer, R_{ij} is the separation between site i and site j , k_0 is the rate constant at closest contact, and β is an attenuation parameter. This definition assumes that the electronic coupling between the donor and acceptor arises from a direct orbital overlap.

A migration “trajectory” is started by randomly choosing one of the metal sites as the initial location of the excited state. Each trajectory is comprised of a series of steps in which a Ru excited state either hops to another site (with a rate constant of k_{ij}^{Ru} or k_{ij}^{Os}) or decays to its ground state at a rate given by the Ru excited-state lifetime, $k_{\text{em}}^{\text{Ru}}$. Each step is calculated by using a stochastic kinetic algorithm adapted from Gillespie,⁸⁹ the details of which are presented in the Appendix. Once energy transfer to an Os site occurs, energy migration is halted (i.e. Os*→Ru energy transfer is not allowed), and the Os excited state decays to the ground state at a rate given by the Os emission lifetime, $k_{\text{em}}^{\text{Os}}$. About 5 million trajectories are calculated starting with different chain structures and Ru/Os loading configurations.

There are six rate constant parameters that enter into the simulation: k_0^{Ru} , k_0^{Os} , β_{Ru} , β_{Os} , $k_{\text{em}}^{\text{Ru}}$, and $k_{\text{em}}^{\text{Os}}$. The last two parameters, the Ru and Os complex emission rates, are measured in separate experiments on the PS-Ru₂₀ and PS-Os₂₀ homopolymers to be 1000 and 49 ns, respectively. In the simulation these are treated as fixed parameters. The attenuation parameters, β_{Ru} and β_{Os} , reflect the decrease in the exchange integral with increasing donor–acceptor distance. The attenuation parameters for Ru*→Ru and Ru*→Os are expected to be similar to each other, and thus for simplicity the two are taken to have the same value, i.e. $\beta_{\text{Ru}} = \beta_{\text{Os}} = \beta$. Although we do not know the exact value for the attenuation parameter, we can identify a typical range of values based on studies of energy transfer in other systems.

In many instances the magnitude of β has been estimated based on the distance dependence of the through-space energy transfer rate constants. Yamamoto and co-workers^{88,90–92} investigated methylene-linked donor–acceptor complexes based on organic chromophores embedded in frozen solutions, polymethyl-methacrylate (PMMA) resins, and Langmuir–Blodgett films. They find β for *intramolecular* energy transfer to be in the neighborhood of 1.7–2.1 Å⁻¹, which is quite similar to the attenuation parameters measured for *intermolecular* energy transfer in similar materials.^{93,94} There are also examples in the literature involving donor–acceptor assemblies based on transi-

Table 1. Monte Carlo simulation parameters (k_0^{Ru} and k_0^{Os}) that yield best agreement between experiment and simulation for different values of the attenuation parameter, β and the most probable Ru*→Ru and Ru*→Os energy transfer times that are obtained from distributions like those shown in Figure 11

β (Å ⁻¹)	k_0^{Ru} (ns ⁻¹)	k_0^{Os} (ns ⁻¹)	$\tau_{\text{max}}^{\text{Ru}}$	$\tau_{\text{max}}^{\text{Os}}$
1.2	0.370	2.86	4.0	0.63
1.3	0.588	3.33	2.5	0.50
1.5	0.800	4.00	1.6	0.40
1.7	1.250	5.00	1.0	0.32
1.9	2.220	5.00	0.6	0.32

tion metal coordination complexes. Elliott and co-workers⁹⁵ examined a rigidly linked Ru(II)/Fe(II) complex in fluid solutions, and concluded that energy transfer proceeded by means of a through-space Dexter mechanism with an attenuation parameter of 2.0 Å⁻¹. Ohno and co-workers⁹⁶ investigated energy transfer in Ru(bpy)₃²⁺ crystals doped with Os(bpy)₃²⁺, and in that system, they estimate the attenuation parameter to be about 1.2 Å⁻¹, although even they remark that this value is somewhat low compared to the typically observed values. If we use these systems as a guidepost, they suggest that β should fall in the neighborhood of 1.2–2.1 Å⁻¹.

One limitation of this model is that the same polymer structure is used throughout the entire migration trajectory. This is clearly not the case in the experiment, especially for trajectories that span hundreds of nanoseconds. It is possible that the relative motion between complexes may facilitate energy migration, and by performing simulations on a “frozen” structure, this aspect of the dynamics is omitted. At the moment it is not clear how large this effect will be. Because of the dense loading, the space between the peripheries of the complexes is relatively small and thus large changes in the separation between nearest neighbors is probably not occurring to a great extent. What might be taking place, on the other hand, is that the identity of the nearest neighbors may be changing with time. Although each complex has 4–5 nearest neighbors, because of the exponential fall off in the rate constant with separation, only 1–3 of these are “connected” to the excited state through energy transfer. As the complexes move relative to each other some of these connections will be broken and new ones will be formed. The role that this plays in the energy migration process is currently under investigation and will be presented in a forthcoming publication.

3. Simulation Results. Since we cannot identify a unique value for the attenuation parameter, we have performed simulations for a range of β values between 1.2 and 2.1 Å⁻¹. The specific values investigated are listed in Table 1.

The simulation generates two emission transients: one for the Os growth and one for the Ru decay. These two transients were fit to the experimental data. For a given β , this was accomplished by adjusting only k_0^{Ru} and k_0^{Os} . The Ru transient was compared directly with the time-resolved emission detected at 640 nm, and the Os transient was compared to the emission detected at 780 nm, with the Ru contribution removed (Section C-1). The “goodness of fit” was determined by eye with special emphasis placed on the rise and rollover part of the transient (first 50–100 ns), the rationale being that the majority of

(93) Kobashi, H.; Morita, T.; Mataga, N. *Chem. Phys. Lett.* **1973**, *20*, 376.

(94) Strambini, G. B.; Galley, W. C. *J. Chem. Phys.* **1975**, *63*, 3467.

(95) Larson, S. L.; Hendrickson, S. M.; Ferrere, S.; Derr, D. L.; Elliott, C. M. *J. Am. Chem. Soc.* **1997**, *119*, 9937. The value for the attenuation parameter, β , should be multiplied by 2.302.

(96) Tsushima, M.; Ikeda, N.; Nozaki, K.; Ohno, T. *J. Phys. Chem. A* **2000**, *104*, 5176.

(89) Gillespie, D. T. *J. Phys. Chem.* **1977**, *81* (25), 2340–2361.

(90) Hisada, K.; Ito, S.; Yamamoto, M. *J. Phys. Chem. B* **1997**, *101*, 6827–6833.

(91) Katayama, H.; Ito, S.; Yamamoto, M. *J. Phys. Chem.* **1992**, *96*, 10115.

(92) Katayama, H.; Maruyama, S.; Ito, S.; Tsujii, Y.; Tsuchida, A.; Yamamoto, M. *J. Phys. Chem.* **1991**, *95*, 3480.

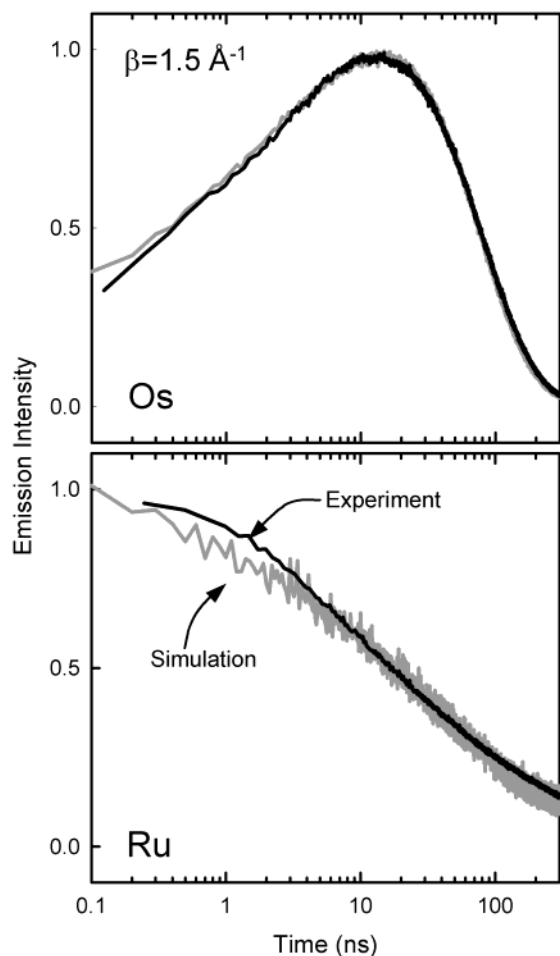


Figure 10. Comparison between the experimental data and the emission transients calculated by the simulation. The experimental Os transient corresponds to the emission detected at 780 nm minus the contribution from the Ru emission at that wavelength. The Ru transient is the emission detected at 640 nm.

sensitization events are occurring in this time window and should be weighted accordingly.

A comparison of the simulation results (obtained with $\beta = 1.5 \text{ \AA}^{-1}$) with the experimental data is shown in Figure 10. The time axis is plotted on a log scale to better represent both the short and long time aspects of the data. In both the Ru and Os cases there is excellent qualitative agreement between the simulation-generated transients and the experimental data. Overall, the agreement obtained with the other β values listed in Table 1 is qualitatively similar to that shown in Figure 10. Thus, we are unable to eliminate any of the β values listed in the table based solely on the inability of the simulation to reproduce the experimental data. This is not universally true, however, as there are some values of the attenuation parameter that do not reproduce the experimental data. We also examined β values outside this range and found that in general the quality of the fit deteriorates when β is less than 1.0 \AA^{-1} or greater than 2.1 \AA^{-1} . Reasonable agreement can be achieved with $\beta = 2.1 \text{ \AA}^{-1}$; however, the results are physically unreasonable ($k_0^{\text{Ru}} > k_0^{\text{Os}}$), and for this reason this value is omitted from the table.

The kinetics of the energy migration process are largely determined by the energy transfer rate constants that connect the metal centers. The distribution of the $\text{Ru}^* \rightarrow \text{Ru}$ and $\text{Ru}^* \rightarrow \text{Os}$ energy transfer rate constants is displayed in Figure 11, for the case where $\beta = 1.5 \text{ \AA}^{-1}$. Both distributions are highly asymmetric, with the larger rate constants (faster hopping times)

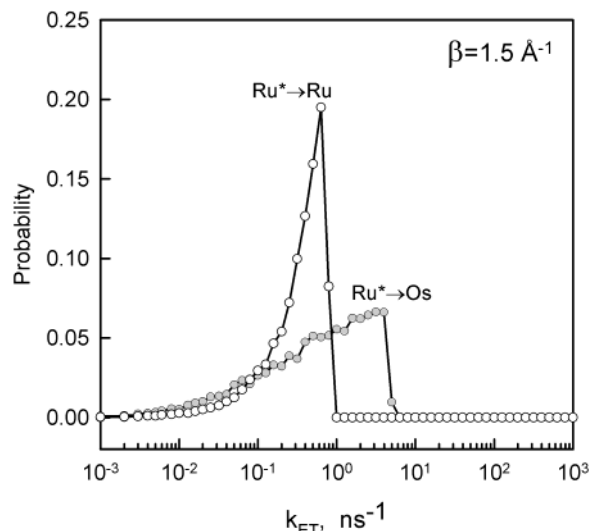


Figure 11. Distribution of rate constants for $\text{Ru}^* \rightarrow \text{Ru}$ and $\text{Ru}^* \rightarrow \text{Os}$ energy transfer observed during the Monte Carlo simulation.

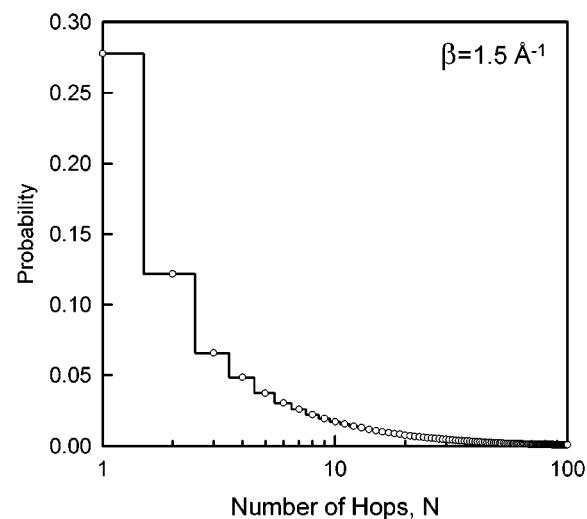


Figure 12. Distribution in the number of energy transfer jumps observed during a given trajectory. $N = 1$ corresponds to a single $\text{Ru}^* \rightarrow \text{Os}$ step. $N > 1$ corresponds to $(N - 1)$ $\text{Ru}^* \rightarrow \text{Ru}$ migration steps followed by one $\text{Ru}^* \rightarrow \text{Os}$ step.

occurring more often. For the distributions shown in Figure 11, the most probable hopping times—denoted by $\tau_{\text{max}}^{\text{Ru}}$ and $\tau_{\text{max}}^{\text{Os}}$ —are 1.6 and 0.4 ns, respectively. It is interesting to note that the most probable $\text{Ru}^* \rightarrow \text{Os}$ hopping time is similar in magnitude to the fast (400 ps) component observed in the rise of the sensitized Os emission (Section C-1), supporting the assignment that the fast kinetic component is due to Os sensitization by Ru excited states that are formed directly adjacent to Os traps. Displayed in Table 1 are the most probable hopping times observed for each β . The $\text{Ru}^* \rightarrow \text{Os}$ energy transfer times are fairly insensitive to the value used for the attenuation parameter. This is not the case for the $\text{Ru}^* \rightarrow \text{Ru}$ rate constant distribution, which shows a decrease in the hopping time with increasing β . The explanation for this trend is fairly simple.

As β is increased, the average distance that an excited Ru state can transfer on any given step is reduced. Hence, there is a definite correlation between β and the average number of hops an excited state takes before sensitization. The distribution of the number of $\text{Ru}^* \rightarrow \text{Ru}$ hops that take place prior to sensitization is shown in Figure 12. Only migration trajectories that terminate in the sensitization of an Os site are included in this

distribution. The most probable number of hops occurs at $N = 1$, which corresponds to trajectories comprised of only the $\text{Ru}^* \rightarrow \text{Os}$ energy transfer step. Although this prompt sensitization process is the most probable, it does not imply that $\text{Ru}^* \rightarrow \text{Ru}$ energy migration is a minor component. Quite the contrary, the distribution has a long tail that extends to large N , indicating that there are some trajectories in which the excited state undergoes as many as 100 to 1000 $\text{Ru}^* \rightarrow \text{Ru}$ steps. When these are added together they account for about 80% of the total probability, and thus the majority of trajectories involve some degree of $\text{Ru}^* \rightarrow \text{Ru}$ migration. When the attenuation parameter is increased, the distribution in the number of $\text{Ru}^* \rightarrow \text{Ru}$ hops shifts toward larger N , reflecting the smaller average distance per step.

A convenient measure of the polymer's performance is the efficiency of a single $\text{Ru}^* \rightarrow \text{Ru}$ step, which can be defined in terms of the average hopping time as,

$$\chi_{\text{ss}} = 1 - \frac{\langle \tau_{\text{Ru}} \rangle}{\tau_{\text{em}}^{\text{Ru}}} \quad (9)$$

The single step efficiency associated with a $\text{Ru}^* \rightarrow \text{Ru}$ hopping time on the order of 1–4 ns is in the range of 99.6–99.9%, suggesting that these polymeric systems could conduct excited-state energy over long distances without a significant loss in excited-state population. With a 99.6% single-step efficiency, an excited state could make 100 energy transfer jumps with an excited-state survival probability of about 65%. This increases to 90% when χ_{ss} is 99.9%.

IV. Summary and Implications

In this paper we present a detailed dynamics study of the excited state energy migration that occurs following photoexcitation of a multicentered assembly based on polypyridyl $\text{Ru}(\text{II})$ and $\text{Os}(\text{II})$ complexes. These results demonstrate that the $\text{Ru}(\text{II})$ derivatized polymers act as efficient “antennas” for collecting visible light and transferring its energy along the polymer backbone. This polymer system offers the design flexibility to readily create longer arrays, end functionalized arrays that have a single trap or charge-separating structure placed at one end, or nonrandom systems based on block copolymer architectures, all of which are currently under investigation in our laboratory. In addition to being soluble in a variety of nitrile solvents, it can also be embedded into plastic resins and inorganic glasses. This combined with its broad absorption throughout the visible makes it a candidate for use in molecular scale devices and solar energy conversion applications.

One path to optimizing the efficiency of these systems involves increasing the rate of $\text{Ru}^* \rightarrow \text{Ru}$ self-exchange, for this will be the limiting factor in the overall efficiency of the polymer. It is possible that the chemical structure of the $\text{Ru}(\text{II})$ monomer units may play a role in the energy transfer rate. By replacing the *dab* ligands with *bpy* we can force the MLCT

excitation to localize on the *mab* ligand rather than *dab*. We are beginning to investigate the role that the chemical structure of the monomer unit plays in the energy transfer process.

Another route to enhancing efficiency is extending the excited-state lifetime of the $\text{Ru}(\text{II})$ monomer units. This can be accomplished by ligand modification or by immersing the polymer into rigid solvents. The use of rigid environments can increase the Ru lifetime by a factor of 2 or more. Thus, to the extent that the energy transfer times remain the same, the increase in lifetime afforded by the rigid solvent could greatly enhance the overall efficiency of the molecular assemblies. Presently we are investigating the energy transfer dynamics of these molecular arrays doped into polymer films and silica xerogel monoliths. These room temperature rigid solvents are attractive in terms of their ease of processing and long-term stability needed for potential molecular device applications.

Acknowledgment. Funding for this project was provided by the U.S. Department of Energy (DE-FG02-96ER14607) and the Research Corporation (RI0048). We thank Dr. Dan Allen Myers from Kinston, North Carolina, whose gift to the UNC-CH Faculty Partners Fund also provided support for this project.

Appendix

The stochastic kinetic algorithm is adapted from Gillespie.⁸⁹ The calculation requires the selection of two random numbers, r_1 and r_2 , from a uniform distribution on the interval (0,1). One of the random numbers is used to calculate the amount of time it will take the step to occur, i.e.

$$\Delta t = \frac{1}{\sum k} \ln\left(\frac{1}{r_1}\right) \quad (10)$$

where $\sum k$ is the sum of all rate constants for all the pathways (energy transfer and deactivation) leading from the initial excited state; i.e., $\sum k = (k_{i,1} + k_{i,2} + k_{i,3} \dots k_{i,20} + k_{\text{em}})$, where $k_{i,1}$ is the rate constant for energy transfer from *site i* to *site 1*. The second random number is used to determine which of the possible pathways (e.g. energy transfer to another site, excited-state decay, etc.) the system will follow. The probability that the excited state will transfer to *site 1*, for example, is given by

$$P_{i,1} = \frac{k_{i,1}}{\sum k} \quad (11)$$

The selection of the pathway is then fairly straightforward. The interval (0,1) is divided into 20 subintervals, the sizes of which are given by the probabilities for each of the 19 possible energy transfer pathways and excited-state deactivation. The interval in which the second random number, r_2 , lies corresponds to the pathway that the system follows. After selecting the pathway, the simulation time is increased by Δt , i.e. $t = t + \Delta t$, and a new step is initiated.